From Nuclei to Compact Stars

Contents

1 Topics

The study of compact objects such as white dwarfs, neutron stars and black holes requires the interplay between nuclear and atomic physics together with relativistic field theories, e.g., general relativity, quantum electrodynamics, quantum chromodynamics, as well as particle physics. In addition to the theoretical physics aspects, the study of astrophysical scenarios characterized by the presence of at least one of the above compact object is focus of extensive research within our group. The research of our group can be divided into the following topics:

- **Nuclear and Atomic Astrophysics**. We study the properties and processes occurring in compact stars in which nuclear and atomic physics have to be necessarily applied. We focus on the properties of nuclear matter under extreme conditions of density, pressure and temperature in the compact star interiors. The matter equation of state is studied in detail taking into account all the interactions between the constituents within a full relativistic framework.

- **White Dwarfs Physics and Structure**. The aim of this part of our research is the construction of the white dwarf structure within a self-consistent description of the equation of state of the interior together with the solution of the hydrostatic equilibrium equations in general relativity. Non-magnetized, magnetized, non-rotating and rotating white dwarfs are studied. The interaction and evolution of a central white dwarf with a surrounding disk, as occurred in the aftermath of white dwarf binary mergers, is also a subject of study.

- **White Dwarfs Astrophysics**. We are interested in the astrophysics of white dwarfs both isolated and in binaries. Magnetized white dwarfs, soft gamma repeaters, anomalous X-ray pulsars, white dwarf pulsars, cataclysmic variables, binary white dwarf mergers, and type Ia supernovae are studied. The role of a realistic white dwarf interior structure is particularly emphasized.

- **Neutron Stars Physics and Structure**. We calculate the properties of the interior structure of neutron stars using realistic models of the nuclear matter equation of state within the general relativistic equations of equilibrium. Strong, weak, electromagnetic and gravitational interactions have to be jointly taken into due account within a self-consistent fully relativistic framework. Non-magnetized, magnetized, non-rotating and rotating neutron stars are studied.

- **Neutron Stars Astrophysics**. We study astrophysical systems harboring neutron stars such as isolated and binary pulsars, low and intermediate X-ray binaries, inspiraling and merging double neutron stars. Most extreme cataclysmic events involving neutron stars and their role in the explanation of extraordinarily energetic astrophysical events such as gamma-ray bursts are analyzed in detail.

- **Radiation Mechanisms of White Dwarfs and Neutron Stars**. We here study the possible emission mechanisms of white dwarfs and neutron stars. We are thus interested in the electromagnetic, neutrino and gravitational wave emission at work in astrophysical systems such as compact star magnetospheres, accretion disks surrounding them and inspiraling and merging relativistic binaries such as double neutron stars, neutron star-white dwarfs, white dwarf-white dwarf and neutron star-black hole.

- **Exact and Numerical Solutions of the Einstein and Einstein-Maxwell Equations in Astrophysics**. We analyze the ability of analytic exact solutions of the Einstein and Einstein-Maxwell equations to describe the exterior spacetime of compact stars such as white dwarfs and neutron stars. For this we compare and contrast exact analytic with numerical solutions of the stationary axisymmetric Einstein equations. The problem of matching between interior and exterior spacetime is addressed in detail. The effect of the quadrupole moment on the properties of the spacetime is also investigated. Particular attention is given to the application of exact solutions in astrophysics, e.g. the dynamics of particles around compact stars and its relevance in astrophysical systems such as X-ray binaries and gamma-ray bursts.

- **Critical Fields and Non-linear Electrodynamics Effects in Astrophysics**. We study the conditions under which ultrastrong electromagnetic fields can develop in astrophysical systems such as neutron stars and in the process of gravitational collapse to a black hole. The effects of non-linear electrodynamics minimally coupled to gravity are investigated. New analytic and numeric solutions to the Einstein-Maxwell equations representing black holes or the exterior field of a compact star are obtained and analyzed. The consequences on extreme astrophysical systems, for instance gamma-ray bursts, are studied.

2 Participants

2.1 ICRANet

- C. L. Bianco (ICRANet, Italy)
- J. A. Rueda (ICRANet, Italy)
- R. Ruffini (ICRANet, Italy)
- N. Sahakyan (ICRANet, Armenia)
- G. Vereschagin (ICRANet, Italy)
- S.-S. Xue (ICRANet, Italy)

2.2 External on going collaborations

- K. Boshkayev (Al-Farabi Kazakh National University, Kazakhstan)
- R. Camargo (Universidade do Estado de Santa Catarina, Florianópolis, Brazil)
- C. Cherubini (Università Campus Biomedico, Rome, Italy)
- J. G. Coelho (Universidade Tecnológica Federal do Paraná, Brazil)
- S. Filippi (Università Campus Biomedico, Rome, Italy)
- C. L. Fryer (University of Arizona; Los Alamos National Laboratory, USA)
- G. A. González (Universidad Industrial de Santander, Colombia)
- M. M. Guzzo (Universidade Estadual de Campinas, Brazil)

- F. D. Lora-Clavijo (Universidad Industrial de Santander, Colombia)
- P. Lorén Aguilar (University of Exeter, United Kingdom)
- S. O. Kepler (Universidade Federal do Rio Grande do Sul, Brazil)
- M. Malheiro (Instituto Tecnológico de Aeronáutica, Brazil)
- R. M. Jr. Marinho (Instituto Tecnológico de Aeronáutica, Brazil)
- G. Mathews (University of Notre Dame, USA)
- L. A. Nuñez (Universidad Industrial de Santander, Colombia)
- R. Riahi (Department of Science, Shahrekord Branch, Islamic Azad University, Iran)
- C. V. Rodrigues (Instituto Nacional de Pesquisas Espaciais, Brazil)
- F. Rossi-Torres (Universidade Estadual de Campinas, Brazil)
- J. I. Zuluaga (Universidad de Antioquia, Colombia)

2.3 Postdocs

- L. Becerra (Universidad Pontificia Católica de Chile, Chile)
- C. L. Ellinger (Los Alamos National Laboratory, USA)
- J. P. Pereira (Universidade Federal do ABC, Brazil; Mathematical Sciences and STAG Research Centre, University of Southampton, United Kingdom)
- Y. Wang (ICRANet, Italy)

2.4 Graduate Students

- E. Becerra (ICRANet; Sapienza University of Rome, Italy)
- J. M. Blanco-Iglesias (Universitat Politècnica de Catalunya)

- S. Campion (ICRANet; Sapienza University of Rome, Italy)
- G. A. Carvalho (Instituto Tecnológico de Aeronáutica, Brazil)
- R. V. Lobato (ICRANet; Sapienza University of Rome, Italy; Instituto Tecnológico de Aeronáutica, Brazil)
- R. Moradi (ICRANet; Sapienza University of Rome, Italy)
- J. F. Rodriguez (ICRANet; Sapienza University of Rome, Italy)
- J. D. Uribe (ICRANet; Sapienza University of Rome, Italy)

3 Publications 2019

3.1 Refereed Journals

3.1.1 Printed

1. Rodríguez, J. F.; Rueda, J. A.; Ruffini, R., *SPH Simulations of the Induced Gravitational Collapse Scenario of Long Gamma-Ray Bursts Associated with Supernovae*, The Astrophysical Journal 871, 14, 2019.

   We present the first three-dimensional smoothed particle hydrodynamics simulations of the induced gravitational collapse scenario of long-duration gamma-ray bursts (GRBs) associated with supernovae (SNe). We simulate the SN explosion of a carbon-oxygen core (CO_{core}) forming a binary system with a neutron star (NS) companion. We follow the evolution of the SN ejecta, including their morphological structure, subject to the gravitational field of both the new NS (νNS) formed at the center of the SN and the one of the NS companion. We compute the accretion rate of the SN ejecta onto the NS companion, as well as onto the νNS from SN matter fallback. We determine the fate of the binary system for a wide parameter space including different CO_{core} and NS companion masses, orbital periods, and SN explosion geometry and energies. We identify, for selected NS nuclear equations of state, the binary parameters leading the NS companion, by hypercritical accretion, either to the mass-shedding limit or to the secular axisymmetric instability for gravitational collapse to a black hole (BH), or to a more massive, fast-rotating, stable NS. We also assess whether the binary remains gravitationally bound after the SN explosion, hence exploring the space of binary and SN explosion parameters leading to νNS-NS and νNS-BH binaries. The consequences of our results for the modeling of long GRBs, i.e., X-ray flashes and binary-driven hypernovae, are discussed.

2. Rueda, J. A.; Ruffini, R.; Becerra, L. M.; Fryer, C. L., *Universal relations*

for the Keplerian sequence of rotating neutron stars, Physical Review D 99, 043004, 2019.

We investigate the Keplerian (mass-shedding) sequence of rotating neutron stars. Twelve different equations of state are used to describe the nuclear structure. We find four fitting relations which connect the rotating frequency, mass and radius of stars in the mass-shedding limit to the mass and radius of stars in the static sequence. We show the breakdown of approximate relation for the Keplerian frequency derived by Lattimer and Prakash [Science 304, 536 (2004)] and then we present a new, equation of state (EOS)-independent and more accurate relation. This relation fits the Keplerian frequency of rotating neutron stars to about 2% for a large range of the compactness MS/RS of the reference nonrotating neutron star, namely the static star with the same central density as the rotating one. The performance of the fitting formula is close to 4% for $M_S/R_S \leq 0.05\ M_\odot/\mathrm{km}$ ($f_K \leq 350$ Hz). We present additional EOS-independent relations for the Keplerian sequence including relations for $M_K f_K$ and $R_K f_K$ in terms of $M_S f_S$ and $R_S f_S$, respectively, one of M_K/R_K as a function of f_K/f_S and M_S/R_S, and a relation between the MK, RK and fK. These new fitting relations are approximately EOS independent with an error in the worst case of 8%. The universality of the Keplerian sequence properties presented here add to the set of other neutron star universal relations in the literature such as the I -Love-Q relation, the gravitational binding energy and the energy, angular momentum and radius of the last circular orbit of a test particle around rotating neutron stars. This set of universal, analytic formulas facilitates the inclusion of general relativistic effects in the description of relativistic astrophysical systems involving fast rotating neutron stars.

3. Wang, Y.; Rueda, J. A.; Ruffini, R.; Becerra, L.; Bianco, C.; Becerra, L.; Li, L.; Karlica, M., *Two Predictions of Supernova: GRB 130427A/SN 2013cq and GRB 180728A/SN 2018fip* , The Astrophysical Journal 874, 39, 2019.

   On 2018 July 28, GRB 180728A triggered Swift satellites and, soon after the determination of the redshift, we identified this source as a type II binary-driven hypernova (BdHN II) in our model. Consequently, we predicted the appearance time of its associated supernova (SN), which was later confirmed as SN 2018fip. A BdHN II originates in a binary composed of a carbon-oxygen core (CO_{core}) undergoing SN, and the SN ejecta hypercritically accrete onto a companion neutron star (NS). From the time of the SN shock breakout to the time when the hypercritical accretion starts, we infer the binary separation $\approx 3 \times 10^{10}$ cm. The accretion explains the prompt emission of isotropic energy $\approx 3 \times 10^{51}$ erg, lasting 10 s, and the accompanying observed blackbody emission from a thermal convective instability bubble. The new neutron star (νNS) originating from the SN powers the late afterglow from which a νNS initial spin of 2.5 ms is inferred. We compare GRB 180728A with GRB 130427A, a type I binary-driven hypernova (BdHN I) with isotropic energy $> 10^{54}$ erg. For GRB 130427A we have inferred an initially closer binary separation of $\approx 10^{10}$ cm, implying a higher accretion rate leading to the collapse of the NS companion with consequent black hole formation, and a faster, 1 ms spinning νNS. In both cases, the optical spectra of the SNe are similar, and not correlated to the energy of the GRB. We present three-dimensional smoothed-particle-hydrodynamic simulations and visualizations of the BdHNe I and II.

4. Rueda, J. A.; Ruffini, R.; Wang, Y.; Bianco, C. L.; Blanco-Iglesias, J. M.; Karlica, M.; Lorén-Aguilar, P.; Moradi, R.; Sahakyan, N., *Electromagnetic emission of white dwarf binary mergers*, Journal of Cosmology and Astroparticle Physics, Issue 03, 044, 2019.

   It has been recently proposed that the ejected matter from white dwarf (WD) binary mergers can produce transient, optical and infrared emission similar to the “kilonovae” of neutron star (NS) binary mergers. To confirm this we calculate the electromagnetic emission from WD-WD mergers and compare with kilonova observations. We simulate WD-WD mergers leading to a massive, fast rotating, highly magnetized WD with an adapted version of the smoothed-particle-hydrodynamics (SPH) code Phantom. We thus obtain initial conditions for the ejecta such as escape velocity, mass and initial position and distribution. The subsequent thermal and dynamical evolution of the ejecta is obtained by integrating the energy-conservation equation accounting for expansion cooling and a heating source given by the fallback accretion onto the newly-formed WD and its magneto-dipole radiation. We show that magnetospheric processes in the merger can lead to a prompt, short gamma-ray emission of up to $\approx 10^{46}$ erg in a timescale of 0.1–1 s. The bulk of the ejecta initially expands non-relativistically with velocity 0.01 c and then it accelerates to 0.1 c due to the injection of fallback accretion energy. The ejecta become transparent at optical wavelengths around $\sim$ 7 days post-merger with a luminosity 10^{41}–10^{42} erg s^{-1}. The X-ray emission from the fallback accretion becomes visible around $\sim$ 150–200 day post-merger with a luminosity of 10^{39} erg s^{-1}. We also predict the post-merger time at which the central WD should appear as a pulsar depending on the value of the magnetic field and rotation period.

5. Rueda, J. A.; Ruffini, R.; Wang, Y., *Induced Gravitational Collapse, Binary-Driven Hypernovae, Long Gramma-ray Bursts and Their Connection with Short Gamma-ray Bursts*, Universe, 5, issue 5, 2019. Invited Review Published by Universe as part of the Special Issue Accretion Disks, Jets, Gamma-Ray Bursts and Related Gravitational Waves.

   There is increasing observational evidence that short and long Gamma-ray bursts (GRBs) originate in different subclasses, each one with specific energy release, spectra, duration, etc, and all of them with binary progenitors. The binary components involve carbon-oxygen cores (CO_{core}), neutron stars (NSs), black holes (BHs), and white dwarfs (WDs). We review here the salient features of the specific class of binary-driven hypernovae (BdHNe) within the induced gravitational collapse (IGC) scenario for the explanation of the long GRBs. The progenitor is a CO_{core}-NS binary. The supernova (SN) explosion of the CO core , producing at its center a new NS (νNS), triggers onto the NS companion a hypercritical, i.e., highly super-Eddington accretion process, accompanied by a copious emission of neutrinos. By accretion the NS can become either a more massive NS or reach the critical mass for gravitational collapse with consequent formation of a BH. We summarize the results on this topic from the first analytic estimates in 2012 all the way up to the most recent three-dimensional (3D) smoothed-particle-hydrodynamics (SPH) numerical simulations in 2018. Thanks to these results it is by now clear that long GRBs are richer and more complex systems than thought before. The SN explosion and its hypercritical accretion onto the NS explain the X-ray precursor. The feedback of the NS accretion, the NS collapse and the BH formation produce asymmetries in the SN ejecta, implying the necessity of a 3D analysis for GRBs. The newborn BH, the surrounding matter and the magnetic field inherited from the NS, comprises the inner engine from which the GRB electron-positron plasma and the high-energy emission are initiated. The impact of the electron-positron plasma on the asymmetric ejecta transforms the SN into a hypernova (HN). The dynamics of the plasma in the asymmetric ejecta leads to signatures depending on the viewing angle. This explains the ultrarelativistic prompt emission in the MeV domain and the mildly-relativistic flares in the early afterglow in the X-ray domain. The feedback of the νNS pulsar-like emission on the HN explains the X-ray late afterglow and its power-law regime. All of the above is in contrast with a simple GRB model attempting to explain the entire GRB with the kinetic energy of an ultrarelativistic jet extending through all of the above GRB phases, as traditionally proposed in the "collapsar-fireball" model. In addition, BdHNe in their different flavors lead to νNS-NS or νNS-BH binaries. The gravitational wave emission drives these binaries to merge producing short GRBs. It is thus established a previously unthought interconnection between long and short GRBs and their occurrence rates. This needs to be accounted for in the cosmological evolution of binaries within population synthesis models for the formation of compact-object binaries.

6. Becerra, L.; Boshkayev, K.; Rueda, J. A.; Ruffini, R., *Time evolution of rotating and magnetized white dwarf stars*, Monthly Notices of the Royal Astronomical Society 487, 812, 2019.

   We investigate the evolution of isolated, zero and finite temperature, massive, uniformly rotating and highly magnetized white dwarf stars under angular momentum loss driven by magnetic dipole braking. We consider the structure and thermal evolution of white dwarf isothermal cores taking also into account the nuclear burning and neutrino emission processes. We estimate the white dwarf lifetime before it reaches the condition either for a type Ia supernova explosion or for the gravitational collapse to a neutron star. We study white dwarfs with surface magnetic fields from 10^6 to 10^9 G and masses from 1.39 to 1.46 $M_\odot$ and analyse the behaviour of the white dwarf parameters such as moment of inertia, angular momentum, central temperature, and magnetic field intensity as a function of lifetime. The magnetic field is involved only to slow down white dwarfs, without affecting their equation of state and structure. In addition, we compute the characteristic time of nuclear reactions and dynamical time scale. The astrophysical consequences of the results are discussed.

7. Ruffini, R.; Moradi, R.; Rueda, J. A.; Becerra, L.; Bianco, C. L.; Cherubini,

C.; Filippi, S.; Chen, Y. C.; Karlica, M.; Sahakyan, N.; Wang, Y.; Xue, S. S., *On the GeV Emission of the Type I BdHN GRB 130427A*, The Astrophysical Journal 852, 120, 2018.

We propose that the "inner engine" of a type I binary-driven hypernova (BdHN) is composed of Kerr black hole (BH) in a non-stationary state, embedded in a uniform magnetic field B_0 aligned with the BH rotation axis and surrounded by an ionized plasma of extremely low density of 10^{-14} g cm^{-3}. Using GRB 130427A as a prototype, we show that this "inner engine" acts in a sequence of elementary impulses. Electrons accelerate to ultrarelativistic energy near the BH horizon, propagating along the polar axis, $\theta = 0$, where they can reach energies of $\sim 10^{18}$ eV, partially contributing to ultrahigh-energy cosmic rays. When propagating with $\theta \neq 0$ through the magnetic field B_0, they produce GeV and TeV radiation through synchroton emission. The mass of BH, $M = 2.31 M_\odot$, its spin, $\alpha = 0.47$, and the value of magnetic field $B_0 = 3.48 \times 10^{10}$ G, are determined self consistently to fulfill the energetic and the transparency requirement. The repetition time of each elementary impulse of energy $\mathcal{E} \sim 10^{37}$ erg is $\sim 10^{-14}$ s at the beginning of the process, then slowly increases with time evolution. In principle, this "inner engine" can operate in a gamma-ray burst (GRB) for thousands of years. By scaling the BH mass and the magnetic field, the same inner engine can describe active galactic nuclei.

3.1.2 Accepted for publication or in press

1. Uribe, J. D.; Rueda, J. A., *Some recent results on neutrino oscillations in hypercritical accretion*, to appear in Astronomische Nachrichten.

   The study of neutrino flavour oscillations in astrophysical sources have been boosted in the last two decades thanks to achievements in experimental neutrino physics and in observational astronomy. We here discuss two cases of interest in the modeling of short and long gamma-ray bursts (GRBs): hypercritical, i.e. highly super-Eddington spherical/disk accretion onto a neutron star (NS)/black hole (BH). We show that in both systems the ambient conditions of density and temperature imply the occurrence of neutrino flavour oscillations, with a relevant role of neutrino self-interactions.

3.1.3 Submitted for publication

1. Rodríguez, J. F.; Rueda, J. A.; Ruffini, R.; Zuluaga, J. I; Blanco-Iglesias, J. M.; Lorén-Aguilar, P., *Chirping compact stars: gravitational radiation and detection degeneracy with binary systems. A conceptual pathfinder for space-based gravitational-wave observatories*, submitted to Physical Review D.

   Compressible, Riemann S-type ellipsoids can emit gravitational waves (GWs) with a chirp-like behavior (hereafter *chirping* ellipsoids, CELs). We show that the GW frequency-amplitude evolution of CELs (mass $\sim$ 1 $M_\odot$, radius $\sim$ 10^3 km, polytropic equation of state with index $n \approx 3$) is indistinguishable from that emitted by double white dwarfs (DWDs) and by extreme mass-ratio inspirals (EMRIs) composed of an intermediate-mass (e.g. 10^3 $M_\odot$) black hole and a planet-like (e.g. 10^{-4} $M_\odot$) companion, in a specific frequency interval within the detector sensitivity band in which the GWs of all these systems are quasi-monochromatic. We estimate that for reasonable astrophysical assumptions, the rates in the local Universe of CELs, DWDs and EMRIs in the mass range considered here, are very similar, posing a detection-degeneracy challenge for space-based GW detectors. The astrophysical implications of this CEL-binary detection degeneracy by space-based GW-detection facilities, are outlined.

2. Riahi, R.; Rueda, J. A., *New constraints on the equation of state and the critical mass of non-rotating neutron stars from PSR J0740+6620*, submitted to Acta Astronomica.

   The mass of the millisecond pulsar PSR J0740+6620, with a rotation frequency of 346 Hz, has been recently measured to be $2.14^{+0.1}_{-0.09}$ $M_\odot$ (68% confidence interval), becoming the most massive neutron star observed, surpassing the $2.01 \pm 0.04 M_\odot$ of PSR J0348-432, with a rotation frequency of 25 Hz. We investigate the direct impact of this new measurement on the equation of state (EOS) of neutron star matter, and on the critical mass of non-rotating neutron stars. We use 21 EOS representative of different nuclear matter models (2 microscopic, 17 relativistic mean-field and 2 Skyrme models), and the structure and stellar parameters (mass, polar and equatorial radii, etc) are obtained by numerical integration of the axially symmetric Einstein equations with the LORENE public code. First, we show that PSR J0348-432 rules out 7 EOS of the sample. Then, we show that of the 14 surviving EOS, 6 are ruled out by PSR J0740+6620, leaving only 8 survivors: 1 microscopic, 6 relativistic mean-field, and 1 Skyrme models. Being a much faster rotator, we evaluate the contribution of rotation to the mass of PSR J0740+6620, so by subtracting it off, we obtain the actual new constraint to the critical mass of a non-rotating neutron star. We found that, adopting the central value of the mass-interval, $2.14 M_{\odot}$, the rotational energy contributes $\approx 0.02\ M_{\odot}$, so only 1% to the total mass. This implies that PSR J0740+6620 is more massive than PSR J0348-432 because it is a denser object, hence its measured mass indeed imposes a new, more stringent constraint to the critical mass of non-rotating neutron star with respect to PSR J0348-432: it must be above $2.12 M_{\odot}$. Adopting the 1σ interval, the critical mass must be larger than 2.02–$2.22 M_{\odot}$. For the upper edge value, only 4 of the 21 EOS of the sample survive.

3. Uribe, J. D., Rueda, J. A., *Neutrino oscillations in a neutrino-dominated accretion disk around a Kerr BH*, submitted to Journal of Cosmology and Astroparticle Physics.

   In the binary-driven hypernova (BdHN) model of long gamma-ray bursts, a carbon-oxygen star explodes as a supernova (SN) in presence of a neutron star binary companion in close orbit. Hypercritical (i.e. highly super-Eddington) accretion of the ejecta matter onto the neutron star sets in, making it reach the critical mass with consequent formation of a Kerr black hole (BH). We have recently shown that, during the accretion process onto the neutron star, fast neutrino flavour oscillations occur. Numerical simulations of the above system show that a part of the ejecta keeps bound to the newborn Kerr BH, leading to a new process of hypercritical accretion. We here address, also for this phase of the BdHN, the occurrence of neutrino flavour oscillations given the extreme conditions of high density (up to 10^{12} g cm^{-3}) and temperatures (up to tens of MeV) inside this disk. We estimate the evolution of the electronic and non-electronic neutrino content within the two-flavour formalism ($\nu_e \nu_x$) under the action of neutrino collective effects by neutrino self-interactions. We find that neutrino oscillations inside the disk have frequencies between $\sim (10^5$–$10^9)$ s^{-1}, leading the disk to achieve flavour equipartition. This implies that the energy deposition rate by neutrino annihilation ($\nu + \bar{\nu} \rightarrow e^- + e^+$) in the vicinity of the Kerr BH, is smaller than previous estimates in the literature not accounting by flavour oscillations inside the disk. The exact value of the reduction factor depends on the ν_e and ν_x optical depths but it can be as high as ~ 5. The results of this work are a first step toward the analysis of neutrino oscillations in a novel astrophysical context and, as such, deserve further attention.

4. Moradi, R.; Rueda, J. A.; Ruffini, R.; Wang, Y., *The newborn black hole in GRB 191014C manifests that is alive*, submitted to Astronomy and Astrophysics.

   The popular view that BHs (BH) are dark objects, a sink of energy rather than an energy source, arises from three assumptions, that they are (i) in vacuum, (ii) in an asymptotically flat space-time, and (iii) stationary. As a result, despite theoretical efforts, the search for an efficient mechanism to extract the energy from a BH, able to power the most energetic astrophysical sources, gamma-ray bursts (GRBs) and active galactic nuclei (AGNs), has been unsuccessful for decades. Here we show that an extremely efficient electrodynamical process of BH energy extraction occurs in the "inner engine", violating the assumptions (i)–(iii), composed of a rotating BH in a background of very low density ionized plasma and a test, ordered magnetic field, aligned and parallel with the rotation axis. It operates in a sequence of "quantized" steps, each emitting a "blackholic quantum", initially of energy 10^{37} erg, over a timescale of 10^{-14} s, leading to GeV and TeV photons with luminosities of 10^{51} erg s^{-1}. Every event takes away only 10^{-16} of the extractable energy of the BH, allowing the "inner engine" to operate for thousands of years or more. The blackholic quantum of energy, with such a characteristic short timescale, is emitted in the entire Universe in view of the ubiquitous and homogeneous cosmological presence of GRBs. This suggests the intriguing possibility that, rather than representing the end of life, BHs may have a relevant role in the evolution of life in our Universe.

5. Rueda, J. A.; Ruffini, R., *The blackholic quantum*, submitted to European Physical Journal C.

   We show that the high-energy emission of GRBs originates in the *inner engine*: a Kerr black hole (BH) surrounded by matter and a magnetic field B_0. It radiates a sequence of discrete events of particle acceleration, each of energy $\mathcal{E} = \hbar\,\Omega_{\rm eff}$, the *blackholic quantum*, where $\Omega_{\rm eff} = 4(m_{\rm Pl}/m_n)^8(c\,a/G\,M)(B_0^2/\rho_{\rm Pl})\Omega_+$. Here M, $a = J/M$, $\Omega_+ =$

$c^2\partial M/\partial J = (c^2/G)\, a/(2Mr_+)$ and r_+ are the BH mass, angular momentum per unit mass, angular velocity and horizon; m_n is the neutron mass, $m_{\rm Pl}$, $\lambda_{\rm Pl} = \hbar/(m_{\rm Pl}c)$ and $\rho_{\rm Pl} = m_{\rm Pl}c^2/\lambda_{\rm Pl}^3$, are the Planck mass, length and energy density. The timescale of each process is $\tau_{\rm el} \sim \Omega_+^{-1}$. We show an analogy with the Zeeman and Stark effects, properly scaled from microphysics to macrophysics, that allows us to define the *BH magneton*, $\mu_{\rm BH} = (m_{\rm Pl}/m_n)^4 (c\,a/G\,M) e\hbar/(Mc)$. We give quantitative estimates for GRB 130427A adopting $M = 2.3\ M_\odot$, $c\,a/(G\,M) = 0.3$ and $B_0 = 2.9 \times 10^{14}$ G. Each emitted *quantum*, $\mathcal{E} \sim 10^{44}$ erg, extracts only 10^{-9} times the BH rotational energy, guaranteeing that the process can be repeated for thousands of years. The *inner engine* can also work in AGN as we here exemplified for the supermassive BH at the center of M87.

6. Rueda, Jorge A.; Ruffini, R.; Karlica, M.; Moradi, R.; Wang, Y., *Inferences from GRB 190114C: Magnetic Field and Afterglow of BdHN*, submitted the The Astrophysical Journal.

   GRB 190114C is the first binary-driven hypernova (BdHN) fully observed from the initial supernova appearance to the final emergence of the optical SN signal. It offers an unprecedented testing ground for the BdHN theory and it is here determined and further extended to additional gamma-ray bursts (GRBs). BdHNe comprise four subclasses of long GRBs with progenitors a binary system composed of a carbon-oxygen star ($\rm CO_{core}$) and a neutron star (NS) or a black hole (BH) companion. The CO core explodes as a SN leaving at its center a newborn NS (νNS). The SN ejecta hypercritically accretes both on the νNS and the NS/BH companion. BdHNe I are the tightest binaries where the accretion leads the companion NS to gravitational collapse into a BH. In BdHN II the accretion onto the NS is lower, so there is no BH formation. In BdHN IV the accretion occurs on an already formed BH. We infer the same structure of the afterglow for GRB 190114C and other selected examples of BdHNe I (GRB 130427A, GRB 160509A, GRB 160625B) and for BdHN II (GRB 180728A). In all the cases the explanation of the afterglow is reached via the synchrotron emission powered by the νNS: their magnetic fields structures and their spin are determined. For BdHNe I, we discuss the properties of the magnetic field embedding the newborn BH, inherited from the collapsed NS and amplified during the gravitational collapse process, and surrounded by the SN ejecta.

7. de Lima, R. C. R.; Coelho, J. G.; Pereira, J. P.; Rodrigues, C. V.; Rueda, J. A., *Constraining the hot spots on SGR J1745-2900 using X-ray light-curve data*, submitted to The Astrophysical Journal.

   SGR J1745–2900 was detected from its outburst activity in April 2013 and it was the first soft gamma repeater (SGR) detected near the center of the Galaxy (Sagittarius A*). We use a 3.5-year Chandra X-ray light-curve data to constrain some neutron star (NS) geometric parameters. We assume that the flux modulation comes from hot spots on the stellar surface. Our model includes the NS mass, radius, a maximum of three spots of any size, temperature and positions, and general relativistic effects. We find that one or two (either free or antipodal) hot spots are unable to fit well the data, whereas three hot spots – two of them antipodal – lead to better fits. The three spots are large, with angular semi-apertures ranging from 16–67 degrees. The large size found for the spots points to a magnetic field with a nontrivial poloidal and toroidal structure (in accordance with magnetohydrodynamics investigations) and is consistent with the small characteristic age of the star. Finally, we also discuss possible constraints on the mass and radius of SGR J1745–2900 and briefly envisage possible scenarios accounting for the 3.5-year evolution of SGR J1745–290 hot spots.

3.2 Conference Proceedings

1. Romero Jorge, A. W.; Rodriguez Querts, E.; Perez Rojas, H.; Perez Martinez, A.; Cruz Rodriguez, L.; Piccinelli Bocchi, G.; Rueda, J. A., *The photon time delay in magnetized vacuum magnetosphere*, 5th Caribbean Symposium on Cosmology, Nuclear and Astroparticle Physics (STARS2019); 6th International Symposium on Strong Electromagnetic Fields and Neutron Stars (SMFNS2019).

   We study the transverse propagation of photons in a magnetized vacuum considering radiative corrections in the one-loop approximation. The dispersion equation is modified due to the magnetized photon self-energy in the transparency region ($0 < \omega < 2m_e$). The aim of our study is to explore the propagation of photons in a neutron star magnetosphere (described by magnetized vacuum). The solution of the dispersion equation is obtained in terms of analytic functions. The larger the magnetic field, the higher the phase velocity and the more the dispersion curve deviates from the light-cone. For fixed values of the frequency, we study the dependence of photon time delay with the magnetic field strength, as well as with distance. For the latter, we adopt a magnetic dipole configuration and obtain that, contrary to the expectation, photons of higher energy experience a longer time delay. A discussion of potential causes of this behaviour is presented.

The Astrophysical Journal, 871:14 (29pp), 2019 January 20 https://doi.org/10.3847/1538-4357/aaf6b3

SPH Simulations of the Induced Gravitational Collapse Scenario of Long Gamma-Ray Bursts Associated with Supernovae

L. Becerra[1,2], C. L. Ellinger[3], C. L. Fryer[3], J. A. Rueda[1,2,4], and R. Ruffini[1,2,4]
[1] ICRA, Dipartimento di Fisica, Sapienza Università di Roma, Piazzale Aldo Moro 5, I-00185 Rome, Italy
[2] ICRANet, Piazza della Repubblica 10, I-65122 Pescara, Italy
[3] CCS-2, Los Alamos National Laboratory, Los Alamos, NM 87545, USA
[4] ICRANet-Rio, Centro Brasileiro de Pesquisas Físicas, Rua Dr. Xavier Sigaud 150, 22290-180 Rio de Janeiro, Brazil
Received 2018 March 12; revised 2018 December 3; accepted 2018 December 4; published 2019 January 18

Abstract

We present the first three-dimensional smoothed particle hydrodynamics simulations of the induced gravitational collapse scenario of long-duration gamma-ray bursts (GRBs) associated with supernovae (SNe). We simulate the SN explosion of a carbon–oxygen core (CO_{core}) forming a binary system with a neutron star (NS) companion. We follow the evolution of the SN ejecta, including their morphological structure, subject to the gravitational field of both the new NS (νNS) formed at the center of the SN and the one of the NS companion. We compute the accretion rate of the SN ejecta onto the NS companion, as well as onto the νNS from SN matter fallback. We determine the fate of the binary system for a wide parameter space including different CO_{core} and NS companion masses, orbital periods, and SN explosion geometry and energies. We identify, for selected NS nuclear equations of state, the binary parameters leading the NS companion, by hypercritical accretion, either to the mass-shedding limit or to the secular axisymmetric instability for gravitational collapse to a black hole (BH), or to a more massive, fast-rotating, stable NS. We also assess whether the binary remains gravitationally bound after the SN explosion, hence exploring the space of binary and SN explosion parameters leading to νNS–NS and νNS–BH binaries. The consequences of our results for the modeling of long GRBs, i.e., X-ray flashes and binary-driven hypernovae, are discussed.

Key words: accretion, accretion disks – binaries: close – gamma-ray burst: general – supernovae: general – stars: black holes – stars: neutron

1. Introduction

The induced gravitational collapse (IGC) concept was initially introduced to explain the temporal and spatial coincidence of long gamma-ray bursts (GRBs) with energies $E_{iso} > 10^{52}$ erg and Type Ic supernovae (SNe). In a binary system composed of a carbon–oxygen core (CO_{core}) and a neutron star (NS), the explosion of the CO_{core} triggers the hypercritical accretion onto the NS. For the most compact binary systems, the accretion rate onto the NS is such that it can reach the critical mass against gravitational collapse and form a black hole (BH) with consequent emission of a GRB. These systems have been called binary-driven hypernovae (BdHNe; see Ruffini et al. 2014). Later, the IGC paradigm was extended to X-ray flashes (XRFs) with energies $E_{iso} < 10^{52}$ erg that occur when the accretion rate onto the NS is lower, so it does not induce its gravitational collapse to a BH but instead leads to a massive, fast-rotating, stable NS. For further theoretical and observational details on these two subclasses of long GRBs, we refer the reader to Ruffini et al. (2016) and references therein.

The physical picture of the IGC was first proposed in Ruffini et al. (2001), formally formulated in Rueda & Ruffini (2012), and then applied for the first time for the explanation of GRB 090618 in Izzo et al. (2012). Rueda & Ruffini (2012) presented analytical estimates of the accretion rate and the possible fate of the accreting NS binary companion. This first simple model assumed (1) a pre-SN uniform density profile following a homologous expansion and (2) approximately constant masses of the NS ($\approx 1.4\,M_\odot$) and the pre-SN core ($\approx$4–8 $M_\odot$).

The first one-dimensional (1D) simulations of the IGC process were presented in Fryer et al. (2014). These simulations included (1) detailed SN explosions of the CO_{core} obtained from a 1D core-collapse SN code (Fryer et al. 1999a), (2) hydrodynamic details of the hypercritical accretion process, and (3) the evolution of the SN ejecta falling into the Bondi–Hoyle accretion region all the way up to its incorporation into the NS surface. Following the Bondi–Hoyle formalism, they estimated accretion rates exceeding $10^{-3}\,M_\odot\,s^{-1}$, making it highly possible that the NS reaches the critical mass and the BH formation.

Already from these works, it is clear that the main binary properties that decide the occurrence of the IGC process are (1) the orbital period, P; (2) the SN ejecta velocity, v_{ej}; and (3) the initial NS companion mass. The shorter the period, the slower the ejecta, the higher the Bondi–Hoyle accretion rate, and the more massive the NS companion, the less mass is needed to induce its gravitational collapse to a BH. Both P and v_{ej} have a direct effect on the Bondi–Hoyle accretion rate via the gravitational capture radius, but they also have an indirect role via the density of the accreted matter. Since the ejecta decompress during their expansion until the NS gravitational capture radius position, there is the obvious effect that the shorter the P and the slower the v_{ej}, the higher the density at the accretion site, hence the higher the accretion rate. Clearly, the effect of v_{ej} can be seen as the effect of the SN kinetic/explosion energy, since the stronger the explosion, the higher the kinetic energy and expansion velocity, and vice versa.

There were still additional effects that needed to be included in the model to have a more general picture. Becerra et al. (2015) improved the analytical model by relaxing assumptions made in Rueda & Ruffini (2012). The ejecta density profile was adopted as a power law in radius, and its evolution with time-homologous. The amount of angular momentum transported by the ejecta entering the Bondi–Hoyle region and how much of it can be transferred to the NS was also estimated. It was shown that the ejecta have enough angular momentum to circularize around the NS, forming a disklike structure and accreting on short timescales. Bearing in mind the above-mentioned effect of P on the accretion rate, it was then determined that below the critical binary period $P \lesssim P_{\max}$, the NS accretes enough mass and angular momentum such that its gravitational collapse to a BH is induced. Conversely, for $P \gtrsim P_{\max}$, the NS does not gain enough mass and angular momentum to form a BH but just becomes a more massive NS.

Later, we presented in Becerra et al. (2016) a first attempt at a smoothed particle hydrodynamics (SPH)–like simulation of the SN ejecta expansion under the gravitational field of the NS companion. Specifically, we described the SN matter formed by point-like particles and modeled the initial power-law density profile of the $\mathrm{CO_{core}}$ by populating the inner layer with more particles and defined the initial conditions of the SN ejecta assuming a homologous velocity distribution in free expansion; i.e., $v \propto r$. The particles trajectories were computed by solving the Newtonian equations of motion, including the effects of the gravitational field of the NS companion. In these simulations, we assumed a circular motion of the NS around the SN center, implemented the changes in the NS gravitational mass owing to the accretion process via the Bondi–Hoyle formalism following Becerra et al. (2015), and, accordingly, removed from the system the particles falling within the Bondi–Hoyle surface. The accretion process was shown to proceed hypercritically thanks to the copious neutrino emission near the NS surface, which produces neutrino luminosities of up to 10^{52} erg s^{-1} and mean neutrino energies of 20 MeV. A detailed analysis of the fundamental neutrino emission properties in XRFs and BdHNe was presented in Becerra et al. (2018).

Becerra et al. (2016) made the first wide exploration of the binary parameters for the occurrence of the IGC process, and hence of the systems leading to XRFs ($P \gtrsim P_{\max}$) and BdHNe ($P \lesssim P_{\max}$), as well as of the dependence of $P_{\max}$ on the $\mathrm{CO_{core}}$ and NS companion mass. In addition, these simulations produced a first visualization of the SN ejecta morphology. Indeed, we showed in Becerra et al. (2016) how the structure of the SN ejecta, becoming asymmetric by the presence of the accreting NS companion, becomes crucial for the inference of observable signatures in the GRB afterglow. The specific example of XRF 060218 was examined to show the asymmetry effect in the X-ray emission and the feedback of the accretion energy injected into the SN ejecta on its optical emission.

It became clear that the SN ejecta morphology and the feedback of GRB emission onto the SN could also be relevant in BdHNe. In Ruffini et al. (2018b), we showed that the GRB e^+e- plasma, expanding at relativistic velocities from the newborn BH site, engulfs different amounts of mass along different directions owing to the asymmetries developed in SN density profile, leading to different dynamics and, consequently, to different signatures for different viewing angles. The agreement of such a scenario with the observed emission from the X-ray flares in the BdHN early afterglow was shown (see also Section 6 below for a discussion on this topic). The SN ejecta geometry also affects the GeV emission observed in BdHNe (Ruffini et al. 2018a).

Ruffini et al. (2018b) also showed the relevance of the binary effects and SN morphology on a most fundamental phenomenon: the GRB exploding within the SN impacts it, affecting its dynamics by transferring energy and momentum and, finally, transforming the ordinary SN into a hypernova (HN). Therefore, this model predicts that broad-lined SNe or HNe are not born as such but instead are the outcome of the GRB impact on the SN. We have given evidence of such an SN–HN transition in a BdHN by identifying the moment of its occurrence in the case of GRB 151027A (Ruffini et al. 2018c).

All of these results point to the necessity of detailed knowledge of the physical properties of the SN ejecta, and of the binary system in general, in 3D space and as a function of time for the accurate inference of the consequences on the X-ray, gamma-ray emission in XRFs and BdHNe and the GeV emission in BdHNe.

In view of the above, we present here the first 3D hydrodynamic simulations of the IGC scenario. We have used the SPH technique as developed in the SNSPH code (Fryer et al. 2006b). The SNSPH is a tree-based parallel code that has undergone rigorous testing and has been applied to study a wide variety of astrophysical problems (see, e.g., Fryer & Warren 2002; Young et al. 2006; Diehl et al. 2008; Batta et al. 2017). The simulation starts from the moment at which the SN shock front reaches the $\mathrm{CO_{core}}$ external radius, and, besides calculating the accretion rate onto the NS companion, we also follow the evolution of the binary parameters (e.g., the binary separation, period, and eccentricity) in order to determine if the final configuration becomes disrupted or not. This implies that we have also introduced the gravitational effects of the remnant NS, the νNS formed at the center of the SN explosion, allowing us to calculate the accretion onto it via matter fallback.

This article is organized as follows. In Section 2, we describe the main aspects of the SNSPH code (Fryer et al. 2006b) and the algorithm applied to simulate the accretion process. In Section 3, we give the details of the construction of the initial binary configuration. Section 4 shows the results of the simulations. We have covered a wide range of initial conditions for the binary system; i.e., we have varied the $\mathrm{CO_{core}}$ progenitors, binary initial separation, SN total energy, and initial NS mass companion. In Section 5, we analyze whether or not the binary system is disrupted by the mass loss due to the SN explosion of the $\mathrm{CO_{core}}$, and in Section 6, we compute the evolution of the binary and determine whether the stars' gravitational collapse is possible. In Section 7, we discuss the consequences of our results. Specifically, in Section 7.1, we analyze in depth the main parameters of the system that decide the fate of the NS companion; then, in Section 7.2, we discuss how these conditions could be realized in a consistent binary evolutionary path. Section 7.3 contains estimates of the occurrence rate of these systems, and Section 7.4 outlines the consequences for the explanation of the GRB prompt and afterglow emission, as well as the prediction of new observables. Finally, in Section 8, we present our conclusions and perspectives for future work. In the Appendix, we present convergence tests of the numerical simulations.

2. SPH Simulation

We use the 3D Lagrangian hydrodynamic code SNSPH (Fryer et al. 2006b) to model the evolution of the binary system after the $\mathrm{CO_{core}}$ collapses and the SN explosion occurs. The code follows the prescription of the SPH formalism in

Benz & Buchler (1990). Basically, the fluid is divided by N particles with determined position, $\boldsymbol{r}_i$; mass, m_i; and smooth length, h_i. Physical quantities for each particle are calculated through an interpolation of the form

$$A_i(\boldsymbol{r}_i) = \sum_j A_j\left(\frac{m_j}{\rho_j}\right)W(|\boldsymbol{r}_{ij}|, h_{ij}), \tag{1}$$

where $|\boldsymbol{r}_{ij}| = |\boldsymbol{r}_i - \boldsymbol{r}_j|$, W is the smoothing kernel (that is equal to zero if $r > 2h$), and $h_{ij} = (h_i + h_j)/2$ is the symmetric smooth length between particles i and j. The code allows us to evolve the smooth length with time as $dh_i/dt = -1/3(h_i/\rho_i)(d\rho_i/dt)$.

Then, the hydrodynamical equations of conservation of linear momentum and energy are written as

$$\frac{d\boldsymbol{v}_i}{dt} = -\sum_{j=1}^{N} m_j\left(\frac{P_i}{\rho_i^2} + \frac{P_j}{\rho_j^2} + \Pi_{ij}\right)\boldsymbol{\nabla}_i\, W(r, h_{ij}) + \boldsymbol{f}_g; \tag{2}$$

$$\frac{du_i}{dt} = \sum_{j=1}^{N} m_j\left(\frac{P_i}{\rho_i^2} + \frac{1}{2}\Pi_{ij}\right)(\boldsymbol{v}_i - \boldsymbol{v}_j)\cdot\boldsymbol{\nabla}_i\, W(r, h_{ij}), \tag{3}$$

where $\boldsymbol{v}_i$, P_i, ρ_i, and u_i are the particle velocity, pressure, density, and internal energy, respectively. In order to handle shocks, an artificial viscosity term is introduced through Π_{ij} as in Monaghan (1992, 2005),

$$\Pi_{ij} = \begin{cases} \frac{-\alpha(c_i + c_j)\mu_{ij} + 0.5\beta\mu_{ij}^2}{\rho_i + \rho_j} & \text{if} \quad \boldsymbol{v}_{ij}\cdot\boldsymbol{r}_{ij} < 0 \\ 0 & \text{otherwise} \end{cases}, \tag{4}$$

where c_i is the sound speed, $\boldsymbol{v}_{ij} = \boldsymbol{v}_i - \boldsymbol{v}_j$, and

$$\mu_{ij} = \frac{h_{ij}\boldsymbol{v}_{ij}\cdot\boldsymbol{r}_{ij}}{|\boldsymbol{r}_{ij}|^2 + \epsilon h_{ij}^2}. \tag{5}$$

The form for the viscosity of Equation (4) can be interpreted as a bulk and von Neuman–Richtmyer viscosity parameterized by α and β viscosity coefficients. In the simulations we adopt, as usual, $\alpha = 1.0$ and $\beta = 2.0$.

The last term of Equation (2) refers to the fluid self-gravity force. The particles are organized in a hashed oct-tree, and the gravitational force is evaluated using the multipole acceptability criterion described in Warren & Salmon (1993, 1995).

Finally, the equation of state (EOS) adopted treats the ions as a perfect gas and takes into account the radiation pressure,

$$P = \frac{1}{3}aT^4 + n_{\text{ion}}\kappa T, \tag{6}$$

$$u = aT^4 + \frac{3}{2}n_{\text{ion}}\kappa T, \tag{7}$$

where n_{ion} is the number density of ions, T is the temperature, and a is the radiation constant.

2.1. Accretion Algorithm

In the simulation, the remnants of the CO_{core} and the NS companion are model as two point masses that only interact gravitationally with each other as well as with the ejecta particles. Their equation of motion will be

$$\frac{d\boldsymbol{v}_s}{dt} = \sum_{j=1}^{N}\frac{Gm_j}{|\boldsymbol{r}_s - \boldsymbol{r}_j|^3}(\boldsymbol{r}_j - \boldsymbol{r}_s) + \frac{GM_{s'}}{|\boldsymbol{r}_s - \boldsymbol{r}_{s'}|^3}(\boldsymbol{r}_{s'} - \boldsymbol{r}_s), \tag{8}$$

where subindices s and s' make reference to the stars. In the same way, each particle of the fluid will feel an additional force from the stars' gravitational field:

$$\boldsymbol{f}_{s,i} = \frac{GM_s}{|\boldsymbol{r}_s - \boldsymbol{r}_i|^3}(\boldsymbol{r}_s - \boldsymbol{r}_i). \tag{9}$$

The stars accrete a particle j from the SN ejecta if the following conditions are fulfilled (Bate et al. 1995):

1. the particle is inside the star accretion radius, i.e.,
$$|\boldsymbol{r}_j - \boldsymbol{r}_s| < R_{j,\text{acc}};$$
2. the gravitational potential energy of the particle in the field of the star is larger than its kinetic energy, i.e.,
$$\frac{GM_s m_j}{|\boldsymbol{r}_j - \boldsymbol{r}_s|} > \frac{1}{2}m_j|\boldsymbol{v}_j - \boldsymbol{v}_s|^2;$$
and
3. the angular momentum of the particle relative to the star is less than the one it would have in a Keplerian orbit at $R_{j,\text{acc}}$, i.e.,
$$|(\boldsymbol{r}_j - \boldsymbol{r}_s)\times(\boldsymbol{v}_j - \boldsymbol{v}_s)| < \sqrt{GM_s R_{j,\text{acc}}}.$$

The accretion radius for a particle j is defined as

$$R_{j,\text{acc}} = \min\left(\xi\frac{2GM_s}{v_{js}^2 + c_j^2}, h_j\right), \tag{10}$$

and we adopt $\xi = 0.05$–0.1 (see below for further details on this parameter) in the simulations.

These conditions are evaluated at the beginning of every time step. The particles that fulfill them are removed from the simulation, and we update the properties of the star as

$$M_{s,\text{new}} = M_s + \sum_j m_j, \tag{11}$$

$$\boldsymbol{v}_{s,\text{new}} = \frac{M_s\boldsymbol{v}_s + \sum_j m_j\boldsymbol{v}_j}{M_{s,\text{new}}}, \tag{12}$$

and

$$\boldsymbol{L}_{s,\text{new}} = M_{s,\text{new}}\frac{\boldsymbol{L}_s\boldsymbol{v}_s + \sum_j m_j(\boldsymbol{r}_{s,j}\times\boldsymbol{v}_{s,j})}{M_s}. \tag{13}$$

The above sum is over the particles accreted during the corresponding time step.

3. Initial Setup

Our calculations include a suite of pre-SN progenitors with zero-age main-sequence (ZAMS) masses ranging from 15 to 40 $M_\odot$ obtained via the *KEPLER* code (Heger & Woosley 2010). The SN explosions are simulated with the 1D core-collapse code (Fryer et al. 1999a) and the multiparameter prescriptions introduced in Fryer et al. (2018) to mimic the SN engine: the energy deposition rate and duration, the size of the convection cell above the base of the proto-NS, and the time after bounce when the convective engine starts. These

Table 1
Properties of the CO_{core} Progenitors

M_{ZAMS} ($M_\odot$)	M_{rem} ($M_\odot$)	M_{ej} ($M_\odot$)	R_{core} (10^8 cm)	R_{star} (10^9 cm)	$v_{star,0}$ (10^8 cm s^{-1})	E_{grav} (10^{51} erg)	m_j ($10^{-6}\,M_\odot$)
15	1.30	1.606	8.648	5.156	9.75	0.2149	0.2–4.4
25	1.85	4.995	2.141	5.855	5.43	1.5797	2.2–11.4
30[a]	1.75	7.140	28.33	7.830	8.78	1.7916	1.9–58.9
30[b]	1.75	7.140	13.84	7.751	5.21	1.5131	1.9–58.9
40	1.85	11.50	19.47	6.529	6.58	4.4305	2.3–72.3

Notes. Each progenitor was evolved with the *KEPLER* stellar evolution code (Heger & Woosley 2010) and then exploded artificially using the 1D core-collapse code presented in Fryer et al. (1999a).
[a] $E_{sn} = 1.09 \times 10^{52}$ erg.
[b] $E_{sn} = 2.19 \times 10^{51}$ erg.

parameters are designed to include the uncertainties in the convection-enhanced SN engine (see Herant et al. 1994; Fryer & Young 2007; Murphy et al. 2013 for details).

When the shock front reaches the edge of the CO_{core}, the configuration is mapped into a 3D SPH configuration of about 1 million particles with variable mass. This is done using the weighted Voronoi tessellation (WVT), as described in Diehl et al. (2015).

The SPH configuration of the SN ejecta is constructed in the rotating reference frame of the progenitor star. In order to translate it to the center-of-mass reference frame of the initial binary system (CO_{core} + NS), the positions and velocities of the particles are modified as

$$\boldsymbol{r}_{i,\mathrm{new}} = \mathbb{R}\boldsymbol{r}_i - \boldsymbol{r}_{\mathrm{CO}}, \tag{14}$$

$$\boldsymbol{v}_{i,\mathrm{new}} = \mathbb{R}\boldsymbol{v}_i - \boldsymbol{r}_i \times \boldsymbol{\Omega}_{\mathrm{orb}} - \boldsymbol{v}_{\mathrm{CO}}, \tag{15}$$

where $\mathbb{R}$ is a rotation matrix, $\boldsymbol{r}_{\mathrm{CO}}$ and $\boldsymbol{v}_{\mathrm{CO}}$ are the position and velocity of the CO_{core} before the explosion, and Ω_{orb} is the binary orbital angular velocity that is determined once the orbital separation and star masses are established,

$$\Omega_{\mathrm{orb}} = \sqrt{\frac{G(M_{\mathrm{CO}} + M_{\mathrm{ns}})}{a_{\mathrm{orb}}^3}}, \tag{16}$$

with M_{CO} being the CO_{core} total mass, M_{NS} the NS mass, and a_{orb} the binary separation. The equatorial plane of the binary corresponds to the x–y plane; then, the initial positions of the stars (NS and νNS) are on the x-axis and the initial motion is counterclockwise.

The minimum binary period that the system can have is given by the condition that the compactness of the CO_{core} is such that there is no Roche lobe overflow before the SN explosion. Then, the minimum binary separation is determined by Eggleton (1983):

$$\frac{R_{\mathrm{star}}}{a_{\mathrm{orb}}} = \frac{0.49q^{2/3}}{0.6q^{2/3} + \ln(1 + q^{1/3})}, \tag{17}$$

with $q = M_{CO}/M_{ns}$.

Since we are interested in identifying the favorable conditions for which the NS companion can accrete enough mass and collapse into a BH, we will explore different initial conditions for the system. We have worked with four progenitors for the CO_{core} with different ZAMS masses: M_{ZAMS} = 15, 25, 30, and 40 $M_\odot$. In Table 1, we present the main proprieties of each of these progenitors at the mapping moment: the SN mass ejected, M_{ej}; the gravitational mass of the remnant star, M_{rem} (i.e., the CO_{core} mass before its collapse is $M_{star} = M_{ej} + M_{rem}$); the SN ejecta innermost radius, R_{core}; the CO_{core} radius when the collapse happens, R_{star}; and the forward shock velocity, $v_{star,0}$. In the last two columns of Table 1, we specify the gravitational energy of the star, E_{grav}, and the maximum and minimum masses of the SPH particles, m_j. Figure 1 shows the density profile of each progenitor at the moment of the mapping to the 3D SPH configuration (when the shock front of the explosion has reached the star surface). We have two models for the 30 $M_\odot$ progenitor, each with different SN explosion energy.

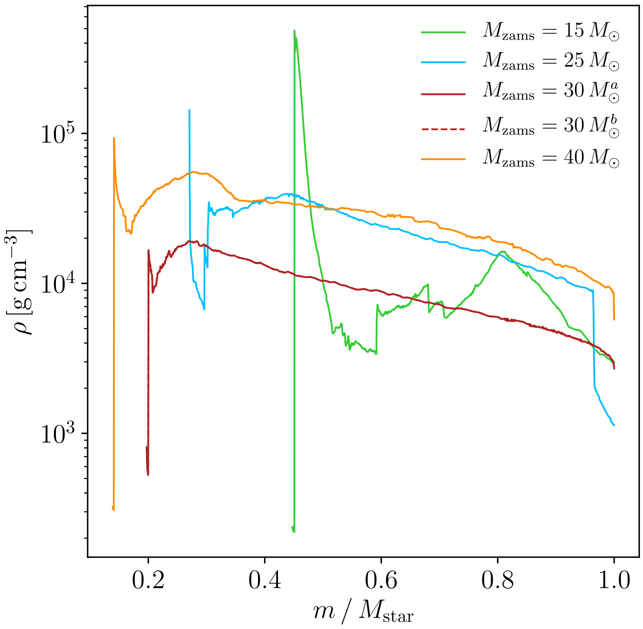

Figure 1. Density profile of the SN ejecta when the shock has reached the carbon–oxygen edge for the M_{ZAMS} = 15, 25, 30, and 40 $M_\odot$ progenitors (see Table 1). The density is given as a function of the variable m/M_{star}, namely the mass coordinate, m, normalized to the total mass of the CO_{core}, M_{star}. At this moment, the 1D simulation is mapped into a 3D SPH configuration.

It is important to notice that we are working with progenitors that were evolved as isolated stars, i.e., without taking into account that they are part of a binary system. However, as indicated in Fryer et al. (2014), there is a 3–4 order of magnitude pressure jump between the CO_{core} and helium layer; this means that the star will not expand significantly when the helium layer is removed. The CO_{core} can be 1.5–2 times larger (Moriya et al. 2010); then, the minimum period of the system might increase by a factor of 1.8–2.8.

The final fate of the system will also depend on the characteristics of the SN explosion. We run simulations varying the explosion energy of the SN. Rather than produce a broad range of explosion energies (as we did with the $30\,M_{\odot}$ progenitor), we scaled the kinetic and internal energy of the particles behind the forward shock by a factor η. In this way, the internal structure of the progenitor does not change, just the velocity and temperature.

In order to study the effect of an asymmetric SN expansion (see, e.g., Janka 2012), we adopt a single-lobe prescription (Hungerford et al. 2005) following Hungerford et al. (2003) and Young et al. (2006). Namely, the explosion is modified to a conical geometry parameterized by Θ, the opening angle of the cone, and f, the ratio of the velocities between the particles inside and outside the cone. The velocities of the SPH particles behind the forward shock are then modified as

$$V_{\text{in-cone}} = f\left[\frac{1-f^2}{2}\cos\Theta + \frac{1+f^2}{2}\right]^{-1/2} V_{\text{symm}}, \qquad (18)$$

$$V_{\text{out-cone}} = \left[\frac{1-f^2}{2}\cos\Theta + \frac{1+f^2}{2}\right]^{-1/2} V_{\text{symm}}, \qquad (19)$$

where V_{symm} is the radial velocity of the original explosion. This prescription conserves the kinetic energy of the symmetry explosion; to conserve the total energy of the SN, we scale the particles' internal energy in the same way.

In the next section, we present the results of our SPH simulations.

4. Results

In Table 2, we summarize the properties of the SN and the parameters that characterize the state of the initial binary systems with the different CO_{core} values obtained with the progenitors of Table 1. The models are labeled as "x_1mx_2px_3e," where x_1 is the M_{ZAMS} of the CO_{core} progenitor star, x_2 is the fraction between the initial orbital period and the minimum orbital period of the system that has no Roche lobe overflow, and x_3 is the value of the η factor by which the SPH particle velocities and internal energy are scaled. For each model in Table 2, we specify the sum of the ejecta kinetic and internal energy, $E_k + U_i$; the initial orbital period, $P_{\text{orb,i}}$; and the initial binary separation, $a_{\text{orb,i}}$.

For each model, we first run a simulation of the SN expansion assuming that the CO_{core} collapses and explodes as an isolated star, i.e., without the NS companion. In Table 2, we summarize the final mass of the νNS, indicated as $M_{\text{orb,i}}$, and the magnitude of the νNS kick velocity, V_{kick}. The latter is the νNS velocity due to the linear momentum accreted by the star from the fallback particles.

Then, we run simulations of the SN expansion with the CO_{core} as part of a binary system with a $2\,M_{\odot}$ NS as a companion. We expect a massive initial NS companion because the binary system evolutionary path leading to these systems has at least one common-envelope episode (see, e.g., Fryer et al. 1999b; Becerra et al. 2015, and Section 6). However, we have also performed simulations with an NS companion with an initial mass 1.4 and $1.6\,M_{\odot}$. In Table 2, we summarize the parameters that characterize the final outcome of these simulations: the νNS final mass, $M_{\nu\text{ns}}$; the NS final mass, M_{NS}; the velocity of the final binary system center of mass, V_{CM}; the final orbital period, $P_{\text{orb,f}}$; the major semi-axis and eccentricity of the orbit of the final system, $a_{\text{orb,f}}$ and e, respectively; and the amount of mass that is still bounded to the binary stars at the moment when the simulation is stopped, m_{bound}. This bound material circularizes around the stars and, at some moment, might be accreted by any of them. In the final column of Table 2, we have specified whether the system remains bound as a new binary system or is disrupted in the explosion.

4.1. Fiducial Model: 25 $M_{\odot}$ Progenitor

We are going to take the $25\,M_{\odot}$ progenitor star for the CO_{core} and a $2\,M_{\odot}$ NS as our fiducial initial binary system in order to describe in detail the main features of the simulations while the SN expands in the presence of the NS companion (model 25m1p1e of Table 2). This fiducial binary system has the minimum orbital period allowed for the system to have no Roche lobe overflow, 4.86 minutes, which corresponds to a binary separation of 1.34×10^{10} cm. Thus, this model presents the most favorable conditions for the occurrence of the induced collapse: a short period for the binary system and a massive initial NS companion. Later, we will change the initial conditions one by one and compare the outcomes with that of this fiducial system.

Figure 2 shows snapshots of the mass density in the x–y plane, the binary equatorial plane (upper panel) and x–z plane (lower panel), at different simulation times. In the plot, the reference system has been rotated and translated in such a way that the x-axis is along the line that joins the stars of the binary system and the origin is at the NS companion. In general, when the SN starts to expand, the faster outermost particles of the SN will pass almost without being disturbed by the NS gravitational field. The slower-moving material is gravitationally captured by the NS, initially forming a tail and ultimately forming a thick disk around it. In addition, there are particles from the innermost layers of the SN ejecta that do not have enough kinetic energy to escape, leading to fallback accretion onto the νNS. Then, at some point, the material that has been captured by the NS companion starts to also be attracted by the νNS and accreted by it.

To confirm the formation of the disk around the NS companion, in Figure 3, we have calculated the angular velocity profile with respect the NS companion position at different times and for two different directions: the line that joins the binary stars with the νNS in the $-x$ direction, labeled as $\theta = 0$, and the line perpendicular to it on the orbital binary plane, labeled as $\theta = \pi/2$. The angular velocity of the particles close to the NS companion ($r/a_0 < 0.25$) superpose the Keplerian angular velocity profile. This confirms the estimates from analytical approximations made in Becerra et al. (2015), where it was shown that the SN ejecta have enough angular momentum to circularize around the NS before being accreted.

Figure 4 shows the mass accretion rate as a function of simulation time onto the binary system stars: the NS companion, the νNS, and the sum of both. Either the fallback accretion rate or the NS accretion rate is much greater than the Eddington limit. The NS is allowed to accrete at this high rate by the emission of neutrinos at its surface via e^+e^- pair annihilation, which is the most efficient neutrino emission process at these density and temperature conditions (see Becerra et al. 2016 for details). This allows the matter to cool fast enough to be incorporated onto the star, and we can add the mass of the particles that fulfill the accretion conditions (see

Table 2
SPH Simulations

Model	$E_k + U_i$ (10^{51} erg)	$P_{orb,i}$ (minutes)	$a_{orb,i}$ (10^{10} cm)	$M_{\nu ns,fb}$ ($m_\odot$)	V_{kick} (10^4 cm s^{-1})	$M_{\nu ns}$ ($m_\odot$)	M_{ns} ($m_\odot$)	V_{CM} (10^7 cm s^{-1})	$P_{orb,f}$ (minutes)	$a_{orb,f}$ (10^{10} cm)	e	m_{bound} ($m_\odot$)	Bound
$M_{ZAMS} = 15\,M_\odot$ Progenitor													
15m1p07e	1.395	6.58	1.361	1.302	3.99	1.302	2.003	4.05	19.0	2.437	0.443	2.7×10^{-6}	Yes
15m1p05e	1.101	6.58	1.361	1.303	4.83	1.303	2.006	4.02	18.6	2.393	0.433	4.8×10^{-5}	Yes
15m1p03e	0.607	6.58	1.361	1.304	18.93	1.315	2.023	3.91	15.9	2.182	0.398	6.9×10^{-4}	Yes
15m1p01e	0.213	6.58	1.361	2.478	6.62	1.916	2.199	0.39	3.04	0.773	0.233	0.098	Yes
15m1p005e	0.135	6.58	1.361	2.731	1.73	2.649	2.034	0.08	5.92	1.257	0.036	0.029	Yes
15m2p03e	0.607	11.7	2.000	1.304	18.93	1.304	2.007	0.39	···	···	1.192	5.8×10^{-3}	No
15m2p01e	0.213	11.7	2.000	2.478	6.62	2.238	2.101	0.08	12.9	2.068	0.419	0.0759	Yes
15m3p01e	0.213	17.6	2.000	2.478	6.62	2.405	2.057	0.32	14.5	2.249	0.103	0.0313	Yes
$M_{ZAMS} = 25\,M_\odot$ Progenitor													
25m1p1e	3.14	4.81	1.352	1.924	1.35	1.963	2.085	7.49	116.9	8.747	0.866	0.081	Yes
25m1p09e	2.84	4.81	1.352	1.935	2.97	2.013	2.162	7.17	38.29	4.199	0.744	0.043	Yes
25m1p08e	2.53	4.81	1.352	1.953	3.57	2.081	2.441	6.09	16.5	2.454	0.600	0.075	Yes
25m1p07e	2.22	4.81	1.352	2.172	41.30	2.371	2.621	3.77	4.33	1.043	0.381	0.160	Yes
25m2p1e	3.14	8.56	1.988	1.924	1.35	1.929	2.029	6.46	···	···	1.005	0.073	No
25m3p1e	3.14	11.8	2.605	1.924	1.35	1.924	2.024	5.76	···	···	1.086	0.025	No
25m4p1e	3.14	15.9	2.984	1.924	1.35	1.916	2.014	5.34	···	···	1.096	0.013	No
25m2p07e	2.22	8.56	1.988	2.172	41.30	2.352	2.522	3.43	18.3	2.699	0.461	0.185	Yes
25m3p07e	2.22	11.8	2.605	2.172	41.30	2.301	2.523	3.25	23.5	3.11	0.477	0.138	Yes
25m5p07e	2.22	19.8	3.463	2.172	41.30	2.166	2.401	3.24	27.8	3.49	0.526	0.0051	Yes
25m15p07e	2.22	59.4	7.203	2.172	41.30	2.088	2.208	2.72	321.5	17.41	0.639	3.4×10^{-3}	Yes
$M_{ZAMS} = 30\,M_\odot$ Progenitor—exp 1													
30m1p1ea	8.43	5.82	1.667	1.756	40.80	1.757	2.007	9.67	···	···	1.701	0.0	No
30m1p07ea	5.95	5.82	1.667	1.755	39.36	1.758	2.015	9.58	···	···	1.647	9.6×10^{-4}	No
30m1p05ea	4.26	5.82	1.667	1.758	96.20	1.764	2.031	9.46	···	···	1.501	0.012	No
30m1p03ea	2.59	5.82	1.667	2.178	3.93×10^3	1.869	2.455	7.79	101.5	8.137	0.852	0.168	Yes
30m2p03ea	2.59	10.8	2.449	2.178	3.93×10^3	1.837	2.192	7.21	···	···	1.095	0.0854	No
$M_{ZAMS} = 30\,M_\odot$ Progenitor—exp 2													
30m1p1eb	3.26	5.82	1.667	4.184	141.30	3.675	2.382	3.59	12.1	2.209	0.569	0.331	Yes
30m1p12eb	3.91	5.82	1.667	2.462	147.79	2.515	2.376	5.86	46.1	5.009	0.733	0.133	Yes
30m2p12eb	3.91	10.8	2.410	2.462	147.79	2.621	2.228	4.85	157.1	11.302	0.848	0.029	Yes
30m1p2eb	6.45	5.82	1.667	1.771	13.89	1.783	2.077	9.50	···	···	1.447	5.7×10^{-3}	No
30m1p31eb	10.02	5.82	1.667	1.766	5.21	1.768	2.017	9.95	···	···	1.712	6.5×10^{-4}	No
$M_{ZAMS} = 40\,M_\odot$ Progenitor													
40m1p1e	10.723	3.49	1.295	1.871	176.43	1.874	2.119	13.68	···	···	1.845	0.038	No
40m1p09e	9.670	3.49	1.295	1.872	141.38	1.881	2.274	13.35	···	···	1.538	0.027	No
40m1p08e	8.618	3.49	1.295	1.873	242.93	1.886	2.545	12.52	···	···	1.276	0.016	No
40m1p07e	7.506	3.49	1.295	1.879	464.82	2.095	3.033	10.12	85.9	7.712	0.881	0.051	Yes
40m1p06e	6.513	3.49	1.295	6.568	69.73	3.784	3.209	4.57	2.42	0.792	0.612	1.053	Yes
40m1p05e	5.145	3.49	···	···	0.91	5.430	3.642	···	0.06	0.339	0.243	1.250	Yes
40m2p1e	10.723	6.22	1.904	1.871	176.43	1.873	2.046	10.79	–	···	2.194	6.13×10^{-3}	No

Table 2
(Continued)

Model	$E_k + U_i$ (10^{51} erg)	$P_{orb,i}$ (minutes)	$a_{orb,i}$ (10^{10} cm)	$M_{\nu ns,fb}$ ($m_\odot$)	V_{kick} (10^4 cm s^{-1})	$M_{\nu ns}$ ($m_\odot$)	M_{ns} ($m_\odot$)	V_{CM} (10^7 cm s^{-1})	$P_{orb,f}$ (minutes)	$a_{orb,f}$ (10^{10} cm)	e	m_{bound} ($m_\odot$)	Bound
40m2p07e	7.506	6.22	1.904	1.879	464.82	2.064	2.755	8.757	4408	104.26	0.984	0.078	Yes
40m4p07e	7.506	12.45	3.022	1.879	464.82	1.959	2.507	7.799	⋯	⋯	1.180	0.0744	No
40m2p06e	6.513	6.22	1.904	6.568	69.73	5.581	2.961	2.58	5.79	1.523	0.648	0.509	Yes

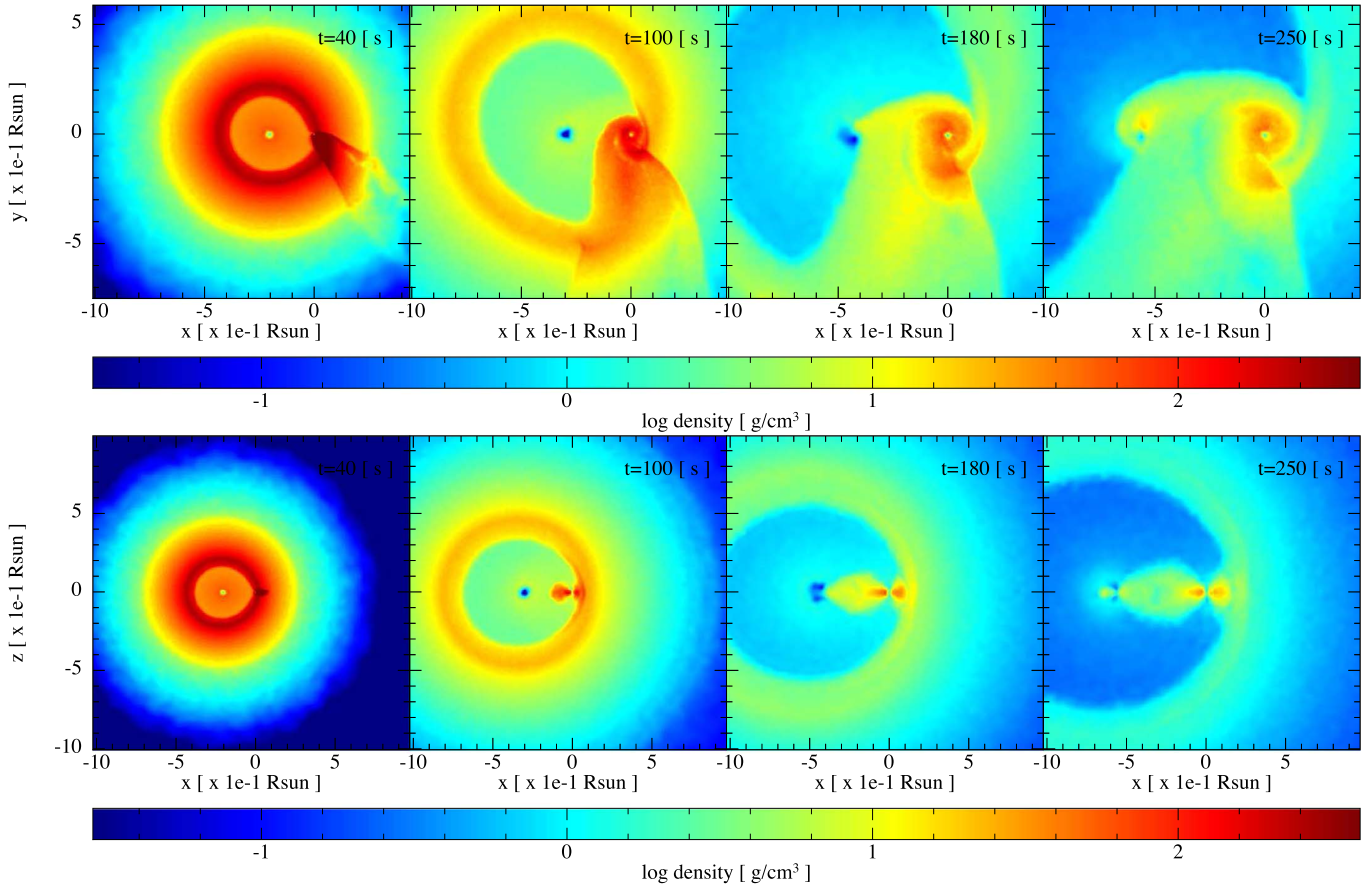

Figure 2. Snapshots of the SPH simulation of the IGC scenario. The initial binary system is formed by a CO_{core}, the progenitor of which is an $M_{ZAMS} = 25\,M_{\odot}$, and a $2\,M_{\odot}$ NS with an initial orbital period of approximately 5 minutes (model 25M1p1e of Table 2). The upper panel shows the mass density on the binary equatorial plane at different times of the simulation, while the lower panel corresponds to the plane orthogonal to the binary equatorial plane. The reference system was rotated and translated in such a way that the x-axis is along the line that joins the binary stars and the origin of the reference system is at the NS position. At $t = 40$ s (first frame from left), it can be seen that the particles captured by the NS have formed a kind of tail behind it, then these particles star to circularize around the NS and a kind of thick disk is observed at $t = 100$ s (second frame from left). The material captured by the gravitational field of the NS companion is also attracted by the νNS and starts to be accreted by it, as can be seen at $t = 180$ s (third frame). After around one initial orbital period, at $t = 250$ s, a kind of disk structure has been formed around both stars. The νNS is along the x-axis at -2.02, -2.92, -3.73, and -5.64 for $t = 40$, 100, 180, and 250 s, respectively. Note that this figure and all snapshot figures were done with the SNSPLASH visualization program (Price 2011).

Section 2.1 and Equation (13)). As we have shown, the SN ejecta might transport a high amount of angular momentum and form a thick disk around the NS before the accretion take place. There, the densities and temperatures are not high enough to cool the matter by neutrino emission, and outflows might occur (see, e.g., Blandford & Begelman 1999; Kohri et al. 2005; Dexter & Kasen 2013). Up to 25% of the infalling matter can be ejected in strong outflows, removing much of the system angular momentum (Fryer et al. 2006a; Fryer 2009). This means that the mass accretion rate calculated here might overestimate the actual accretion rate onto the star but up to a factor of order unity. It is also important to note that the accretion rate directly depends on the value adopted for the ξ parameter in Equation (10). For this simulation, we adopted $\xi = 0.1$. In Section 6.1, we are going to vary this parameter and establish the influence of it on the system's final fate.

As we anticipated, we have also run the simulation of the SN ejecta expansion without the NS companion, in order to calculate the fallback accretion rate (black dotted line in Figure 4) and compare it with the accretion rate onto the νNS in the binary simulation. At the beginning of the simulation, there is no difference between both accretion rates: an almost flatter high accretion phase at early time and then a decline as $t^{-5/3}$ (Chevalier 1989; Zhang et al. 2008; Fryer 2009; Dexter & Kasen 2013; Wong et al. 2014). However, at around $t/P_{orb} \lesssim 1.0$, there is a jump in the fallback accretion rate of the binary simulation that can be associated with the time at which the νNS starts to accrete the material decelerated by the NS companion. The high early-time accretion rate calculated here is due to the fallback of those particles that did not have enough kinetic energy to escape from the νNS gravitational field. This can occur either because after the forward shock is launched, the proto-NS cools and contracts, sending a rarefaction wave to the ejecta that decelerates it (Colgate 1971), or because the SN shock is smoothly decelerated when it goes outward, pushing the star material out (Woosley & Weaver 1995; Fryer 1999).

4.2. SN Explosion Energy

In the following, we start to systematically change the initial parameters that will affect the fate of the final configuration. We will do it one by one, in order to determinate the most favorable conditions that increase the accretion rate onto the NS companion. Figure 5 shows the mass accretion rate onto the

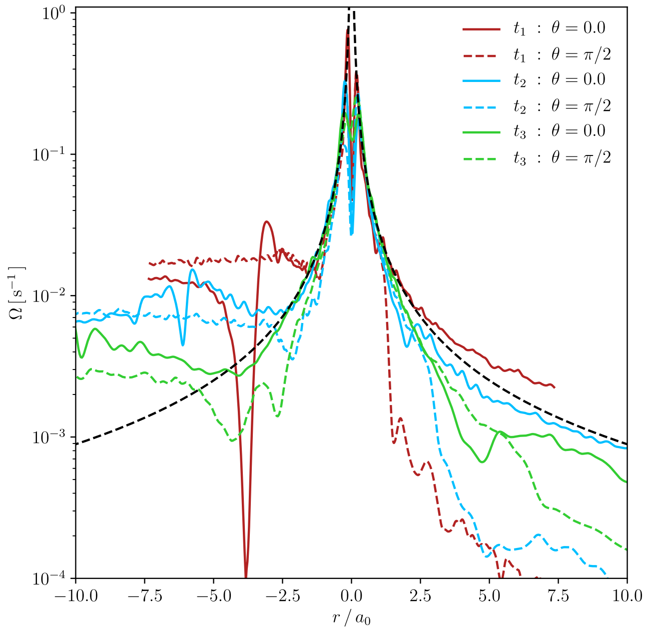

Figure 3. Angular velocity profiles of the SN material close to the NS companion at three different times: $t_1 = 140.0$ s, $t_2 = 280.0$ s, and $t_3 = 599.9$ s. The label $\theta = 0$ corresponds to the line that joins the binary stars, and the label $\theta = \pi/2$ is the line perpendicular to the latter and lies on the equatorial binary system. Close to the NS, the angular velocity approaches the Keplerian angular velocity (black line). This suggests that, before being accreted, the particles have enough angular momentum to circularize around the star and form a kind of disk structure. The minimum of the solid line in the $-x$ direction indicates the position of the νNS: at 3.01, 5.04, and 10.49 for t_1, t_2, and t_3, respectively.

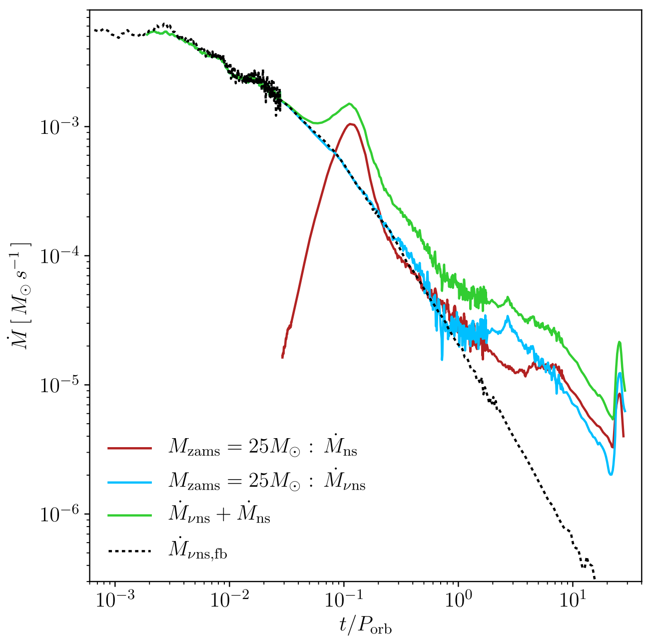

Figure 4. Mass accretion rate onto the NS (red line) and the νNS (blue line) during the SPH simulation of the expansion of the SN ejecta. The green line shows the sum of both accretion rates. The initial binary system is formed by the $CO_{\rm core}$ of an $M_{\rm ZAMS} = 25\,M_\odot$ progenitor and an NS of $2\,M_\odot$ with an initial binary period of approximately 5 minutes. The dotted black line corresponds to the fallback mass accretion onto the νNS when the $CO_{\rm core}$ collapses in a single-star configuration, i.e., without the presence of the NS companion.

NS and νNS for different energies of the SN explosion with the same progenitor star: the $25\,M_\odot$ of Table 1. As we explain in Section 2, in these simulations, we scale the kinetic and internal energy by a factor η (i.e., the velocities of the particles by $\sqrt{\eta}$) once we map the 1D exploded configuration to the 3D one. As expected, the total mass accreted by the NS companion is larger for low-energetic SNe than for high-energetic ones, and then more favorable to the collapse of the NS (see models from 25m1p1e to 25m1p07e in Table 2). On the other hand, the energy of the SN explosion needs to be high enough, otherwise a considerable part of the ejected mass causes fallback and can instead induce the collapse of the νNS to a BH. This is a novel and alternative possibility not considered in the original version of the IGC scenario (see, e.g., Rueda & Ruffini 2012; Fryer et al. 2014). Additionally, the energy of the SN explosion does not have a big influence on the magnitude of the peak of the mass accretion rate, but it does on its shape. The NS companion accretes more mass in the weakest SN explosion ($\eta = 0.7$) because the accretion rate is maintained almost constant for a longer time than in the strongest explosion ($\eta = 1$), where a clear peak appears. We can see that the late decay of the accretion rate depends on the SN explosion energy.

For these simulations, Figure 6 shows snapshots of the mass density and specific internal energy on the equatorial plane after about one orbital period of the initial configuration (~5 minutes). Each panel corresponds to a different value of the η parameter: $\eta = 1.0$ and 0.9 for the left and right upper panels, $\eta = 0.8$ and 0.7 for the left and right lower panels. The asymmetries of the interior ejecta layer are more pronounced for the less energetic explosion. The orbital period of the final configuration shortens with the decreases of the SN energy, i.e., with the accretion of mass by the binary stars. For example, the accretion onto the νNS and the NS companion is around 20% and 16%, respectively, more efficient for the weakest explosion ($\eta = 0.7$) with respect to the strongest one ($\eta = 1$), and the final orbital period is almost 90% shorter than the one of the final system from the most energetic explosion (see Table 2).

As we did before, we calculate the fallback accretion rate for these explosions onto the νNS for the isolated progenitors and compare and contrast it with its binary system counterpart. The right panel of Figure 5 shows the evolution of the mass accretion rate onto the νNS. The black lines correspond to the single-progenitor simulations. The accretion rate peaks at an early time and then decays as $\dot{M} \propto t^{-5/3}$ (Chevalier 1989). For the binary simulations (colored lines), a late peak on the fallback accretion rate is produced from the accretion of the material captured by the gravitational field of the NS companion. This is higher and even early for low-energetic SNe (around one order of magnitude for the less energetic explosion).

In order to compare the SN evolution in the single and binary simulations, in Figure 7, we show the SN density profile as seen from the νNS at different times and for two different SN energies (models 25M1p1e and 25M1p07e of Table 2). The left plots correspond to the explosion of the $CO_{\rm core}$ of the $25\,M_\odot$ progenitor of Table 1, while the right plots show its binary counterpart with a $2\,M_\odot$ NS companion. For the isolated SN explosions, the SN ejecta density profiles evolve approximately following a homologous evolution, keeping its spherical symmetry around the explosion center. For the explosions occurring in the close binaries, the NS companion gravitational field induced asymmetries in the SN fronts closer to it that will

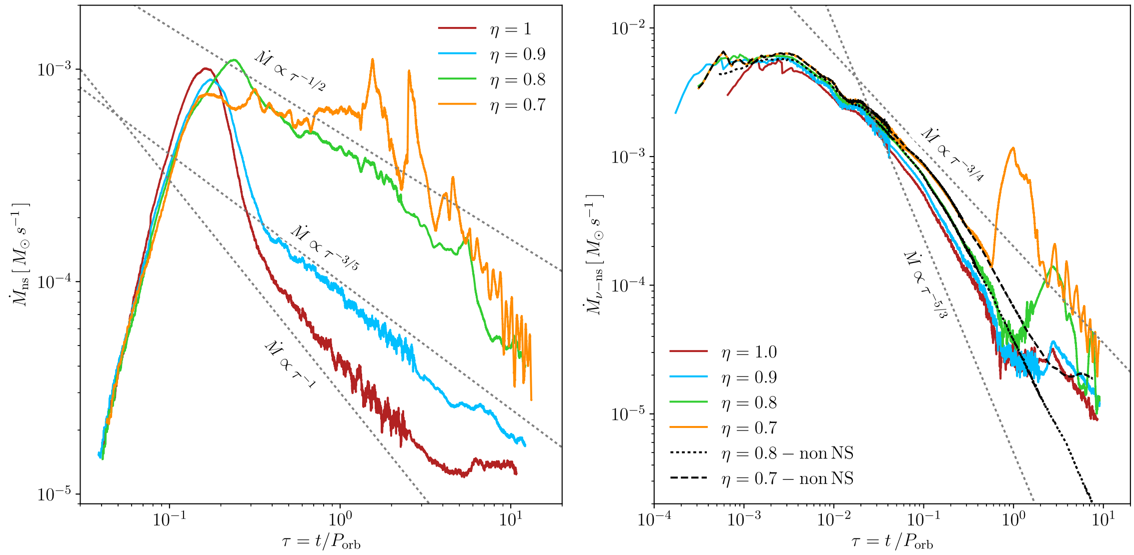

(a) NS star mass accretion rate (b) νNS mass accretion rate

Figure 5. Mass accretion rate on the NS (left panel) and νNS (right panel) in the IGC scenario. The initial binary system is the same as the one in Figure 4, but the SN explosion energy has been varied, scaling the kinetic and internal energy of the SPH particles by a factor $\eta < 1$. The accretion rate onto the NS presents a peak for the more energetic SN, while in the weaker ones, this peak is flattened; i.e., the accretion happens at a nearly constant rate for a longer time, causing the star to increase its mass faster. At early times, the fallback accretion rate onto the νNS is nearly independent of the SN energy, although the late bump induced by the accretion of the matter gravitational capture by the NS companion is stronger for the weakest explosions.

be more pronounced for the low-energetic explosions (see also Figure 6). We have shown in Becerra et al. (2016) that these asymmetries lead to observational effects both in the SN optical emission and in the GRB X-ray afterglow.

4.3. Initial Binary Period

We continue the exploration of the parameter space of the initial binary configuration by running simulations with different values of the initial orbital period. Figure 9 shows the mass accretion rate onto the NS companion for three different initial orbital periods—4.8, 8.1, and 11.8 minutes—and two different SN energies, the fiducial explosion (with $\eta = 1$) and the $\eta = 0.7$ modified explosion. For the two explosion energies, the accretion rate seems to scale with the initial binary period of the configuration and follow the same power law at the late times of the accretion process. On the other hand, for longer binary periods, as expected, the accretion onto the νNS tends to equal the fallback accretion when the $CO_{\rm core}$ explodes as an isolated star. This can be seen by comparing the final mass of the νNS in both scenarios (columns $M_{\rm orb,i}$ and $M_{\nu\rm ns}$ in Table 2).

Figure 8 shows snapshots, at two different times, of the surface density on the orbital plane for the same initial binary periods of Figure 9 and the modified explosion with $\eta = 0.7$. The system appears to evolve self-similarly with the increase of the binary period.

4.4. Initial Mass of the NS

Up to now, we have considered a massive initial NS companion of $2.0\,M_\odot$, since we expect that the progenitor of the $CO_{\rm core}$ loses its hydrogen and helium layers interacting with its companion (through common-envelope and Roche lobe overflow episodes; Lee & Cho 2014). Observationally, the measured NS masses in double-NS binaries are lighter than $1.5\,M_\odot$ (Lattimer & Prakash 2007), and massive, $\sim 2\,M_\odot$ NSs have been measured in binaries with white dwarf companions, i.e., PSR J1614–2230 (Demorest et al. 2010) and PSR J0348+0432 (Antoniadis et al. 2013).

In order to increase the parameter space, we have also run simulations with different initial masses for the NS companion: 1.4 and $1.6\,M_\odot$. In Table 3, we summarize the results of these simulations. In these cases, the models are labeled as "x_1Mnsx_2px_3e," where x_1 is the initial mass of the NS companion, and x_2 and x_3 have the same meaning as the model labels of Table 2. We also report the same columns as in Table 2. For the progenitor of the $CO_{\rm core}$, we used $M_{\rm ZAMS} = 25\,M_\odot$.

Figure 10 shows the evolution of the mass accretion rate onto the NS companion as a function of time normalized to the initial orbital period. As expected, for an initial binary system with a massive NS companion, the mass accretion rate onto it increases during the SN expansion; i.e., the gravitational force due to a massive NS is stronger. For example, the NS companion gained around 4.2%, 3.9%, and 3.1% of its initial mass for the 25Mns1p1e, 16Mns1p1e, and 14Mns1p1e models, respectively, and 36.3% and 31.1% for the 14Mns1p07e and 25Mns1p07e models, respectively. On the other hand, the evolution of the mass accretion rate seems to not be influenced by the NS companion initial mass. For the most energetic explosion ($\eta = 1.0$), there is an early peak, followed by a power-law decay and a late bump. This bump is early and bigger for a more massive NS companion. For the less energetic explosion ($\eta = 0.7$), there is a nearly constant mass accretion phase, followed by some oscillations and a power-law decay. Finally, the total accreted mass on the νNS from the fallback seems not to be affected by the initial mass of the NS companion. In the case of the most energetic explosion, the νNS final mass, in these simulations, is around $1.9\,M_\odot$, and for the less energetic one, it is around $2.4\,M_\odot$. The differences between the simulations of equal SN energy could be due to numerical errors.

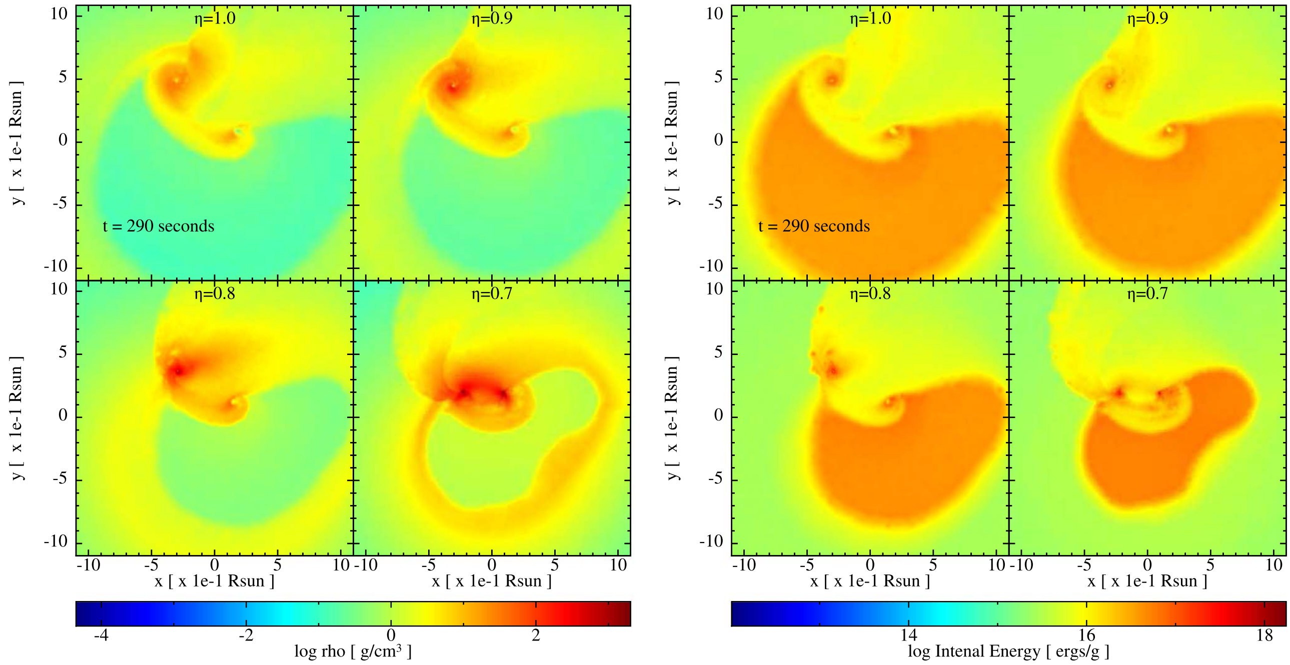

(a) Surface density (b) Surface specific internal energy

Figure 6. Snapshots of the mass density (left panel) and specific internal energy (right panel) on the equatorial plane after 290.0 s from the beginning of the SPH simulation (around one orbital period of the initial binary system). The initial binary system parameters are the same as the one represented in Figure 2, but the SN explosion energy has been scaled by a factor η, shown at the upper side of each panel (these simulations correspond to models 25M1p1e with $\eta = 1$, 25M1p09e with $\eta = 0.9$, 25M1p08e with $\eta = 0.8$, and 25M1p07e with $\eta = 0.7$ of Table 2). If the accretion onto the νNS and onto the NS companion is higher for the weaker SN explosions, then the star masses increases faster and the final orbital period of the system shortens. Also, in these explosions, the amount of mass accreted by the νNS is larger.

4.5. Asymmetric SN Expansion

We now explore how an SN explosion with an asymmetry blast wave affects the evolution of the system. In Table 4, we summarize the results of these simulations. In these cases, the models are labeled as "x_1f$x_2\Theta$:x_3," where x_1 and x_2 are the values of the parameter f and Θ, respectively, of Equations (18) and (19), and x_3 is the direction of the lobe. We started the simulations with the parameters $f = 2.0$ (in-cone to out-cone velocity ratio) and $\Theta = 20.0$ (cone amplitude), with the direction of the lobe in the z-axis (perpendicular to the equatorial binary plane) and in the $+x$-axis (directed to the NS companion) and $-x$-axis (opposed to the NS companion). Additionally, we explore the dependence with the opening angle and the velocities ratio, running simulations with $f = 4.0$ and $\Theta = 40$. Figure 11 shows the accretion rate onto the NS companion for these simulations. We can see that the introduction of asymmetries in the SN expansion velocity increases the accretion rate onto the NS companion, as well as the fallback accretion rate onto the νNS. This is expected because, in order to conserve the SN energy explosion, we increased the velocities of the particles inside the cone, while we decreased the velocities of the particles outside it. These slower particles are then more probably captured by the stars. The direction on the lobe does not introduce great changes in the evolution of the accretion rate or the final star mass of the configurations, but it does when the parameters f or Θ are increased.

Figure 12 shows snapshots of the surface density for the simulations of the asymmetric SN expansion. As was previously done, the reference system was rotated and translated in such a way that its center corresponds to the NS companion position and the x-axis joins the binary stars. Contrary to the symmetry cases, the binary orbital plane changes after the SN explosion if the lobe of the explosion is outside the equatorial plane of the initial binary. For example, for $f = 2.0$, the final orbital plane makes an angle of $2\overset{\circ}{.}55$ with respect to the initial orbital plane, and for $f = 4.0$, this angle grows up to $11\overset{\circ}{.}5$. However, for either the symmetry or asymmetry explosion, the magnitude of the velocity of the center of mass of the final binary system remains around 100–800 km s^{-1}. The kick velocities given in Table 2 are due to the accretion of linear momentum from the accreted particles and the gravitational attraction that the ejecta material has on the νNS (Janka & Mueller 1994). Another source for the NS kick velocity can be due to the anisotropic emission of the neutrino during the star's collapse (Woosley 1987; Bisnovatyi-Kogan 1993; Fryer & Kusenko 2006).

4.6. CO_{core} *Progenitor Mass*

Finally, we have varied the progenitor of the CO_{core}. Figure 13 shows the mass accretion rate onto the NS companion for all of the progenitors listed in Table 1. In Table 2, we summarize the results for these simulations, and, additionally, we have run more simulations with each of these progenitors, changing the SN energy and initial binary separation. We now present the salient properties of these simulations.

The 15 $M_\odot$ ejects just around 1.6 $M_\odot$, then the energy of the SN explosion needs to be low (on the order of 10^{50} erg) and the binary system compact enough in order to have significant accretion onto the NS companion. However, if the SN energy is considerably reduced, most of the SN material will fall back

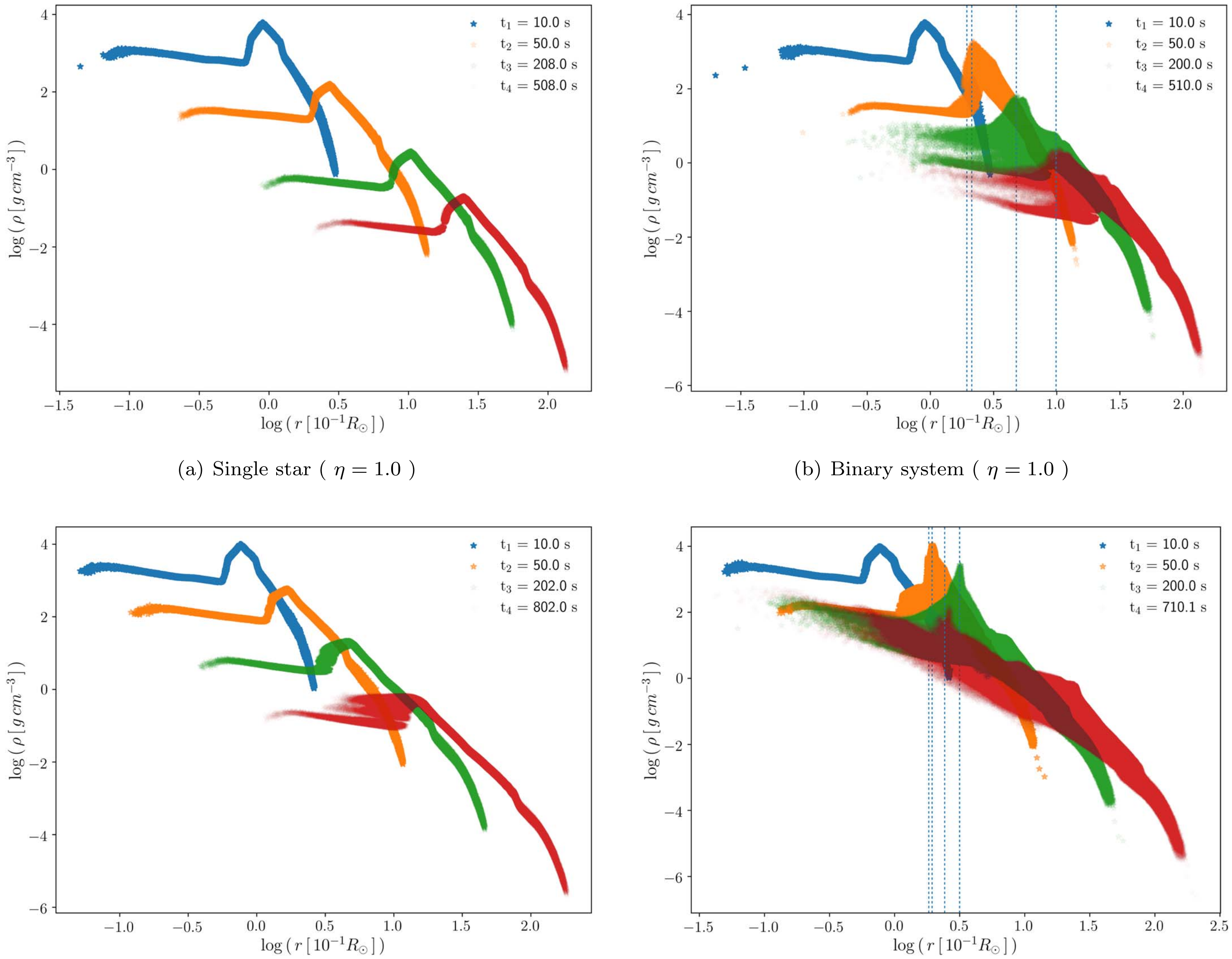

(a) Single star ($\eta = 1.0$)

(b) Binary system ($\eta = 1.0$)

(c) Single star ($\eta = 0.7$)

(d) Binary system ($\eta = 0.7$)

Figure 7. Density profile evolution of the SN ejecta after the core collapse of the CO_{core} of a 25 $M_\odot$ progenitor. The r coordinate is measured from the νNS position. The plots in the left panels correspond to the evolution of the SN in a single-star system, while the ones in the right panels show that the CO_{core} belongs to a binary system with an NS companion of 2 $M_\odot$ and an initial binary separation of 1.36×10^{10} cm. The blue dotted lines indicate the position of the NS companion. The SN energy of the upper plots is 1.56×10^{51} erg (model 25M1p1e of Table 2), and for the lower plots, the SN energy is 6.4×10^{50} erg (model 25M1p07e of Table 2). For isolated SN explosions (or for very wide binaries), the density of the SN ejecta would approximately follow the homologous evolution, as is seen in the left panels. For explosions occurring in close binaries with compact companions (as is the case of for IGC progenitors), the SN ejecta is subjected to a strong gravitational field that produces an accretion process onto the NS companion and a deformation of the SN fronts closer to the accreting NS companion, as seen in the right panels.

onto the νNS. For example, when scaling the SN kinetic and internal energy by $\eta = 0.05$, almost 80% of the SN ejecta is accreted by the νNS, while scaling the parameter to $\eta = 0.1$ means that the accreted material via fallback is reduced to 30%. It is important to point out that, if the initial orbital period is increased by a factor of 1.7, the amount of ejected mass that cannot escape the νNS gravitational field grows to 55%. Namely, the presence of a close NS companion could avoid the collapse of the νNS in the weak explosion cases.

For the 30 $M_\odot$ progenitor, we worked with two simulated explosions with different energies, one almost an order of magnitude stronger than the other. For the lowest-energetic explosion, $E_{sn,1}$, a significant amount of mass is making fallback; then, the collapse due to the hypercritical accretion onto the νNS is more probable than the one of the NS companion. The mass accretion rate on the NS companion flattens for this SN explosion (see Figure 13). On the other hand, the velocities of the stronger energetic explosion, $E_{sn,2}$, are so high that almost all of the SN ejecta surpass the NS companion without being captured by it. For these explosions, the ratio between the total SN energy and the kinetic energy is 0.45 and 0.81, respectively.

We have performed more simulations scaling the energy of these two explosions, and we summarize their results in Table 2. In these cases, we can evaluate the accuracy of our alternative path of changing the explosion energy by scaling the velocities and the internal energy of the SPH particles, instead of rerunning new simulations of the CO_{core} collapse and bounce of the shock. Figure 14 shows the density profile at around the same time for the two explosions of the 30 $M_\odot$ progenitor and their respective simulations with the scaled SN energy. In general, the internal radius of the low-energetic

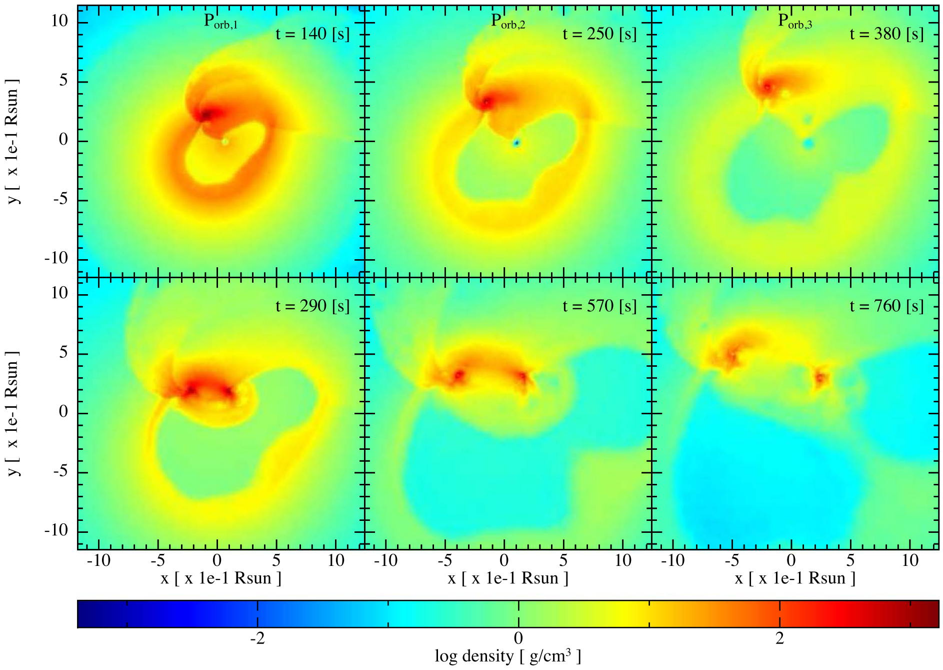

Figure 8. Snapshots of the surface density on the equatorial plane for systems with three different initial binary periods. The initial binary system is formed by the CO_{core} of the $M_{ZAMS} = 25\,M_\odot$ progenitor (see Table 1) and a $2\,M_\odot$ NS. The SN energy has been reduced to 6.5×10^{50} erg, scaling the particles' velocity and internal energy by a factor $\eta = 0.7$. The periods of the labels are $P_{orb,1} = 4.8$, 8.1, and 11.8 minutes, which correspond to models 25m1p07e, 25m3p07e, and 25m2p07e of Table 2, respectively.

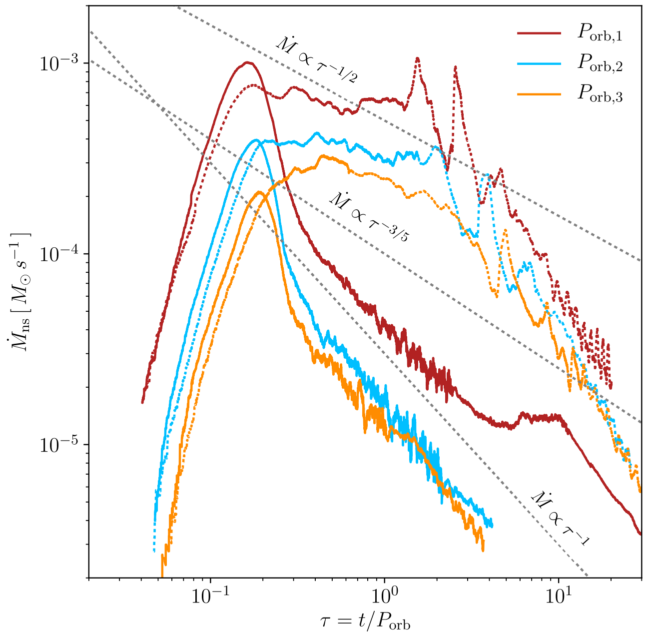

Figure 9. Mass accretion rate onto the NS companion in the IGC scenario. Different colors correspond to different initial orbital periods: $P_{orb,1} = 4.8$ (red line), 8.1 (blue line), and 11.8 (orange line) minutes. The other parameters that characterize the initial binary system are the same as in Figure 4. The solid lines correspond to an SN energy of 1.57×10^{51} erg, while the dotted ones correspond to a lower SN energy of 6.5×10^{50} erg. It can be seen that the mass accretion rate scales with the binary orbital period.

explosion is about two times smaller that the one of the high-energetic explosion (see Figure 1). These will increase the material that will make fallback in the single-star, as well as in the binary system, simulations, even when the scaled energy of the explosion becomes comparable.

Finally, we use the $40\,M_\odot$ progenitor of the CO_{core}. Since for this progenitor, the ejected mass in the SN is around $11\,M_\odot$, the energy of the explosion needs to be low to allow the configuration to remain bound and also for the NS companion to be able to accrete enough mass to collapse. If we use a factor $\eta = 0.7$ to reduce the SPH particles' velocity and internal energy, we see that the amount of mass accreted by the νNS is low, but the mass accreted by the NS companion could be enough to induced its collapse. Instead, for $\eta = 0.5$, most of the ejecta make fallback accretion onto the νNS. In Table 5, we estimate the initial and final mean bulk SN velocity in the simulations, $\langle v\rangle_{initial}$ and $\langle v\rangle_{final}$, computed as

$$\langle v\rangle = \sqrt{\frac{2E_k}{M_{ej}}}, \tag{20}$$

where E_k is the total kinetic energy of the SPH particles and M_{ej} is the total mass of the expanding material particles. We compute this for all of the CO_{core} progenitors and for different values of the η parameter. We do not account for the acceleration of the SN ejecta arising from the energy injection in the accretion process and in the GRB emission via the impact onto the SN by the e^+e^- plasma. As was shown in Ruffini et al. (2018b), the high velocities that characterize the HNe associated with GRBs are explained by this mechanism.

Fryer et al. (2014) performed a 1D numerical simulation of the CO_{core} collapse, bounce, and explosion and estimated the accretion rate onto the NS companion using the Bondy–Hoyle formalism (Hoyle & Lyttleton 1939; Bondi & Hoyle 1944; Bondi 1952). In these simulations, at the beginning of the accretion process, there is a burst in the accretion rate, growing up to $10^{-1}\,M_\odot\,s^{-1}$, that is two orders of magnitude greater than the accretion rate that we obtain with the SPH simulation. However, the total time of the accretion process is much shorter

Table 3
SPH Simulations with Different Mass for the NS Companion

Model	$M_{\rm ns,0}$ ($m_\odot$)	$P_{\rm orb,i}$ (minutes)	$a_{\rm orb,i}$ (10^{10} cm)	$M_{\nu \rm ns}$ ($m_\odot$)	$M_{\rm ns}$ ($m_\odot$)	$V_{\rm CM}$ (10^7 cm s^{-1})	$P_{\rm orb,f}$ (minutes)	$a_{\rm orb,f}$ (10^{10} cm)	e	$m_{\rm bound}$ ($M_\odot$)	Bound
14Mns1p1e	1.4	4.29	1.216	1.971	1.443	6.47	293	15.28	0.929	4.2×10^{-3}	Yes
16Mns1p1e	1.6	4.35	1.244	1.956	1.664	7.19	1872	53.566	0.979	5.1×10^{-2}	Yes
14Mns1p07e	1.4	4.29	1.216	2.457	1.909	3.33	4.20	0.977	0.375	9.8×10^{-2}	Yes

Note. For the progenitor of $\rm CO_{core}$, we used the one with $M_{\rm ZAMS} = 25\,M_\odot$.

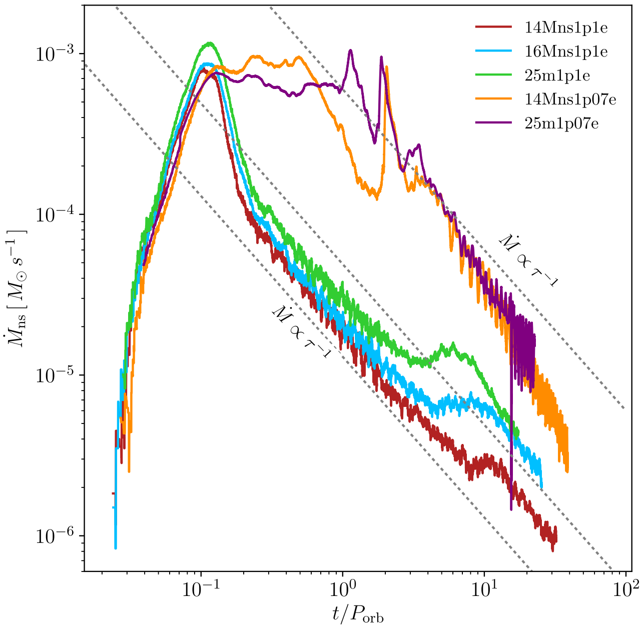

Figure 10. Mass accretion rate on the NS companion for different initial masses. The initial orbital period is close to the minimum period that the system can have in order that there is no Roche lobe overflow before the collapse of the $\rm CO_{core}$.

in those simulations that the one presented here, making the amount of mass accreted by the NS companion comparable between the simulations. This discrepancy is a direct consequence of the increase of the dimension of the simulation. While the 1D simulation is stopped when the SN innermost layer reaches the NS, the 3D simulation can continue because there are particles that remain bound to the NS companion in a kind of disk structure, and the star continues the accretion process.

5. Bound and Unbound Systems

We have also studied the evolution of the binary parameters during the SN expansion.

If we were to assume that the ejected mass in the SN explosion leaves the system instantaneously, the semimajor axis of the post-explosion system, a, is given by $a/a_0 = (M_0 - \Delta M)/(M_0 - 2a_0\Delta M/r)$, where M_0 and a_0 are the total mass and semimajor axis of the initial binary system, ΔM is the mass ejected in the SN, and r is the star separation at the moment of the explosion (Hills 1983). Then, binaries with circular initial orbits become unbound after an SN event if more than half of its total initial mass is lost. However, as shown in Fryer et al. (2015), in the IGC scenario, the mass loss cannot be considered instantaneous because the binary initial periods are of the same order as the time it takes for the slowest SN layer to reach the NS companion. For example, the innermost layers of the 25 $M_\odot$ progenitor have a velocity of the order of 10^8 cm s^{-1}, so they reach the NS initial position in a time of $\sim$100 s, nearly 2/5 of the initial binary period. Moreover, it has to be considered that either the νNS or the NS companion will accrete mass and momentum from the SN ejecta, and this will reduce the system mass loss.

Figure 15 shows the evolution of the binary semimajor axis with time for the same cases as in Figure 5. In these simulations, which correspond to the minimum orbital period of the initial binary system ($\sim$5 minutes) independently of the SN energy, the post-explosion system remains bound. This occurs even if the system loses more than half of its total initial mass. For example, for the $\eta = 1$ case, the mass loss in the system is around 4.82 $M_\odot$, namely, about 54.7% of its total initial mass.

For the fiducial SN model, an increase of a factor of 1.7 of the orbital period changes the fate of the post-explosion binary system, leading to an unbound final configuration. However, for the less energetic explosion, the system remains bounded in all scenarios in which we have increased the initial binary period (up to $\approx$60 minutes, i.e., $\approx$12 times the minimum orbital period). The determination of the maximum orbital period that the system can have in order to remain bound after the SN explosion is left for future work.

6. Mass Accretion Rate, NS Critical Mass, and Gravitational Collapse

We turn now to evaluating whether or not the NS companion collapses to a BH due to the accretion of part of the SN ejecta. For this, we need to both study how the NS gravitational mass and angular momentum evolve with time and set a value for the NS critical mass. As a first approximation, we assume that the NS evolves from one equilibrium configuration to the next, using the uniformly rotating NS equilibrium configurations in Cipolletta et al. (2015, 2017). These configurations were constructed using the public code RNS (Stergioulas & Friedman 1995) to solve the axisymmetric Einstein equations for three selected relativistic mean-field nuclear matter EOS models: NL3, GM1, and TM1. The mass–radius relations obtained for these EOSs satisfy the current observational constraints (see Figure 5 in Cipolletta et al. 2015). The most stringent constraint is that the critical mass for the gravitational collapse of a nonrotating NS must be larger than the mass of the most massive NS observed: the pulsar PSR J0348+0432 with 2.01 $\pm$ 0.04 $M_\odot$ (Antoniadis et al. 2013).[5] Recently, the measurement of a more massive NS, PSR J2215+5135 with

[5] We recall that this pulsar constrains the nonrotating NS mass–radius relation because the structure of an NS rotating at the measured rate of PSR J0348+0432, $f \approx 26$ Hz (Antoniadis et al. 2013), in practice "overlaps" with that of a nonrotating NS (see, e.g., Cipolletta et al. 2015).

Table 4
SPH Simulations with an Asymmetric Blast Wave

Model	$M_{\nu\rm ns,fb}$ $(m_\odot)$	$V_{\rm kick}$ $(10^4\ {\rm cm\ s^{-1}})$	$M_{\nu\rm ns}$ $(m_\odot)$	$M_{\rm ns}$ $(m_\odot)$	$V_{\rm CM}$ $(10^7\ {\rm cm\ s^{-1}})$	$P_{\rm orb,f}$ (s)	$a_{\rm orb,f}$ $(10^{10}\ {\rm cm})$	e	$m_{\rm bound}$ $(M_\odot)$	Bound
2f20Θ : z	1.931	1.18×10^3	2.009	2.161	7.31	2852.15	4.849	0.774	0.065	Yes
2f20Θ : x	1.931	1.18×10^3	1.959	2.142	7.13	8225.79	9.772	0.892	0.056	Yes
2f20Θ : $-x$	1.931	1.18×10^3	2.002	2.182	7.82	3170.17	5.209	0.801	0.054	Yes
4f20Θ : z	2.826	5.08×10^3	2.382	2.424	5.16	456.51	1.496	0.438	0.189	Yes
2f40Θ : z	2.364	5.38×10^3	2.316	2.395	5.84	529.37	1.643	0.589	0.105	Yes

Note. The initial binary system is formed by the $CO_{\rm core}$ of the $M_{\rm ZAMS}=25\ M_\odot$ progenitor and an NS of $2\ M_\odot$. The initial binary parameters are the same as those of the model 25m1p1e of Table 2, but the SN velocity profile was modified with Equations (18) and (19).

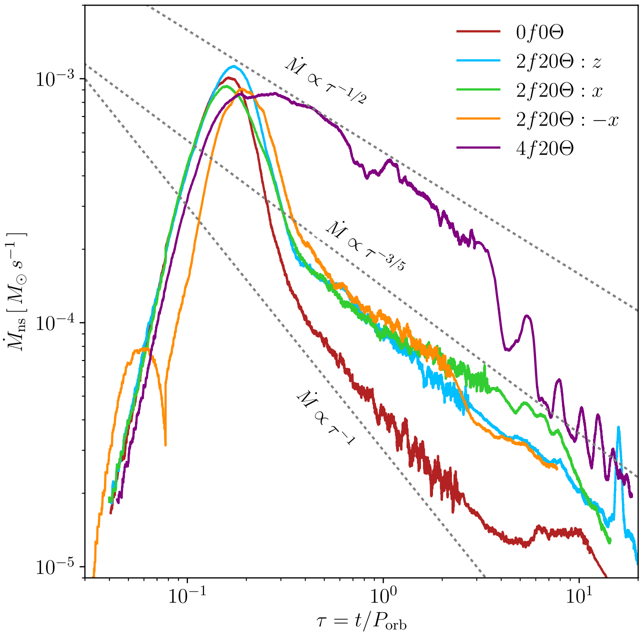

Figure 11. Mass accretion rate onto the NS companion introducing a conical geometry for the SN velocity profile of the $M_{\rm ZAMS}=25\ M_\odot$ progenitor (see Table 1). The parameters of the initial binary system are the same as that for Figure 4. The cone was opened along the z-axis (perpendicular to the orbital plane; blue and purple lines) and x-axis (on the orbital plane; green and orange lines). Since the SN energy is conserved, the introduction of the asymmetry reduces the particles' velocity and increases the accretion rate.

$2.27^{+0.17}_{-0.15}\ M_\odot$ (Linares et al. 2018) and $f\approx 383$ Hz (Breton et al. 2013), was claimed. This measurement is still under debate, and for this paper, we use the constraint imposed by the mass of PSR J0348+0432. Unfortunately, the current measurements of NS radii, e.g., from X-ray observations, poorly constrain the mass–radius relation and thus the nuclear EOS (see, e.g., Cipolletta et al. 2015 for details).

In general, for uniformly rotating NS configurations, when the star accretes an amount of baryonic mass, $M_{\rm b}$, and angular momentum, $J_{\rm ns}$, its gravitational mass, $M_{\rm ns}$, evolves as

$$\dot M_{\rm ns} = \left(\frac{\partial M_{\rm ns}}{\partial M_{\rm b}}\right)_{J_{\rm ns}} \dot M_{\rm b} + \left(\frac{\partial M_{\rm ns}}{\partial J_{\rm ns}}\right)_{M_{\rm b}} \dot J_{\rm ns}. \tag{21}$$

From Cipolletta et al. (2015), we know the relation $M_{\rm ns}(M_{\rm b}, J_{\rm ns})$,

$$\frac{M_{\rm b}}{M_\odot} = \frac{M_{\rm ns}}{M_\odot} + \frac{13}{200}\left(\frac{M_{\rm ns}}{M_\odot}\right)^2\left(1-\frac{1}{130}j_{\rm ns}^{1.7}\right), \tag{22}$$

where $j_{\rm ns}\equiv cJ_{\rm ns}/(GM_\odot^2)$. This relation is common to all of the NS matter EOSs studied in Cipolletta et al. (2015) within an error of 2%. The mass and angular momentum of the accreted particle add to the baryonic mass and angular momentum of the NS; thus, we can integrate Equation (21) and follow the evolution of the gravitational mass of both the νNS and the NS companion. The NS accretes mass until it reaches an instability point: the mass-shedding limit or the secular axisymmetric instability. The first limit is met if the star angular velocity has growth enough that the gravitational force at the stellar equator equals the centrifugal force; then, a faster rotation will induce the ejection of matter. Although the dimensionless angular momentum parameter has a nearly EOS-independent value along the mass-shedding sequence, $cJ_{\rm ns}/(GM_{\rm ns}^2)\approx 0.7$ (Cipolletta et al. 2015), the numerical value of $J_{\rm ns}$ at the shedding point depends on the specific EOS, since $M_{\rm ns}$ is different. On the other hand, the secular axisymmetric instability that defines the critical mass for gravitational collapse arises because the star became unstable to axisymmetric perturbations. From Cipolletta et al. (2015), we have that, within a maximum error of 0.45%, the critical mass is given by

$$M_{\rm max}^{J_{\rm ns}\neq0} = M_{\rm max}^{J_{\rm ns}=0}(1+kj_{\rm ns}^l), \tag{23}$$

where $M_{\rm max}^{J_{\rm ns}=0}=[2.81, 2.39, 2.20]$, $l=[1.68, 1.69, 1.61]$, and $k=[0.006, 0.011, 0.017]$ for the NL3, GM1, and TM1 EOSs.

Table 6 lists some properties of the NS critical mass configurations for the NL3, GM1, and TM1 EOSs. In particular, we show the minimum and maximum values of the critical mass, $M_{\rm max}^{J_{\rm ns}=0}$ and $M_{\rm max}^{J_{\rm ns}\neq0}$, respectively; $M_{\rm max}^{J_{\rm ns}=0}$ corresponds to the configuration along the secular axisymmetric instability line, which is nonrotating, and $M_{\rm max}^{J_{\rm ns}\neq0}$ corresponds to the maximally rotating one, which is the configuration that intersects the Keplerian mass-shedding sequence. We also list the rotation frequency of the maximally rotating critical configuration, $f_{\rm max}$.

In the upper panel of Figure 16, we show the track followed by the NS companion (solid line) and the νNS (dashed line) in the $M_{\rm star}$–$j_{\rm star}$ plane for the $25\ M_\odot$ progenitor of the $CO_{\rm core}$ for two different SN explosion energies (models 25M1p1e and 25M1p07e of Table 2). For the system with the stronger SN explosion, the νNS and the NS companion reach the mass-shedding limit at $t=21.66$ minutes with $1.93\ M_\odot$ and $t=20.01$ minutes with $2.055\ M_\odot$, respectively. For the less energetic SN explosion, this occurs early, at $t=5.51$ minutes with $2.04\ M_\odot$ for the νNS and $t=2.91$ minutes with $2.09\ M_\odot$ for the NS companion. The dotted line shows the continuation of the integration of Equation (22) for all of the simulation time. For the NS companion, there is a decrease of angular

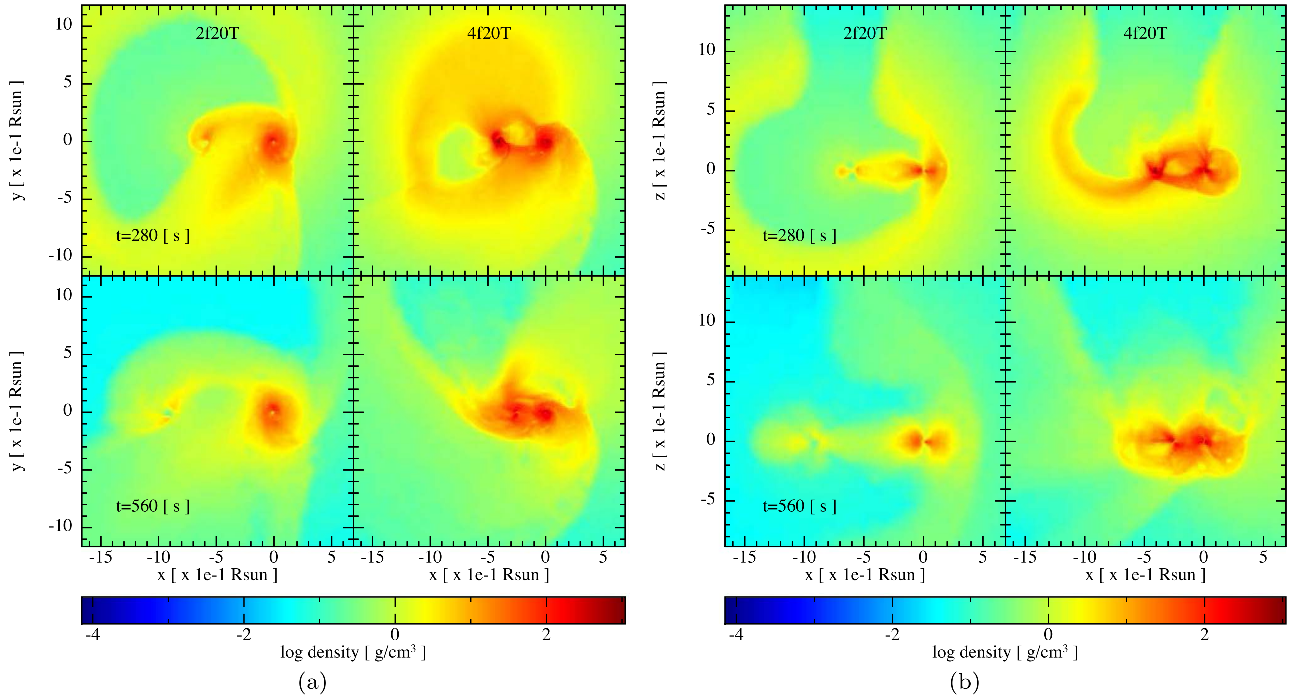

Figure 12. Snapshots of the surface density on the binary equatorial plane (left panel) and the plane orthogonal to it (right panel). The reference system has been rotated and translated in such a way that the x-axis becomes directed in the line that joins the binary stars, and its origin is at the NS companion. The initial binary system is the same as the one represented in Figure 2, but the SN velocity profile has been modified to a conical geometry following Equations (18) and (19). In all cases, the cone opens along the z-axis. The left frames of each plot have the parameters $f = 2.0$ and $\Theta = 20.0$ (model 25m2f20tz of Table 2), while the right ones have $f = 4.0$ and $\Theta = 20.0$ (model 25m4f20tz of Table 2). If the lobe of the explosion is directed outside of the initial orbital plane, as here, the orbital plane of the final configuration changes. For the case of $f = 2.0$, the final orbital plane makes an angle of 2°.55 with respect to the initial orbital plane, and for $f = 4.0$, this angle grows up to 11°.5.

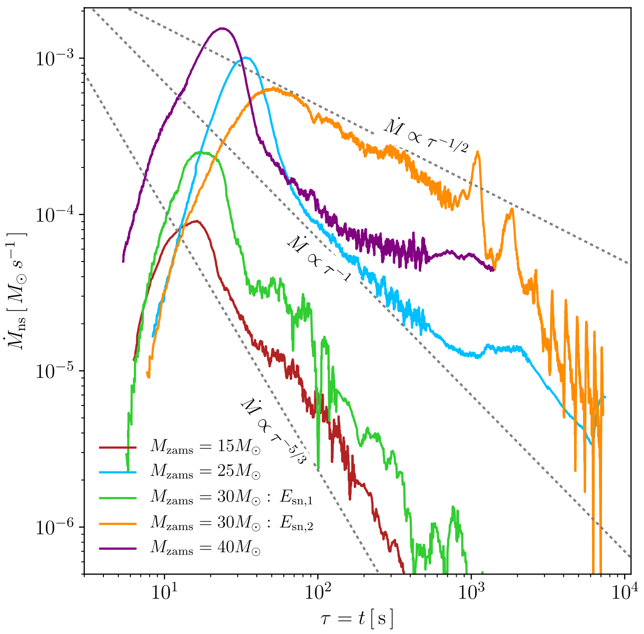

Figure 13. Mass accretion rate on the NS companion using the explosion of all of the CO_{core} progenitors summarized in Table 1. The NS companion has an initial mass of 2 $M_\odot$, and the orbital period is close to the minimum period that the system can have in order for there to be no Roche lobe overflow before the collapse of the CO_{core}: 6.5, 4.8, 6.0, and 4.4 minutes for the $M_{\rm ZAMS} = 15$, 25, 30, and 40 $M_\odot$ progenitors, respectively.

momentum. This occurs because there is a change in the direction of rotation of the accreted particles with respect to the one of the accreting NS.

Since we are assuming that the angular momentum of the accreted particles is totally transferred to the NS, even the accretion of a small amount of mass might soon bring it to the mass-shedding limit (see Figure 16). However, we see in the simulations that a kind of disk is formed around the NS, then the particles circularize, loose angular momentum, and finally are accreted. In this picture, we need to integrate Equation (21), assuming that the star angular momentum evolution is given by the disk accretion torque, i.e.,

$$\dot{J}_{\rm ns} = l(R_d)\dot{M}_{\rm b}, \tag{24}$$

where $l(R_d)$ is the specific angular momentum of the particles at the disk interior radius, R_d. We now adopt that the disk interior radius is given by the radius of the last circular orbit (LCO) of a test particle around the NS. From Cipolletta et al. (2017), we have that the specific angular momentum of the LCO, independent of the studied EOS, is given by

$$l(R_d) = l_{\rm LCO} = \frac{GM_{\rm ns}}{c}\left[2\sqrt{3} \mp 0.37\left(\frac{j_{\rm ns}}{M_{\rm ns}/M_\odot}\right)^{0.85}\right], \tag{25}$$

where the upper sign corresponds to the corotating particles and the lower sign to the counterrotating particles. This fitting formula is accurate, with a maximum error of 0.3%.

In the lower panel of Figure 16, we show the evolution of the νNS and the NS companion in the $M_{\rm star}$–$j_{\rm star}$ plane for the same models as in the upper panel. In this case, we have integrated Equations (21) and (25) assuming, again, that the particle mass sums to the star baryonic mass and the disk viscous timescale is smaller than the accretion timescale; i.e., we used the mass

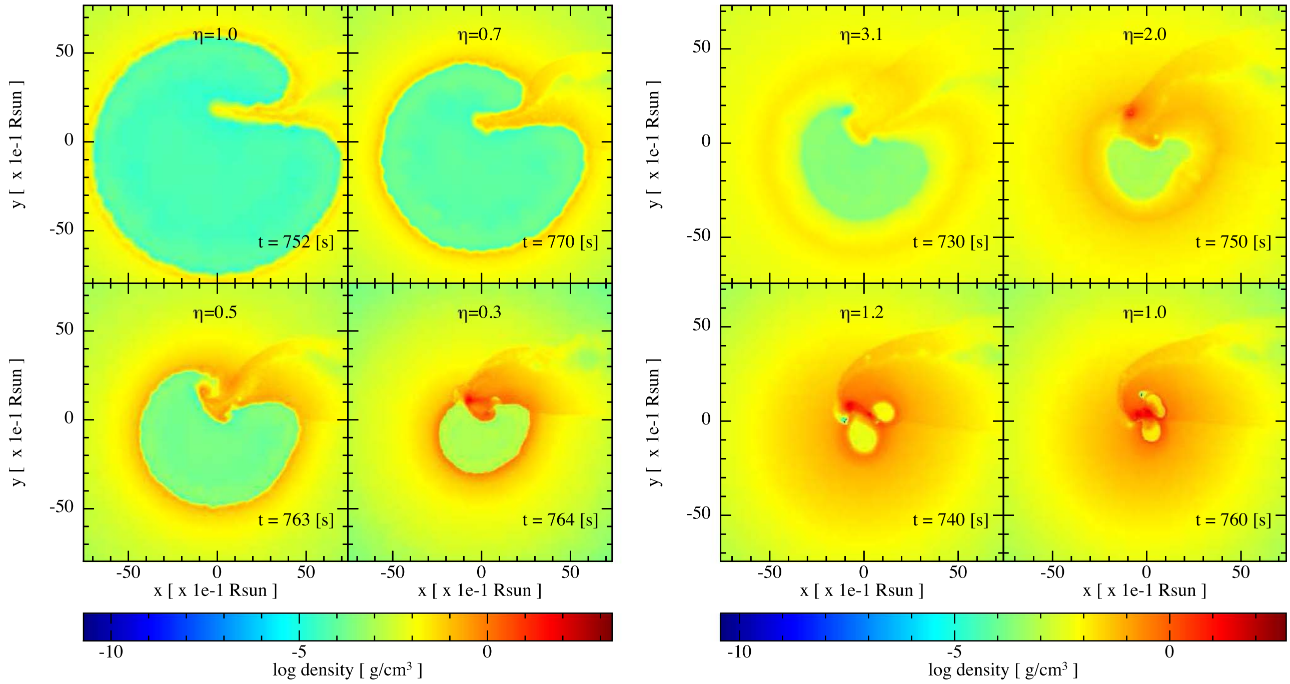

(a) $E_{\rm sn} = 1.09 \times 10^{52}$ erg (b) $E_{\rm sn} = 2.19 \times 10^{51}$ erg

Figure 14. Snapshots of the surface density on the binary equatorial plane. The initial binary system is formed by the $CO_{\rm core}$ of the $M_{\rm ZAMS} = 30\,M_\odot$ progenitor and a $2\,M_\odot$ NS with an orbital period of around 6 minutes. We have simulated the collapse and bounce of the $30\,M_\odot$ progenitor with two different SN energies, as specified in the left and right panel labels. We show the simulations scaling the SN energy of these two explosions by a factor η (specified in the upper part of each frame). In general, the internal radius of the low-energetic explosion is about two times smaller that the one of the high-energetic explosion. This increases the fallback accretion onto the νNS, and the region near the binary system becomes denser.

accretion rate obtained from the SPH simulations. In this case, only the NS companion for the less energetic SN simulation reaches the mass-shedding limit.

The evolution of Equations (21) and (24) is general, while the binding energy and LCO angular momentum equations are, in general, EOS-dependent relations. Fortunately, it was shown in Cipolletta et al. (2017) that Equations (22) and (25) remain valid for the set of EOSs used in this work (and for a wider variety of EOSs) with high accuracy; namely, they are nearly EOS-independent. This implies that the evolution track followed by the NS, given the initial mass, is the same for all these EOSs. However, this does not imply that the fate of the NS is the same, since the instability boundaries depend on the EOS; namely, the numerical values of the mass and angular momentum of the NS at the mass-shedding limit and secular instability depend on the EOS, as can be seen from Figures 16 and 17.

We have assumed until now a totally efficient angular momentum transfer of the particles from the inner disk to the NS surface. However, additional angular momentum losses should be taken into account. We model these losses by introducing a parameter for the efficiency of the angular momentum transfer, $\chi \leqslant 1$ (see, e.g., Becerra et al. 2016), defined as

$$\dot{J}_{\rm ns} = \chi l(R_d)\dot{M}_{\rm b}. \tag{26}$$

Therefore, $\chi = 1.0$ implies that the particles lose angular momentum only in their downward motion within the disk, while $\chi < 1$ introduces the possible losses in their final infall to the NS, e.g., from accretion outflows and/or from the deceleration of the matter from the inner disk radius to its final incorporation into the NS surface (see, e.g., Shakura & Sunyaev 1988; Inogamov & Sunyaev 1999; Babkovskaia et al. 2008; Inogamov & Sunyaev 2010; Philippov et al. 2016 and references therein). In Figure 17, we compare the evolutionary path on the mass-dimensionless angular momentum plane for two values of the efficiency parameter, $\chi = 0.5$ and 1.0. It can be seen that angular momentum losses make the star reach the secular instability limit of the TM1 and GM1 EOSs, namely, the critical mass to collapse to a BH, instead of the mass-shedding limit. This result is in agreement with previous results presented in Becerra et al. (2015, 2016).

Table 7 lists the total angular momentum of the particles accreted by the stars when they cross an instability limit (if they do) or when the simulation was stopped. In these cases, we worked with the TM1 EOS. We show the results for two selected values of the angular momentum transfer efficiency parameter, $\chi = 1.0$ and 0.5. For low-energetic SN explosions, it is more probable that the νNS arrives at the mass-shedding limit when $\chi = 1.0$ or the secular instability limit when $\chi = 0.5$. This is the case for the less energetic explosions of the $15\,M_\odot$ progenitor, the 30 and $40\,M_\odot$ ones. On the other hand, there are a few cases in which the NS companion arrives at the mass-shedding limit first. This is the case for the $25\,M_\odot$ progenitor with SN energy scaled by $\eta = 0.7$ and the minimum orbital period and for the $40\,M_\odot$ progenitor with SN energy scaled by $\eta = 0.8$, 0.7, and 0.6. Notice that in the case with $\eta = 0.8$ and $\chi = 1.0$, the NS companion arrives at the mass-shedding limit, but the final system is unbound after the SN ejecta leave the system.

Table 5
SN Initial and Final Mean Bulk Velocity

Progenitor M_{ZAMS}	η	$\langle v \rangle_{initial}$ 10^8 cm s^{-1}	$\langle v \rangle_{final}$ 10^8 cm s^{-1}	Progenitor M_{ZAMS}	η	$\langle v \rangle_{initial}$ 10^8 cm s^{-1}	$\langle v \rangle_{final}$ 10^8 cm s^{-1}
15 $M_\odot$	0.7	7.316	8.763	30 $M_\odot$[a]	0.7		7.931
	0.5	6.183	7.103		0.7	4.912	6.227
	0.3	4.789	5.066	30 $M_\odot$[b]	1.0	3.097	4.845
					1.2	3.393	5.538
25 $M_\odot$	1.0	4.186	5.805	40 $M_\odot$	1.0	4.949	7.232
	0.9	3.889	5.079		0.9	4.667	6.624
	0.8	3.560	4.341		0.8	4.405	5.976
	0.7	3.217	3.945		0.7	4.114	5.288

[a] $E_{sn} = 1.09 \times 10^{52}$ erg.
[b] $E_{sn} = 2.19 \times 10^{51}$ erg.

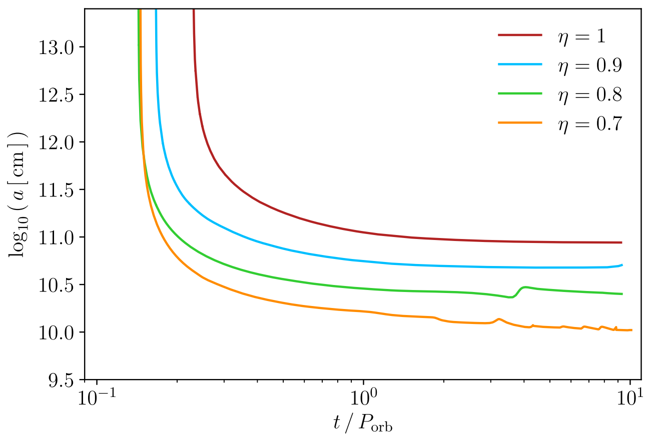

Figure 15. Evolution of the semimajor axis of the νNS–NS binary system. The initial configuration is a binary system formed by the CO_{core} of an $M_{ZAMS} = 25\,M_\odot$ progenitor and an NS of $2\,M_\odot$ with an initial binary period of approximately 5 minutes. The CO_{core} collapses and undergoes an SN explosion ejecting around $5\,M_\odot$ and leaving a proto-NS of $1.85\,M_\odot$. Not all of the material ejected in the SN leaves the binary system. Some part of this material falls back and is accreted by the remnant star from the collapse of the CO_{core}, while some other part is accreted by the NS companion. The final binary configuration can remain bound even when the system loses half of its initial total mass.

6.1. Accuracy of the Mass Accretion Rate

We turn now to analyzing the relevance of the ξ-parameter of Equation (10) on the mass accretion rate onto the star. Until now, we have assumed a value $\xi = 0.1$ for this parameter. A larger value of ξ results in higher accretion rates: it allows a bigger gravitational capture radius, and then more particles can be accreted by the star. In this way, $\xi = 1.0$, the maximum value that ξ can have, will establish an upper limit for the mass accretion rate onto the star. We can also establish a lower limit for the accretion rate, if we allow the star to just accrete the particle whose angular momentum is equal to or smaller than the angular momentum that a particle orbiting the star would have at the LCO. An equivalent condition is to adopt a varying ξ parameter that equates the capture radius to the radius of the LCO, r_{LCO}. But, since the r_{LCO} for the NS is of the order of the NS radius, i.e., $\sim$10 km, we will need to considerably increase the number of particles to be able to resolve the NS surface.

Table 6
Properties of the NS Critical Mass for the NL3, TM1, and GM1 EOSs

EOS	$M_{max}^{J_{ns}=0}$ ($M_\odot$)	$M_{max}^{J_{ns}\neq 0}$ ($M_\odot$)	f_{max} (kHz)
NL3	2.81	3.38	1.40
GM1	2.39	2.84	1.49
TM1	2.20	2.62	1.34

Note. $M_{max}^{J_{ns}=0}$: critical mass for the nonrotating case. $M_{max}^{J_{ns}\neq 0}$: maximum critical mass value, i.e., the mass of the configuration along the secular instability line and rotating at the Keplerian value. f_{max}: rotation frequency of the NS with $M_{max}^{J_{ns}\neq 0}$. Table taken from Cipolletta et al. (2015).

We have rerun the SPH simulations, adopting different values of ξ, for the binary system formed by the CO_{core} of the $25\,M_\odot$ progenitor and a $2\,M_\odot$ NS companion and an orbital period of about 5 minutes. In Figure 18, we show the accretion rate onto the NS companion for $\xi = 1.0$, 0.5, and 0.1. The label $\xi = \xi_{j_{LCO}}$ corresponds to the case in which the star just accretes the particles with an angular momentum lower than the one of the LCO. The late mass accretion rate of the simulations with $\xi = \xi_{j_{LCO}}$ and $\xi = 0.5$ and 1.0 fall almost within the same power law, $\dot{M} \propto t^{-5/3}$. Also, for the same simulation, Figure 19 shows snapshots of the density surface at the binary equatorial plane at two different times.

The simulation with $\xi = 1.0$ and 0.5 gives greater peaks for the mass accretion rate. This is expected, since in these cases, the NS capture radius is larger and the star cleans up its surroundings and, at later times, produces a quickly dropping accretion rate. Comparing this simulation with the one with $\xi = 0.1$, we can deduce that there is a delay time between the particles that are gravitationally captured by the star and the time they are actually accreted by it. We expect that the simulation with $\xi_{j_{LCO}}$ gives a better resolution of the disk around the NS companion. However, the artificial viscosity used in the code was introduced in order to resolve shocks and does not model the disk viscosity. Then, we are seeing that the particles that circularize around the star at some point escape from the NS gravitational field, causing the mass accretion rate to drop (see Figure 19). In Table 8, we summarize the parameters that characterize the final state of the NS companion, as well as the final binary system. We have rerun simulations with the 25, 30, and 40 $M_\odot$ progenitors of the CO_{core}. For each model, we summarized the total mass and angular

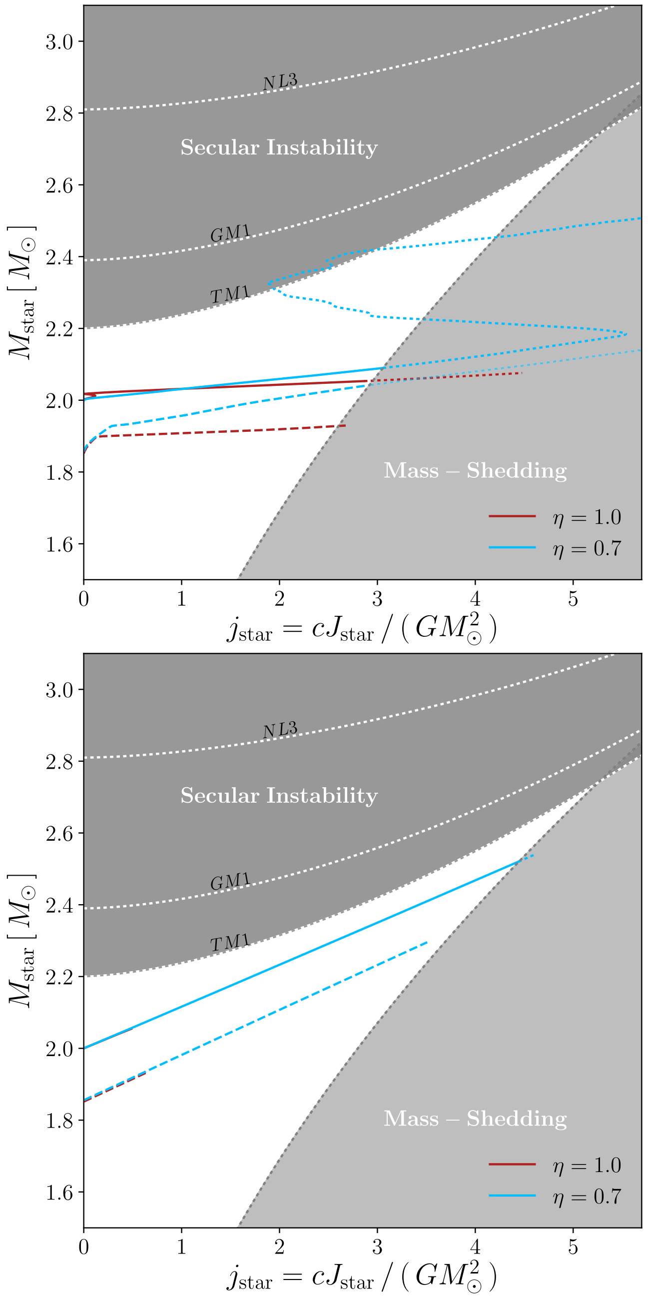

Figure 16. Evolution of the νNS (dashed line) and the NS companion (solid line) in the mass-dimensionless angular momentum ($M_{\rm star}$–$j_{\rm star}$) plane. The mass of the particles accreted contributes to the NS baryonic mass. In the upper plot, we adopt that the star accretes all of the particles' angular momentum. In the lower plot, we adopt that the star accretes from a disklike structure, namely, that the angular momentum evolution is dictated by the disk accretion torque (see text for details). In this example, the initial binary system is formed by the $\mathrm{CO_{core}}$ of the $M_{\rm ZAMS} = 25\,M_\odot$ progenitor and a $2\,M_\odot$ NS with an orbital period of about 5 minutes. The red lines correspond to an SN explosion of $\times 10^{51}$ erg, while for the blue line, the explosion energy has been scaled by a factor $\eta = 0.7$, leading to $\times 10^{51}$ erg.

momentum on the accreted particles, $\Delta M_{\rm acc}$ and $\Delta l_{\rm acc}$; the mass bound to the system when the simulation is stopped, $m_{\rm bound}$; and the final orbital separation, $a_{\rm orb,f}$. In general, the larger the ξ parameter, the more $\Delta l_{\rm acc}$ and $\Delta M_{\rm acc}$ depend on both ξ and the SN explosion energy. The accreted mass increases with ξ, but the increment decreases with a decrease of the SN energy; e.g., for

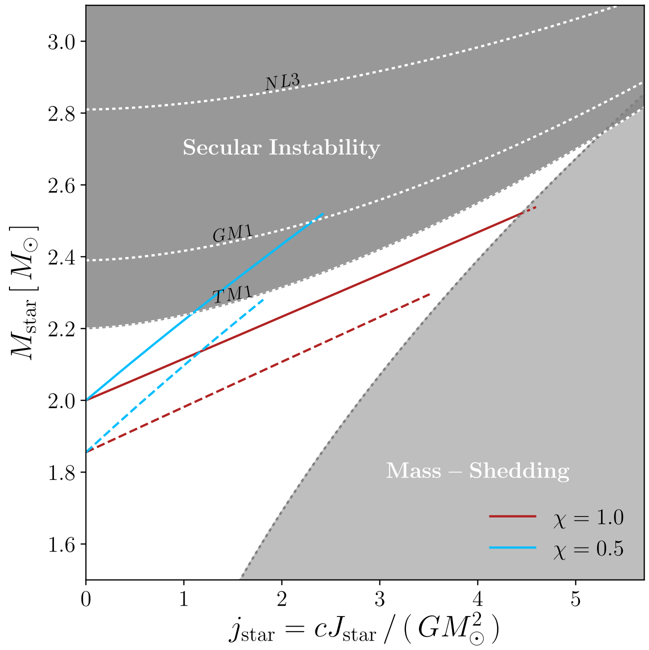

Figure 17. Evolution of the νNS (dashed line) and the NS companion (solid line) in the mass-dimensionless angular momentum ($M_{\rm star}$–$j_{\rm star}$) plane. The angular momentum evolution is dictated by the disk accretion torque given by Equation (26), where we have introduced the efficiency parameter, $\chi \leqslant 1$, that accounts for angular momentum losses between the disk and the stellar surface. The initial binary system is formed by the $\mathrm{CO_{core}}$ of the $M_{\rm ZAMS} = 25\,M_\odot$ progenitor and a $2\,M_\odot$ NS with an orbital period of about 5 minutes. The SN explosion energy has been scaled by $\eta = 0.7$ (model 25M1p07e of Table 2).

$M_{\rm ZAMS} = 25\,M_\odot$ and $\eta = 1.0$, the accreted mass increases by $\approx$170% when going from $\xi = 0.1$ to 1.0, while for $\eta = 0.7$, the accreted mass is almost the same for both values of ξ.

7. Consequences of the Simulations on the XRF/BdHN Model

7.1. Parameters Leading to a Successful IGC

The accretion rate increases for higher densities and lower velocities, so we expect that it increases with time as the inner ejecta layers, which are denser and slower, pass by the NS. Using a homologously expanding SN ejecta density profile, Becerra et al. (2016) derived approximate analytic formulae for the peak accretion rate, $\dot{M}_{\rm peak}$, and the corresponding peak time, $t_{\rm peak}$ (see Equations (33)–(34) of that paper). From this estimate, they showed that, at the lowest order in $M_{\rm ns}/M$, the system satisfies

$$t_{\rm peak} \propto \frac{M^{1/3} P_{\rm orb,i}^{2/3}}{v_{\rm star,0}}, \qquad \dot{M}_{\rm peak} \propto \left(\frac{M_{\rm ns}}{M}\right)^{5/2} \frac{1}{P_{\rm orb,i}}, \tag{27}$$

where $M_{\rm ns}$ is the initial mass of the NS companion, $M = M_{\rm ns} + M_{\rm CO}$ is the initial total binary mass, $M_{\rm CO} = M_{\nu\rm ns} + M_{\rm ej}$ is the mass of the $\mathrm{CO_{core}}$, $P_{\rm orb,i}$ is the initial orbital period, and $v_{\rm star,0}$ is the velocity of the outermost layer of the SN ejecta. The above dependence confirms that the shorter/smaller the orbital period/separation, the higher the peak accretion rate, $\dot{M}_{\rm peak}$, and the shorter the peak time, $t_{\rm peak}$. It is also confirmed that the highest velocity layer has a negligible contribution to the accretion rate, but it is important in the determination of the time

Table 7
Final State of the νNS and the NS Companion

		νNS							NS						
			$\chi = 0.5$			$\chi = 1.0$				$\chi = 0.5$			$\chi = 1.0$		
CO_{core} M_{ZAMS}	Model	L_{tot} $c/(GM_\odot^2)$	$M_{\nu ns}$ $M_\odot$	$j_{\nu ns}$ $c/(GM_\odot^2)$	Fate	$M_{\nu ns}$ $M_\odot$	$j_{\nu ns}$ $c/(GM_\odot^2)$	Fate	L_{tot} $c/(GM_\odot^2)$	M_{ns} $M_\odot$	j_{ns} $c/(GM_\odot^2)$	Fate	M_{ns} $M_\odot$	j_{ns} $c/(GM_\odot^2)$	Fate
15 $M_\odot$	15m1p07e	0.027	1.302	0.007	Stb	1.302	0.008	Stb	0.085	2.004	0.009	Stb	2.002	0.018	Stb
	15m1p05e	0.069	1.303	0.009	Stb	1.303	0.016	Stb	0.323	2.004	0.019	Stb	2.004	0.037	Stb
	15m1p03e	0.019	1.315	0.041	Stb	1.315	0.077	Stb	0.362	2.023	0.101	Stb	2.023	0.204	Stb
	15m2p03e	0.091	1.303	0.08	Stb	1.303	0.017	Stb	0.579	2.006	0.026	Stb	2.006	0.056	Stb
	15m1p01e	13.63	1.815	1.571	Stb	1.636	1.874	M-sh	19.373	2.157	0.701	Stb	2.159	1.377	Stb
	15m2p01e	38.38	2.077	2.534	Stb	1.639	1.892	M-sh	12.533	2.080	0.35	Stb	2.080	0.693	Stb
	15m3p01e	30.95	1.759	1.377	Stb	1.862	3.253	M-sh	2.004	2.045	1.197	Stb	2.045	0.388	Stb
25 $M_\odot$	25m1p1e	3.469	1.931	0.321	Stb	1.933	0.627	Stb	4.746	2.055	0.2467	Stb	2.056	0.497	Stb
	25m2p1e	1.779	1.912	0.242	Stb	1.914	0.472	Stb	1.927	2.022	0.099	Stb	2.022	0.198	Stb
	25m3p1e	1.085	1.912	0.229	Stb	1.912	0.399	Stb	1.944	2.018	0.0813	Stb	2.019	0.1639	Stb
	25m1p09e	6.243	1.982	0.513	Stb	1.983	1.010	Stb	6.538	2.127	0.584	Stb	2.129	1.187	Stb
	25m1p08e	7.331	2.038	1.449	Stb	2.031	1.365	Stb	9.870	2.258	1.242	Sc-in	2.348	3.576	Stb
	25m1p07e	18.146	2.284	1.826	Stb	2.289	3.434	Stb	8.491	2.246	1.105	Sc-in	2.528	4.506	M-sh
	25m2p07e	19.51	2.250	1.663	Stb	2.265	3.215	Stb	9.908	2.252	1.135	Sc-in	2.426	3.648	Stb
	25m3p07e	21.34	2.214	1.476	Stb	2.226	2.812	Stb	17.292	2.004	2.246	Sc-in	2.425	3.638	Stb
	14M1p1e	6.61	1.945	0.399	Stb	1.951	0.791	Stb	3.933	1.438	0.110	Stb	1.437	0.221	Stb
	16M1p1e	5.172	1.935	0.672	Stb	1.935	0.672	Stb	5.742	1.652	0.357	Stb	1.652	0.178	Stb
	14M1p07e	22.87	2.312	1.972	Sc-in	2.327	3.788	M-sh	3.079	1.837	1.509	Stb	1.711	2.05	M-sh
30 $M_\odot$ [a]	30m1p1ea	0.077	1.756	0.021	Stb	1.756	0.044	Stb	0.059	2.006	0.026	Stb	2.006	0.052	Stb
	30m1p07ea	0.954	1.758	0.032	Stb	1.758	0.062	Stb	0.366	2.012	0.053	Stb	2.012	0.106	Stb
	30m1p05ea	1.828	1.764	0.053	Stb	1.764	0.107	Stb	4.073	2.028	0.125	Stb	2.028	0.251	Stb
	30m1p03ea	3.560	1.842	0.3494	Stb	1.843	0.692	Stb	33.083	2.246	2.358	Sc-in	2.356	3.532	Stb
	30m2p03ea	4.266	1.821	0.267	Stb	1.821	0.522	Stb	36.161	2.151	0.7006	Stb	2.154	1.426	Stb
30 $M_\odot$ [b]	30m1p1eb	64.935	2.379	2.614	Sc-in	2.215	3.507	M-sh	19.995	2.244	1.099	Sc-in	2.307	2.634	Stb
	30m1p12eb	28.432	2.362	2.541	Stb	2.200	3.392	M-sh	33.681	2.244	1.100	Sc-in	2.304	2.606	Stb
	30m2p12eb	26.508	2.397	2.807	Sc-in	2.162	3.297	M-sh	23.922	2.1801	0.802	Stb	2.1827	1.572	Stb
	30m1p2eb	2.819	1.777	0.106	Stb	1.777	0.196	Stb	7.846	2.061	0.271	Stb	2.061	0.546	Stb
	30m1p31eb	0.721	1.766	0.0611	Stb	1.766	0.105	Stb	1.6715	2.014	0.062	Stb	2.014	0.122	Stb
40 $M_\odot$	40m1p1e	1.125	1.874	0.081	Stb	1.873	0.132	Stb	11.504	2.056	0.2453	Stb	2.056	0.4918	Stb
	40m1p09e	2.189	1.875	0.087	Stb	1.875	0.164	Stb	25.669	2.236	1.097	Stb	2.236	2.247	Stb
	40m1p08e	3.468	1.879	0.105	Stb	1.879	0.199	Stb	30.146	2.254	1.22	Sc-in	2.405	4.060	M-sh

Table 7
(Continued)

		νNS							NS						
			$\chi = 0.5$			$\chi = 1.0$				$\chi = 0.5$			$\chi = 1.0$		
CO_{core} M_{ZAMS}	Model	L_{tot} $c/(GM_{\odot}^2)$	$M_{\nu ns}$ $M_{\odot}$	$j_{\nu ns}$ $c/(GM_{\odot}^2)$	Fate	$M_{\nu ns}$ $M_{\odot}$	$j_{\nu ns}$ $c/(GM_{\odot}^2)$	Fate	L_{tot} $c/(GM_{\odot}^2)$	M_{ns} $M_{\odot}$	j_{ns} $c/(GM_{\odot}^2)$	Fate	M_{ns} $M_{\odot}$	j_{ns} $c/(GM_{\odot}^2)$	Fate
	40m1p07e	9.963	2.042	0.7631	Stb	2.042	1.486	Stb	34.074	2.243	1.09	Sc-in	2.526	4.491	M-sh
	40m2p07e	9.6264	2.023	0.689	Stb	2.024	1.343	Stb	42.97	2.245	1.100	Sc-in	2.522	4.458	M-sh
	40m4p07e	10.333	1.942	0.342	Stb	1.942	0.652	Stb	27.474	2.246	1.129	Sc-in	2.4135	3.6104	Stb
	40m1p06e	171.063	2.310	1.948	Sc-in	2.338	3.857	M-sh	63.31	2.244	1.098	Sc-in	2.529	4.518	M-sh
	40m2p06e	121.594	2.318	1.987	Sc-in	2.331	3.793	M-sh	45.944	2.244	1.096	Sc-in	2.527	4.506	M-sh
	40m1p05e	11.593	2.316	1.197	Sc-in	2.338	3.861	M-sh	5.434	2.133	0.588	Stb	2.134	1.158	Stb

Notes. Stb: stable configuration; M-sh: mass-shedding limit; Sc-in: secular axisymmetric instability. In this table, we report the results for the TM1 EOS, and the gravitational mass value takes into account the angular momentum transfer by accretion. These values could differ from those reported in Table 2, where the angular momentum transfer is not considered.
[a] $E_{sn} = 1.09 \times 10^{52}$ erg.
[b] $E_{sn} = 2.19 \times 10^{51}$ erg.

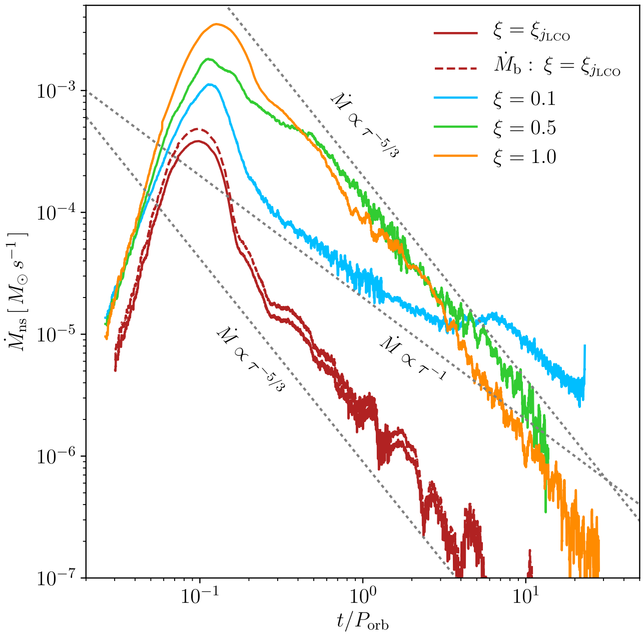

Figure 18. Mass accretion rate onto the NS companion adopting different values for the ξ parameter in Equation (10). This parameter controls the size of the NS capture radius. A value $\xi = 1.0$ establishes an upper limit on the mass accretion rate. We also defined a lower limit on the accretion (red line), allotting to the star just accreted those particles that have an angular momentum smaller than the one of the LCO around the NS. The initial binary configuration is the one of Figure 4.

at which accretion starts and, consequently, of the peak time. These formulae are relevant to having insight on the properties of the system and are valid to obtain typical and/or order-of-magnitude estimates of the accretion rate. An analysis of the performance of the analytic formulae with respect to the values obtained from a full numerical integration can be found in Appendix A of Becerra et al. (2016).

Using the above and approximating the accreted mass as $\Delta M_{\rm acc,an} \approx \dot{M}_{\rm peak}\, t_{\rm peak}$, it can be checked that it satisfies

$$\Delta M_{\rm acc,an} \propto \frac{M_{\rm ns}^2}{P_{\rm orb,1}^{1/3}\, v_{\rm star,0}} \tag{28}$$

for a fixed $\mathrm{CO_{core}}$ mass. For some of the models of Table 2, we summarize in Table 9 their corresponding order-of-magnitude values of $t_{\rm peak}$, $M_{\rm peak}$, and $\Delta M_{\rm acc}$ from Equations (27) and (28). In order to evaluate the accuracy of these analytic estimates, we have calculated the ratio

$$\eta^* \equiv \frac{\Delta M_{\rm acc,sim}}{\Delta M_{\rm acc,an}}, \tag{29}$$

between the mass accreted by the NS companion obtained numerically in the simulation and the one predicted by Equation (28). We confirm the behavior found in Becerra et al. (2016) that the accuracy of the analytic estimate increases (η^* parameter approaches unity) for longer orbital periods (less compact binaries), and we found that here also for more energetic SNe. We also confirm that the analytic formula underestimates (η^* much larger than unity) the accretion rate for the short orbital period binaries. Indeed, we found that when η^* is in excess of unity, the gravitational collapse of the NS is more probable. It is important to recall that both equations in Equation (27) were derived assuming that the binary period is constant while the SN ejecta expand and neglecting the contribution of the νNS in the evolution of the system. In order to have an idea of the goodness of those assumptions, we also show in Table 9 the ratio between the final and initial binary separation and the final and initial mass of the νNS.

From Equation (28), we see that not only the larger the $M_{\rm ns}$, the less mass it needs to accrete to reach the critical mass for gravitational collapse and BH formation,

$$\Delta M_{\rm crit} \equiv M_{\rm crit} - M_{\rm ns}, \tag{30}$$

where $M_{\rm crit} = M_{\rm max}^{J_{\rm ns}\neq 0}$ (see Equation (23)), but also the larger the $M_{\rm ns}$, the higher the accretion rate and the larger the mass it accretes in a time $t_{\rm peak}$. The above analysis places as the main parameters of the system for the occurrence of an XRF or a BdHN the initial mass of the NS companion, the orbital period, and the SN velocity, or, equivalently, the SN explosion/kinetic energy.

We defined in Becerra et al. (2016) the orbital period $P_{\rm max}$ separating the XRF and BdHN subclasses, namely, the maximum orbital period up to which the collapse of the NS companion to a BH, induced by accretion, occurs. Thus, $P_{\rm max}$ is set by the orbital period for which $\Delta M_{\rm acc} = \Delta M_{\rm crit}$, which leads to

$$P_{\rm max} \propto \frac{M_{\rm ns}^6}{v_{\rm star,0}^3 (M_{\rm crit} - M_{\rm ns})^3}, \tag{31}$$

which is a monotonically increasing function of $M_{\rm ns}$, as obtained in Becerra et al. (2016; see Figure 5 there) from the full numerical integration of the NS evolution equations.

7.2. Binary Evolutionary Path

As we have discussed, in our binary scenario, the presence of the $\mathrm{CO_{core}}$ provides a natural explanation for the association of long GRBs with Type Ic SNe/HNe. The requirement of the $\mathrm{CO_{core}}$, at the same time, leads to the formation of the compact orbits (a few minutes' orbital period) needed for the occurrence of high accretion rates onto the NS companion. The HNe, i.e., the high-velocity SNe associated with GRBs, are explained by the feedback of the energy injected into the SN by the hypercritical accretion (Becerra et al. 2016) and the GRB e^+e^- plasma (Ruffini et al. 2018b). This implies that the initial SN explosion/kinetic energy is initially ordinary.

Once we have established the main binary parameters needed for the explanation of the XRFs and BdHNe following the IGC scenario, it is natural to discuss whether these conditions, namely, $\mathrm{CO_{core}}$–NS binaries with these features, occur in a given evolutionary path. It is known that massive binaries can evolve into compact object binaries, such as NS–NS and NS–BH. Typical formation scenarios argue that, after the first SN explosion, the compact remnant enters a common-envelope phase with the companion. Such a phase leads to a compaction of the binary orbit. Finally, after the collapse of the companion star, an NS–BH or NS–NS binary is formed if the system remains bound (Fryer et al. 1999b; Dominik et al. 2012; Postnov & Yungelson 2014). More recently, a different evolutionary scenario has been proposed in which, after the collapse of the primary star to an NS, namely, after the first SN,

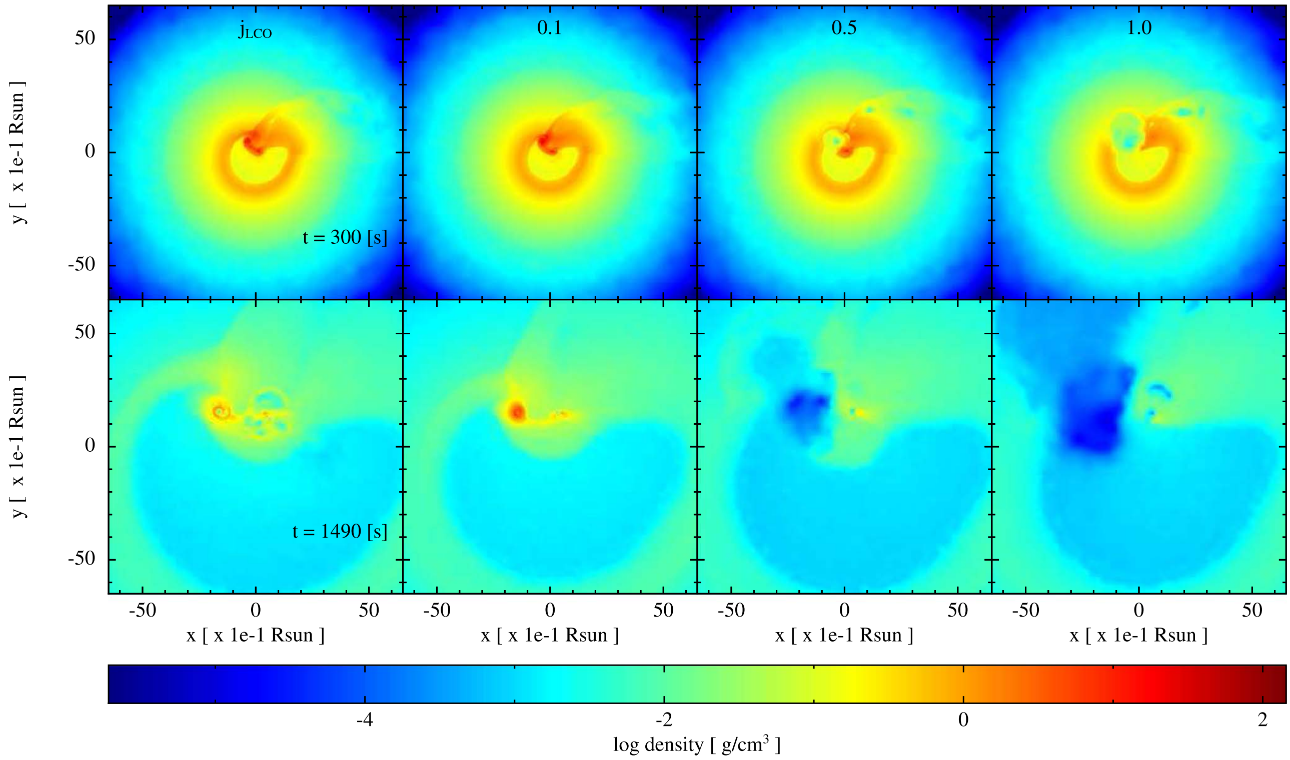

Figure 19. Snapshots of the surface mass density. The initial binary system is formed by the CO_{core} of a 25 $M_{\odot}$ progenitor and a 2 $M_{\odot}$ NS with an initial orbital period of around 5 minutes. For the plots in the upper panel, the system has evolved a time close to one initial orbital period, 300 s, and for the plots of the lower panel, the time corresponds to about 24 minutes from the beginning of the simulation. The vertical panels correspond to different values for the ξ parameter in Equation (10); from the second to the fourth are given 0.1, 0.5, and 1.0. In the simulation label $j_{\rm LCO}$, the star accretes just the particles with an angular momentum lower than the one of the NS LCO.

Table 8
NS Companion Final State

Progenitor $M_{\rm ZAMS}$	η	ξ	$\Delta M_{\rm acc}$ $M_{\odot}$	$\Delta l_{\rm acc}$ $c/(GM_{\odot}^2)$	$m_{\rm bound}$ $M_{\odot}$	$a_{\rm orb,f}$ 10^{10} cm
25 $M_{\odot}$	1.0	$j_{\rm LCO}$	0.011	0.0097	0.00238	14.96
		0.1	0.078	4.7460	0.08100	8.110
		0.5	0.171	31.921	0.00497	9.780
		1.0	0.211	42.148	0.00131	48.87
	0.7	$j_{\rm LCO}$	0.049	0.0870	0.07700	1.724
	0.7	0.1	0.659	7.7650	0.16030	1.021
		1.0	0.633	225.64	0.00453	1.575
30 $M_{\odot}$	2.0	0.1	0.077	7.8460	0.00560	…
	2.0	1.0	0.172	22.166	0.00053	…
40 $M_{\odot}$	0.8	0.1	0.457	30.147	0.01650	…
	0.8	1.0	0.545	56.835	0.00703	…

the binary undergoes a series of mass transfer phases leading to the ejection of both the hydrogen and helium shells of the secondary. This process naturally leads to a binary composed of a CO_{core} and an NS. When the CO_{core} collapses, namely, after the second SN in the binary evolutionary path, a compact binary system is formed. The X-ray binary/SN community refers to these systems as "ultrastripped" binaries. Such systems have also been called in to explain the population of NS–NS and low-luminosity SNe (see, e.g., Tauris et al. 2013, 2015). The rate of these ultrastripped binaries is expected to be 0.1%–1% of the total SN rate (Tauris et al. 2013). Most of the theoretically derived population of these binaries shows tight orbital periods in the range 50–5000 hr. Ultrastripped systems have been proposed in these works to dominate the formation channel of NS–NS. In addition, the formation of NS–BH systems was not considered, since (1) they did not find systems where the CO_{core} collapses directly to a BH, and (2) they did not consider the possibility of an IGC process in which the BH is formed by the NS companion and not by the collapse of the CO_{core}.

Binary evolutionary paths similar to the above for ultrastripped binaries and leading to the tight CO_{core}–NS binaries studied here were proposed in Rueda & Ruffini (2012), Becerra et al. (2015), and Fryer et al. (2015). However, population synthesis analyses scrutinizing the possibility of even tighter binaries than the ones previously considered, as well as the physics of the hypercritical accretion process onto the NS companion in the second SN explosion, leading to XRFs and/or BdHNe, have not yet been considered in the literature and deserve a dedicated analysis.

7.3. Occurrence Rate Density

The existence of ultrastripped binaries supports our scenario from the stellar evolution side. Clearly, XRF and BdHN progenitors should be only a small subset that result from the binaries with initial orbital separation and component masses leading to CO_{core}–NS binaries with short orbital periods, e.g., 100–1000 s for the occurrence of BdHNe. This requires fine-tuning both the CO_{core} mass and the binary orbit. From an astrophysical point of view, the IGC scenario is characterized by the BH formation induced by the hypercritical accretion

Table 9
Comparison between the Analytic Estimate of the Accretion Process and the Full Numerical Results

Model	$v_{\rm star,0}$ 10^8 cm s^{-1}	$t_{\rm peak}$ s	$\dot{M}_{\rm peak}$ 10^{-4} $M_\odot$ s^{-1}	$\Delta M_{\rm acc,an}$ $M_\odot$	η^*	$\frac{a_{\rm orb,f}}{a_{\rm orb,i}}$	$\frac{M_{\nu ns}}{M_{\nu ns,0}}$
$M_{\rm ZAMS} = 25\ M_\odot$ Progenitor ($\rho_{\rm core}R_{\rm star}^3 = 3.237\ M_\odot$)							
25m1p1e	9.5	48.14	5.87	0.028	3.01	6.47	1.06
25m2p1e	9.5	70.69	3.30	0.023	1.24	…	1.04
25m3p1e	9.5	87.56	2.39	0.021	1.14	…	1.04
25m4p1e	9.5	106.8	1.77	0.019	0.74	…	1.04
25m1p09e	9.1	50.74	5.87	0.029	5.43	3.10	1.09
25m1p08e	8.5	53.82	5.87	0.032	13.95	1.82	1.12
25m1p07e	7.9	57.54	5.87	0.034	18.37	0.77	1.28
25m2p07e	7.9	84.49	3.30	0.028	18.71	1.99	1.27
25m3p07e	7.9	104.65	2.39	0.025	20.87	2.30	1.24
25m5p07e	7.9	147.78	1.43	0.021	19.02	2.58	1.17
14Mns1p1e	9.5	43.58	3.71	0.016	2.65	12.6	1.07
14Mns1p07e	7.9	52.08	3.71	0.019	21.16	0.80	1.33
$M_{\rm ZAMS} = 30\ M_\odot$ Progenitor $-$exp 1 ($\rho_{\rm core}R_{\rm star}^3 = 5.280\ M_\odot$)							
30m1p1e	8.78	96.22	0.91	0.009	0.798	…	1.004
30m1p07e	7.35	115.01	0.91	0.018	1.431	…	1.004
30m1p05e	6.213	136.07	0.91	0.022	2.498	…	1.008
30m1p03e	4.81	175.67	0.91	0.016	28.41	4.88	1.068
30m2p03e	4.81	265.28	0.52	0.013	13.84	…	1.05
$M_{\rm ZAMS} = 30\ M_\odot$ Progenitor $-$exp 2 ($\rho_{\rm core}R_{\rm star}^3 = 5.280\ M_\odot$)							
30m1p1e	5.21	340.06	0.984	0.033	11.428	1.32	2.10
30m2p1e	5.21	513.53	0.767	0.039	5.784	…	1.02
30m1p12e	5.71	310.43	0.984	0.031	11.428	3.01	1.44
30m1p2e	5.21	239.91	0.984	0.023	0.719	…	1.02
30m1p31e	9.18	193.15	0.984	0.019	0.895	…	1.01
$M_{\rm ZAMS} = 40\ M_\odot$ Progenitor ($\rho_{\rm core}R_{\rm star}^3 = 7.47\ M_\odot$)							
40m1p1e	6.58	33.74	9.39	0.032	3.74	…	1.01
40m2p1e	6.58	49.67	5.58	0.028	1.65	…	1.01
40m1p09e	6.24	35.62	9.39	0.033	8.14	…	1.012
40m1p08e	5.88	37.78	9.39	0.035	15.06	…	1.02
40m1p07e	5.51	40.39	9.39	0.038	27.21	8.08	1.13
40m2p07e	5.51	59.38	5.59	0.033	22.76	54.8	1.12
40m4p07e	5.51	94.29	2.99	0.028	17.97	…	1.06

Note. In the first two columns, we present the label of the model and the SN velocity of the last layer at the beginning of the simulation. The next three columns correspond to the estimations of $t_{\rm peak}$, $\dot{M}_{\rm peak}$, and $M_{\rm acc}$, calculated from Equations (27) and (28). The η^* parameter from the sixth column corresponds to the ratio between the accreted mass obtained from the simulations and the one calculated with Equation (28). The last two columns are the ratio between the initial and final orbital separation and the initial and final mass of the νNS, respectively. We reported these last two quantities since, in the analytical approximation, they were assumed as constant.

onto the NS companion and the associated GRB emission. Indeed, GRBs are a rare phenomenon, and the number of systems approaching the conditions for their occurrence must be low. If we assume that XRFs and BdHNe can be the final stages of ultrastripped binaries, then the percentage of the ultrastripped population leading to these long GRBs must be very small. The observed occurrence rate of XRFs and BdHNe has been estimated to be $\sim$100 and $\sim$1 Gpc^{-3} yr^{-1}, respectively (Ruffini et al. 2016), namely, 0.5% and 0.005% of the Type Ibc SNe rate, 2×10^4 Gpc^{-3} yr^{-1} (see, e.g., Guetta & Della Valle 2007). It has been estimated that 0.1%–1% of the SN Ibc could originate from ultrastripped binaries (Tauris et al. 2013), which would lead to an approximate density rate of 20–200 Gpc^{-3} yr^{-1}. This would imply that a small fraction ($\lesssim$5%) of the ultrastripped population would be needed to explain the BdHNe, while, roughly speaking, almost the whole population would be needed to explain the XRFs. These numbers, while waiting for a confirmation by further population synthesis analyses, would suggest that most SNe that originated from ultrastripped binaries should be accompanied by an XRF. It is interesting that the above estimates are consistent with traditional estimates that only $\sim$0.001%–1% of massive binaries lead to double compact object binaries (see, e.g., Fryer et al. 1999b; Dominik et al. 2012; Postnov & Yungelson 2014).

7.4. Consequences of GRB Observations and Analysis

We have recently addressed in Ruffini et al. (2018b) the essential role of X-ray flares in differentiating and acting as separatrix between the BdHN model and the "collapsar-fireball" model of GRBs (Woosley 1993). The gamma-ray

Table 10
Convergence Study of the SPH Simulation of the IGC Scenario

Progenitor $M_{\rm ZAMS}$	N Million	η	ξ	$m_{\nu ns}$ ($M_\odot$)	Er($m_{\nu ns}$)	$L_{\nu-ns}$ (10^{51} g cm^2 s^{-1})	Er($L_{\nu ns}$)	$m_{\rm ns}$ ($M_\odot$)	Er($m_{\rm ns}$)	$L_{\rm ns}$ (10^{51} g cm^2 s^{-1})	Er($L_{\rm ns}$)	$p_{\rm orb,f}$ (s)	Er($p_{\rm orb}$)	e	Er(e)
25 $M_\odot$	1.0	1.0	0.1	1.964		3.478		2.078		3.288		6298.29		0.860	
	1.5			1.951	0.0066	3.522	0.0127	2.064	0.0067	3.323	0.0106	8274.54	0.3137	0.883	0.0267
	2.0			1.943	0.0106	3.455	0.0066	2.065	0.0063	3.250	0.0115	7868.58	0.2493	0.880	0.0232
	3.0			1.935	0.0147	3.482	0.0012	2.051	0.0129	3.292	0.0012	10744.9	0.706	0.897	0.0430
	1.0	1.0	0.5	1.915		3.627		2.126		3.255		9843.52		0.892	
	1.5			1.906	0.0046	3.434	0.053	2.099	0.0126	3.118	0.0428	14031.1	0.4254	0.923	0.0348
	2.0			1.900	0.0078	3.499	0.035	2.102	0.0112	3.155	0.0307	12871.2	0.3075	0.913	0.0235
	1.0	1.0	1.0	1.937		3.669		2.209		3.217		91557.2		0.979	
	1.5			1.926	0.0056	3.119	0.1499	2.189	0.0091	2.745	0.1467	25489.6	0.7215	0.962	0.0174
	2.0			1.919	0.0092	3.461	0.0566	2.179	0.0135	3.047	0.0528	145340.6	0.5874	0.985	0.0061
30 $M_\odot$[a]	1.0	2.0	0.1	1.783		4.499		2.077		3.861		⋯		1.44	
	2.0			1.772	0.0061	4.451	0.0106	2.043	0.0164	3.859	0.00051	⋯		1.50	0.0416
	1.0	2.0	1.0	1.781		4.087		2.172		3.351		⋯		1.38	
	2.0			1.769	0.0067	4.614	0.1289	2.115	0.0262	3.859	0.1550	⋯		1.55	0.1096
40 $M_\odot$	1.0	1.0	0.1	1.875		4.419		2.124		3.902		⋯		1.84	
	2.0			1.869	0.0032	4.276	0.0323	2.069	0.0259	3.862	0.0102	⋯		2.00	0.0869

Notes. For each simulation, the four first columns show the progenitor of the $CO_{\rm core}$, the number of particles used in the simulation, the η factor that scales the kinetic and internal energy of the SPH particles to mimic a weaker or stronger SN explosion, and the ξ parameter that determines the size of the capture radius. In the following columns, we show the final mass and angular momentum of the νNS and the NS companion, as well as the orbital period and eccentricity of the final binary system. For each of these values, we give the relative errors with respect to the 1 million particle simulation.

[a] $E_{\rm sn} = 2.19 \times 10^{51}$ erg.

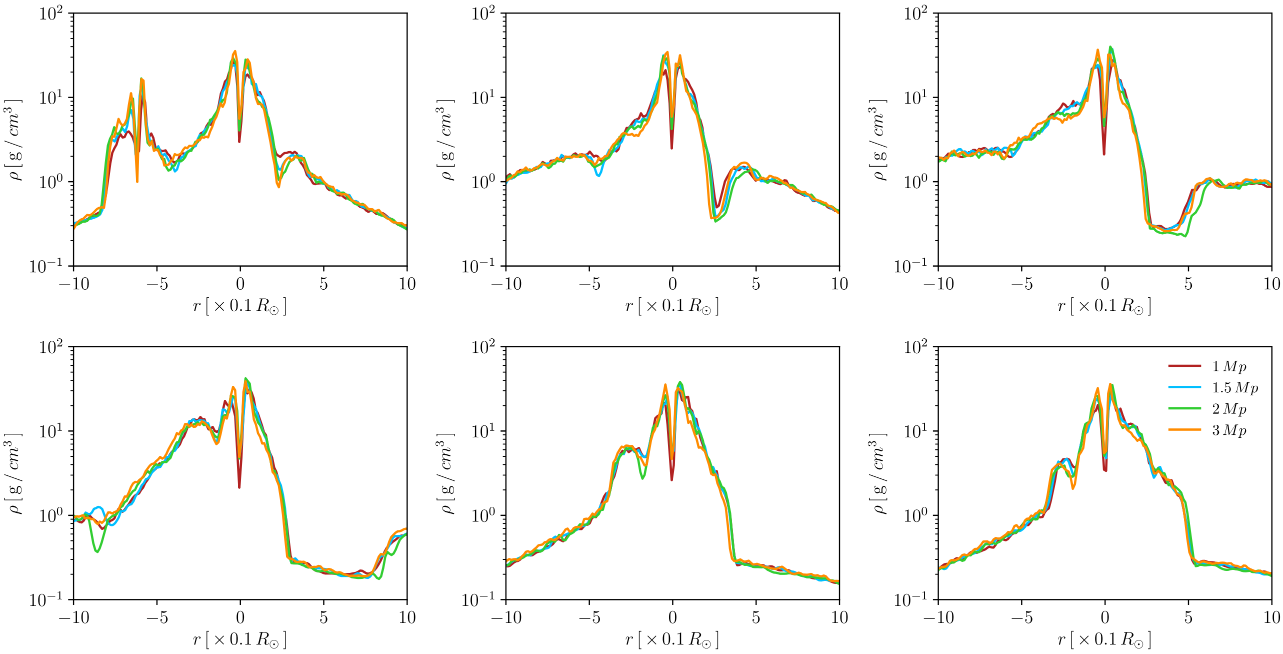

Figure 20. Density along different directions θ on the orbital binary system plane (νNS–NS). From left to right in the upper row, $\theta = 0.0$, $\pi/6$, and $\pi/3$; in the lower row, $\theta = \pi/2$, $2\pi/3$, and $5\pi/6$. The center of the reference system is on the NS position, and the νNS is on the $-x$-axis. The θ direction is measured from the $+x$-axis. The initial binary system is formed by the $CO_{\rm core}$ of the $M_{\rm ZAMS} = 25\,M_\odot$ progenitor and a $2\,M_\odot$ NS in an orbital period of about 5 minutes. Different colors correspond to different numbers of particles: 1 million (red line), 1.5 million (blue line), 2 million (green line), and 3 million (orange line).

spikes in the GRB prompt emission occur at 10^{15}–10^{17} cm from the source and have a Lorentz factor $\Gamma \sim 10^2$–10^3. Instead, the analysis of the thermal emission in the X-ray flares in the early (source rest-frame time $t \sim 10^2$ s) afterglow of BdHNe showed that X-ray flares occur at radii $\sim 10^{12}$ cm and expand mildly relativistically, e.g., $\Gamma \lesssim 4$ (Ruffini et al. 2018b). These model-independent observations are in contrast with an ultrarelativistic expansion all the way from the GRB prompt emission to the afterglow, as traditionally adopted in the majority of the GRB literature in the context of the collapsar-fireball scenario.

In Ruffini et al. (2018b), we tested whether the BdHN scenario could explain both the ultrarelativistic gamma-ray prompt emission and the mildly relativistic X-ray flare data. Our numerical simulations in Becerra et al. (2016) showed that, at the moment of BH formation and GRB emission, the SN ejecta become highly asymmetric around the collapsing NS. In the direction pointing from the $CO_{\rm core}$ to the accreting NS outward and lying on the orbital plane, the NS carves a region of low baryonic contamination in which the GRB e^+e- plasma, created once the NS collapses and forms the BH, can expand with high $\Gamma \sim 10^2$–10^3, explaining the GRB prompt emission. In the other directions, the GRB e^+e- plasma impacts the SN ejecta at approximately 10^{10} cm and evolves carrying a large amount of baryons reaching transparency at radii 10^{12} cm with a mildly $\Gamma \lesssim 4$. This result is in clear agreement with the X-ray flare data (see Melon Fuksman et al. 2018; Ruffini et al. 2018b for details). The most important prediction of this scenario is that the injection of energy and momentum from the GRB plasma into the ejecta transforms the SN into an HN (see Ruffini et al. 2018c for a detailed analysis of GRB 151027A).

The strong dependence of $P_{\rm max}$ on the initial mass of the NS companion opens up the interesting possibility of producing XRFs and BdHNe from binaries with similar short (e.g., $P \sim$ few minutes) orbital periods and $CO_{\rm core}$ properties: while a system with a massive (e.g., $\gtrsim 2\,M_\odot$) NS companion would lead to a BdHN, a system with a lighter (e.g., $\lesssim 1.4\,M_\odot$) NS companion would lead to an XRF. This predicts systems with a similar initial SN leading to a similar νNS but with different GRB prompt and afterglow emission. Clearly, since the GRB energetics are different, the final SN kinetic energy should also be different, since it is larger for the BdHNe.

Besides confirming that XRFs and BdHNe can be produced by these binaries, the present new 3D SPH simulations have also shown new, possibly observable features in the GRB light curves and spectra. Examples are as follows.

(1) The hypercritical accretion occurs on both the NS companion and the νNS with a comparable accretion rate, hence roughly doubling the accretion power of the system.

(2) The above leads to the clear possibility that, under specific conditions, a BH–BH binary can be produced; see, e.g., the simulation "30m1p1eb" in Table 7. Since the system remains bound (see Table 2), the two stellar-mass BHs will merge in due time owing to the emission of gravitational waves. However, no electromagnetic emission is expected from such a merger, and, in view of the typically large cosmological distances of GRBs, their detection by gravitational-wave detectors such as the ground-based interferometers of the LIGO-Virgo network appears to be difficult.

(3) The SNe with lower explosion energy create a long-lived hypercritical accretion process and produce an enhancement at late times of the accretion rate onto the νNS. Such a revival of the accretion rate does not exist in the case of single SNe, namely, in the absence of the NS companion (see Figure 5). In these cases, there is a higher probability of the detection of the early phase of an XRF/BdHN by X-ray detectors.

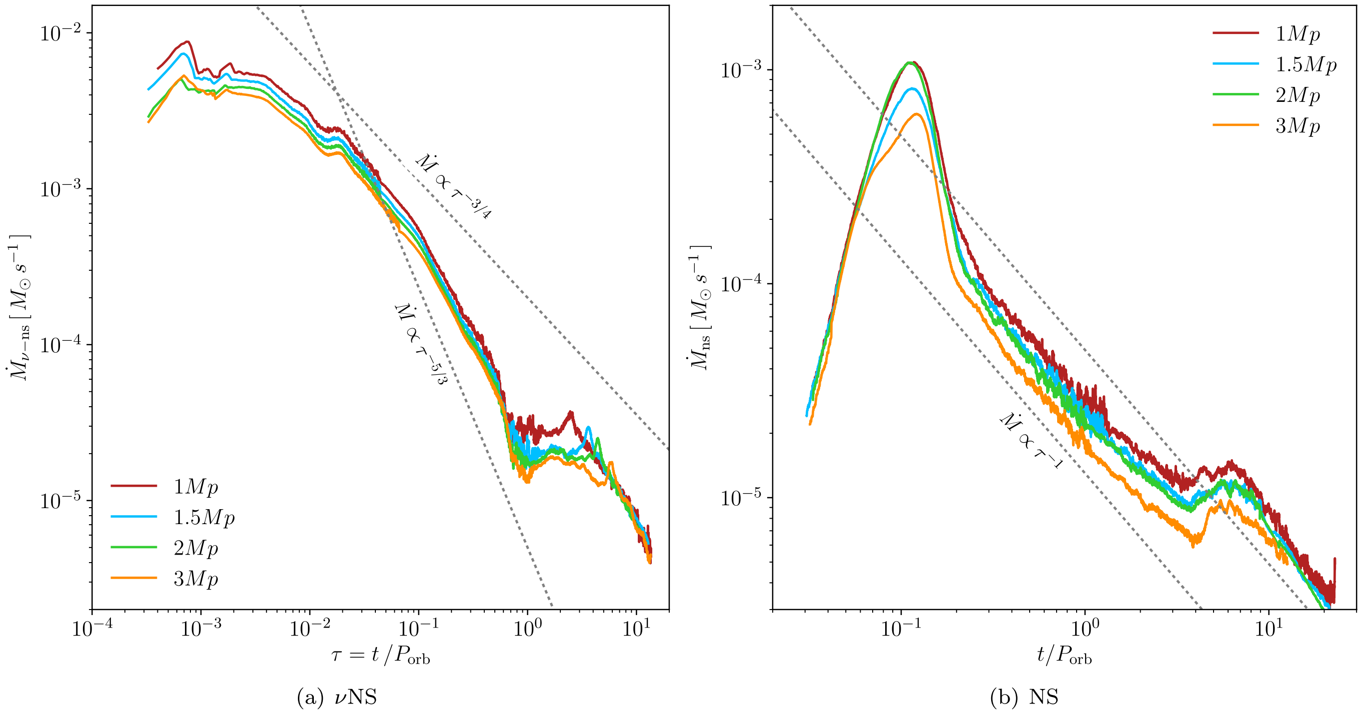

Figure 21. Mass accretion rate on the νNS (left panel) and the NS companion (right panel) for different numbers of particles modeling the SN expansion in the simulation. The initial binary period is the same as in Figure 20.

(4) The asymmetric SN explosions lead to quasi-periodic behavior of the accretion rate that could be detectable by the X-ray instruments (see, e.g., Figure 11). A possible detection of this feature would be a further test of the binary nature and would pinpoint the orbital period of the binary progenitor.

On the other hand, we have evaluated in our simulations whether the binary remains gravitationally bound or becomes unbound by the SN explosion. Therefore, we are determining the space of the initial binary and SN explosion parameters leading to the formation of νNS–NS or νNS–BH binaries. This shows the interesting feature that long GRBs (XRFs and BdHNe) lead to the binary progenitors of short GRBs; hence, this topic is relevant for the understanding of their relative density rate and will be further analyzed in forthcoming works.

8. Conclusions

We have performed the first full numerical 3D SPH simulations of the IGC scenario: in a $\mathrm{CO_{core}}$–NS binary system, the $\mathrm{CO_{core}}$ collapses and explodes in an SN, triggering a hypercritical accretion process onto the NS companion. The initial conditions for the simulations were constructed as follows. The $\mathrm{CO_{core}}$ stars are evolved using the *KEPLER* evolution code (Heger & Woosley 2010) until the conditions for the collapse are met. Then, the stars are exploded with the 1D core-collapse code (Fryer et al. 1999a). When the forward SN shock reaches the stellar radius, we map the explosion to a 3D SPH configuration and continue the evolution of the SN expansion with an NS binary companion using the SNSPH code (Fryer et al. 2006b).

We followed the evolution of the SN ejecta, including their morphological structure, under the action of the gravitational field of both the νNS and the NS companion. We estimated the accretion rate onto both stars with the aid of Equation (22). The baryonic mass accretion rates are calculated from the mass of the SPH particles accreted. We have shown that matter circularizes in a disklike structure around the NS companion (see, e.g., Figure 2). Therefore, for the angular momentum transfer to the NS, we have adopted that the particles are accreted from the LCO.

We determined the fate of the binary system for a wide parameter space including different $\mathrm{CO_{core}}$ masses (see Table 1), orbital periods, SN explosion geometry, and energies, as well as different masses of the NS companion. For selected NS nuclear EOSs, we evaluated whether the accretion process leads the NS to the mass-shedding limit, the secular axisymmetric instability for gravitational collapse to a BH, or a more massive, fast-rotating, but stable NS. We have also analyzed the case of asymmetric SN explosions. We assessed whether the binary remains gravitationally bound or becomes unbound by the explosion. With this information, we determined the space of the initial binary and SN explosion parameters, leading to the formation of νNS–NS or νNS–BH binaries.

It is worth mentioning some issues not included in the numerical calculations presented here that deserve to be further studied and/or improved.

(1) We need to improve the resolution of the code to handle the spatial region in the vicinity of the NS companion at scales 10^6–10^7 cm. This will allow us to better resolve the structure of the circularized matter (accretion disk) near the NS and evaluate more accurately the angular momentum transfer to the NS (e.g., the value of the angular momentum efficiency parameter, χ). These distances are of the order of the NS Schwarzschild radius; therefore, a general relativistic code is needed for this task.

(2) The above will also allow us to study the possible outflows from the hypercritical accretion process previously found in the case of fallback accretion (Fryer 2009) and in which heavy nuclei via r-process nucleosynthesis can be produced (Fryer et al. 2006a).

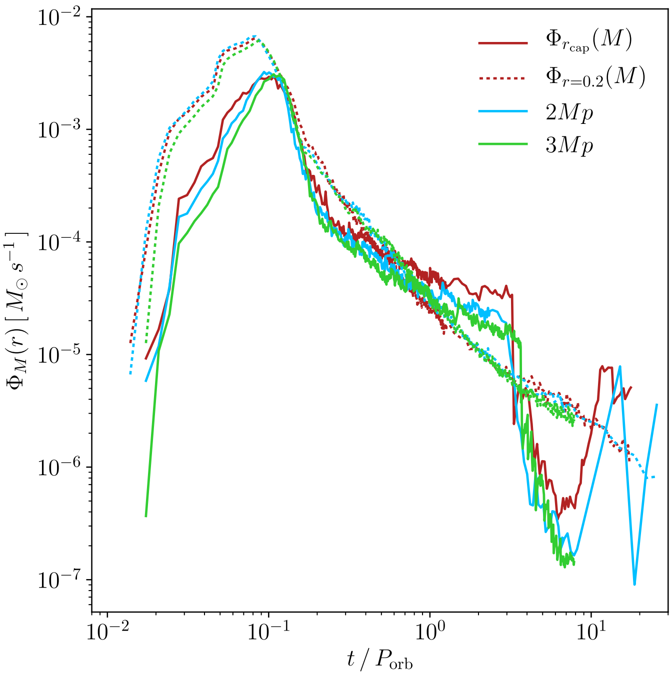

(a) Mass flux

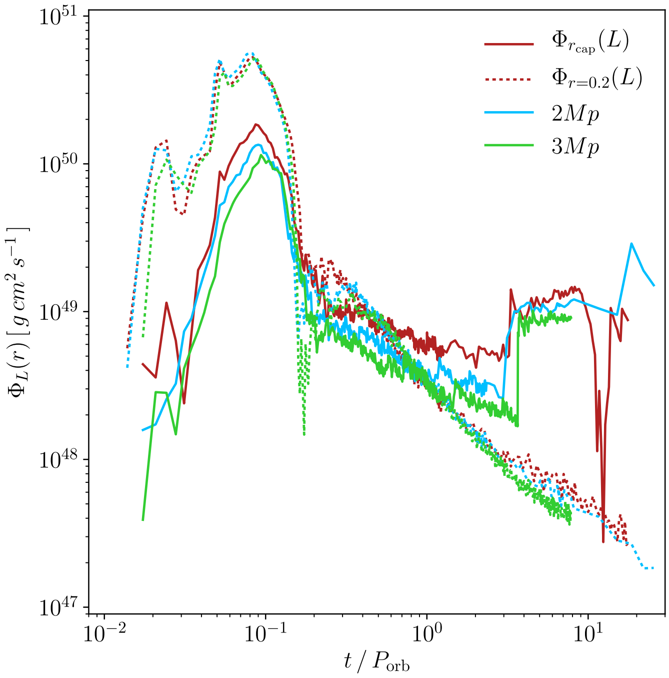

(b) Angular momentum flux

Figure 22. Mass (left panel) and angular momentum flux (right panel) through spheres of radius $r = 0.2\,R_\odot$ and $r = R_{\rm cap}$ with the NS in the center. Here the $R_{\rm cap}$ surface is defined as the maximum capture radius between the particles accreted by the NS in each iteration. The initial binary period is the same as in Figure 20.

(3) Another issue is the transformation of the SN into an HN by the impact of the GRB into the ejecta. We are currently performing hydrodynamical simulations of the interaction of the GRB e^+e^- plasma using a 1D relativistic hydrodynamical module included in the freely available PLUTO (see Ruffini et al. 2018b for further details). We have used in these calculations the SN ejecta profiles at the moment of the NS collapse obtained by Becerra et al. (2016) and evolved them from that instant on under the assumption of homologous expansion.

(4) In view of the above, the present simulations remain accurate/valid up to the instant where the NS reaches the critical mass, hence forming a BH. After that instant, the GRB–SN interaction becomes relevant. In the systems when the NS companion does not reach the critical mass, our simulations remain accurate/valid all the way up to the instant where the entire SN ejecta blows past the NS position.

We discussed in Section 6 some of the consequences of our simulations in the analysis of GRBs within the context of the IGC scenario. The simulations have confirmed, extended, and improved important previous results.

(1) We showed that long GRBs (XRFs and BdHNe) can be produced by these binaries, depending on the binary parameters. We showed that the main parameters defining the fate of the system are the initial mass of the NS companion, the orbital period, and the SN velocity (or kinetic/explosion energy).

(2) The accreting NS companion induces high asymmetries in the SN ejecta that are relevant in the GRB analysis. Recent results of the thermal emission of the X-ray flares in the early (source rest-frame time $t \sim 10^2$ s) afterglow of long GRBs show that they occur at radii $\sim 10^{12}$ cm and expand mildly relativistically with $\Gamma \lesssim 4$. This was shown to be in agreement with the BdHNe of the IGC scenario (see Ruffini et al. 2018b and Section 6 for details): the e^+e- plasma of the GRB, relativistically expanding from the newborn BH, collides with the SN ejecta at distances of the order of 10^{10} cm and then reaches transparency at 10^{12} cm with $\Gamma \lesssim 4$. The 3D simulations presented in this work will be essential to explore the dynamics of the e^+e- plasma along all spatial directions and to estimate, as a function of the viewing angle, the light-curve and spectral properties of BdHNe (see, e.g., Ruffini et al. 2018a, 2018b, 2018c).

(3) One of the most interesting issues is that we have confirmed that some of the systems remain bound after the explosion, implying that XRFs form νNS–NS binaries and BdHNe form νNS–BH systems. Therefore, long GRBs (XRFs and BdHNe) produce the binary progenitors of short GRBs after the shrinking of their orbit until the coalescence by the emission of gravitational waves. The analysis of the number of systems leading to νNS–NS and νNS–BH binaries becomes very important for the explanation of the relative occurrence rate of long and short GRBs.

(4) We have also outlined the consequences of the accretion process and its observational features in the case of relatively weak SN explosion energies, as well as for intrinsically asymmetric ones. We have addressed new features in GRB light curves and spectra, e.g., systems experiencing longer, stronger, and quasi-periodic accretion episodes, to be possibly observed by X-ray instruments. The observation of this kind of phenomenon in the early phases of a GRB would benefit from a new mission operating in soft X-rays like, e.g., *THESEUS* (Amati et al. 2018).

(5) We have shown that some $CO_{\rm core}$–NS binaries could produce BdHNe leading to BH–BH binaries. This happens when the νNS experiences a massive fallback accretion and collapses to a BH. The final merger of the two stellar-mass BHs has no electromagnetic counterpart to detect, and its gravitational-wave emission, in view of the large distances of these sources, appears to be much too weak to be detected by current interferometers such as LIGO-Virgo.

We thank the referee for the comments and suggestions to improve the presentation of our results. The work of L.B., C.E., and C.F. was partially funded under the auspices of the U.S. Dept. of Energy and supported by contract W-7405-ENG-36 to Los Alamos National Laboratory. Simulations at LANL were performed on HPC resources provided under the Institutional Computing program.

Appendix
Numerical Convergence

In order to evaluate the convergence of our SPH simulation, we have done some numerical experiments varying the number of particles with which we model the SN ejecta for the different pre-SN progenitors.

We performed simulations with 1, 1.5, 2, and 3 million particles with different progenitors and different values of the ξ parameter in Equation (10). We summarize the results of these simulations in Table 10. We compare and contrast the final accreted mass and angular momentum of the νNS and the NS companion and the final orbital period and eccentricity of the orbit. We also report the relative error of these quantities, taking as the reference values the ones of the simulation of about 1 million particles.

We show in Figure 20 profiles of the density on the binary orbital plane and along different directions, taking the NS companion as the center of the reference frame. Figure 21 shows the mass accretion rate on the νNS and the NS companion. Finally, we plot in Figure 22 the flux of the mass and angular momentum onto the NS companion at two different distances from it: $r = 0.02\,R_\odot$ and $r = R_{\rm cap}$, defined as the maximum capture radius of the NS in each iteration. All of these figures correspond to the simulation of an initial binary system formed by the $\mathrm{CO_{core}}$ of the $25\,M_\odot$ progenitor (see Table 1) and a $2\,M_\odot$ NS with an initial orbital period of $\approx$2 minutes.

ORCID iDs

C. L. Fryer https://orcid.org/0000-0003-2624-0056
J. A. Rueda https://orcid.org/0000-0002-3455-3063

References

Amati, L., O'Brien, P., Götz, D., et al. 2018, AdSpR, 62, 191
Antoniadis, J., Freire, P. C. C., Wex, N., et al. 2013, Sci, 340, 448
Babkovskaia, N., Brandenburg, A., & Poutanen, J. 2008, MNRAS, 386, 1038
Bate, M. R., Bonnell, I. A., & Price, N. M. 1995, MNRAS, 277, 362
Batta, A., Ramirez-Ruiz, E., & Fryer, C. 2017, ApJL, 846, L15
Becerra, L., Bianco, C. L., Fryer, C. L., Rueda, J. A., & Ruffini, R. 2016, ApJ, 833, 107
Becerra, L., Cipolletta, F., Fryer, C. L., Rueda, J. A., & Ruffini, R. 2015, ApJ, 812, 100
Becerra, L., Guzzo, M. M., Rossi-Torres, F., et al. 2018, ApJ, 852, 120
Benz, W. 1990, in Numerical Modelling of Nonlinear Stellar Pulsations Problems and Prospects, ed. J. R. Buchler (Dordrecht: Kluwer), 269
Bisnovatyi-Kogan, G. S. 1993, A&AT, 3, 287
Blandford, R. D., & Begelman, M. C. 1999, MNRAS, 303, L1
Bondi, H. 1952, MNRAS, 112, 195
Bondi, H., & Hoyle, F. 1944, MNRAS, 104, 273
Breton, R. P., van Kerkwijk, M. H., Roberts, M. S. E., et al. 2013, ApJ, 769, 108
Chevalier, R. A. 1989, ApJ, 346, 847
Cipolletta, F., Cherubini, C., Filippi, S., Rueda, J. A., & Ruffini, R. 2015, PhRvD, 92, 023007
Cipolletta, F., Cherubini, C., Filippi, S., Rueda, J. A., & Ruffini, R. 2017, PhRvD, 96, 024046
Colgate, S. A. 1971, ApJ, 163, 221
Demorest, P. B., Pennucci, T., Ransom, S. M., Roberts, M. S. E., & Hessels, J. W. T. 2010, Natur, 467, 1081
Dexter, J., & Kasen, D. 2013, ApJ, 772, 30
Diehl, S., Fryer, C., & Herwig, F. 2008, in ASP Conf. Ser. 391, Hydrogen-Deficient Stars, ed. A. Werner & T. Rauch (San Francisco, CA: ASP), 221
Diehl, S., Rockefeller, G., Fryer, C. L., Riethmiller, D., & Statler, T. S. 2015, PASA, 32, e048
Dominik, M., Belczynski, K., Fryer, C., et al. 2012, ApJ, 759, 52
Eggleton, P. P. 1983, ApJ, 268, 368
Fryer, C., Benz, W., Herant, M., & Colgate, S. A. 1999a, ApJ, 516, 892
Fryer, C. L. 1999, ApJ, 522, 413
Fryer, C. L. 2009, ApJ, 699, 409
Fryer, C. L., Andrews, S., Even, W., Heger, A., & Safi-Harb, S. 2018, ApJ, 856, 63
Fryer, C. L., Herwig, F., Hungerford, A., & Timmes, F. X. 2006a, ApJL, 646, L131
Fryer, C. L., & Kusenko, A. 2006, ApJS, 163, 335
Fryer, C. L., Oliveira, F. G., Rueda, J. A., & Ruffini, R. 2015, PhRvL, 115, 231102
Fryer, C. L., Rockefeller, G., & Warren, M. S. 2006b, ApJ, 643, 292
Fryer, C. L., Rueda, J. A., & Ruffini, R. 2014, ApJL, 793, L36
Fryer, C. L., & Warren, M. S. 2002, ApJL, 574, L65
Fryer, C. L., Woosley, S. E., & Hartmann, D. H. 1999b, ApJ, 526, 152
Fryer, C. L., & Young, P. A. 2007, ApJ, 659, 1438
Guetta, D., & Della Valle, M. 2007, ApJL, 657, L73
Heger, A., & Woosley, S. E. 2010, ApJ, 724, 341
Herant, M., Benz, W., Hix, W. R., Fryer, C. L., & Colgate, S. A. 1994, ApJ, 435, 339
Hills, J. G. 1983, ApJ, 267, 322
Hoyle, F., & Lyttleton, R. A. 1939, PCPS, 35, 405
Hungerford, A. L., Fryer, C. L., & Rockefeller, G. 2005, ApJ, 635, 487
Hungerford, A. L., Fryer, C. L., & Warren, M. S. 2003, ApJ, 594, 390
Inogamov, N. A., & Sunyaev, R. A. 1999, AstL, 25, 269
Inogamov, N. A., & Sunyaev, R. A. 2010, AstL, 36, 848
Izzo, L., Rueda, J. A., & Ruffini, R. 2012, A&A, 548, L5
Janka, H.-T. 2012, ARNPS, 62, 407
Janka, H.-T., & Mueller, E. 1994, A&A, 290, 496
Kohri, K., Narayan, R., & Piran, T. 2005, ApJ, 629, 341
Lattimer, J. M., & Prakash, M. 2007, PhR, 442, 109
Lee, C.-H., & Cho, H.-S. 2014, NuPhA, 928, 296
Linares, M., Shahbaz, T., & Casares, J. 2018, ApJ, 859, 54
Melon Fuksman, J. D., Becerra, L., Bianco, C. L., et al. 2018, European Physical Journal Web of Conferences, 168, 04009
Monaghan, J. J. 1992, ARA&A, 30, 543
Monaghan, J. J. 2005, RPPh, 68, 1703
Moriya, T., Tominaga, N., Tanaka, M., et al. 2010, ApJ, 719, 1445
Murphy, J. W., Dolence, J. C., & Burrows, A. 2013, ApJ, 771, 52
Philippov, A. A., Rafikov, R. R., & Stone, J. M. 2016, ApJ, 817, 62
Postnov, K. A., & Yungelson, L. R. 2014, LRR, 17, 3
Price, D. J. 2011, SPLASH: An Interactive Visualization Tool for Smoothed Particle Hydrodynamics Simulations, Astrophysics Source Code Library, ascl:1103.004
Rueda, J. A., & Ruffini, R. 2012, ApJL, 758, L7
Ruffini, R., Becerra, L., Bianco, C. L., et al. 2018c, ApJ, 869, 151
Ruffini, R., Bianco, C. L., Fraschetti, F., Xue, S.-S., & Chardonnet, P. 2001, ApJL, 555, L117
Ruffini, R., Moradi, R., Wang, Y., et al. 2018a, arXiv:1803.05476
Ruffini, R., Muccino, M., Bianco, C. L., et al. 2014, A&A, 565, L10
Ruffini, R., Rueda, J. A., Muccino, M., et al. 2016, ApJ, 832, 136
Ruffini, R., Wang, Y., Aimuratov, Y., et al. 2018b, ApJ, 852, 53
Shakura, N. I., & Sunyaev, R. A. 1988, AdSpR, 8, 135
Stergioulas, N., & Friedman, J. L. 1995, ApJ, 444, 306
Tauris, T. M., Langer, N., Moriya, T. J., et al. 2013, ApJL, 778, L23
Tauris, T. M., Langer, N., & Podsiadlowski, P. 2015, MNRAS, 451, 2123
Warren, M. S., & Salmon, J. K. 1993, in Proc. 1993 ACM/IEEE Conf. on Supercomputing (New York: ACM), 12
Warren, M. S., & Salmon, J. K. 1995, CoPhC, 87, 266
Wong, T.-W., Fryer, C. L., Ellinger, C. I., Rockefeller, G., & Kalogera, V. 2014, arXiv:1401.3032
Woosley, S. E. 1987, in IAU Symp. 125, The Origin and Evolution of Neutron Stars, ed. D. J. Helfand & J.-H. Huang (Dordrecht: Reidel), 255
Woosley, S. E. 1993, ApJ, 405, 273
Woosley, S. E., & Weaver, T. A. 1995, ApJS, 101, 181
Young, P. A., Fryer, C. L., Hungerford, A., et al. 2006, ApJ, 640, 891
Zhang, W., Woosley, S. E., & Heger, A. 2008, ApJ, 679, 639

Universal relations for the Keplerian sequence of rotating neutron stars

R. Riahi,[1,2,*] S. Z. Kalantari,[1,†] and J. A. Rueda[2,3,4,‡]
[1]*Department of Physics, Isfahan University of Technology, Isfahan 84156-83111, Iran*
[2]*ICRANet, Piazza della Repubblica 10, I-65122 Pescara, Italy*
[3]*Dipartimento di Fisica and ICRA, Sapienza Università di Roma, P.le Aldo Moro 5, I-00185 Rome, Italy*
[4]*ICRANet-Rio, Centro Brasileiro de Pesquisas Físicas, Rua Dr. Xavier Sigaud 150, Rio de Janeiro, RJ 22290-180, Brazil*

(Received 11 October 2018; revised manuscript received 14 January 2019; published 11 February 2019)

We investigate the Keplerian (mass-shedding) sequence of rotating neutron stars. Twelve different equations of state are used to describe the nuclear structure. We find four fitting relations which connect the rotating frequency, mass and radius of stars in the mass-shedding limit to the mass and radius of stars in the static sequence. We show the breakdown of approximate relation for the Keplerian frequency derived by Lattimer and Prakash [Science **304**, 536 (2004)] and then we present a new, equation of state (EOS)-independent and more accurate relation. This relation fits the Keplerian frequency of rotating neutron stars to about 2% for a large range of the compactness M_S/R_S of the reference nonrotating neutron star, namely the static star with the same central density as the rotating one. The performance of the fitting formula is close to 4% for $M_S/R_S \leq 0.05\ M_\odot/\mathrm{km}$ ($f_K \leq 350$ Hz). We present additional EOS-independent relations for the Keplerian sequence including relations for $M_K f_K$ and $R_K f_K$ in terms of $M_S f_S$ and $R_S f_S$, respectively, one of M_K/R_K as a function of f_K/f_S and M_S/R_S, and a relation between the M_K, R_K and f_K. These new fitting relations are approximately EOS independent with an error in the worst case of 8%. The universality of the Keplerian sequence properties presented here add to the set of other neutron star universal relations in the literature such as the I-Love-Q relation, the gravitational binding energy and the energy, angular momentum and radius of the last circular orbit of a test particle around rotating neutron stars. This set of universal, analytic formulas facilitates the inclusion of general relativistic effects in the description of relativistic astrophysical systems involving fast rotating neutron stars.

DOI: 10.1103/PhysRevD.99.043004

I. INTRODUCTION

Neutron stars are the densest stars in the Universe and play a fundamental role in the understanding of a large number of relativistic physics and astrophysics issues, e.g., the behavior of matter at supranuclear densities, the mechanisms that trigger the most energetic cataclysmic events in the Universe (supernovae and gamma-ray bursts), the formation of heavy nuclei via r-process nucleosynthesis in the ejecta of neutron star binary mergers and the population of high-frequency (kHz) gravitational-waves sources. In addition, the observation of neutron stars in less energetic systems, e.g., pulsars in binary systems, the thermal x-ray emission from isolated neutron stars and of the quasiperiodic oscillations from accreting neutron stars, is important to obtain information about neutron stars radii, masses, ages, internal composition and temperatures.

The relation between the structure of a neutron star (mass, radius, etc.) and the microphysical input, namely the equation of state (EOS) of ultradense matter, is crucial for the understanding of all the above physical and astrophysical scenarios. In view of the absence of a complete knowledge of the nuclear EOS at supranuclear conditions, a variety of approaches has been used for modeling neutron stars and deriving their properties which depend on the selected EOS [1–5]. These properties have been compared with the observational constraints that help to narrow down the physically plausible nuclear EOS (see e.g., [6]).

Many attempts have been made to obtain approximate, EOS-independent relations between neutron star properties which become useful tools in astrophysical applications without suffering from the EOS indeterminacy. Those relations are usually EOS independent to within $O(1\%)$ error and they have been called *universal* relations (see e.g., [7] and references therein). For instance, Laarakkers and Poisson [8] calculated the quadrupole moment of the mass distribution, Q, and concluded that for a fixed mass and EOS, the Q-dependence on the angular momentum J can be fitted by a quadratic formula. In [9] a fitting relation was found between the parameter QM/J^2 and the ratio of the circumferential radius of star to its Schwarzschild radius, $R/(2M)$, for rotating neutron stars within the

*r.riahi@ph.iut.ac.ir
†zafar@cc.iut.ac.ir
‡jorge.rueda@icra.it

Hartle-Thorne, slow-rotation approximation. In [10] an EOS-independent relation for the maximum rotational frequency of stars in terms of mass and radius of non-rotating stars was introduced. Reference [11] connected the frequency and damping rate of the quadrupole f-mode to the mass and moment of inertia of nonrotating neutron stars. In [12,13] there were derived relations, within the framework of the Hartle-Thorne approximation, which connect the moment of inertia I, the Love number and the quadrupole moment Q of rotating neutron stars, called I-Love-Q relations. Afterwards, [14] demonstrated the breakdown of such relations in fast rotating stars, then [15] extended these relations to fast rotating by replacing the dimensional frequency with the dimensionless angular momentum, $j = cJ/(GM_{\odot}^2)$. Finally, in [16] other dimensionless quantities such as $M \times f$ and $R \times f$ were used to extend these relations. In [17] a pair of relations connecting the maximum and minimum masses of a rotating star of rotation frequency f, to the maximum mass of static configuration, were derived. Additional relations between the redshift (polar, forward and backward) and the minimum and maximum compactness of the star were also presented. It was there reproduced the formula suggested in [18] and reformulated in [19], with different coefficients. In [20] formulas for the binding energy of static and rotating stars as a function of the gravitational mass and dimensionless angular momentum, j, were presented. Also, they provided a formula connecting the maximum mass, i.e., along the secular instability limit, and j. Reference [21] studied the last circular orbit of a test particle around fast rotating neutron stars. They presented a pair of fitting relations that connect the radius and orbital frequency of this orbit to the rotation frequency f and mass M of the rotating neutron star.

The aim of this work is to investigate the Keplerian (mass-shedding) sequence of rotating neutron stars to search for EOS-independent relations useful for astrophysical applications. We present here universal relations connecting the mass and frequency of a configuration along the Keplerian sequence, to the mass and radius of the non-rotating (static) configuration with the same central density as the rotating star, and to the Keplerian frequency of a test particle in an orbit of size equal to the static neutron star radius. Although we use $c = G = 1$ geometric units in our calculations, we restore physical units to simplify the use of results in astrophysical situations. We use units $M_{\odot}$, km and Hz, respectively for the mass, radius and frequency.

II. KEPLERIAN (MASS-SHEDDING) SEQUENCE OF ROTATING NEUTRON STARS

The EOS, namely relation between energy density and pressure, is an essential requirement for describing the macroscopic properties of stars. The EOS is used as input to the Einstein field equations. Nonrelativistic [22] and relativistic models [23] have been used to obtain stellar properties. In this work, we use 12 EOSs with different theoretical features including microscopic calculations, relativistic mean field and Skyrme mean field to find the universal relations. All of our selected EOSs used in the fits of the numerical data support a nonrotating neutron star with a maximum mass larger than $M_S \gtrsim 2.0\ M_{\odot}$, consistent with the current observational constraints [24,25]. There are two EOSs based on microscopic calculations, APR [26] and BL [27], eight relativistic mean-field models, BKA22, BKA24 [28], CMF [29], DDHδ (with hyperons) [30,31], DD-MEδ [32], G1 [33], GM1 (with hyperons) [34–36] and TW99 [37] and two Skyrme mean-field models, SKa [38] and SLy4 [39], to find the fitting relations. In order to test the robustness of the universal relations and the obtained fits, we compute the relative error for three additional EOS, not used in the fitting procedure, and check their relative error lies with the error attached to the given fits. For this task we use a soft EOS, G2* [40], a moderately stiff EOS, GM1 (without hyperons)[34], and a stiff EOS, NL3 [41].

In order to solve Einstein field equations and investigate the structure and gravitational field of relativistic, axisymmetric, stationary and uniform rotating stars, many numerical methods have been developed since the 1970s (see e.g., [42–47]). Based on these methods a few publicly numerical codes have been developed [48] to solve them. We use the public LORENE library [49] for the numerical solution. This code has being developed based on the multidomain spectral method which had presented by Bonazzola *et al.* [50,51] and developed by Ansorg *et al.* [52].

One of the most important sequences limiting the equilibrium states of the rotating star is the mass-shedding or Keplerian sequence. This limiting configuration is usually determined by obtaining the configuration for which the velocity of a fluid element at the stellar equator equals the one of a test particle in a stable circular orbit at the equator of the star, namely the limit when the centrifugal and gravitational forces are in balance (see [53] for a review on rotating stars). At the equator of the star, fluid elements are dislodged at velocities higher than this and the star begins to shed mass. Assuming the observed rotation frequency f of the neutron star is not close to the absolute maximum rotation frequency, or that the mass of the star is not near the maximum stable mass (see e.g., Fig. 1), then the Keplerian frequency can be assumed as the maximum frequency at which the star can rotate and therefore the condition $f \leq f_K$ imposes a lower limit to M, the Keplerian mass, M_K or, equivalently, an upper limit to R, the Keplerian radius, R_K.

III. RESULTS

A. EOS-dependent sequence

Despite many studies on high density matter, there is still no agreement on its EOS and a large number of EOSs are

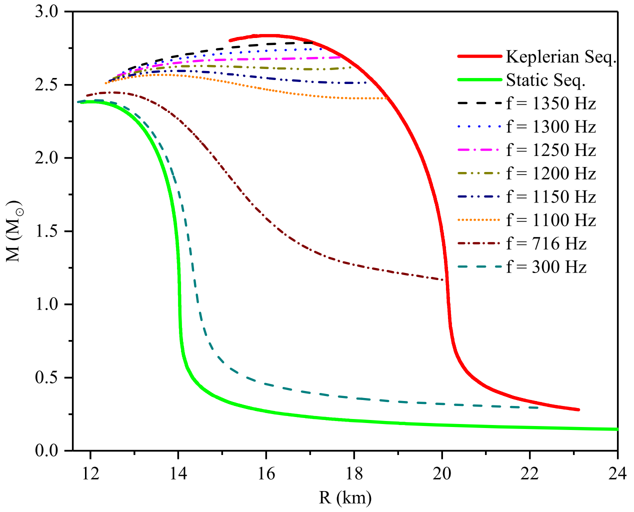

FIG. 1. Mass versus equatorial radius along constant high-frequency sequences for the GM1 EOS. It can be seen how above some frequency value (here ≈1200 Hz) the mass at which the constant frequency sequence cuts the Keplerian sequence does not represent a minimum mass bound.

presented in the literature. Each EOS determines the different equilibrium sequences of static and rotating stars. In Fig. 2 we show, for the selected EOS, the mass-radius relation of a star in the Keplerian sequence. It is obvious that the sequences depend on the EOS. This apparent strong dependence on the EOS is our motivation to unveil possible universal relations.

B. Universal (EOS-independent) relations

Lattimer and Prakash (hereafter L&P) derived in [10] a relation, nearly independent of the EOS, which gives the Keplerian frequency of a rotating neutron star, in terms of the radius R_S and mass M_S of the reference nonrotating neutron star (star with the same central density as the rotating one), providing it is not close to the maximum stable mass allowed by the EOS. The relation is

$$f_K = 1045\left(\frac{M_S}{M_\odot}\right)^{1/2}\left(\frac{10\ \mathrm{km}}{R_S}\right)^{3/2}\ \mathrm{Hz} \approx 0.5701 f_S, \qquad (1)$$

where $f_S = 1833(M_S/M_\odot)^{1/2}(10\ \mathrm{km}/R_S)^{3/2}$ Hz is the orbital frequency of a test particle spins around a spherical mass M_S at a distance R_S. First, in Fig. 3 we plot the f_K/f_S ratio against M_S and it shows that Eq. (1) underestimates this ratio and the relative error between this relation and the calculated ratio from EOSs reaches up to 30% by increasing M_S.

In order to find a more accurate relation for f_K, we consider as a parameter the compactness of the nonrotating configuration of the same central density, M_S/R_S (dimensionless parameter in geometric units). We plot f_K/f_S as a function of M_S/R_S in Fig. 4. It becomes clear that this is approximately EOS independent and follows the universal relation fitted by

$$y = a_0 + a_1 x + a_2 x^2 + a_3 x^3, \qquad (2)$$

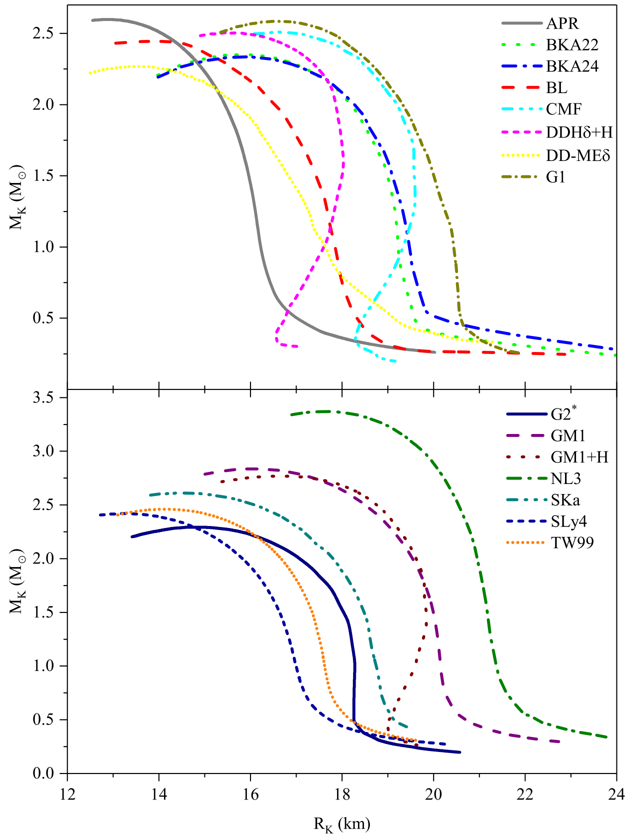

FIG. 2. Mass versus equatorial radius of the configurations at the Keplerian sequence for the selected EOS used in this work.

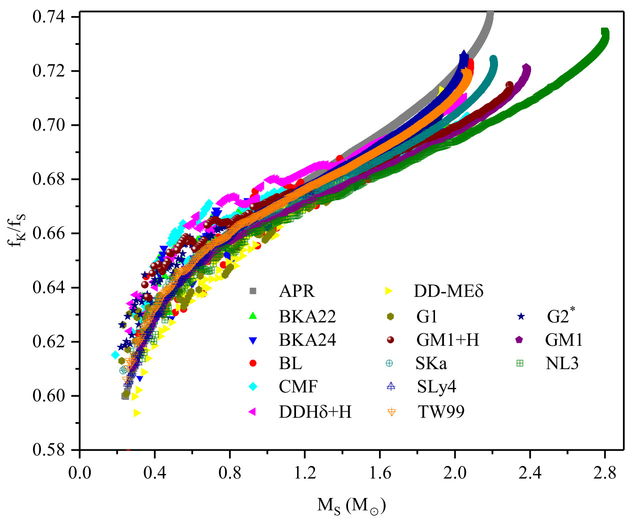

FIG. 3. f_K/f_S ratio versus M_S for each selected EOS.

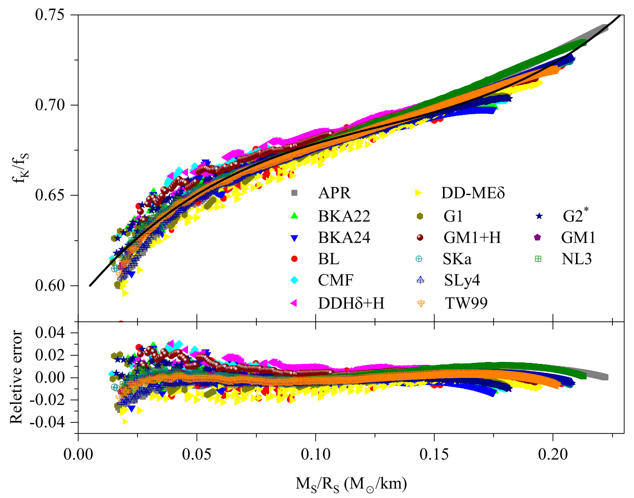

FIG. 4. The fitting curve given by Eq. (2) (black solid curve) and f_K/f_S ratio versus M_S/R_S for each selected EOS (upper panel). The relative error between the calculated data and Eq. (2) (lower panel).

where $y = f_K/f_S$ and $x = (M_S/M_\odot)(\mathrm{km}/R_S)$ and the fitting parameters are $a_0 = 0.5926$, $a_1 = 1.5933$, $a_2 = -9.9582$ and $a_3 = 26.2608$. The order of the polynomial is chosen in such a way that the relative error is small (e.g., $\lesssim 5\%$) and that the addition of more terms does not improve the fit. In the upper panel of Fig. 4, the fitting relation is indicated by a black solid line and, in the lower panel, the relative error between the numerical calculations y_{cal} and the fitting relation y, $(y_{\mathrm{cal}} - y)/y$ is shown. We conclude the numerical data can be fitted by Eq. (2) with a relative error about 2% for a large range of M_S/R_S and increases up to 4% for $M_S/R_S \leq 0.05\ M_\odot/\mathrm{km}$ which related to $f_K \leq 350$ Hz. It is worth mentioning that, for some EOS (see e.g., the BL one), the code numerical results show some "fluctuations" which could in principle affect the accuracy of our results. The problem persists even if we use an EOS table with 500 points or more. Fortunately, those fluctuations are observed only in the low mass range, e.g., $M < 1.0\ M_\odot$, which is of no astrophysical relevance. In addition, we have checked that the order of magnitude of such fluctuations in that low-mass region is of the order of 0.1 km for the equatorial radius. The relative error introduced is therefore $\sim 0.1/20 = 0.005$. In the case of the frequency ratio f_K/f_S, the fluctuations are of the order of 0.02, then the relative error introduced is $\sim 0.02/0.66 = 0.03$ which is due to the Keplerian frequency error. This shows that these fluctuations, very likely, are not affecting our numerical results. This is further strengthened by the fact that the majority of EOSs of our sample are well behaved. In the calculations, we have used around 750 points for each EOS, when using more than these numbers of points does not improve the fitting results.

We can now compare the new relation, Eq. (2), and the L&P relation, Eq. (1). To this aim we use the up-to-now considered fastest known pulsar, PSR J1748–2446ad [54], which rotates with a frequency of 716 Hz. In addition to this, for completeness purpose, we do the same analysis using the XTE J1739-285 [55], which has been claimed to rotate with a frequency of 1122 Hz. If these latter observations will be fully confirmed, this pulsar will become the fastest observed neutron star. It can be seen that the approximate relation of L&P is more stringent than ours, namely the lower limit to M_S it imposes for PSR J1748–2446ad ($f = 716$ Hz) is larger than the one set by our Eq. (2) or, equivalently the upper limit to R_S is lower than ours.

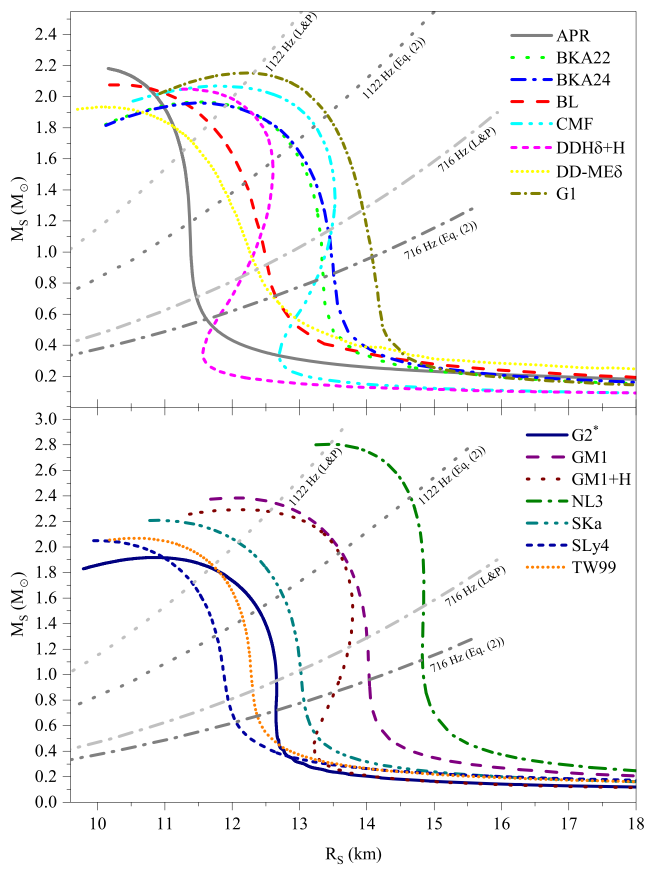

FIG. 5. Comparison of the new relation, Eq. (2), and the L&P relation, Eq. (1). We here use the fastest observed pulsar up to now, PSR J1748-2446ad [54] with $f = 716$ Hz and a frequency of $f = 1122$ Hz, the rotation rate claimed of the neutron star in the XTE J1739-285 [55], but not yet confirmed. The light gray dot-dashed and dotted curves give the relation (1) from Ref. [10]. The dark gray dot-dashed and dotted curves are obtained from our Eq. (2). We also show the nonrotating mass-radius relation obtained with all the EOSs used in this work.

This EOS-independent property motivates us to seek additional independent quantities. We investigate other dimensionless parameters: $M_K f_K$, $R_K f_K$ and M_K/R_K where M_K and R_K are the mass and circumferential equatorial radius of the star in the Keplerian sequence,

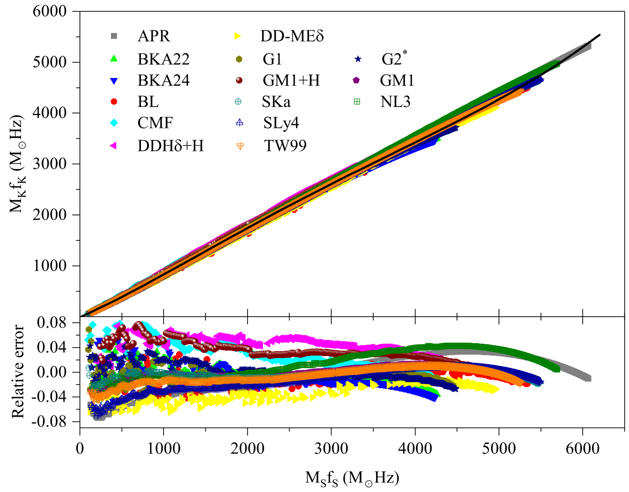

FIG. 6. $M_K f_K$ versus $M_S f_S$ for each selected EOS. The black solid curve indicates Eq. (3) (upper panel). The relative error between the curve and data (lower panel).

respectively. Figures 6 and 7 show $M_K f_K$ and $R_K f_K$ in terms of $M_S f_S$ and $R_S f_S$, respectively. It is clear they are approximately EOS independent. $M_K f_K$ can be fitted by

$$y = b_0 + b_1 x + b_2 x^2 + b_3 x^3 + b_4 x^4 + b_5 x^5, \qquad (3)$$

where $y = M_K f_K$ and $x = M_S f_S$ are in $M_\odot$ Hz unit. This equation is shown by a solid curve in the upper panel of Fig. 6. The fitting parameters are $b_0 = -11.4297$, $b_1 = 7.3839 \times 10^{-1}$, $b_2 = 1.4973 \times 10^{-4}$, $b_3 = -5.2280 \times 10^{-8}$, $b_4 = 6.3072 \times 10^{-12}$, $b_5 = -1.7919 \times 10^{-16}$. The relative error between the calculated data and the fitting relation is presented in the lower panel of Fig. 6. We can see the data can be fitted by this equation with relative error to about 6%.

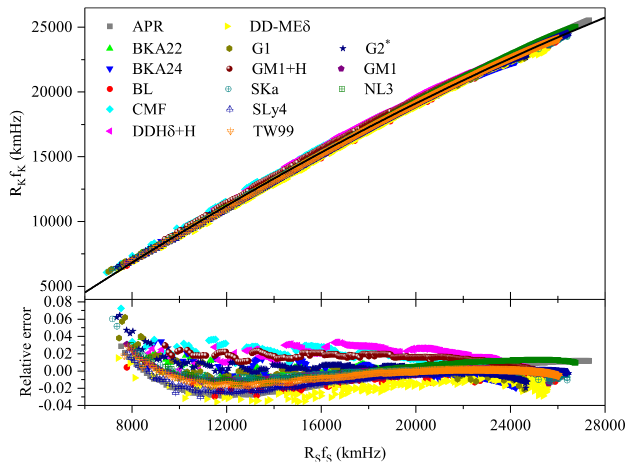

FIG. 7. $R_K f_K$ versus $R_S f_S$ for each selected EOS. The black solid curve indicates Eq. (4) (upper panel). The relative error between the curve and data (lower panel).

Another interesting parameter we study is $R_K f_K$. As Fig. 7 shows, we fit this data with a relation (black solid curve) which is written

$$y = c_0 + c_1 x + c_2 x^2 + c_3 x^3, \qquad (4)$$

where $y = R_K f_K$ and $x = R_S f_S$ are in kmHz unit. The fitting parameters are $c_0 = -2.8321 \times 10^3$, $c_1 = 1.2792$, $c_2 = -8.6628 \times 10^{-6}$ and $c_3 = -2.0203 \times 10^{-11}$. The lower panel of Fig. 7 shows the relative error between the numerical data and the fit is about 4% for a large range of $R_S f_S$ and increases up to 8% for $R_S f_S \leq 8000$ kmHz which related to $f_K \leq 350$ Hz and $M_S \leq 0.3\ M_\odot$.

The next parameter we study is the compactness along the Keplerian sequence, M_K/R_K. Figure 8 shows in the upper panel the numerical data and the fitting relation (block solid curve). The relative error, which is around 4%, is shown in the lower panel.

The numerical relation is well fitted by

$$y = d_1 x + d_2 x^2 + d_3 x^3 + d_4 x^4, \qquad (5)$$

where $x = (M_S/M_\odot)(\mathrm{km}/R_S)(f_K/f_S)$ is a dimensionless quantity and the fitting parameters are obtained in such a way that $y = M_K/R_K$ is also dimensionless. The fitting parameters are $d_1 = 1.7658$, $d_2 = 7.0424$, $d_3 = -7.5442 \times 10^1$ and $d_4 = 2.2236 \times 10^2$. This equation, which shows the relation between the compactness of the rotating neutron star in the Keplerian sequence and that of the reference static neutron star, gives the least compact rotating neutron star for a given rotation frequency.

The introduced equations give the relation between the various quantities of rotating and static neutron stars.

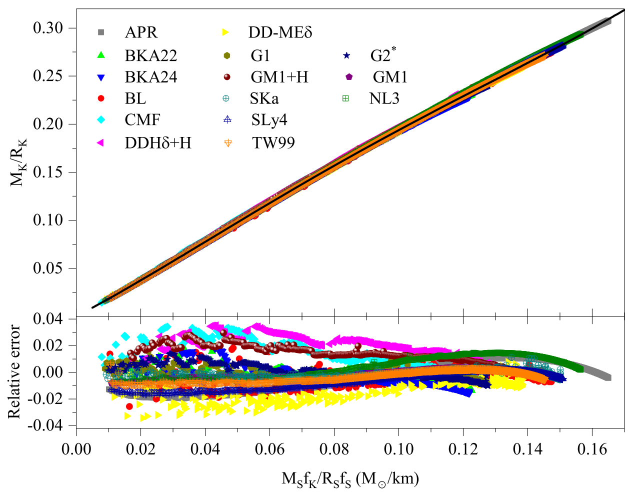

FIG. 8. The dimensionless parameter, compactness, versus $(M_S/R_S)(f_K/f_S)$ for each selected EOS. The black solid curve indicates Eq. (5) (upper panel). The relative error between the curve and data (lower panel).

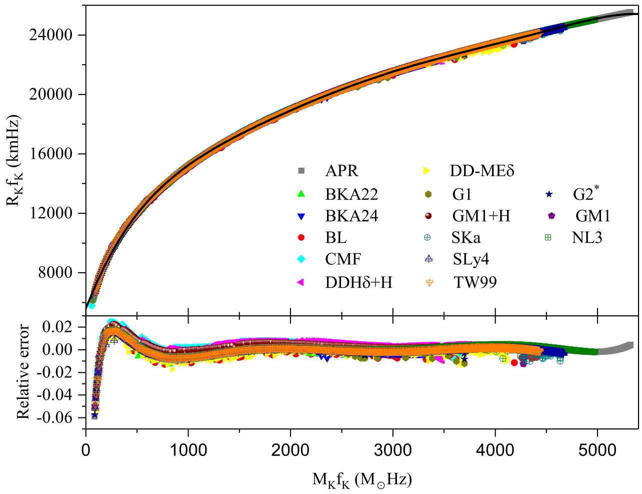

FIG. 9. $R_K f_K$ versus $M_K f_K$ for each selected EOS. The black solid curve indicates Eq. (6) (upper panel). The relative error between the curve and data (lower panel).

The following equations give the relation between dimensionless parameters, e.g., $R_K f_K$ and $M_K f_K$. Figure 9 shows that these quantities can be related in an EOS-independent fashion and a fitting relation is

$$y = e_0 + e_1 x + e_2 x^2 + e_3 x^3 + e_4 x^4 + e_5 x^5 + e_6 x^6, \qquad (6)$$

where $y = R_K f_K$, $x = M_K f_K$ are in kmHz and $M_\odot$ Hz units, respectively. The fitting parameters are $e_0 = 56.8408 \times 10^2$, $e_1 = 17.5480$, $e_2 = -1.2587 \times 10^{-2}$, $e_3 = 5.9763 \times 10^{-6}$, $e_4 = -1.5983 \times 10^{-9}$, $e_5 = 2.1962 \times 10^{-13}$ and $e_6 = -1.2032 \times 10^{-17}$. The relative error is about 1% for $M_K f_K \geq 500\ M_\odot$ Hz and increases to 4% for smaller amounts. We can also reverse the above relation to obtain

$$y = h_0 + h_1 x + h_2 x^2 + h_3 x^3 + h_4 x^4 + h_5 x^5 + h_6 x^6, \qquad (7)$$

where $y = M_K f_K$ and $x = R_K f_K$. The fitting parameters are $h_0 = -28.1955 \times 10^2$, $h_1 = 1.3433$, $h_2 = -2.5528 \times 10^{-4}$, $h_3 = 2.5133 \times 10^{-8}$, $h_4 = -1.3087 \times 10^{-12}$, $h_5 = 3.5361 \times 10^{-17}$ and $h_6 = -3.8115 \times 10^{-22}$. This relation fits the numerical data to about 2% for $R_K f_K \geq 1000$ kmHz and the relative error increases to 13% for smaller $R_K f_K$.

IV. CONCLUSIONS

We studied the Keplerian (mass-shedding) sequence of uniformly rotating neutron stars by using a variety of EOSs. We searched for nearly EOS-independent relations that connect structure properties of the star to each other.

We showed that the relation (1) by L&P [10], namely the ratio between the rotation frequency of a neutron star at the Keplerian sequence, f_K, and the Keplerian frequency f_S of a particle in a circular orbit at the surface of the nonrotating neutron star with the same central density as the rotating one, is neither accurate nor EOS independent as originally thought at the time it was proposed (see Fig. 4). We thus found the new relation given by Eq. (2) of the ratio f_K/f_S as a function of the nonrotating neutron star compactness, M_S/R_S, which is EOS independent within only a 4% error. We use this new relation to put new constraints to the neutron star mass-radius relation using the fastest pulsar observed (see Fig. 5).

We proceeded to search for additional (nearly) EOS-independent relations and derive fitting polynomials for $M_K f_K$ in terms of $M_S f_S$ [see Eq. (3) and Fig. 6]; $R_K f_K$ in terms of $R_S f_S$ [see Eq. (4) and Fig. 7]; for M_K/R_K in terms of $M_S f_K/(R_S f_S)$ [see Eq. (5) and Fig. 8]; and for $R_K f_K$ in terms of $M_K f_K$ [see Eqs. (6) or (7) and Fig. 9]. These new fitting relations are nearly EOS independent within a maximum error of 8%.

The universality of the Keplerian sequence properties found in this article, in particular Eqs. (2), (5) and (6) or Eq. (7) which have been shown to be most accurate, add to the set of other universal relations of neutron stars known in the literature such as the I-Love-Q relation [12,13], the binding energy of nonrotating and rotating neutron stars [56] and the nearly EOS-independent behavior of the energy, angular momentum and radius of the last circular orbit of a test particle around rotating neutron stars [20,21]. This set of universal, analytic formulas, facilitates the inclusion of general relativistic effects in the description of relativistic astrophysical systems involving fast rotating neutron stars (see e.g., [57–59]) and can be also used to put constraints to the mass-radius relation of neutron stars and so to the EOS of nuclear matter (see Fig. 5).

ACKNOWLEDGMENTS

R. R. thanks ICRANet headquarters in Pescara for hospitality and the faculty members and researchers for valuable discussions. We thank the team members of LORENE for developing the public code.

[1] P. Haensel, A. Y. Potekhin, and D. G. Yakovlev, *Neutron Stars 1: Equation of State and Structure* (Springer Science & Business Media, New York, 2007), Vol. 326.
[2] A. W. Steiner, J. M. Lattimer, and E. F. Brown, Astrophys. J. **722**, 33 (2010).
[3] J. M. Lattimer, Astrophys. Space Sci. **336**, 67 (2011).
[4] J. L. Zdunik and P. Haensel, Astron. Astrophys. **551**, A61 (2013).
[5] J. M. Lattimer and M. Prakash, Phys. Rep. **621**, 127 (2016), memorial volume in honor of Gerald E. Brown.
[6] F. Özel, Nature (London) **441**, 1115 (2006).
[7] K. Yagi and N. Yunes, Phys. Rep. **681**, 1 (2017).
[8] W. G. Laarakkers and E. Poisson, Astrophys. J. **512**, 282 (1999).
[9] M. Urbanec, J. C. Miller, and Z. Stuchlk, Mon. Not. R. Astron. Soc. **433**, 1903 (2013).
[10] J. M. Lattimer and M. Prakash, Science **304**, 536 (2004).
[11] H. K. Lau, P. T. Leung, and L. M. Lin, Astrophys. J. **714**, 1234 (2010).
[12] K. Yagi and N. Yunes, Phys. Rev. D **88**, 023009 (2013).
[13] K. Yagi and N. Yunes, Science **341**, 365 (2013).
[14] D. D. Doneva, S. S. Yazadjiev, N. Stergioulas, and K. D. Kokkotas, Astrophys. J. **781**, L6 (2014).
[15] G. Pappas and T. A. Apostolatos, Phys. Rev. Lett. **112**, 121101 (2014).
[16] S. Chakrabarti, T. Delsate, N. Gürlebeck, and J. Steinhoff, Phys. Rev. Lett. **112**, 201102 (2014).
[17] M. Bejger, Astron. Astrophys. **552**, A59 (2013).
[18] J. M. Lattimer and M. Prakash, Astrophys. J. **550**, 426 (2001).
[19] M. Bejger and P. Haensel, Astron. Astrophys. **396**, 917 (2002).
[20] F. Cipolletta, C. Cherubini, S. Filippi, J. A. Rueda, and R. Ruffini, Phys. Rev. D **96**, 024046 (2017).
[21] S.-S. Luk and L.-M. Lin, Astrophys. J. **861**, 141 (2018).
[22] M. Dutra, O. Lourenco, J. S. Sá Martins, A. Delfino, J. R. Stone, and P. D. Stevenson, Phys. Rev. C **85**, 035201 (2012).
[23] M. Dutra, O. Lourenco, S. S. Avancini, B. V. Carlson, A. Delfino, D. P. Menezes, C. Providência, S. Typel, and J. R. Stone, Phys. Rev. C **90**, 055203 (2014).
[24] P. B. Demorest, T. Pennucci, S. M. Ransom, M. S. E. Roberts, and J. W. T. Hessels, Nature (London) **467**, 1081 (2010).
[25] J. Antoniadis, P. C. C. Freire, N. Wex, T. M. Tauris, R. S. Lynch, M. H. van Kerkwijk, M. Kramer, C. Bassa, V. S. Dhillon, T. Driebe *et al.*, Science **340**, 448 (2013).
[26] A. Akmal, V. R. Pandharipande, and D. G. Ravenhall, Phys. Rev. C **58**, 1804 (1998).
[27] I. Bombaci and D. Logoteta, Astron. Astrophys. **609**, A128 (2018).
[28] B. K. Agrawal, Phys. Rev. C **81**, 034323 (2010).
[29] V. Dexheimer, R. Negreiros, and S. Schramm, Phys. Rev. C **92**, 012801 (2015).
[30] T. Gaitanos, M. D. Toro, S. Typel, V. Baran, C. Fuchs, V. Greco, and H. Wolter, Nucl. Phys. **A732**, 24 (2004).
[31] F. Grill, H. Pais, C. Providência, I. Vidaña, and S. S. Avancini, Phys. Rev. C **90**, 045803 (2014).
[32] X. Roca-Maza, X. Viñas, M. Centelles, P. Ring, and P. Schuck, Phys. Rev. C **84**, 054309 (2011).
[33] R. Furnstahl, B. D. Serot, and H.-B. Tang, Nucl. Phys. **A615**, 441 (1997).
[34] N. K. Glendenning and S. A. Moszkowski, Phys. Rev. Lett. **67**, 2414 (1991).
[35] F. Douchin and P. Haensel, Astron. Astrophys. **380**, 151 (2001).
[36] M. Oertel, C. Providencia, F. Gulminelli, and A. R. Raduta, Phys. Part. Nucl. **46**, 830 (2015).
[37] S. Typel and H. Wolter, Nucl. Phys. **A656**, 331 (1999).
[38] F. Gulminelli and A. R. Raduta, Phys. Rev. C **92**, 055803 (2015).
[39] F. Douchin and P. Haensel, Phys. Lett. B **485**, 107 (2000).
[40] A. Sulaksono and T. Mart, Phys. Rev. C **74**, 045806 (2006).
[41] G. A. Lalazissis, J. König, and P. Ring, Phys. Rev. C **55**, 540 (1997).
[42] J. R. Wilson, Astrophys. J. **176**, 195 (1972).
[43] S. Bonazzola and J. Schneider, Astrophys. J. **191**, 273 (1974).
[44] J. L. Friedman, J. R. Ipser, and L. Parker, Phys. Rev. Lett. **62**, 3015 (1989).
[45] H. Komatsu, Y. Eriguchi, and I. Hachisu, Mon. Not. R. Astron. Soc. **237**, 355 (1989).
[46] G. Neugebauer and H. Herold, in *Relativistic Gravity Research*, *Lecture Notes in Physics* Vol. 410, edited by J. Ehlers and G. Schäfer (Springer-Verlag, Berlin, 1992), p. 305.
[47] N. Stergioulas and J. L. Friedman, Astrophys. J. **444**, 306 (1995).
[48] V. Paschalidis and N. Stergioulas, Living Rev. Relativity **20**, 7 (2017).
[49] https://lorene.obspm.fr.
[50] S. Bonazzola, E. Gourgoulhon, and J.-A. Marck, Phys. Rev. D **58**, 104020 (1998).
[51] S. Bonazzola, E. Gourgoulhon, M. Salgado, and J. A. Marck, Astron. Astrophys. **278**, 421 (1993).
[52] M. Ansorg, A. Kleinwchter, and R. Meinel, Astron. Astrophys. **405**, 711 (2003).
[53] N. Stergioulas, Living Rev. Relativity **6**, 3 (2003).
[54] J. W. T. Hessels, S. M. Ransom, I. H. Stairs, P. C. C. Freire, V. M. Kaspi, and F. Camilo, Science **311**, 1901 (2006).
[55] P. Kaaret, Z. Prieskorn, J. J. M. in t Zand, S. Brandt, N. Lund, S. Mereghetti, D. Gtz, E. Kuulkers, and J. A. Tomsick, Astrophys. J. Lett. **657**, L97 (2007).
[56] F. Cipolletta, C. Cherubini, S. Filippi, J. A. Rueda, and R. Ruffini, Phys. Rev. D **92**, 023007 (2015).
[57] L. Becerra, F. Cipolletta, C. L. Fryer, J. A. Rueda, and R. Ruffini, Astrophys. J. **812**, 100 (2015).
[58] L. Becerra, C. L. Bianco, C. L. Fryer, J. A. Rueda, and R. Ruffini, Astrophys. J. **833**, 107 (2016).
[59] L. Becerra, C. L. Ellinger, C. L. Fryer, J. A. Rueda, and R. Ruffini, arXiv:1803.04356.

The Astrophysical Journal, 874:39 (11pp), 2019 March 20 https://doi.org/10.3847/1538-4357/ab04f8

Two Predictions of Supernova: GRB 130427A/SN 2013cq and GRB 180728A/SN 2018fip

Y. Wang[1,2], J. A. Rueda[1,2,3], R. Ruffini[1,2,3,4], L. Becerra[5], C. Bianco[1,2], L. Becerra[5], L. Li[2], and M. Karlica[1,2,4]
[1] ICRA and Dipartimento di Fisica, Sapienza Università di Roma, P.le Aldo Moro 5, I-00185 Rome, Italy; ruffini@icra.it
[2] ICRANet, P.zza della Repubblica 10, I-65122 Pescara, Italy
[3] ICRANet-Rio, Centro Brasileiro de Pesquisas Físicas, Rua Dr. Xavier Sigaud 150, 22290–180 Rio de Janeiro, Brazil
[4] Université de Nice Sophia Antipolis, CEDEX 2, Grand Château Parc Valrose, Nice, France
[5] Escuela de Física, Universidad Industrial de Santander, A.A.678, Bucaramanga, 680002, Colombia
Received 2018 November 13; revised 2019 February 1; accepted 2019 February 5; published 2019 March 19

Abstract

On 2018 July 28, GRB 180728A triggered *Swift* satellites and, soon after the determination of the redshift, we identified this source as a type II binary-driven hypernova (BdHN II) in our model. Consequently, we predicted the appearance time of its associated supernova (SN), which was later confirmed as SN 2018fip. A BdHN II originates in a binary composed of a carbon–oxygen core (CO_{core}) undergoing SN, and the SN ejecta hypercritically accrete onto a companion neutron star (NS). From the time of the SN shock breakout to the time when the hypercritical accretion starts, we infer the binary separation $\simeq 3 \times 10^{10}$ cm. The accretion explains the prompt emission of isotropic energy $\simeq 3 \times 10^{51}$ erg, lasting ~ 10 s, and the accompanying observed blackbody emission from a thermal convective instability bubble. The new neutron star (νNS) originating from the SN powers the late afterglow from which a νNS initial spin of 2.5 ms is inferred. We compare GRB 180728A with GRB 130427A, a type I binary-driven hypernova (BdHN I) with isotropic energy $>10^{54}$ erg. For GRB 130427A we have inferred an initially closer binary separation of $\simeq 10^{10}$ cm, implying a higher accretion rate leading to the collapse of the NS companion with consequent black hole formation, and a faster, 1 ms spinning νNS. In both cases, the optical spectra of the SNe are similar, and not correlated to the energy of the gamma-ray burst. We present three-dimensional smoothed-particle-hydrodynamic simulations and visualizations of the BdHNe I and II.

Key words: binaries: general – black hole physics – gamma-ray burst: general – hydrodynamics – stars: neutron – supernovae: general

1. Introduction

By the first minutes of data retrieved from Konus-*Wind*, *Swift*, *Fermi*, *AGILE* or other gamma-ray telescopes (Aptekar et al. 1995; Barthelmy et al. 2005; Atwood et al. 2009; Tavani et al. 2009), and the determination of redshift by VLT/X-shooter, Gemini, NOT, or other optical telescopes (Vernin & Munoz-Tunon 1992; Hook et al. 2004; Vernet et al. 2011), it is possible to promptly and uniquely identify to which of the nine (9) subclasses of gamma-ray bursts (GRBs) a source belongs (see Table 1 and the references therein). Consequently, it is possible to predict its further evolution, including the possible appearance time of an associated supernova (SN) expected in some of the GRB subclasses. This is what we have done in the case of GRB 130427A (Ruffini et al. 2015, 2018d), and in the present case of GRB 180728A.

GRB 130427A is a BdHN I in our model; see details in Section 2 and in Fryer et al. (2014, 2015) and Becerra et al. (2015, 2016, 2018). The progenitor is a tight binary system, of orbital period ~ 5 minutes, composed of a carbon–oxygen core (CO_{core}), undergoing an SN event, and a neutron star (NS) companion accreting the SN ejecta and finally collapsing to a black hole (BH). The involvement of an SN in BdHN I and the low redshift of $z = 0.34$ (Flores et al. 2013; Levan et al. 2013; Xu et al. 2013b) enable us to predict that the optical signal of the SN will peak and be observed ~ 2 weeks after the GRB occurrence at the same position of the GRB (Ruffini et al. 2013). Indeed the SN was observed (de Ugarte Postigo et al. 2013; Xu et al. 2013a). Details of GRB 130427A are given in Section 3.

The current GRB 180728A is a BdHN II in our model; it has the same progenitor as BdHN I, a binary composed of a CO_{core} and an NS companion, but with longer orbital period ($\gtrsim 10$ minutes), which is here determined for the first time. The CO_{core} undergoes SN explosion, the SN ejecta hypercritically accrete onto the companion NS. In view of the longer separation, the accretion rate is lower, it is not sufficient for the companion NS to reach the critical mass of BH. Since an SN is also involved in BdHN II and this source is located at low redshift $z = 0.117$ (Rossi 2018), its successful prediction and observation were also possible and it is summarized in Section 4. From a time-resolved analysis of the data in Section 5, we trace the physical evolution of the binary system. For the first time we observed a 2 s signal evidencing the SN shockwave, namely the emergence of the SN shockwave from the outermost layers of the CO_{core} (see, e.g., Arnett 1996). The SN ejecta expand and, after 10 s, reach the companion NS inducing onto it a high accretion rate of about $10^{-3}\ M_\odot\ s^{-1}$. Such a process lasts about 10 s producing the prompt phenomena and an accompanying thermal component. The entire physical picture is described in Section 6, giving special attention to the new neutron star (νNS) originating from the SN. We explicitly show that the fast spinning νNS powers the afterglow emission by converting its rotational energy to synchrotron emission (see also Ruffini et al. 2018d), which has been never well considered in previous GRB models. We compare the initial properties of the νNS in GRB 130427A and in GRB 180728A, and derive that a 1 ms νNS is formed in GRB 130427A, while a 2.5 ms νNS is formed in GRB 180728A. In Section 7 we relate the very different energetic of the prompt emission to the orbital separation of the progenitors, which in turn determines the spin of the νNS, and the rest-frame luminosity afterglows. We simulate the accretion of

Table 1
Summary of the GRB Subclasses

Class	Type	Previous Alias	Number	In-state	Out-state	$E_{\rm p,i}$ (MeV)	$E_{\rm iso}$ (erg)	$E_{\rm iso,Gev}$ (erg)
Binary Driven	I	BdHN	329	CO_{core}–NS	νNS–BH	$\sim$0.2–2	$\sim 10^{52}$–10^{54}	$\gtrsim 10^{52}$
Hypernova	II	XRF	(30)	CO_{core}–NS	νNS–NS	$\sim$0.01–0.2	$\sim 10^{50}$–10^{52}	⋯
(BdHN)	III	HN	(19)	CO_{core}–NS	νNS–NS	$\sim$0.01	$\sim 10^{48}$–10^{50}	⋯
	IV	BH-SN	5	CO_{core}–BH	νNS–BH	$\gtrsim 2$	$> 10^{54}$	$\gtrsim 10^{53}$
	I	S-GRF	18	NS–NS	MNS	$\sim$0.2–2	$\sim 10^{49}$–10^{52}	⋯
Binary	II	S-GRB	6	NS–NS	BH	$\sim$2–8	$\sim 10^{52}$–10^{53}	$\gtrsim 10^{52}$
Merger	III	GRF	(1)	NS–WD	MNS	$\sim$0.2–2	$\sim 10^{49}$–10^{52}	⋯
(BM)	IV	FB-KN[a]	(1)	WD–WD	NS/MWD	<0.2	$<10^{51}$	⋯
	V	U-GRB	(0)	NS–BH	BH	$\gtrsim 2$	$>10^{52}$	⋯

Notes. This table is an updated version of the one presented in Ruffini et al. (2016, 2018e). We unify here all the GRB subclasses under two general names, BdHNe and BMs. Two new GRB subclasses are introduced; BdHN Type III and BM Type IV. In addition to the subclass name in the "Class" column and the "Type" column, as well as the previous names in the "Previous Alias" column, we report the number of GRBs with known redshift identified in each subclass updated by the end of 2016 in the "number" column (the value in brackets indicates the lower limit). We recall as well the "in-state" representing the progenitors and the "out-state" representing the outcomes, as well as the the peak energy of the prompt emission, $E_{\rm p,i}$, the isotropic gamma-ray energy, $E_{\rm iso}$ defined in the 1 keV–10 MeV energy range, and the isotropic emission of ultra-high-energy photons, $E_{\rm iso,Gev}$, defined in the 0.1–100 GeV energy range. We can see from this last column that this GeV emission, for the long GRBs is only for the BdHN Type I and Type IV, and in the case of short bursts is only for BM Type II and, in all of them, the GeV emission has energy more than 10^{52} erg.

[a] We here adopt a broad definition of kilonova as its name, a phenomenon that is 1000 times more luminous than a nova. A kilonova can be an infrared-optical counterpart of an NS–NS merger. In that case the transient is powered by the energy release from the decay of *r*-process heavy nuclei processed in the merger ejecta (e.g., Li & Paczyński 1998; Metzger et al. 2010; Berger et al. 2013; Tanvir et al. 2013). FB-KN stands for fallback-powered kilonova. We have shown that a WD–WD merger produces an infrared-optical transient from the merger ejecta, a kilonova, peaking at ∼5 days post-merger but powered in this case by accretion of fallback matter onto the merged remnant (Rueda et al. 2018a, 2018b).

the SN matter onto the NS companion in the tight binaries via three-dimensional (3D) smoothed-particle-hydrodynamic (SPH) simulations (Becerra et al. 2019) that also provide a visualization of the BdHNe. The conclusions are given in Section 8.

2. Binary-driven Hypernova

Since the *Beppo-SAX* discovery of the spatial and temporal coincidence of a GRB and an SN (Galama et al. 1999), largely supported by many additional following events (Woosley & Bloom 2006; Cano et al. 2017), a theoretical paradigm has been advanced for long GRBs based on a binary system (Rueda & Ruffini 2012). This differs from the traditional theoretical interpretation of GRB, which implicitly assumes that all GRBs originate from a BH with an ultrarelativistic jet emission (see, e.g., Piran 1999, 2004; Mészáros 2002, 2006; Berger 2014; Kumar & Zhang 2015).

Specifically, the binary system is composed of a CO_{core} and an NS companion in tight orbit. Following the onset of the SN, a hypercritical accretion process of the SN ejecta onto the NS occurs, which markedly depends on the binary period of the progenitor (Fryer et al. 2014, 2015; Becerra et al. 2015, 2016). For short binary periods of the order of 5 minutes the NS reaches the critical mass for gravitational collapse and forms a BH (see, e.g., Ruffini et al. 2014b, 2018b, 2018f). For longer binary periods, the hypercritical accretion onto the NS is not sufficient to bring it to the critical mass and a more massive NS (MNS) is formed. These sources have been called BdHNe because the feedback of the GRB transforms the SN into a hypernova (HN; Ruffini et al. 2018b). The former scenario of short orbital period is classified as BdHN type I (BdHN I), which leads to a binary system composed by the BH, generated by the collapse of the NS companion, and the νNS generated by the SN event. The latter scenario of longer orbital period is classified as BdNH type II (BdHN II), which leads to a binary NS system composed of the MNS and the νNS.

Having developed the theoretical treatment of such a hypercritical process, and considering as well other binary systems with progenitors composed alternatively of CO_{core} and BH, to NS and white dwarf (WD), a general classification of GRBs has been developed; see Ruffini et al. (2016) and Table 1 for details. We report in the table estimates of the energetic, spectrum, and different component of the prompt radiation, of the plateau, and all the intermediate phases, all the way to the final afterglow phase. The GRBs are divided into two main classes, the BdHNe, which cover the traditional long duration GRBs (Woosley 1993; Paczyński 1998), and the binary mergers, which are short-duration GRBs (Goodman 1986; Paczynski 1986; Eichler et al. 1989). There are currently nine subclasses in our model, the classification depends on the different compositions of the binary progenitors and outcomes, which are CO_{core} and compact objects as BH, NS, and WD. The same progenitors can possibly produce different outcomes, due to the different masses and binary separations.

3. GRB 130427A as BdHN I

GRB 130427A, as a BdHN I in our model, has been studied in our previous articles (Ruffini et al. 2015, 2018d). This long GRB is nearby ($z = 0.314$) and energetic ($E_{\rm iso} \sim 10^{54}$ erg; Flores et al. 2013; Levan et al. 2013; Xu et al. 2013b; Maselli et al. 2014). It has overall the most comprehensive data to date, including the well observed γ-ray prompt emission (Golenetskii 2013; von Kienlin 2013), the full coverage of X-ray, optical, and radio afterglow (Kouveliotou et al. 2013; Anderson et al. 2014; Levan et al. 2014; Perley et al. 2014; van der Horst et al. 2014; Vestrand et al. 2014; Becerra et al. 2017), and the long observation of the ultra-high-energy emission (UHE; Tam et al. 2013; Ackermann et al. 2014; Abeysekara et al. 2015). Also it has been theoretically well-studied, involving many interpretations, including a BH or a magnetar as the central engine (Bernardini et al. 2014); unaccountable temporal spectral

Table 2
Parameters of the Blackbody Evolution in Two Time Intervals

Time (s)	Total Flux (erg s^{-1} cm^{-2})	Thermal Flux (erg s^{-1} cm^{-2})	Percentage	Temperature (keV)
8.72–10.80	$5.6^{+1.1}_{-0.9} \times 10^{-6}$	$4.1^{+3.2}_{-1.9} \times 10^{-7}$	$7.3^{+5.8}_{-3.7}$%	$7.9^{+0.7}_{-0.7}$
10.80–12.30	$2.0^{+0.1}_{-0.1} \times 10^{-5}$	$7.1^{+6.0}_{-3.3} \times 10^{-7}$	$3.6^{+3.3}_{-1.6}$%	$5.6^{+0.5}_{-0.5}$

Note. Parameters include the total flux, the thermal flux, the percentage of thermal flux, and the temperature. One example of data fitting by Monte-Carlo iteration is shown in Appendix B. The time bin of 12.30–22.54 s does not show a convincing thermal component from the model comparison, still we report the fitting value, as a reference, from the cutoff power law plus blackbody model, that the temperature is found as $2.1^{+0.5}_{-0.9}$ keV, the thermal flux is $1.2^{+9.0}_{-1.1} \times 10^{-8}$ erg s^{-1} cm^{-2}, and the total flux is $3.1^{+0.22}_{-0.2} \times 10^{-6}$ erg s^{-1} cm^{-2}.

behaviors of the first 2.5 s pulse by the traditional models (Preece et al. 2014); the reverse-forward shock synchrotron model and its challenges in explaining the afterglow (Laskar et al. 2013; De Pasquale et al. 2016, 2017; Fraija et al. 2016); the synchrotron or the inverse Compton origins for the ultra-high-energy photons (Fan et al. 2013; Liu et al. 2013; Panaitescu et al. 2013; Tam 2014; Vurm et al. 2014); and the missing of the neutrino detection and its interpretation (Gao et al. 2013; Joshi et al. 2016). Our interpretation is alternative to the above traditional approach: (1) Long GRBS are traditionally described as single systems while we assume a very specific binary systems as their progenitors. (2) The roles of the SN and of the νNS are there neglected, while they are essential in our approach as evidenced also in this article. (3) A central role in the energetics is traditionally attributed to the kinetic energy of ultrarelativistic blast waves extending from the prompt phase all the way to the late phase of the afterglow, in contrast to model-independent constraints observed in the mildly relativistic plateau and afterglow phases (Ruffini et al. 2015, 2018c, 2018d). In our approach the physics of the e^+e^- plasma and its interaction with the SN ejecta as well as the pulsar-like behavior of the νNS are central to the description from the prompt radiation to the late afterglow phases (Ruffini et al. 2018f). One of the crucial aspects in our approach is the structure of the SN ejecta which, under the action of the hypercritical accretion process onto the NS companion and the binary interaction, becomes highly asymmetric. Such a new morphology of the SN ejecta has been made possible to visualized thanks to a set of three-dimensional numerical simulations of BdHNe (Fryer et al. 2014; Becerra et al. 2016, 2019).

On this ground, soon after the observational determination of the redshift (Levan et al. 2013), by examining the detailed observations in the early days, we identified the BdHN origin of this source. On 2013 May 2, we made the prediction of the occurrence of SN 2013cq on GCN (Ruffini et al. 2013, quoted in Appendix A), which was duly observed in the optical band on 2013 May 13 (de Ugarte Postigo et al. 2013; Xu et al. 2013a).

To summarize our work on this GRB: in Ruffini et al. (2015) we presented the multiwavelength light-curve evolution and interpreted them by a tight binary system with orbital separation $\sim 10^{10}$ cm. GRB 130427A has a very bright prompt γ-ray spike in the first 10 s, then it decays, coinciding with the rising of the UHE (100 MeV–100 GeV) emission. The UHE peaks at $\sim$20 s, then gradually dims for some thousand seconds. Soft X-ray observations start from 195 s, and a steep decay then follows a normal power-law decay $\sim t^{-1.3}$. We evidenced the presence of a blackbody component in the soft X-ray data in the time-interval from 196 to 461 s; within which the temperature decreases from 0.5 to 0.1 keV. The thermal component indicates an emitter expanding from $\sim 10^{12}$ to $\sim 10^{13}$ cm with velocity $\sim 0.8c$. This mildly relativistic expansion from our model-independent inference contrasts with the traditional ultrarelativistic external shockwave interpretation (see, e.g., Sari et al. 1998). We attributed this thermal emission to the transparency of the SN ejecta outermost layer after being heated and accelerated by the energetic e^+e^- plasma outflow of the GRB. The numerical simulations of this hydrodynamics process were presented in Ruffini et al. (2018f). As is shown there, the resulting distance, velocity, and occurring time of this emission are all in agreement with the observations. Later in Ruffini et al. (2018d), we showed that the mildly relativistic ejecta can also account for the nonthermal component, in the early thousands of seconds powered by its kinetic energy, and afterward powered by the release of rotational energy of the millisecond-period νNS via a pulsar-like mechanism. The synchrotron emission well reproduces the observed optical and X-ray afterglow. A similar application of the νNS on GRB 180728A will be presented in Section 6.2, as well as the comparison to GRB 130427A.

4. Observation and Prediction

On 2018 July 28, we had the opportunity to make a prediction of the SN appearance in a BdHN II.

At 17:29:00 UT, On 2018 July 28, GRB 180728A triggered the *Swift*-BAT. The BAT light curve shows a small precursor and $\sim$10 s later it was followed by a bright pulse of $\sim$20 s duration (Starling 2018). *Swift*-XRT did not slew to the position immediately due to the Earth limb; it began observing 1730.8 s after the BAT trigger (Perri 2018). The *Fermi*-GBM triggered and located GRB 180728A at 17:29:02.28 UT. The initial *Fermi*-LAT bore-sight angle at the GBM trigger time is 35°, within the threshold of detecting GeV photons, but no GeV photon was found. The GBM light curve is similar to that of *Swift*-BAT, consisting of a precursor and a bright pulse, the duration (T_{90}) is about 6.4 s (50–300 keV; Veres 2018). A red continuum was detected by VLT/X-shooter and the absorption features of Mg II (3124, 3132), Mg I (3187), and Ca II (4395, 4434) were consistent with a redshift of $z = 0.117$ (Rossi 2018).

After the detection of the redshift, On 2018 July 31, we classify this GRB as an BdHN II in our model, based on its duration, peak energy, isotropic energy, and the existence of photons with energy >100 MeV, criteria in Table 1. BdHN II involves the Type Ib/c SN phenomenon; therefore, we

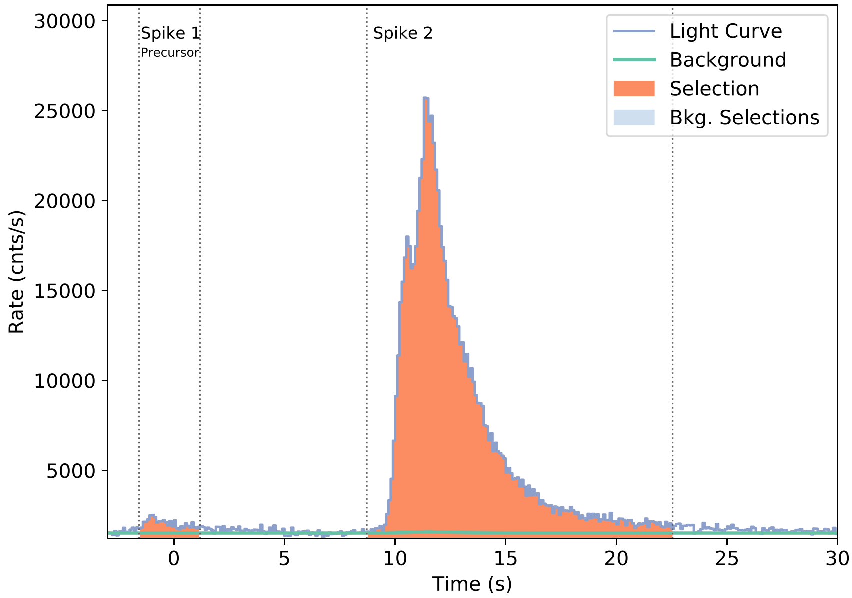

Figure 1. Count rate light curve of the prompt emission: data are retrieved from the NaI7 detector onboard *Fermi*-GBM. The prompt emission of GRB 180728A contains two spikes. The first spike, the precursor, ranges from −1.57 to 1.18 s. The second spike, which contains the majority of energy, rises at 8.72 s, peaks at 11.50 s, and fades at 22.54 s.

predicted that an SN would appear at 14.7 ± 2.9 days (Ruffini 2018) and be observed due to its low redshift. On 2018 August 18, Izzo (2018) on behalf of the VLT/X-shooter team reported the discovery of the SN appearance, which was confirmed in Selsing (2018). The texts of these GCNs are reported in the Appendix A. The SN associated with GRB 180728A was named SN 2018fip. Our prediction was confirmed.

We also predicted the SN appearance in GRB 140206A (Ruffini et al. 2014a) and GRB 180720A (Ruffini et al. 2018a), but unfortunately the optical observation does not cover the expected time (∼13 days after the GRB trigger time) of the SN appearance.

5. Data Analysis

GRB 180728A contains two spikes in the prompt emission observed by *Swift*-BAT, *Fermi*-GBM, and Konus-*Wind* (Rossi 2018; Starling 2018; Veres 2018). In the following we defined our t_0 based on the trigger time of *Fermi*-GBM. The first spike, we name it as precursor, ranges from −1.57 to 1.18 s. And the second spike, which contains the majority of energy, rises at 8.72 s, peaks at 11.50 s, and fades at 22.54 s, see Figure 1. These time definitions are based on the count rate light curve observed by *Fermi*-GBM, and determined by applying the Bayesian block method (Scargle 1998). *Swift*-XRT started to observe 1730.8 s after the BAT trigger, the luminosity of the X-ray afterglow follows a shallow decay with a power-law index −0.56 until ∼5000 s, then a normal decay with a power-law index −1.2, which is a typical value (Li et al. 2015, 2018a).

5.1. Prompt Emission: Two Spikes

The first spike, the precursor, shows a power-law spectrum with a power-law index -2.31 ± 0.08 in its 2.75 s duration, shown in Figure 2 and in the Appendix C. The averaged luminosity is $3.24^{+0.78}_{-0.55} \times 10^{49}$ erg s^{-1}, and the integrated energy gives $7.98^{+1.92}_{-1.34} \times 10^{49}$ erg in the energy range from 1 keV to 10 MeV, the Friedmann–Lemaitre–Robertson–Walker metric with the cosmological parameters from the *Planck* mission (Planck Collaboration et al. 2018)[6] are applied on computing the cosmological distance throughout the whole paper.

The second spike rises 10.29 s after the starting time of the first spike (8.72 s since the trigger time), lasts 13.82 s, and emits $2.73^{+0.11}_{-0.10} \times 10^{51}$ erg in the 1 keV–10 MeV energy band, i.e., 84 times more energetic than the first spike. The best fit of the spectrum is a Band function or a cutoff power law, with an additional blackbody; see Table 3 in Appendix C for the model comparison of the time-resolved analysis and Figure 2 for the spectrum. We notice that the thermal component confidently exists in the second spike when the emission is luminous while, at times later than 12.30 s, the confidence of the thermal component drops and a single cutoff power law is enough to fit the spectrum. There could be many reasons for the missing thermal component at later times; for instance, the thermal component becomes less prominent and is covered by the nonthermal emission, or the thermal temperature cools to a value outside of the satellite energy band, or the thermal emission really disappears. In the present case the thermal blackbody component of temperature ∼7 keV contributes ∼5% to the total energy.

From the evolution of the thermal spectrum and the parameters presented in Table 2, it is possible to determine the velocity and the radius of the system in a model-independent way. Following Ruffini et al. (2018f), we obtain that the radius in each of the two time intervals is $1.4^{+0.6}_{-0.4} \times 10^{10}$ cm and $4.3^{+0.9}_{-0.6} \times 10^{10}$ cm, respectively, and the expanding velocity is $0.53^{+0.18}_{-0.15}c$.

[6] Hubble constant $H_0 = (67.4 \pm 0.5)$ km s^{-1} Mpc^{-1}, matter density parameter $\Omega_M = 0.315 \pm 0.007$.

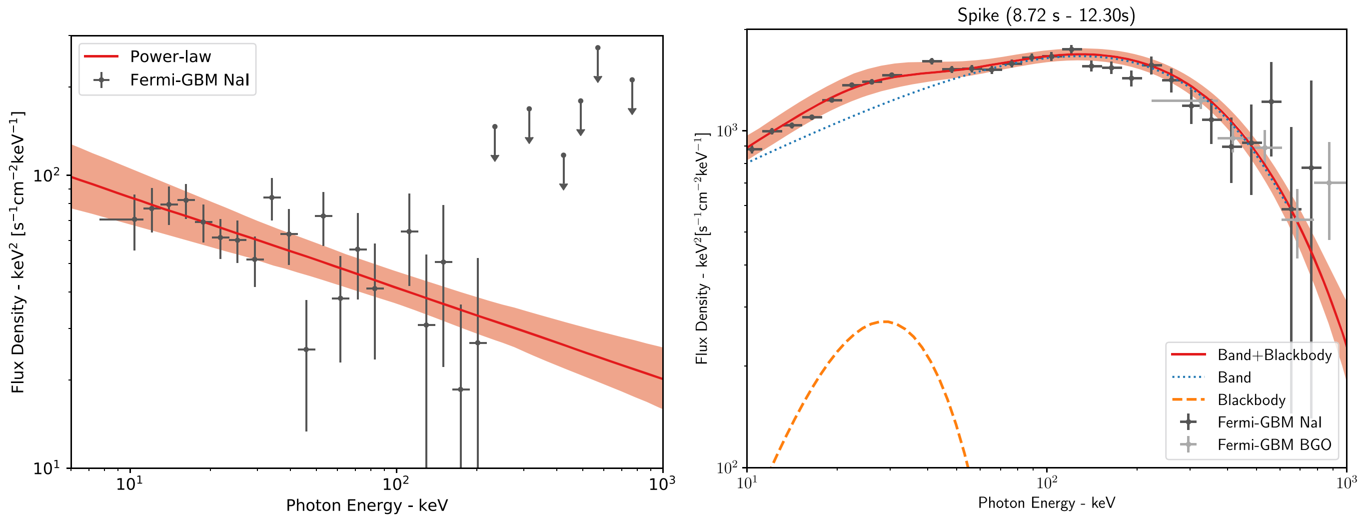

Figure 2. Left: spectrum of the precursor as observed by *Fermi*-GBM in the energy range of 8–900 keV. The red line indicates the power-law fitting with power-law index -2.31, the red shadow is the 1σ region. Right: spectrum of the main prompt emission, from 8.72 to 12.30 s. The dotted curve represents a band function with low-energy index $\alpha = -1.55$ and high-energy index $\beta = -3.48$; the peak energy is $E_p = 129$ keV. The additional blackbody component is represented by the orange dashed curve, with temperature $kT = 7.3$ keV. The composite fit with 1σ confidence area is represented by the red line and red shadow.

5.2. Supernova

The optical signal of SN 2018fip associated with GRB 180728A was confirmed by the observations of the VLT telescope (Izzo 2018; Selsing 2018). The SN 2018fip is identified as a Type Ic SN, its spectrum at ∼8 days after the peak of the optical light-curve matches with the Type Ic SN 2002ap (Mazzali et al. 2002), reported in Selsing et al. (2018). In Izzo (2018), there is the comparison of SN 2018fip with SN 1998bw and SN 2010bh, and in Xu et al. (2013a), there is the comparison of the SN associated with GRB 130427A, SN 2013cq, with SN 1998bw and SN 2010bh, associated with GRB 980425 (Galama et al. 1999) and GRB 100316D (Mazzali et al. 2003), respectively. We show in Figure 3 the spectral comparison of SN 1998bw, SN 2010bh, and SN 2013cq. We may conclude that the SNe are similar, regardless of the differences, e.g., in energetics ($\sim 10^{54}$ erg versus $\sim 10^{51}$ erg), of their associated GRBs (BdHN I versus BdHN II).

6. Physical Interpretation

All the observations in Section 5 can be well interpreted within the picture of a binary system initially composing a massive CO_{core} and an NS.

6.1. Prompt Emission from a Binary Accretion System

At a given time, the CO_{core} collapses forming a νNS at its center and producing an SN explosion. A strong shockwave is generated and emerges from the SN ejecta. A typical SN shockwave carries $\sim 10^{51}$ erg of kinetic energy (Arnett 1996), which is partially converted into electromagnetic emission by sweeping the circumburst medium (CBM) with an efficiency of ∼10% (see, e.g., Bykov et al. 2012). Therefore, the energy of $\sim 10^{50}$ erg is consistent with the total energy in the first spike. The electrons from the CBM are accelerated by the shockwave via the Fermi mechanism and emit synchrotron emission, which explains the nonthermal emission with a power-law index -2.31 in the first spike.

The second spike with a thermal component is a result of the SN ejecta accreting onto the companion NS. The distance of the binary separation can be estimated by the delay time between the two spikes, ∼10 s. Since the outer shell of the SN ejecta moves at velocity $\sim 0.1c$ (Cano et al. 2017), we estimate a binary separation $\approx 3 \times 10^{10}$ cm. Following Becerra et al. (2016), the total mass accreted by the companion NS gives $\sim 10^{-2}\,M_\odot$, which produces an emission of total energy $\sim 10^{51}$ erg, considering the accretion efficiency as ∼10% (Frank et al. 1992). The majority of the mass is accreted in ∼10 s, with an accretion rate $\sim 10^{-3}\,M_\odot\ \mathrm{s}^{-1}$; therefore, a spike with luminosity $\sim 10^{50}\ \mathrm{erg\ s}^{-1}$ and duration ∼10 s is produced; this estimation fits the second spike observed well.

The time-resolved analysis of the blackbody components in the second spike indicate a mildly relativistic expanding source emitting thermal radiation. This emission is explained by the adiabatic expanding thermal outflow from the accretion region (Fryer et al. 2006; Fryer 2009). The Rayleigh–Taylor convective instability acts during the initial accretion phase driving material away from the NS with a final velocity of the order of the speed of light. This material expands and cools, assuming the spherically symmetric expansion, to a temperature (Fryer et al. 1996; Becerra et al. 2016)

$$T = 6.84\left(\frac{S}{2.85}\right)^{-1}\left(\frac{r}{10^{10}\ \mathrm{cm}}\right)^{-1}\ \mathrm{keV}, \tag{1}$$

where S is the the entropy

$$S \approx 2.85\left(\frac{M_{\rm NS}}{1.4\,M_\odot}\right)^{7/8}\left(\frac{\dot{M}_B}{10^{-3}\,M_\odot\ \mathrm{s}^{-1}}\right)^{-1/4} \times \left(\frac{r}{10^{10}\ \mathrm{cm}}\right)^{-3/8}, \tag{2}$$

in units of k_B per nucleon. The system parameters in the above equations have been normalized to self-consistent values that fit the observational data, namely, the thermal emitter has a temperature ∼6 keV, radius $\sim 10^{10}$ cm, and expands with velocity $\sim 0.5c$.

To have more details of the time-resolved evolution: for the two time bins in Table 2, an expanding speed of $0.53c$ gives the

Table 3
Model Comparison of Time-resolved Analysis of *Fermi*-GBM Data

Segment	Time (s)	Model	Log(Likelihood)	AIC	BIC
Spike 1	−1.57–1.18	PL	430.03	864.17	869.59
Precursor		CPL	430.03	866.27	874.35
(NaI7)		Band	429.72	867.80	878.49
		PL+BB	429.77	867.90	878.59
		CPL+BB	429.77	870.08	883.36
		Band+BB	429.61	871.98	887.79
Spike 2	8.72–10.80	PL	947.20	1898.46	1905.33
(NaI7+BGO1)		CPL	838.91	1685.93	1696.22
		Band	831.02	1670.21	1683.90
		PL+BB	947.21	1902.59	1916.27
		CPL+BB	827.67	1665.60	1682.66
		Band+BB	823.90	1660.17	1680.59
	10.80–12.30	PL	1334.10	2672.25	2679.13
		CPL	809.83	1625.76	1636.05
		Band	821.25	1650.68	1664.37
		PL+BB	1334.10	2676.38	2690.06
		CPL+BB	794.79	1599.85	1616.91
		Band+BB	794.80	1599.86	1616.92
	12.30–22.54	PL	1366.08	2736.23	2742.79
		CPL	1216.52	2439.16	2448.97
		Band	1366.43	2741.06	2754.09
		PL+BB	1366.08	2740.37	2753.40
		CPL+BB	1215.52	2443.35	2459.58
		Band+BB	1366.63	2745.69	2765.11

Note. In the segment column, the name and the instruments are presented. The time column gives the time interval. In the model column, the model with an underline is the preferred one. We have used the following abbreviations: PL (Power-law), CPL (cutoff power-law), and BB (blackbody).

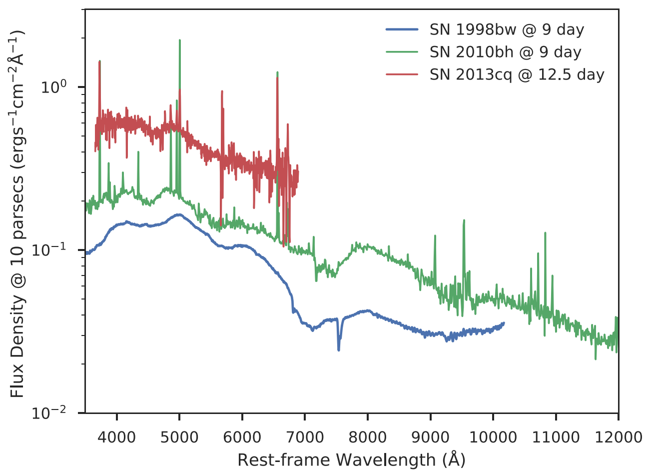

Figure 3. Spectra comparison of three SNe: 1998bw, 2010bh, 2013cq, flux density is normalized at 10 parsec, data are retrieved from the Wiserep website (https://wiserep.weizmann.ac.il).

radius 1.4×10^{10} cm and 4.3×10^{10} cm, respectively, as we fitted from the data. The luminosities are 2.11×10^{50} erg s^{-1} and 7.56×10^{50} erg s^{-1} respectively. If assuming the accretion efficiency is 10%, from the luminosity we obtain the accretion rate as 1.18×10^{-3} $M_\odot$ s^{-1} and 4.32×10^{-3} $M_\odot$ s^{-1}. By applying the above two equations, the theoretical temperature is obtained to be 5.83 ± 1.25 keV and 3.93 ± 0.39 keV, the thermal flux are $1.22 \pm 0.97 \times 10^{-7}$ erg s^{-1} cm^{-2} and $2.37 \pm 0.85 \times 10^{-7}$ erg s^{-1} cm^{-2} respectively. If we assume the accretion efficiency is 7%, following the same procedure, the theoretical temperature shall be 8.32 ± 1.78 keV and 5.61 ± 0.56 keV, the thermal flux shall be $5.78 \pm 3.89 \times 10^{-7}$ erg s^{-1} cm^{-2} and $7.17 \pm 2.51 \times 10^{-7}$ erg s^{-1} cm^{-2} respectively. The observed values in Table 2 are more consistent with the accretion efficiency of 7%.

The loss of rotational energy of the νNS, born after the SN explosion, powers the afterglow. This will be discussed in the next session.

6.2. Afterglow from the Newly Born Pulsar

We have applied the synchrotron model of mildly relativistic outflow powered by the rotational energy of the νNS to GRB 130427A (Ruffini et al. 2018d). From it we have inferred a 1 ms νNS pulsar emitting dipole and quadrupole radiation. Here we summarize this procedure and apply it to GRB 180827A.

The late X-ray afterglow of GRB 180728A also shows a power-law decay of index ~ -1.3 which, as we show below, if powered by the pulsar implies the presence of a quadrupole magnetic field in addition to the traditional dipole one. The "magnetar" scenario with only a strong dipole field ($B_{\rm dip} > 10^{14}$ G) is not capable of fitting the late time afterglow (Dai & Lu 1998; Zhang & Mészáros 2001; Metzger et al. 2011; Li et al. 2018b). The dipole and quadrupole magnetic fields are adopted from Pétri (2015), where the magnetic field is cast into an expansion of vector spherical harmonics, each harmonic mode is defined by a set of the multipole order number l and the azimuthal mode number m. The luminosity from a pure dipole ($l = 1$) is

$$L_{\rm dip} = \frac{2}{3c^3}\Omega^4 B_{\rm dip}^2 R_{\rm NS}^6 \sin^2\chi_1, \quad (3)$$

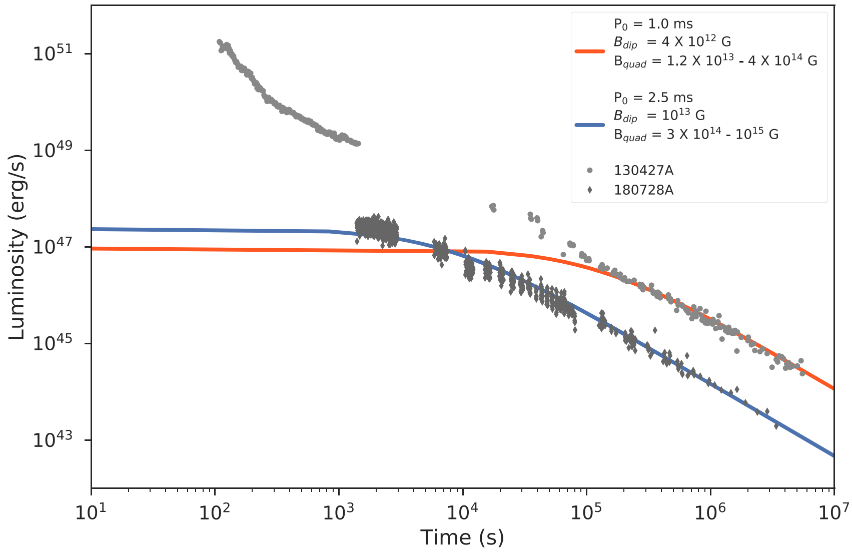

Figure 4. Afterglow powered by the νNS pulsar: the gray and dark points correspond to the bolometric afterglow light curves of GRB 1340427A and 180728A, respectively. The red and blue lines are the fitting of the energy injection from the rotational energy of the pulsar. The fitted parameters are shown in the legend, the quadruple fields are given in a range, and the upper value is 3.16 times the lower value, this is due to the oscillation angle χ_2, which is a free parameter.

and a pure quadrupole ($l = 2$) is

$$L_{\rm quad} = \frac{32}{135c^5}\Omega^6 B_{\rm quad}^2 R_{\rm NS}^8 \times \sin^2\chi_1(\cos^2\chi_2 + 10\sin^2\chi_2), \tag{4}$$

where χ_1 and χ_2 are the inclination angles of the magnetic moment, the different modes are easily separated by taking $\chi_1 = 0$ and any value of χ_2 for $m = 0$, $(\chi_1, \chi_2) = (90, 0)$ degrees for $m = 1$ and $(\chi_1, \chi_2) = (90, 90)$ degrees for $m = 2$.

The observed luminosity is assumed to be equal to the spindown luminosity as

$$\frac{dE}{dt} = -I\Omega\dot{\Omega} = -(L_{\rm dip} + L_{\rm quad}) = -\frac{2}{3c^3}\Omega^4 B_{\rm dip}^2 R_{\rm NS}^6 \sin^2\chi_1\left(1 + \eta^2\frac{16}{45}\frac{R_{\rm NS}^2\Omega^2}{c^2}\right),$$

and

$$\eta^2 = (\cos^2\chi_2 + 10\sin^2\chi_2)\frac{B_{\rm quad}^2}{B_{\rm dip}^2}, \tag{5}$$

where I is the moment of inertia. The parameter η relates to the ratio of quadrupole and dipole strength, $\eta = B_{\rm quad}/B_{\rm dip}$ for the $m = 1$ mode, and $\eta = 3.16 \times B_{\rm quad}/B_{\rm dip}$ for the $m = 2$ mode.

The bolometric luminosity is obtained by integrating the entire spectrum generated by the synchrotron model that fits the soft X-ray (0.3–10 keV) and the optical (see Ruffini et al. 2018d, and Figure 4 for an example). The bolometric luminosity has a factor $\sim$5 times more luminous than the soft X-ray emission. In Figure 4, we show the bolometric luminosity light curve, the shape of the light curve is taken from the soft X-ray data because it offers the most complete time coverage.

We assume that the bolometric luminosity required from the synchrotron model is equal to the energy loss of the pulsar. The numerical fitting result shows that the BdHN II of GRB 180728A forms a pulsar with initial spin $P_0 = 2.5$ ms, which is slower than the $P_0 = 1$ ms pulsar from the BdHN I of GRB 130427A. Both sources have similar dipole magnetic fields 10^{12}–10^{13} G and a quadrupole components $\sim$30–100 stronger ($\eta = 100$) than the dipole one. The strong quadrupole field dominates the emission in the early years, while the dipole radiation starts to be prominent later when the spin decays. This is because the quadrupole emission is more sensitive to the spin period, as $\propto\Omega^6$, while the dipole is $\propto\Omega^4$. Therefore, the νNS shows a dipole behavior when observed today, because the quadrupole dominates a very small fraction ($\lesssim 10^{-5}$) of the pulsar lifetime.

7. A Consistent Picture and Visualization

In the previous sections, we have inferred the binary separation from the prompt emission, and the spin of the νNS from the afterglow data. In the following, we confirm the consistency of these findings by numerical simulations of these systems, and compare the commonalities and diversities of GRB 130427A and GRB 180728A as examples of BdHN I and BdHN II systems in our model, respectively.

From an observational point of view, GRB 130427A and GRB 180728A are both long GRBs, but they are very different in the energetic: GRB 130427A is one of the most energetic GRBs with isotropic energy more than 10^{54} erg, while GRB 180728A is on the order of 10^{51} erg, a thousand times difference. GRB 130427A has observed the most significant ultra-high-energy photons (100 MeV–100 GeV, hereafter we call GeV photons), it has the longest duration (>1000 s) of GeV emission, and it has the highest energy of a photon ever observed from a GRB. In contrast, GRB 180728A has no GeV emission detected. As for the afterglow, the X-ray afterglow of GRB 130427A is more luminous than GRB 180728A, but they both share a power-law decaying index $\sim$−1.3 after 10^4 s. After more than 10 days, in both GRB sites emerges the coincident optical signal of a type Ic SN, and the SNe spectra are almost identical as shown in Section 5.2.

BdHN I and II have the same kind of binary progenitor, a binary composed of a $CO_{\rm core}$ and a companion NS, but the

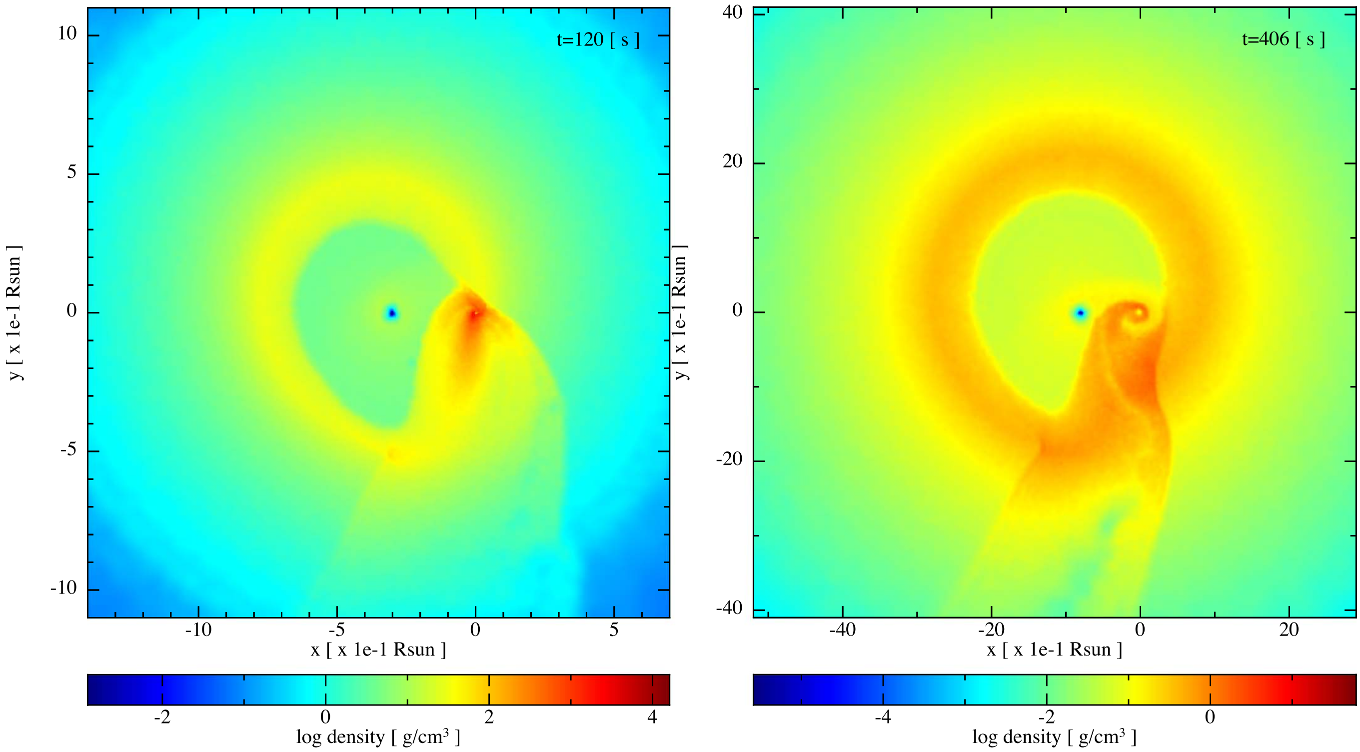

Figure 5. Two selected SPH simulations from Becerra et al. (2019) of the exploding CO_{core} as an SN in the presence of a companion NS: Model "25m1p08e" with $P_{orb} = 4.8$ minutes (left panel) and Model "25m3p1e" with $P_{orb} = 11.8$ minutes (right panel). The CO_{core} is taken from the 25 $M_\odot$ ZAMS progenitor, so it has a mass $M_{CO} = 6.85\,M_\odot$. The mass of the NS companion is $M_{NS} = 2\,M_\odot$. The plots show the density profile on the equatorial orbital plane; the coordinate system has been rotated and translated in such a way that the NS companion is at the origin and the νNS is along the $-x$ axis. The system in the left panel leads to a BdHN I and the snapshot is at the time of the gravitational collapse of the NS companion to a BH, $t = 120$ s from the SN shock breakout ($t = 0$ of our simulation). The system forms a new binary system composed of the νNS (at the center of the deep-blue region) and the BH formed by the collapsing NS companion (at the center of the red vortices). The system in the right panel leads to a BdHN II because the NS in this case does not reach the critical mass. This snapshot corresponds to $t = 406$ s post SN shock breakout. In this simulation, the new system composed of the νNS and the NS companion becomes unbound after the explosion.

binary separation/period is different, being larger/longer for BdHN II.

The angular momentum conservation during the gravitational collapse of the pre-SN core that forms the νNS, i.e., $J_{CO} = J_{\nu NS}$, implies that the latter should be fast rotating, i.e.,

$$\Omega_{\nu NS} = \left(\frac{R_{CO}}{R_{\nu NS}}\right)^2 \Omega_{Fe} = \left(\frac{R_{CO}}{R_{\nu NS}}\right)^2 \Omega_{orb}, \tag{6}$$

where $\Omega_{orb} = 2\pi/P_{orb} = \sqrt{GM_{tot}/a_{orb}^3}$ from the Kepler law, being $M_{tot} = M_{CO} + M_{NS}$ the total mass of the binary before the SN explosion, and $M_{CO} = M_{\nu NS} + M_{ej}$. We have assumed that the mass of the νNS is set by the mass of the iron core of the pre-SN CO_{core} and that it has a rotation period equal to the orbital period owing to tidal synchronization.

From the above we can see that the νNS rotation period, $P_{\nu NS}$, has a linear dependence on the orbital period, P_{orb}. Therefore, the solution we have obtained for the rotation period of the νNS born in GRB 130427A ($P_{\nu NS} \approx 1$ ms) and in the GRB 180728A ($P_{\nu NS} \approx 2.5$ ms), see Figure 4, implies that the orbital period of the BdHN I would be a factor of $\approx$2.5 shorter than that of the BdHN II. Based on this information, we seek two systems in our simulations presented in Becerra et al. (2019) with the following properties: the same (or nearly) SN explosion energy, pre-SN CO_{core}, and initial NS companion mass, but different orbital periods, i.e., $P_{II}/P_{I} \approx 2.5$. The more compact binary leads to the BdHN I and the less compact one to the BdHN II and, by angular momentum conservation, they lead to the abovementioned νNSs.

We examine the results of the simulations for the pre-SN core of a 25 $M_\odot$ zero-age main-sequence progenitor and the initial mass of the NS companion $M_{NS} = 2\,M_\odot$. A close look at Tables 2 and 7 in Becerra et al. (2019) shows that, indeed, Model "25m1p08e" with $P_{orb} = 4.81$ minutes ($a_{orb} \approx 1.35 \times 10^{10}$ cm) and Model "25m3p1e" with $P_{orb} = 11.8$ minutes ($a_{orb} \approx 2.61 \times 10^{10}$ cm) give a consistent solution. In Model "25m1p08e," the NS companion reaches the critical mass (secular axisymmetric instability) and collapses to a BH; this model produces a BdHN I. In the Model "25m3p1e" the NS companion does not reach the critical mass; this system produces a BdHN II. The system leading to BdHN I remains bound after the explosion while, the one leading to the BdHN II, is disrupted. Concerning the νNS rotation period, adopting $R_{CO} \sim 2.141 \times 10^8$ cm (see Table 1 in Becerra et al. 2019), $P_{orb} \sim 4.81$ minutes, and $P_{orb} \sim 11.8$ minutes leads to $P_{\nu NS} \sim 1$ ms and 2.45 ms, respectively. We show in Figure 5 snapshots of the two simulations.

8. Conclusion

The classification of GRBs in nine different subclasses allows us to identify the origin of a new GRB with known redshift from the observation of its evolution in the first hundred seconds. Then, we are able to predict the presence of an associated SN in the BdHN and its occurring time. We reviewed our previous successful prediction of a BdHN I in our model: GRB 130427A/SN 2013cq, and in this article, we presented our recent successful prediction of a BdHN II in our model: GRB 180728A/SN 2018fip.

The detailed observational data of GRB 180728A, for the first time, allowed us to follow the evolution of a BdHN II. The collapse of CO_{core} leads to an SN. We determine that the corresponding shockwave with energy $\sim 10^{51}$ erg emerges and produces the first 2 s spike in the prompt emission. The SN ejecta expands and reaches $\sim 3 \times 10^{10}$ cm away from the NS companion. The accretion process starts with a rate $\sim 10^{-3}\, M_\odot$ s^{-1}, the second powerful spike lasting 10 s with luminosity $\sim 10^{50}$ erg s^{-1}, and a thermal component at temperature ~ 7 keV.

A νNS is formed from the SN. The role of νNS powering the afterglow has been evidenced in our study of GRB 130427A (Ruffini et al. 2018d). This article emphasizes its application on GRB 180728A. The νNS pulsar loses its rotational energy by dipole and quadrupole emission. In order to fit the observed afterglow data using a synchrotron model (Ruffini et al. 2018d), we require an initial 1 ms spin pulsar for GRB 130427A, and a slower spin of 2.5 ms for GRB 180728A. For close binary systems, the binary components are synchronized with the orbital period, from which we are able to obtain the orbital separation by inferring the CO_{core} period from the νNS one via angular momentum conservation. This second independent method leads to a value of the binary separation in remarkable agreement with the one inferred from the prompt emission, which shows the self-consistency of this picture. The SNe spectra observed in BdNH I and in BdHN II are similar, although the associated two GRBs markedly differ in energy. The SN acts as a catalyst; it triggers the GRB process. After losing a part of the ejecta mass by hypercritical accretion, the remaining SN ejecta are heated by the GRB emission, but the nuclear composition, which relates to the observed optical emission owing to the nuclear decay of nickel and cobalt (Arnett 1996), is not influenced by such a GRB-SN interaction.

Besides providing the theoretical support of the BdHN I and II realization, we have presented 3D SPH simulations that help in visualizing the systems (see Figure 5).

In short, we made a successful prediction of SN 2018fip associated with GRB 180728A based on our GRB classification that GRB 180728A belongs to BdHN II. The observations of the prompt emission and the afterglow portray, for the first time, a complete transitional stage of two binary stars. We emphasize the νNS from SN playing a dominant role in the later afterglow, the comparison to GRB 130427A, a typical BdHN I in our model, is demonstrated and visualized.

The confirmation of the SN appearance, as well as the majority of this work were performed during R.R. and Y.W.'s visit to the *Yau Mathematical Sciences Center* in Tsinghua University, Beijing. We greatly appreciate the kind hospitality of and the helpful discussion with Prof. Shing-Tung Yau. We also acknowledge Dr. Luca Izzo for discussions on the SNe treated in this work. We thank the referee for constructive comments that helped clarify many concepts and strengthen the time-resolved analysis.

Appendix A
GCNs

GCN 14526–GRB 130427A: Prediction of SN appearance

The late X-ray observations of GRB 130427A by *Swift*-XRT clearly evidence a pattern typical of a family of GRBs associated with the SN following the Induce Gravitational Collapse (IGC) paradigm (Rueda & Ruffini 2012; Pisani et al. 2013). We assume that the luminosity of the possible SN associated with GRB 130427A would be that of 1998bw, as found in the IGC sample described in Pisani et al. (2013). Assuming the intergalactic absorption in the *I*-band (which corresponds to the *R*-band rest-frame) and the intrinsic one, assuming a Milky Way type for the host galaxy, we obtain a magnitude expected for the peak of the SN of $I = 22$–23 occurring 13–15 days after the GRB trigger, namely between 2013 May 10th and 12th. Further optical and radio observations are encouraged.

GCN 23066–GRB 180728A: A long GRB of the X-ray flash (XRF) subclass, expecting SN appearance

GRB 180728A has $T_{90} = 6.4$ s (Rossi 2018), peak energy 142 $(-15, +20)$ keV, and isotropic energy $E_{iso} = (2.33 \pm 0.10) \times 10^{51}$ erg (Frederiks 2018). It presents the typical characteristic of a subclass of long GRBs called XRFs[7] (see Ruffini et al. 2016), originating from a tight binary of a CO_{core} undergoing an SN explosion in the presence of a companion NS that hypercritically accretes part of the SN matter. The outcome is a new binary composed by a more MNS and a newly born NS (νNS). Using the averaged observed value of the optical peak time of SN (Cano et al. 2017), and considering the redshift $z = 0.117$ (Rossi 2018), a bright optical signal will peak at 14.7 ± 2.9 days after the trigger (2018 August 12, uncertainty from August 9th to 15th) at the location of R. A. = 253.56472 and decl. = −54.04451, with an uncertainty 0.43 arcsec (LaPorte 2018). The follow-up observations, especially the optical bands for the SN, as well as attention to binary NS pulsar behaviors in the X-ray afterglow emission, are recommended.

GCN 23142–GRB 180728A: discovery of the associated SN

Up to now, we have observed at three epochs, specifically at 6.27, 9.32 and 12.28 days after the GRB trigger. The optical counterpart is visible in all epochs using the X-shooter acquisition camera in the *g*, *r*, and *z* filters. We report a rebrightening of 0.5 ± 0.1 mag in the *r* band between 6.27 and 12.28 days. This is consistent with what is observed in many other lo 170827w-redshift GRBs, which in those cases is indicative of an emerging type Ic SN.

Appendix B
Data Fitting

Data are fitted by applying the Monte Carlo Bayesian iterations using a Python package: The Multi-Mission Maximum Likelihood framework (3ML).[8] An example is shown in Figure 6.

Appendix C
Model Comparison

Spectra are fitted by Bayesian iterations. The AIC is preferred for comparing nonnested models, and BIC is preferred for nested models (Kass & Raftery 1995). Log (likelihood) is adopted by the method of the maximum likelihood ratio test, which is treated as a reference of the

[7] The previous name of BdHN I.

[8] https://github.com/giacomov/3ML

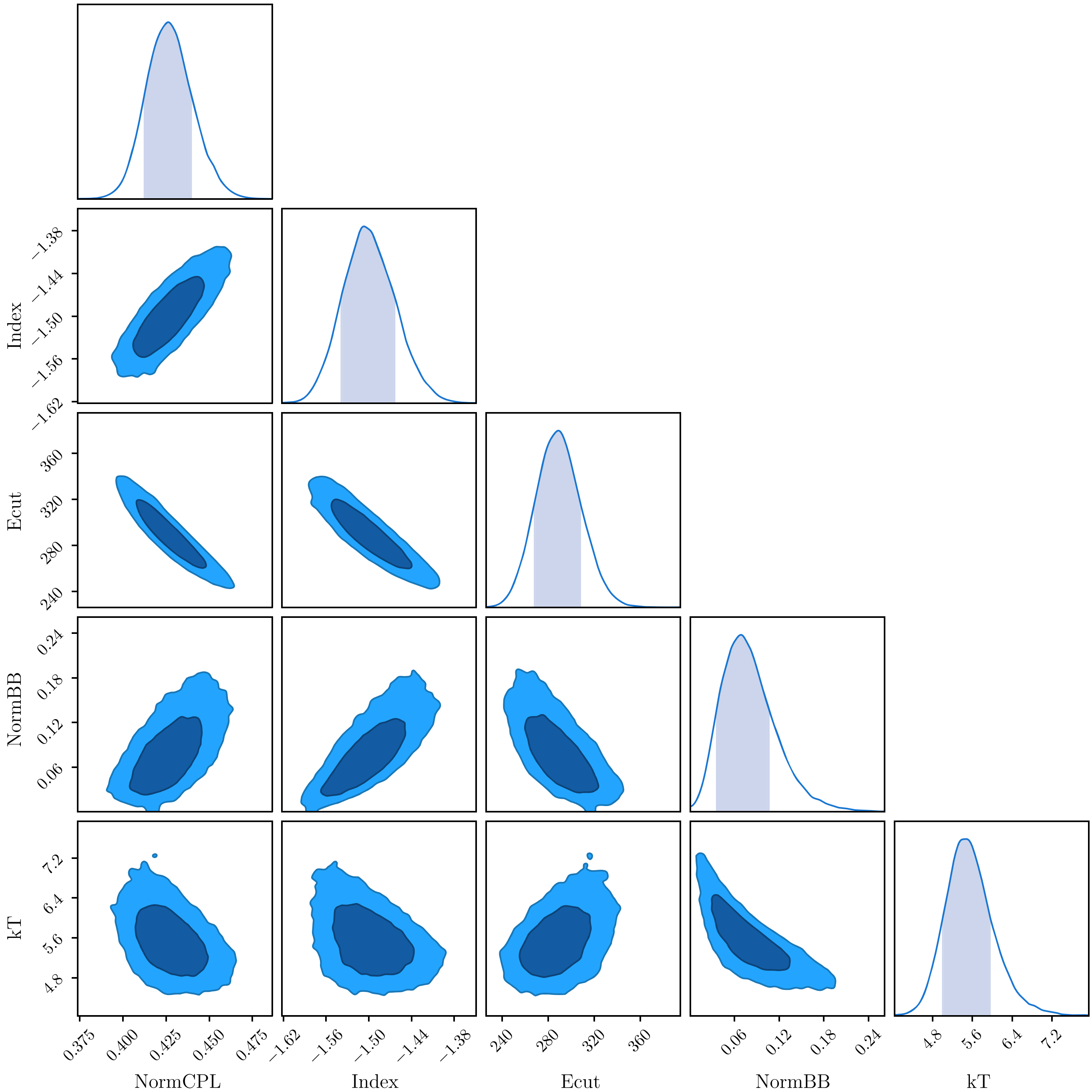

Figure 6. Example of fitting the *Fermi*-GBM data from 10.80 to 12.30 s. We apply 20 chains, each chain iterates 10^4 times and burns the first 10^3 times. The parameters are normalization (NormCPL), cutoff energy (ECut), and power-law index (Index) of the cutoff power-law model, as well as normalization (NormBB) and temperature (kT) of the blackbody model.

model comparison (Vuong 1989). Parameters are shown in Table 3.

ORCID iDs

Y. Wang https://orcid.org/0000-0001-7959-3387
C. Bianco https://orcid.org/0000-0001-7749-4078

References

Abeysekara, A. U., Alfaro, R., Alvarez, C., et al. 2015, ApJ, 800, 78
Ackermann, M., Ajello, M., Asano, K., et al. 2014, Sci, 343, 42
Anderson, G. E., van der Horst, A. J., Staley, T. D., et al. 2014, MNRAS, 440, 2059
Aptekar, R. L., Frederiks, D. D., Golenetskii, S. V., et al. 1995, SSRv, 71, 265
Arnett, D. 1996, Supernovae and Nucleosynthesis: An Investigation of the History of Matter from the Big Bang to the Present (Cambridge: Cambridge Univ. Press)
Atwood, W. B., Abdo, A. A., Ackermann, M., et al. 2009, ApJ, 697, 1071
Barthelmy, S. D., Barbier, L. M., Cummings, J. R., et al. 2005, SSRv, 120, 143
Becerra, L., Bianco, C. L., Fryer, C. L., Rueda, J. A., & Ruffini, R. 2016, ApJ, 833, 107
Becerra, L., Cipolletta, F., Fryer, C. L., Rueda, J. A., & Ruffini, R. 2015, ApJ, 812, 100
Becerra, L., Ellinger, C. L., Fryer, C. L., Rueda, J. A., & Ruffini, R. 2019, ApJ, 871, 14

Becerra, L., Guzzo, M. M., Rossi-Torres, F., et al. 2018, ApJ, 852, 120
Becerra, R. L., Watson, A. M., Lee, W. H., et al. 2017, ApJ, 837, 116
Berger, E. 2014, ARA&A, 52, 43
Berger, E., Fong, W., & Chornock, R. 2013, ApJL, 774, L23
Bernardini, M. G., Campana, S., Ghisellini, G., et al. 2014, MNRAS, 439, L80
Bykov, A., Gehrels, N., Krawczynski, H., et al. 2012, SSRv, 173, 309
Cano, Z., Wang, S.-Q., Dai, Z.-G., & Wu, X.-F. 2017, AdAst, 2017, 8929054
Dai, Z. G., & Lu, T. 1998, A&A, 333, L87
De Pasquale, M., Page, M., Kann, D., et al. 2017, Galax, 5, 6
De Pasquale, M., Page, M. J., Kann, D. A., et al. 2016, MNRAS, 462, 1111
de Ugarte Postigo, A., Xu, D., Leloudas, G., et al. 2013, GCN, 14646, 1
Eichler, D., Livio, M., Piran, T., & Schramm, D. N. 1989, Natur, 340, 126
Fan, Y.-Z., Tam, P. H. T., Zhang, F.-W., et al. 2013, ApJ, 776, 95
Flores, H., Covino, S., Xu, D., et al. 2013, GCN, 14491, 1
Fraija, N., Lee, W., & Veres, P. 2016, ApJ, 818, 190
Frank, J., King, A., & Raine, D. 1992, Accretion Power in Astrophysics (Cambridge: Cambridge Univ. Press)
Frederiks, D. 2018, GCN, 23061, 1
Fryer, C. L. 2009, ApJ, 699, 409
Fryer, C. L., Benz, W., & Herant, M. 1996, ApJ, 460, 801
Fryer, C. L., Herwig, F., Hungerford, A., & Timmes, F. X. 2006, ApJL, 646, L131
Fryer, C. L., Oliveira, F. G., Rueda, J. A., & Ruffini, R. 2015, PhRvL, 115, 231102
Fryer, C. L., Rueda, J. A., & Ruffini, R. 2014, ApJL, 793, L36
Galama, T. J., Vreeswijk, P. M., van Paradijs, J., et al. 1999, A&AS, 138, 465
Gao, S., Kashiyama, K., & Mészáros, P. 2013, ApJL, 772, L4
Golenetskii, S. 2013, GCN, 14487, 1
Goodman, J. 1986, ApJL, 308, L47
Hook, I. M., Jørgensen, I., Allington-Smith, J. R., et al. 2004, PASP, 116, 425
Izzo, L. 2018, GCN, 23142, 1
Joshi, J. C., Razzaque, S., & Moharana, R. 2016, MNRAS, 458, L79
Kass, R. E., & Raftery, A. E. 1995, J. Am. Stat. Assoc., 90, 773
Kouveliotou, C., Granot, J., Racusin, J. L., et al. 2013, ApJL, 779, L1
Kumar, P., & Zhang, B. 2015, PhR, 561, 1
LaPorte, S. J. 2018, GCN, 23064, 1
Laskar, T., Berger, E., Zauderer, B. A., et al. 2013, ApJ, 776, 119
Levan, A. J., Cenko, S. B., Perley, D. A., & Tanvir, N. R. 2013, GCN, 14455, 1
Levan, A. J., Tanvir, N. R., Fruchter, A. S., et al. 2014, ApJ, 792, 115
Li, L., Wang, Y., Shao, L., et al. 2018a, ApJS, 234, 26
Li, L., Wu, X.-F., Huang, Y.-F., et al. 2015, ApJ, 805, 13
Li, L., Wu, X.-F., Lei, W.-H., et al. 2018b, ApJS, 236, 26
Li, L.-X., & Paczyński, B. 1998, ApJL, 507, L59
Liu, R.-Y., Wang, X.-Y., & Wu, X.-F. 2013, ApJL, 773, L20
Maselli, A., Melandri, A., Nava, L., et al. 2014, Sci, 343, 48
Mazzali, P. A., Deng, J., Maeda, K., et al. 2002, ApJL, 572, L61
Mazzali, P. A., Deng, J., Tominaga, N., et al. 2003, ApJL, 599, L95
Mészáros, P. 2002, ARA&A, 40, 137
Mészáros, P. 2006, RPPh, 69, 2259
Metzger, B. D., Giannios, D., Thompson, T. A., Bucciantini, N., & Quataert, E. 2011, MNRAS, 413, 2031
Metzger, B. D., Martínez-Pinedo, G., Darbha, S., et al. 2010, MNRAS, 406, 2650
Paczynski, B. 1986, ApJL, 308, L43
Paczyński, B. 1998, ApJL, 494, L45
Panaitescu, A., Vestrand, W. T., & Woźniak, P. 2013, MNRAS, 436, 3106
Perley, D. A., Cenko, S. B., Corsi, A., et al. 2014, ApJ, 781, 37
Perri, M. 2018, GCN, 23049, 1
Pétri, J. 2015, MNRAS, 450, 714
Piran, T. 1999, PhR, 314, 575
Piran, T. 2004, RvMP, 76, 1143
Pisani, G. B., Izzo, L., Ruffini, R., et al. 2013, A&A, 552, L5
Planck Collaboration, Aghanim, N., Akrami, Y., et al. 2018, arXiv:1807.06209
Preece, R., Burgess, J. M., von Kienlin, A., et al. 2014, Sci, 343, 51
Rossi, R. 2018, GCN, 23055, 1
Rueda, J. A., & Ruffini, R. 2012, ApJL, 758, L7
Rueda, J. A., Ruffini, R., Wang, Y., et al. 2018a, JCAP, 10, 006
Rueda, J. A., Ruffini, R., Wang, Y., et al. 2018b, arXiv:1807.07905
Ruffini, R. 2018, GCN, 23066, 1
Ruffini, R., Aimuratov, Y., Bianco, C. L., et al. 2018a, GCN, 23019, 1
Ruffini, R., Becerra, L., Bianco, C. L., et al. 2018b, ApJ, 869, 151
Ruffini, R., Becerra, L., Bianco, C. L., et al. 2018c, ApJ, 869, 151
Ruffini, R., Bianco, C. L., Enderli, M., et al. 2013, GCN, 14526, 1
Ruffini, R., Bianco, C. L., Enderli, M., et al. 2014a, GCN, 15794, 1
Ruffini, R., Karlica, M., Sahakyan, N., et al. 2018d, ApJ, 869, 101
Ruffini, R., Muccino, M., Bianco, C. L., et al. 2014b, A&A, 565, L10
Ruffini, R., Rodriguez, J., Muccino, M., et al. 2018e, ApJ, 859, 30
Ruffini, R., Rueda, J. A., Muccino, M., et al. 2016, ApJ, 832, 136
Ruffini, R., Wang, Y., Aimuratov, Y., et al. 2018f, ApJ, 852, 53
Ruffini, R., Wang, Y., Enderli, M., et al. 2015, ApJ, 798, 10
Sari, R., Piran, T., & Narayan, R. 1998, ApJL, 497, L17
Scargle, J. D. 1998, ApJ, 504, 405
Selsing, J. 2018, GCN, 23181, 1
Selsing, J., Izzo, L., Rossi, A., & Malesani, D. B. 2018, Transient Name Server Classification Report, 1249, 2609
Starling, R. L. C. 2018, GCN, 23046, 1
Tam, P.-H. T. 2014, IJMPS, 28, 1460174
Tam, P.-H. T., Tang, Q.-W., Hou, S.-J., Liu, R.-Y., & Wang, X.-Y. 2013, ApJL, 771, L13
Tanvir, N. R., Levan, A. J., Fruchter, A. S., et al. 2013, Natur, 500, 547
Tavani, M., Barbiellini, G., Argan, A., et al. 2009, A&A, 502, 995
van der Horst, A. J., Paragi, Z., de Bruyn, A. G., et al. 2014, MNRAS, 444, 3151
Veres, P. 2018, GCN, 23053, 1
Vernet, J., Dekker, H., D'Odorico, S., et al. 2011, A&A, 536, A105
Vernin, J., & Munoz-Tunon, C. 1992, A&A, 257, 811
Vestrand, W. T., Wren, J. A., Panaitescu, A., et al. 2014, Sci, 343, 38
von Kienlin, A. 2013, GCN, 14473, 1
Vuong, Q. H. 1989, Econometrica, 57, 307
Vurm, I., Hascoët, R., & Beloborodov, A. M. 2014, ApJL, 789, L37
Woosley, S. E. 1993, ApJ, 405, 273
Woosley, S. E., & Bloom, J. S. 2006, ARA&A, 44, 507
Xu, D., de Ugarte Postigo, A., Leloudas, G., et al. 2013a, ApJ, 776, 98
Xu, D., de Ugarte Postigo, A., Schulze, S., et al. 2013b, GCN, 14478, 1
Zhang, B., & Mészáros, P. 2001, ApJL, 552, L35

Journal of Cosmology and
Astroparticle Physics

Electromagnetic emission of white dwarf binary mergers

To cite this article: J.A. Rueda *et al* JCAP03(2019)044

Journal of Cosmology and Astroparticle Physics
An IOP and SISSA journal

Electromagnetic emission of white dwarf binary mergers

J.A. Rueda,[a,b,c] **R. Ruffini,**[a,b,c,d] **Y. Wang,**[a,b] **C.L. Bianco,**[a,b] **J.M. Blanco-Iglesias,**[e,f] **M. Karlica,**[a,b,d] **P. Lorén-Aguilar,**[e,f] **R. Moradi**[a,b] **and N. Sahakyan**[g]

[a]ICRA, Dipartimento di Fisica, Sapienza Università di Roma, P.le Aldo Moro 5, I–00185 Rome, Italy
[b]ICRANet, P.zza della Repubblica 10, I–65122 Pescara, Italy
[c]ICRANet-Rio, Centro Brasileiro de Pesquisas Físicas, Rua Dr. Xavier Sigaud 150, 22290–180 Rio de Janeiro, Brazil
[d]Université de Nice Sophia Antipolis, CEDEX 2, Grand Château Parc Valrose, Nice, France
[e]Departament de Física, Universitat Politècnica de Catalunya, c/Esteve Terrades, 5, 08860 Castelldefels, Spain
[f]School of Physics, University of Exeter, Stocker Road, Exeter EX4 4QL, U.K.
[g]ICRANet-Armenia, Marshall Baghramian Avenue 24a, 0019 Yerevan, Armenia

E-mail: jorge.rueda@icra.it, ruffini@icra.it, yu.wang@icranet.org, bianco@icra.it, josemiguelblancoiglesias@gmail.com, mikarlic@gmail.com, p.loren-aguilar@exeter.ac.uk, rahim.moradi@icranet.org, narek@icra.it

Received September 25, 2018
Revised February 25, 2019
Accepted March 19, 2019
Published March 29, 2019

https://doi.org/10.1088/1475-7516/2019/03/044

Abstract. It has been recently proposed that the ejected matter from white dwarf (WD) binary mergers can produce transient, optical and infrared emission similar to the "kilonovae" of neutron star (NS) binary mergers. To confirm this we calculate the electromagnetic emission from WD-WD mergers and compare with kilonova observations. We simulate WD-WD mergers leading to a massive, fast rotating, highly magnetized WD with an adapted version of the smoothed-particle-hydrodynamics (SPH) code Phantom. We thus obtain initial conditions for the ejecta such as escape velocity, mass and initial position and distribution. The subsequent thermal and dynamical evolution of the ejecta is obtained by integrating the energy-conservation equation accounting for expansion cooling and a heating source given by the fallback accretion onto the newly-formed WD and its magneto-dipole radiation. We show that magnetospheric processes in the merger can lead to a prompt, short gamma-ray emission of up to $\approx 10^{46}$ erg in a timescale of 0.1–1 s. The bulk of the ejecta initially expands non-relativistically with velocity $0.01\,c$ and then it accelerates to $0.1\,c$ due to the injection of fallback accretion energy. The ejecta become transparent at optical wavelengths around ~ 7 days post-merger with a luminosity 10^{41}–$10^{42}\,\mathrm{erg\,s^{-1}}$. The X-ray emission from the fallback accretion becomes visible around ~ 150–200 day post-merger with a luminosity of $10^{39}\,\mathrm{erg\,s^{-1}}$. We also predict the post-merger time at which the central WD should appear as a pulsar depending on the value of the magnetic field and rotation period.

Keywords: gamma ray bursts theory, white and brown dwarfs, accretion

ArXiv ePrint: 1807.07905

Contents

1 Introduction

It was recently shown in Rueda et al. [29] that WD-WD mergers can produce optical and infrared emission that resemble the one emitted from the "kilonovae" produced by NS-NS mergers. This novel, previously not addressed possibility of WD-WD mergers emission was there applied to the analysis of the optical and infrared observations of the "kilonova" AT 2017gfo [2, 6, 22, 23], associated with GRB 170817A [1, 10].

The emission in the optical and infrared wavelengths is of thermal character being due to the adiabatic cooling of WD-WD merger ejecta, which is also powered by the fallback accretion onto the newly-formed WD. The ejecta mass is about $10^{-3}\,M_\odot$ [8, 15] and the fallback may inject 10^{47}–$10^{49}\,\mathrm{erg\,s^{-1}}$ at early times and then fall-off following a power-law behavior [15].

The thermal ejecta start to become transparent in the optical wavelengths at $t \sim 7$ days with a peak bolometric luminosity $L_{\rm bol} \sim 10^{42}\,\mathrm{erg\,s^{-1}}$. These ejecta are therefore powered by a different mechanism with respect to the one in the kilonova from NS-NS which are powered by the radioactive decay of r-process heavy material synthesized in the merger.

Since the observational features of WD-WD mergers are an important topic by their own, the aim of this article is to give details on their expected electromagnetic emission, not only in the optical and infrared but also in the X- and gamma-rays.

The article is organized as follows. In section 2 we recall the properties of the WD-WD mergers obtained from numerical simulations, section 3 is devoted to the analysis of the optical and infrared emission from the cooling of the merger ejecta. We show in section 4 the X-ray emission from fallback accretion and spindown of the newly-formed central WD, in section 5 we present a brief discussion on the possible prompt emission in gamma-rays, and in section 6 we present the summary and the conclusions of the article.

2 WD-WD mergers

2.1 Post-merger configuration

Numerical simulations of WD-WD mergers indicate that, when the merger does not lead to a prompt type Ia supernova (SN) explosion, the merged configuration has in general three distinct regions [4, 7, 11, 14, 15, 26, 32]: a rigidly rotating, central WD, on top of which there is a hot, differentially-rotating, convective corona, surrounded by a rapidly rotating Keplerian disk. The corona is composed of about half of the mass of the secondary star which is totally disrupted and roughly the other half of the secondary mass is in the disk. Little mass ($\sim 10^{-3}\,M_\odot$) is ejected during the merger.

Depending on the merging component masses, the central remnant can be a massive (1.0–1.5 $M_\odot$), highly magnetized (10^9–10^{10} G) and fast rotating ($P =$ 1–10 s) WD [3, 28].

Figure 1 shows a series of snapshots of the time evolution of a $0.8 + 0.6\,M_\odot$ WD-WD merger obtained by an adapted version of the smoothed-particle-hydrodynamics (SPH) code Phantom [24, 25]. This simulation was run with 7×10^4 SPH particles. The newly-formed central WD has approximately $1.1\,M_\odot$. The ejected mass has been estimated to be $1.2 \times 10^{-3}\,M_\odot$. The average velocity of the ejected particles is $\approx 10^8$ cm s^{-1}.

It is worth to mention that the above ejecta mass is also consistent with other independent merger simulations, e.g. Dan et al. [7], who showed that the amount of mass expelled in the merger can be obtained by the following fitting rational polynomial

$$m_{\rm ej} = M \frac{0.0001807}{-0.01672 + 0.2463q - 0.6982q^2 + q^3}, \tag{2.1}$$

where $M = m_1 + m_2$ is the total binary mass and $q \equiv m_2/m_1 \leq 1$ is the binary mass-ratio. Indeed, for the present case with $M = 1.4\,M_\odot$ and $q = 0.6/0.8$, the above formula gives $m_{\rm ej} = 0.00128\,M_\odot$.

Figure 2 shows the distribution of the SPH particles in the xy and xz planes of the system as well as a density plot, just after the merger. It can be appreciated a still dissipating spiral arm, the disk and the ejected particles. We show the unbound particles in red and the bound particles in blue. It can be seen that the outer part of the spiral arm is gravitationally unbound while the inner region is bound and will fallback onto the newly-formed WD. With a mass of $1.1\,M_\odot$ the central WD has a radius of $R_{\rm WD} \approx 5 \times 10^8$ cm $\lesssim 0.01\ R_\odot$ (see e.g. [5]), while the disk is shown here up to $\approx 0.05\ R_\odot$.

2.2 WD-WD merger rate

The WD-WD merger rate has been recently estimated to be $(1\text{–}80) \times 10^{-13}\,{\rm yr}^{-1}\,M_\odot^{-1}$ (at 2σ) and $(5\text{–}9) \times 10^{-13}\,{\rm yr}^{-1}\,M_\odot^{-1}$ (at 1σ) [17, 18]. For a Milky Way stellar mass $6.4 \times 10^{10}\,M_\odot$ and using an extrapolating factor of Milky Way equivalent galaxies, 0.016 Mpc^{-3} [13], it leads to a local cosmic rate $(0.74\text{–}5.94) \times 10^6\,{\rm Gpc}^{-3}\,{\rm yr}^{-1}$ (2σ) and $(3.7\text{–}6.7) \times 10^5\,{\rm Gpc}^{-3}\,{\rm yr}^{-1}$ (1σ).

The above rate implies that (12–22)% of WD-WD mergers may end as type Ia SN. This is consistent with previously estimated rates of WD-WD mergers leading to SNe Ia (see e.g. [30]). We are here interested in the rest of the merger population not leading to Ia SNe.

2.3 Magnetic field of the central WD

The hot, rapidly rotating, convective corona can produce, via an efficient $\alpha\omega$ dynamo, magnetic fields of up to $B \approx 10^{10}$ G (see e.g. [9]). Recent two-dimensional magneto-hydrodynamic

JCAP03(2019)044

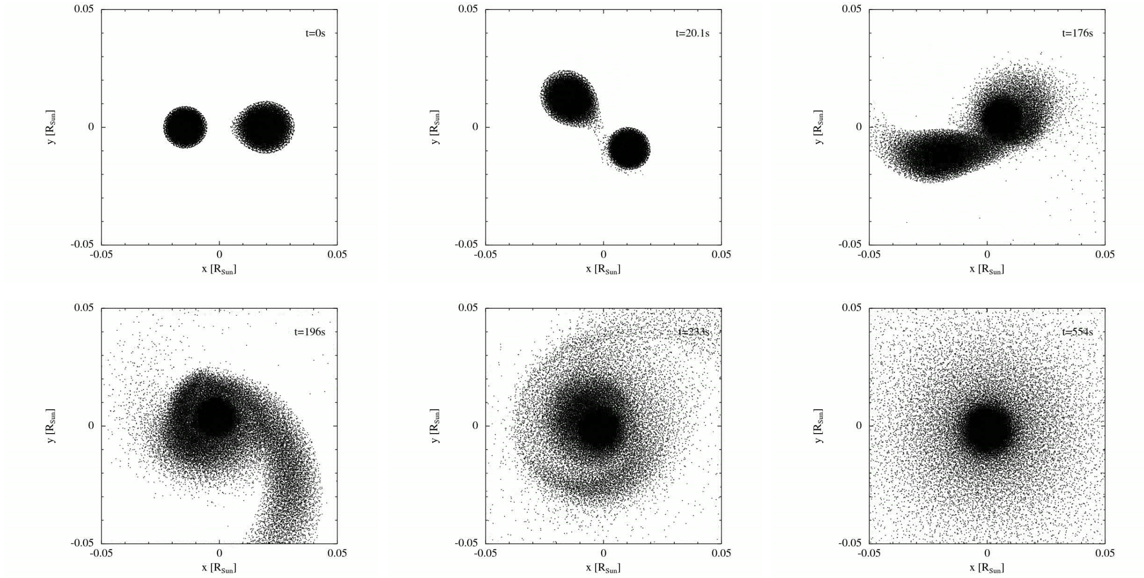

Figure 1. Snapshots of the time evolution of $0.8 + 0.6\,M_{\odot}$ WD-WD merger from the SPH simulation with 7×10^4 particles. The newly-formed central WD has approximately $1.1\,M_{\odot}$. In the sequence it can be seen how the secondary star is disrupted by Roche lobe overflow. Nearly half of the mass of the secondary star is transferred to the primary and the rest remains bound to the newly-formed central WD in form of a Keplerian disk. Little mass is ejected, in the present simulation nearly $1.2 \times 10^{-3}\,M_{\odot}$. These figures have been done using the visualization tool SPLASH [34].

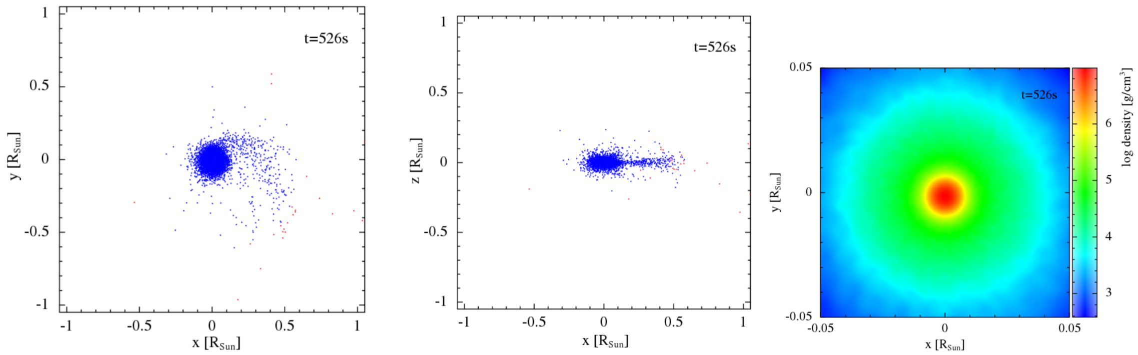

Figure 2. Left panel: distribution of the SPH particles in the xy plane just after the merger. We can see a still dissipating spiral arm, the disk and the ejected particles. Bound particles are shown in blue and unbound particles are shown in red. Center panel: same as in the left panel but for the xz plane. Right panel: density (in $\mathrm{g\,cm^{-3}}$) plot in the xy plane. The central WD has a radius of $\approx 0.01\ R_{\odot}$ while the disk is shown here up to $\approx 0.05\ R_{\odot}$. These figures have been done using the visualization tool SPLASH [34].

simulations of post-merger systems confirm the growth of the WD magnetic field after the merger owing to the magneto-rotational instability [12, 33]. For a summary of the magnetic field configuration and its genesis in WD-WD mergers, as well as its role along with rotation in the aftermath of the dynamical mergers, see Becerra et al. [3].

JCAP03(2019)044

3 Optical and infrared emission

The ejected matter $m_{\rm ej}$ moves with an initial velocity $v_{\rm ej,0}$ and we adopt for simplicity an evolving, uniform density profile

$$\rho_{\rm ej} = \frac{3m_{\rm ej}}{4\pi r_{\rm ej}^3(t)}, \tag{3.1}$$

where $r_{\rm ej}(t)$ is the ejecta radius.

The energy conservation equation is

$$\frac{dE}{dt} = -P\frac{dV}{dt} - L_{\rm rad} + H, \tag{3.2}$$

where E is the energy, P the pressure, $V = (4\pi/3)r_{\rm ej}^3$ is the volume, $L_{\rm rad}$ is the radiated energy and H is the heating source, namely the power injected into the ejecta. For the ejecta we adopt a radiation dominated equation of state, namely $E = 3PV$. The injected power H is represented by the rotational energy coming from the spindown of the WD and the fallback accretion onto the WD:

$$H = L_{\rm sd} + L_{\rm fb}. \tag{3.3}$$

We adopt the spindown power by a dipole magnetic field

$$L_{\rm sd} = \frac{2}{3}\frac{B_d^2 R^6}{c^3}\omega^4, \tag{3.4}$$

where $\omega = 2\pi/P$ is the rotation angular velocity of the WD, P is the rotation period, B_d is the dipole field at the WD surface and R is the WD radius.

Our assumption of the pulsar-like emission as part of the injection power into the ejecta is supported by the analysis of section 4.1 where we show that the magnetic field values of interest are larger than the minimum magnetic field needed for it not to be buried by the accreted matter. This indeed agrees with the recent results of Becerra et al. [3] on the thermal and rotational evolution of the central, massive WD produced by a WD-WD merger accounting for the torque by accretion, propeller, magnetic field-disk interaction and magneto-dipole emission. There, the timescale on which each of these regimes dominates the evolution has been obtained and it is shown the emergence of the magneto-dipole emission already at very early times post-merger even for the highest possible accretion rates which are higher than the ones considered in the present work.

The fallback power can be parametrized by

$$L_{\rm fb} = L_{\rm fb,0}\left(1 + \frac{t}{t_{\rm fb}}\right)^{-n}, \tag{3.5}$$

where $L_{\rm fb,0}$ is the initial fallback luminosity, $t_{\rm fb}$ is the timescale on which the fallback power starts to follow a power-law behavior. This function fits the numerical results by Lorén-Aguilar et al. [15] of the luminosity produced by the fallback of material of the disrupted secondary which remained bound in highly eccentric orbits. The derivation of this luminosity follows the treatment of Rosswog [27]. The material interacts with the disk in a timescale set by the distribution of eccentricities and not by viscous dissipation. The energy released is calculated as the difference in the kinetic plus potential energy of the particles between the initial position and the debris disk (dissipation) radius (obtained from the SPH simulation).

JCAP03(2019)044

Clearly, not all this energy can be released in form e.g. of photons to energize the ejecta so it has to be considered as an upper limit to the energy input from matter fallback.

Using eq. (3.5) we can also estimate the fallback accretion rate onto the WD as

$$\dot{m}_{\rm fb} \approx \frac{L_{\rm fb}}{GM_{\rm WD}/R_{\rm WD}}. \tag{3.6}$$

Since little energy is radiated (see below) by the system, namely it is highly adiabatic, we can assume the radius to evolve according to [21]

$$\frac{1}{2}m_{\rm ej}v_{\rm ej}^2 \approx \frac{1}{2}m_{\rm ej}v_{\rm ej,0}^2 + \int_0^t H dt, \tag{3.7}$$

where $v_{\rm ej} \equiv dr_{\rm ej}/dt$ is the ejecta velocity. It is clear that in this most simple uniform density model under consideration this can be considered as a bulk average velocity. The density profile can have initially a radial dependence and in that case there would exist also a velocity profile with both faster and slower layers with respect to the unique one of our model.

Since the radiation travels on a photon diffusion timescale $t_{\rm ph} = r_{\rm ej}(1+\tau_{\rm opt})/c$, the radiated luminosity can be written as

$$L_{\rm rad} = \frac{cE}{r_{\rm ej}(1+\tau_{\rm opt})}, \tag{3.8}$$

where

$$\tau_{\rm opt} = \kappa\rho_{\rm ej}r_{\rm ej}, \tag{3.9}$$

is the optical depth with κ the opacity. For the optical wavelengths and the composition of the merger ejecta we expect $\kappa \approx 0.1$–$0.2\,{\rm cm^2\,g^{-1}}$. This is different from the higher opacity expected for r-process material composing the kilonova produced in NS-NS mergers.

The effective temperature of the observed blackbody radiation, $T_{\rm eff}$, can be obtained as usual from the bolometric luminosity equation

$$L_{\rm rad} = 4\pi r_{\rm ej}^2\sigma T_{\rm eff}^4, \tag{3.10}$$

where σ is the Stefan-Boltzmann constant. Being thermal, the density flux at the Earth from a source located at a distance D is therefore

$$B_\nu = \frac{2\pi h\nu^3}{c^2}\frac{1}{\exp[h\nu/(kT_{\rm eff})]-1}\left(\frac{r_{\rm ej}}{D}\right)^2, \tag{3.11}$$

where ν is the frequency.

The ejecta radius $r_{\rm ej}$ and effective temperature $T_{\rm eff}$ obtained from the cooling of the merger ejecta are shown in figure 3. Figure 4 shows the expected bolometric luminosity (left panel) as well as the corresponding expected density flux at Earth (right panel) in the optical and infrared, for a source at 10 kpc.

We have chosen fallback power parameters according to numerical simulations of WD-WD mergers (see e.g. section 5.3 and figure 8 in [15]): $L_{\rm fb,0} = 8.0\times10^{47}\,{\rm erg\,s^{-1}}$ and $t_{\rm fb} = 10\,{\rm s}$, and $n = 1.45$. For these parameters, it can be easily checked that the injection power from the WD spindown is negligible: even for a high field $B_d = 10^{10}\,{\rm G}$ and an initial (at $t = 0$) fast rotation period $P_0 = 5\,{\rm s}$, we have $L_{\rm fb} = 8.0\times10^{47}\,{\rm erg\,s^{-1}}$ and $L_{\rm sd} = 9.6\times10^{40}\,{\rm erg\,s^{-1}}$, and for instance at $t = 1$ day, $L_{\rm fb} = 1.6\times10^{42}\,{\rm erg\,s^{-1}}$ and $L_{\rm sd} = 9.6\times10^{40}\,{\rm erg\,s^{-1}}$ (the

JCAP03(2019)044

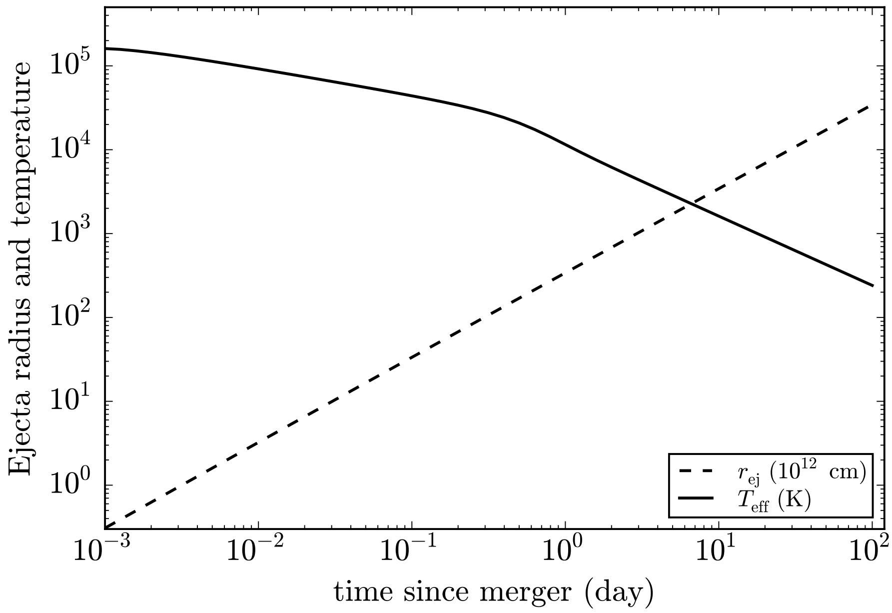

Figure 3. Expected evolution of the ejecta radius and effective temperature from the cooling of $1.3 \times 10^{-3}\, M_\odot$ ejecta heated by fallback accretion onto the newly-formed central WD.

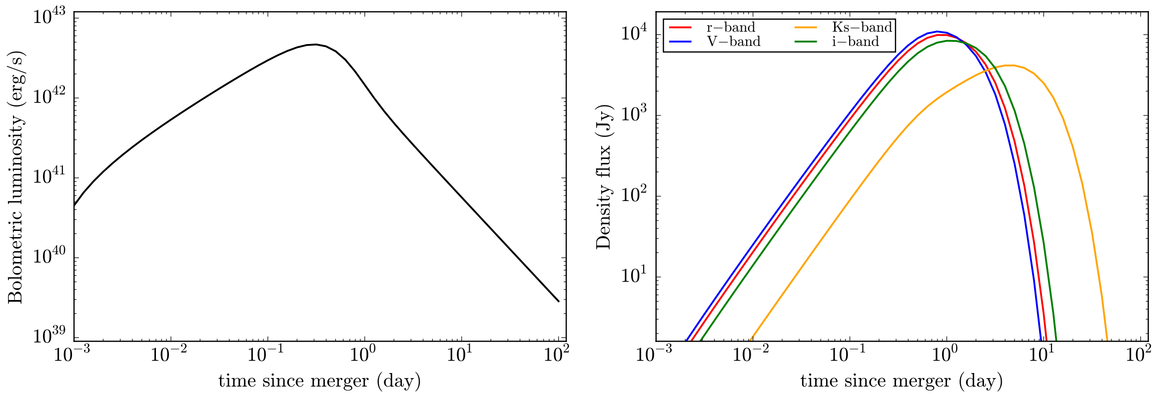

Figure 4. Left panel: expected bolometric luminosity from the cooling of $1.3\times10^{-3}\, M_\odot$ ejecta heated by fallback accretion onto the newly-formed central WD. Right panel: corresponding expected flux density at Earth in the optical and in the infrared for a source located at 10 kpc.

spindown timescale for these WD parameters is much longer than one day). Thus, the ejecta is essentially only fallback-powered, namely $H \approx L_{\rm fb}$.

Again, it is important to check the consistency of our fallback parameters with independent simulations. Dan et al. [7] showed that the fallback mass is well fitted by

$$m_{\rm fb} = M(0.07064 - 0.0648q), \tag{3.12}$$

which for our binary mass-ratio and total mass leads to $m_{\rm fb} = 0.031\, M_\odot$. The fallback accretion leads to an energy injection

$$E_{\rm fb} = \int L_{\rm fb} dt \approx \int \frac{G M_{\rm WD}}{R_{\rm WD}} \dot{m}_{\rm fb} c^2 dt \approx \frac{G M_{\rm WD}}{R_{\rm WD}} m_{\rm fb} c^2, \tag{3.13}$$

JCAP03(2019)044

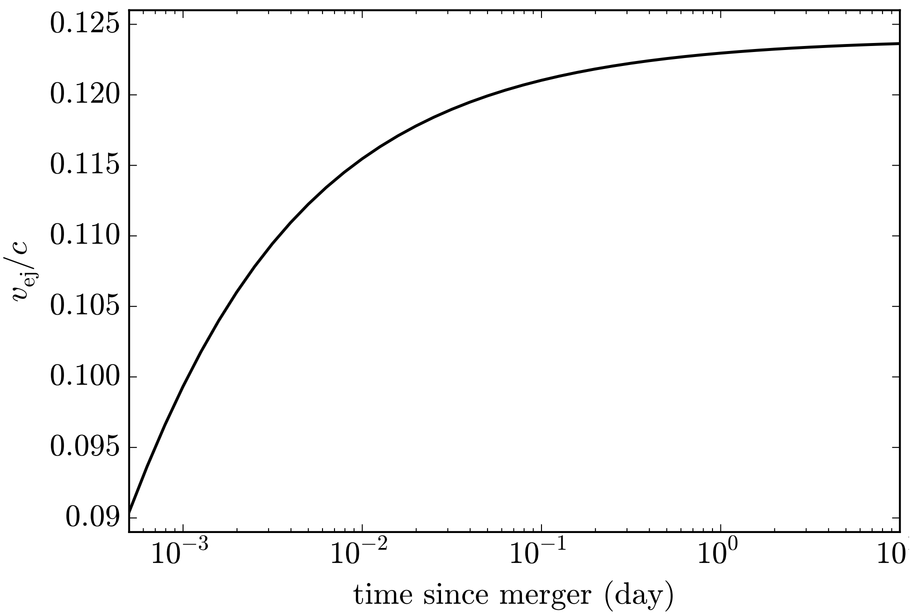

Figure 5. Time-evolution of the ejecta velocity obtained from the integration of eq. (3.7) accounting for the acceleration due to the presence of the heating source $H \approx L_{\rm fb}$.

where $m_{\rm fb}$ is the fallback mass given by eq. (3.12). For our present case, $M_{\rm WD} \approx 1.1\,M_\odot$ and $R_{\rm WD} \approx 5 \times 10^8$ cm, it leads to 1.79×10^{49} erg. This value has to be compared with the full integral $E_{\rm fb} = \int L_{\rm fb} dt \approx 1.78 \times 10^{49}$ erg, where $L_{\rm fb}$ is given by eq. (3.5). The above estimate not only cross-checks the amount of fallback mass as given independently by eqs. (3.6) and (3.12) but, at the same time, the mass and radius of the WD, as obtained from different simulations.

Since the ejecta are highly opaque at early times the fallback accretion and the spindown power are transformed into kinetic energy thereby increasing the expansion velocity of the ejecta; see eq. (3.7). The matter is ejected a few orbits (2–3) before the merger and start to move outward with an initial non-relativistic velocity $0.01\,c$ typical of the WD escape velocity. In the present example, such ejecta is then accelerated to mildly relativistic velocities $0.1\,c$ (see figure 5).

4 X-ray emission

The X-ray luminosity account for the absorption from the ejecta can be calculated as

$$L_X \approx \frac{1 - e^{-\tau_X}}{\tau_X}(L_{\rm fb} + L_{\rm sd}) \approx \frac{L_{\rm fb} + L_{\rm sd}}{1 + \tau_X}, \tag{4.1}$$

where τ_X is the optical depth of the X-rays through the ejecta (see e.g. [19]):

$$\tau_X = \kappa_X \rho_{\rm ej} r_{\rm ej}, \tag{4.2}$$

with κ_X the opacity to the X-rays which we assume to be dominated by bound-free electrons. For 1–10 keV photons it can be in the range 10^2–10^4 cm^2 g^{-1} (see e.g. figure 4 in [20] and [31] for details), therefore for simplicity we here adopt a single value of $\kappa_X \approx 10^3$ cm^2 g^{-1}).

JCAP03(2019)044

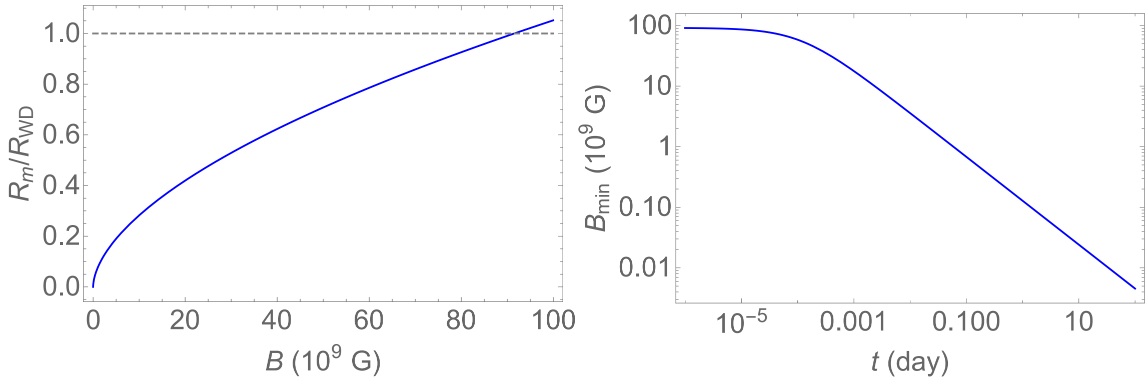

Figure 6. Left panel: magnetospheric to WD radii ratio as a function of the WD surface magnetic field for an accretion rate set to the fallback value at time $t = 0$ post-merger. Right panel: minimum magnetic field $B_{\rm min}$ needed to have $R_m > R_{\rm WD}$, as a function of time, for the fallback accretion rate obtained from eq. (3.6). The mass and radius of the WD are $M_{\rm WD} = 1.1 M_\odot$ and $R_{\rm WD} = 5 \times 10^8$ cm.

In the above general discussion we have assumed that the WD can behave as a pulsar due to its dipole magnetic field and injects energy into the ejecta at a rate given by the radiation power given by eq. (3.4). However, we have first to check whether the magnetic field of the WD can be buried by the fallback accretion.

4.1 Is the magnetic field buried?

The magnetic field is buried inside the star if the magnetospheric radius,

$$R_m = \left(\frac{B^2 R_{\rm WD}^6}{\dot{m}_{\rm fb}\sqrt{2GM_{\rm WD}}} \right)^{2/7}, \tag{4.3}$$

is smaller than the WD radius, $R_{\rm WD}$. Thus, using the value of $\dot{m}_{\rm fb}$ from eq. (3.6) we can compute the ratio $R_m/R_{\rm WD}$ and check if it is smaller or larger than unity.

The left panel of figure 6 shows this ratio for an accretion rate set to the fallback value at time $t = 0$ post-merger, while the right panel shows the value of the magnetic field for which $R_m = R_{\rm WD}$, say $B_{\rm min}$, as a function of time, for the fallback accretion rate given by eq. (3.6). $B_{\rm min}$ is the minimum value of the magnetic field that is not buried inside the star by the matter fallback. Therefore, for fields $B > B_{\rm min}$ the WD can behave as a pulsar and it can inject energy into the ejecta at the expenses of the WD rotational energy.

4.2 Expected X-ray emission

Figure 7 shows the X-ray luminosity (4.1) in comparison with the late-time X-ray emission data of GRB170817A. The comparison is made for selected values of the magnetic field, B, and the initial rotation period of the WD, P_0.

It can be seen that a good agreement with the X-ray data can be obtained. Although the fallback power dominates over the pulsar one, the agreement is improved by adding the presence of the WD-pulsar (spindown) component. It is clear from our plots that the current X-ray data is not yet sufficient to unambiguously identify the WD parameters since an agreement is obtained for different combinations of B and P_0. This is to be expected due to the magnetic dipole power dependence on the ratio B^2/P^4.

JCAP03(2019)044

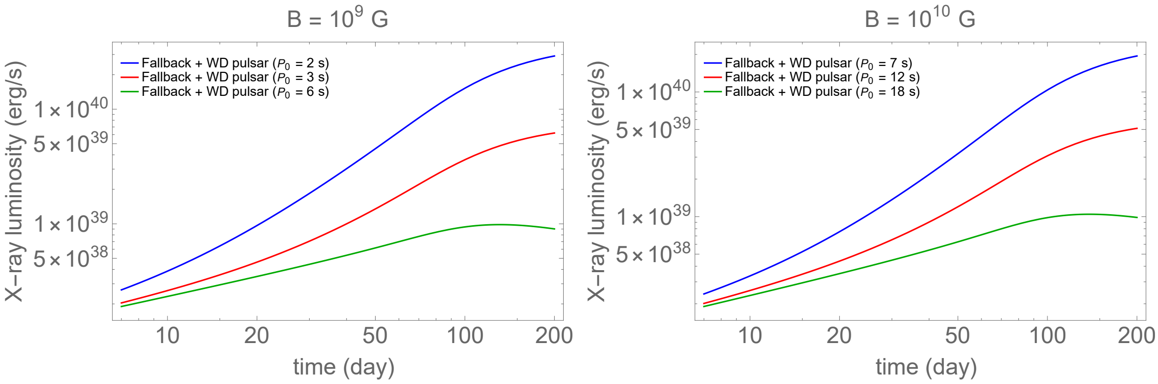

Figure 7. Expected X-ray luminosity calculated via eq. (4.1) for magnetic field values 10^9 G (left panel) and 10^{10} G (right panel).

4.3 WD-pulsar appearance

From the above analysis we can see that additional data from other wavelengths, or X-ray data at later times, are needed to have an unambiguous identification of the WD parameters. Thus, it is interesting to compute when the newly-formed WD is expected to appear as a pulsar-like object in the sky.

At the time of X-ray transparency, $t \sim 100$–150 day, the fallback power is still two orders of magnitude higher than the spindown one. However, at these post-merger timescales the fallback is fading continuously while the spindown power remains constant since, for the parameters in agreement with the current X-ray data (see figure 7), the spindown timescale is much longer. This implies that the WD can show up as a pulsar at a relatively early life of the post-merger system. To verify this we show in figure 8 the two components as a function of time after the X-ray transparency. At these times we can compare the unobserved luminosities given by eq. (3.5) and eq. (3.4) for the fallback and spindown power, respectively. It can be seen that in the two cases a deviation from the fallback power-law behavior to a less steep lightcurve decay appears at $t \gtrsim 500$ day. This is a predicted signature of the WD-pulsar presence. The precise crossing between the fallback power and the spindown component appears, in the case of $(B, P_0) = (10^9\ \text{G}, 6\ \text{s})$ and $(10^{10}\ \text{G}, 18\ \text{s})$, at $t = 2318.3$ day (6.3 yr) and 2023.4 day (5.5 yr), respectively.

5 Gamma-ray emission

The energy observed in gamma-rays in GRB 170817A, $E_{\rm iso} \approx 3\times10^{46}$ erg, can originate from flares owing to the twist and stress of the magnetic field lines during the merger process: a magnetic energy of 2×10^{46} erg is stored in a region of radius 10^9 cm and magnetic field of 10^{10} G [16]. Such a radius would imply a photon travel time of the order of $r/c \sim 0.1$ s, so a peak luminosity of few 10^{47} erg s^{-1}.

We are also currently exploring the temperature properties of the ejecta at the beginning of the expansion. The ejected matter might have temperatures of the order of 10^8 K at radii of 10^9 cm which could clearly gives a luminosity of the order of $4\pi r^2\sigma T^4 \approx 7\times10^{46}$ erg s^{-1} with an energy peak of $\approx 3k_BT \approx 30$ keV, so observable as a hard X-ray (soft gamma-ray) emission. If the matter expands adiabatically and isotropically then the temperature would decrease as $T \propto R^{-1}$ (adopting radiation-dominated matter) and therefore it can rapidly

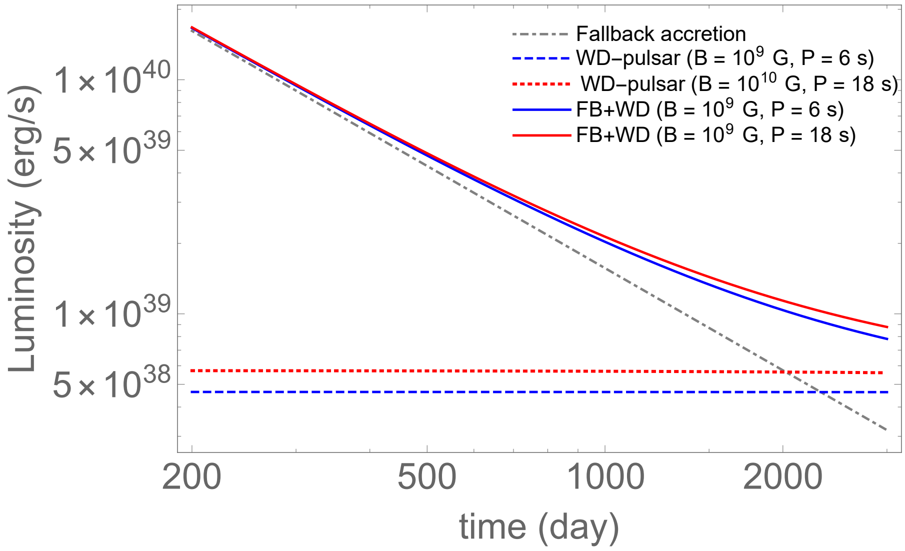

Figure 8. Fallback versus spindown emission at times after the X-ray transparency.

(in seconds timescale) fade to the soft X-rays to then become undetectable for the current X-ray satellites. The above makes the detection of this emission particularly difficult at early times post-merger. These issues are important by their own and deserve further analysis in dedicated forthcoming works.

6 Summary and conclusions

We have investigated the infrared, optical, X and gamma-ray emission associated with a WD-WD merger, the ejected matter and the post-merger signal from the newborn WD.

In view of the high magnetic fields involved in the merger, a prompt emission in the gamma-rays might occur as the result of magnetospheric flaring activity owing to the twist and magnetic stresses. For instance, the release of magnetic energy associated with a field of 10^{10} G in a region of radius 10^9 cm can lead to a total energy release of few 10^{46} erg in a burst of short (~ 0.1–1 s) duration with a peak luminosity of few $10^{47}\,\mathrm{erg\,s^{-1}}$.

We have modeled the time evolution of the ejecta as the expansion of a uniform density profile. We show our results for a fiducial case of a $0.6 + 0.8\,M_\odot$ WD-WD merger leading to a central WD of $1.1\,M_\odot$ and ejecta mass $\sim 10^{-3}\,M_\odot$. The latter start to move outward with initial bulk velocity $0.01\,c$ and from a distance $\sim 10^9$ cm, typical of the escape velocity and radius from a WD-WD binary when the matter is ejected, i.e. 2–3 orbits before merger [15].

The cooling of the expanding ejecta, heated by the fallback accretion onto the WD (see section 3), results in a thermal emission observable in the infrared and in the optical. The bolometric luminosity associated with this thermal emission peaks with a value of 10^{41}–$10^{42}\,\mathrm{erg\,s^{-1}}$ about 0.5–1 day post-merger (see figure 4). We have shown that the ejecta initially expand at low, non-relativistic velocities $0.01\,c$, to then being rapidly accelerated by the fallback energy injection to mildly-relativistic velocities of the order of $0.1\,c$ (see figure 5).

The X-ray emission from the fallback accretion process (see section 4) emerges and peaks with a value of 10^{38}–$10^{39}\,\mathrm{erg\,s^{-1}}$ at 100–150 day post-merger (see figure 7). X-rays from the spindown power of the central WD become observable later at a time that depends on the WD parameters (see figure 8).

Once we have established for these systems their observable signatures across the electromagnetic spectrum and their nature, we can discuss some possibilities for their experimental identification. We have shown that the mass, rotation period and magnetic field of the newly-formed central WD are similar to the ones proposed in the WD model of soft gamma-repeaters (SGRs) and anomalous X-ray pulsars (AXPs) [16]. The merger rate is indeed enough to explain the Galactic population of SGRs/AXPs. Thus, if a WD-WD merger produced GRB 170817A-AT 2017gfo, an SGR/AXP (a WD-pulsar) may become observable in this sky position. As we have shown in section 5 (see figure 8), the identification of first instants of the appearance of the WD-pulsar will allow to establish the WD parameters.

In addition, it is remarkable that, as pointed out in [29] and here further scrutinized, a WD-WD merger and the evolution of the ejecta powered by fallback accretion onto the newborn WD, is able to produce observational features in the X and in the gamma-rays similar to the ones of GRB 170817A and in the infrared and in the optical similar to the ones of AT 2017gfo. The ejecta from a WD-WD merger are, nevertheless, different from the ejecta from a NS-NS merger in that: 1) they have a lighter nuclear composition and 2) they are powered by fallback accretion instead of the radioactive decay of r-process heavy nuclei. It is then clear that the spectroscopic identification of atomic species can discriminate between the two scenarios. However, such an identification has not been possible in any observed kilonovae since it needs accurate models of atomic spectra, nuclear reaction network, density profile, as well as radiative transport (opacity) which are not available at the moment.

Acknowledgments

JMBL thanks support from the FPU fellowship by Ministerio de Educación Cultura y Deporte from Spain. JAR is grateful to Elena Pian for the interesting discussions on kilonovae.

References

[1] LIGO Scientific, Virgo, Fermi-GBM and INTEGRAL collaborations, *Gravitational Waves and Gamma-rays from a Binary Neutron Star Merger: GW170817 and GRB 170817A*, *Astrophys. J.* **848** (2017) L13 [arXiv:1710.05834] [INSPIRE].

[2] I. Arcavi et al., *Optical emission from a kilonova following a gravitational-wave-detected neutron-star merger*, *Nature* **551** (2017) 64 [arXiv:1710.05843] [INSPIRE].

[3] L. Becerra, J.A. Rueda, P. Loren-Aguilar and E. Garcia-Berro, *The Spin Evolution of Fast-Rotating, Magnetized Super-Chandrasekhar White Dwarfs in the Aftermath of White Dwarf Mergers*, *Astrophys. J.* **857** (2018) 134 [arXiv:1804.01275] [INSPIRE].

[4] W. Benz, A.G.W. Cameron, W.H. Press and R.L. Bowers, *Dynamic mass exchange in doubly degenerate binaries. I — 0.9 and 1.2 solar mass stars*, *Astrophys. J.* **348** (1990) 647.

[5] K. Boshkayev, J.A. Rueda, R. Ruffini and I. Siutsou, *On general relativistic uniformly rotating white dwarfs*, *Astrophys. J.* **762** (2013) 117 [arXiv:1204.2070] [INSPIRE].

[6] P.S. Cowperthwaite et al., *The Electromagnetic Counterpart of the Binary Neutron Star Merger LIGO/Virgo GW170817. II. UV, Optical and Near-infrared Light Curves and Comparison to Kilonova Models*, *Astrophys. J.* **848** (2017) L17 [arXiv:1710.05840] [INSPIRE].

[7] M. Dan, S. Rosswog, M. Brüggen and P. Podsiadlowski, *The structure and fate of white dwarf merger remnants*, *Mon. Not. Roy. Astron. Soc.* **438** (2014) 14 [arXiv:1308.1667] [INSPIRE].

[8] M. Dan, S. Rosswog, J. Guillochon and E. Ramirez-Ruiz, *Prelude to a double degenerate merger: the onset of mass transfer and its impact on gravitational waves and surface detonations*, Astrophys. J. **737** (2011) 89 [arXiv:1101.5132] [INSPIRE].

[9] E. Garcia-Berro et al., *Double degenerate mergers as progenitors of high-field magnetic white dwarfs*, Astrophys. J. **749** (2012) 25 [arXiv:1202.0461] [INSPIRE].

[10] A. Goldstein et al., *An Ordinary Short Gamma-Ray Burst with Extraordinary Implications: Fermi-GBM Detection of GRB 170817A*, Astrophys. J. **848** (2017) L14 [arXiv:1710.05446] [INSPIRE].

[11] J. Guerrero, E. García-Berro and J. Isern, *Smoothed Particle Hydrodynamics simulations of merging white dwarfs*, Astron. Astrophys. **413** (2004) 257.

[12] S. Ji et al., *The Post-Merger Magnetized Evolution of White Dwarf Binaries: The Double-Degenerate Channel of Sub-Chandrasekhar Type Ia Supernovae and the Formation of Magnetized White Dwarfs*, Astrophys. J. **773** (2013) 136 [arXiv:1302.5700] [INSPIRE].

[13] V. Kalogera, R. Narayan, D.N. Spergel and J.H. Taylor, *The Coalescence rate of double neutron star systems*, Astrophys. J. **556** (2001) 340 [astro-ph/0012038] [INSPIRE].

[14] R. Longland, P. Lorén-Aguilar, J. José, E. García-Berro and L.G. Althaus, *Lithium production in the merging of white dwarf stars*, Astron. Astrophys. **542** (2012) A117 [arXiv:1205.2538] [INSPIRE].

[15] P. Lorén-Aguilar, J. Isern and E. García-Berro, *High-resolution smoothed particle hydrodynamics simulations of the merger of binary white dwarfs*, Astron. Astrophys. **500** (2009) 1193.

[16] M. Malheiro, J.A. Rueda and R. Ruffini, *SGRs and AXPs as Rotation-Powered Massive White Dwarfs*, Publ. Astron. Soc. Jpn. **64** (2012) 56.

[17] D. Maoz and N. Hallakoun, *The binary fraction, separation distribution and merger rate of white dwarfs from SPY*, Mon. Not. Roy. Astron. Soc. **467** (2017) 1414 [arXiv:1609.02156] [INSPIRE].

[18] D. Maoz, N. Hallakoun and C. Badenes, *The separation distribution and merger rate of double white dwarfs: improved constraints*, Mon. Not. Roy. Astron. Soc. **476** (2018) 2584 [arXiv:1801.04275] [INSPIRE].

[19] R. Margutti et al., *The Binary Neutron Star Event LIGO/Virgo GW170817 160 Days after Merger: Synchrotron Emission across the Electromagnetic Spectrum*, Astrophys. J. **856** (2018) L18 [arXiv:1801.03531] [INSPIRE].

[20] B.D. Metzger, *Kilonovae*, Living Rev. Rel. **20** (2017) 3 [arXiv:1610.09381] [INSPIRE].

[21] B.D. Metzger and A.L. Piro, *Optical and X-ray emission from stable millisecond magnetars formed from the merger of binary neutron stars*, Mon. Not. Roy. Astron. Soc. **439** (2014) 3916 [arXiv:1311.1519] [INSPIRE].

[22] M. Nicholl et al., *The Electromagnetic Counterpart of the Binary Neutron Star Merger LIGO/VIRGO GW170817. III. Optical and UV Spectra of a Blue Kilonova From Fast Polar Ejecta*, Astrophys. J. **848** (2017) L18 [arXiv:1710.05456] [INSPIRE].

[23] E. Pian et al., *Spectroscopic identification of r-process nucleosynthesis in a double neutron star merger*, Nature **551** (2017) 67 [arXiv:1710.05858] [INSPIRE].

[24] D.J. Price et al., *PHANTOM: Smoothed particle hydrodynamics and magnetohydrodynamics code*, Astrophysics Source Code Library (2017).

[25] D.J. Price et al., *PHANTOM: A Smoothed Particle Hydrodynamics and Magnetohydrodynamics Code for Astrophysics*, Publ. Astron. Soc. Austral. **35** (2018) 31 [arXiv:1702.03930] [INSPIRE].

[26] C. Raskin, E. Scannapieco, C. Fryer, G. Rockefeller and F.X. Timmes, *Remnants of Binary White Dwarf Mergers*, *Astrophys. J.* **746** (2012) 62 [arXiv:1112.1420].

[27] S. Rosswog, *Fallback accretion in the aftermath of a compact binary merger*, *Mon. Not. Roy. Astron. Soc.* **376** (2007) L48 [astro-ph/0611440] [INSPIRE].

[28] J.A. Rueda et al., *A white dwarf merger as progenitor of the anomalous X-ray pulsar 4U 0142+61?*, arXiv:1306.5936 [INSPIRE].

[29] J.A. Rueda et al., *GRB 170817A-GW170817-AT 2017gfo and the observations of NS-NS, NS-WD and WD-WD mergers*, *JCAP* **10** (2018) 006 [arXiv:1802.10027] [INSPIRE].

[30] A.J. Ruiter, K. Belczynski and C.L. Fryer, *Rates and Delay Times of Type Ia Supernovae*, *Astrophys. J.* **699** (2009) 2026 [arXiv:0904.3108] [INSPIRE].

[31] D.A. Verner, G.J. Ferland, K.T. Korista and D.G. Yakovlev, *Atomic data for astrophysics. 2. New analytic FITS for photoionization cross-sections of atoms and ions*, *Astrophys. J.* **465** (1996) 487 [astro-ph/9601009] [INSPIRE].

[32] C. Zhu, P. Chang, M. van Kerkwijk and J. Wadsley, *A Parameter-Space Study of Carbon-Oxygen White Dwarf Mergers*, *Astrophys. J.* **767** (2013) 164 [arXiv:1210.3616] [INSPIRE].

[33] C. Zhu, R. Pakmor, M.H. van Kerkwijk and P. Chang, *Magnetized moving mesh merger of a carbon-oxygen white dwarf binary*, *Astrophys. J. Lett.* **806** (2015) L1.

[34] D.J. Price, *SPLASH: An Interactive Visualisation Tool for Smoothed Particle Hydrodynamics Simulations*, *Publ. Astron. Soc. Austral.* **24** (2007) 159 [arXiv:0709.0832].

universe

MDPI

Review

Induced Gravitational Collapse, Binary-Driven Hypernovae, Long Gramma-ray Bursts and Their Connection with Short Gamma-ray Bursts

J. A. Rueda [1,2,3,*], R. Ruffini [1,2,4] and Y. Wang [1,2]

1 ICRANet, Piazza della Repubblica 10, 65122 Pescara, Italy; ruffini@icra.it (R.R.); wangyu@me.com (Y.W.)
2 ICRA, Dipartimento di Fisica, Università di Roma Sapienza, Piazzale Aldo Moro 5, 00185 Rome, Italy
3 INAF, Istituto de Astrofisica e Planetologia Spaziali, Via Fosso del Cavaliere 100, 00133 Rome, Italy
4 INAF, Viale del Parco Mellini 84, 00136 Rome, Italy
* Correspondence: jorge.rueda@icra.it

Received: 25 February 2019; Accepted: 5 May 2019; Published: 9 May 2019

check for updates

Abstract: There is increasing observational evidence that short and long Gamma-ray bursts (GRBs) originate in different subclasses, each one with specific energy release, spectra, duration, etc, and all of them with binary progenitors. The binary components involve carbon-oxygen cores (CO_{core}), neutron stars (NSs), black holes (BHs), and white dwarfs (WDs). We review here the salient features of the specific class of binary-driven hypernovae (BdHNe) within the induced gravitational collapse (IGC) scenario for the explanation of the long GRBs. The progenitor is a CO_{core}-NS binary. The supernova (SN) explosion of the CO_{core}, producing at its center a new NS (νNS), triggers onto the NS companion a hypercritical, i.e., highly super-Eddington accretion process, accompanied by a copious emission of neutrinos. By accretion the NS can become either a more massive NS or reach the critical mass for gravitational collapse with consequent formation of a BH. We summarize the results on this topic from the first analytic estimates in 2012 all the way up to the most recent three-dimensional (3D) smoothed-particle-hydrodynamics (SPH) numerical simulations in 2018. Thanks to these results it is by now clear that long GRBs are richer and more complex systems than thought before. The SN explosion and its hypercritical accretion onto the NS explain the X-ray precursor. The feedback of the NS accretion, the NS collapse and the BH formation produce asymmetries in the SN ejecta, implying the necessity of a 3D analysis for GRBs. The newborn BH, the surrounding matter and the magnetic field inherited from the NS, comprises the *inner engine* from which the GRB electron-positron (e^+e^-) plasma and the high-energy emission are initiated. The impact of the e^+e^- on the asymmetric ejecta transforms the SN into a hypernova (HN). The dynamics of the plasma in the asymmetric ejecta leads to signatures depending on the viewing angle. This explains the ultrarelativistic prompt emission in the MeV domain and the mildly-relativistic flares in the early afterglow in the X-ray domain. The feedback of the νNS pulsar-like emission on the HN explains the X-ray late afterglow and its power-law regime. All of the above is in contrast with a simple GRB model attempting to explain the entire GRB with the kinetic energy of an ultrarelativistic jet extending through all of the above GRB phases, as traditionally proposed in the "collapsar-fireball" model. In addition, BdHNe in their different flavors lead to νNS-NS or νNS-BH binaries. The gravitational wave emission drives these binaries to merge producing short GRBs. It is thus established a previously unthought interconnection between long and short GRBs and their occurrence rates. This needs to be accounted for in the cosmological evolution of binaries within population synthesis models for the formation of compact-object binaries.

Keywords: Gamma-ray Bursts; supernovae; accretion; Neutron Stars; Black Holes; binary systems

1. Introduction

1.1. The Quest for the Binary Nature of GRB Progenitors

We first recall that GRBs have been traditionally classified by a phenomenological division based on the duration of the time-interval in which the 90% of the total isotropic energy in Gamma-rays is emitted, the T_{90}. Long GRBs are those with $T_{90} > 2$ s and short GRBs the sources with $T_{90} < 2$ s [1–5].

In the case of short bursts, rapid consensus was reached in the scientific community that they could be the product of mergers of NS-NS and/or NS-BH binaries (see e.g., the pioneering works [6–9]). We shall return on this issue below by entering into the description of their properties and also to introduce additional mergers of compact-star object binaries leading to short bursts.

For long bursts, possibly the most compelling evidence of the necessity of a binary progenitor comes from the systematic and spectroscopic analysis of the GRBs associated with SNe, the so-called GRB-SNe, started with the pioneering discovery of the spatial and temporal concomitance of GRB 980425 [10] and SN 1998bw [11]. Soon after, many associations of other nearby GRBs with type Ib/c SNe were evidenced (see e.g., [12,13]).

There are models in the literature attempting an explanation of both the SN and the GRB within the same astrophysical system. For instance, GRBs have been assumed to originate from a violent SN from the collapse of a massive and fast rotating star, a "collapsar" [14]. A very high rotating rate of the star is needed to produce a collimated, jet emission. This traditional picture adopts for the GRB dynamics the "fireball" model based on the existence of a single ultrarelativistic collimated jet [15–19]. There is a vast literature devoted to this "traditional" approach and we refer the reader to it for additional details (see, e.g., [20–25], and references therein).

Nevertheless, it is worth to mention here some of the most important drawbacks of the aforementioned"traditional" approach and which has motivated the introduction of an alternative model, based on a binary progenitor, for the explanation of long GRBs:

- SNe Ic as the ones associated with GRBs lack hydrogen and helium in their spectra. It has been recognized that they most likely originate in helium stars, $CO_{\rm core}$, or Wolf-Rayet stars, that have lost their outermost layers (see e.g., [26], and references therein). The pre-SN star, very likely, does not follow a single-star evolution but it belongs to a tight binary with a compact star companion (e.g., a NS). The compact star strips off the pre-SN star outermost layers via binary interactions such as mass-transfer and tidal effects (see e.g., [26–30]).
- Denoting the beaming angle by θ_j, to an observed isotropic energy $E_{\rm iso}$ it would correspond to a reduced intrinsic source energy released $E_s = f_b E_{\rm iso} < E_{\rm iso}$, where $f_b = (1 - \cos\theta_j) \sim \theta_j^2/2 < 1$. Extremely small beaming factors $f_b \sim 1/500$ (i.e., $\theta_j \sim 1^\circ$) are inferred to reduce the observed energetics of $E_{\rm iso} \sim 10^{54}$ erg to the expected energy release by such a scenario $\sim 10^{51}$ erg [31]. However, the existence of such extremely narrow beaming angles have never been observationally corroborated [32–34].
- An additional drawback of this scenario is that it implies a dense and strong wind-like circumburst medium (CBM) in contrast with the one observed in most GRBs (see e.g., [35]). Indeed, the average CBM density inferred from GRB afterglows is of the order of 1 baryon per cubic centimeter [36]. The baryonic matter component in the GRB process is represented by the so-called baryon load [37]. The GRB e^+e^- plasma should engulf a limited amount of baryons in order to be able to expand at ultrarelativistic velocities with Lorentz factors $\Gamma \gtrsim 100$ as requested by the observed non-thermal component in the prompt Gamma-ray emission spectrum [16–18]. The amount of baryonic mass M_B is thus limited by the prompt emission to a maximum value of the baryon-load parameter, $B = M_B c^2/E_{e^+e-} \lesssim 10^{-2}$, where E_{e^+e-} is the total energy of the e^+e- plasma [37].
- GRBs and SNe have markedly different energetics. SNe emit energies in the range 10^{49}–10^{51} erg, while GRBs emit in the range 10^{49}–10^{54} erg. Thus, the origin of GRB energetics point to the gravitational collapse to a stellar-mass BH. The SN origin points to evolutionary stages of a massive

star leading to a NS or to a complete disrupting explosion, but not to a BH. The direct formation of a BH in a core-collapse SN is currently ruled out by the observed masses of pre-SN progenitors, $\lesssim 18\, M_\odot$ [38]. It is theoretically known that massive stars with such a relatively low mass do not lead to a direct collapse to a BH (see [38,39] for details) .

- It was recently shown in [40] that the observed thermal emission in the X-ray flares present in the early (rest-frame time $t \sim 10^2$ s) afterglow implies an emitter of size $\sim 10^{12}$ cm expanding at mildly-relativistic velocity, e.g., $\Gamma \lesssim 4$. This is clearly in contrast with the "collapsar-fireball" scenario in which there is an ultrarelativistic emitter (the jet) with $\Gamma \sim 10^2$–10^3 extending from the prompt emission all the way to the afterglow.

Therefore, it seems most unlikely that the GRB and the SN can originate from the same single-star progenitor. Following this order of ideas, it was introduced for the explanation of the spatial and temporal coincidence of the two phenomena the concept of *induced gravitational collapse* (IGC) [41,42]. Two scenarios for the GRB-SN connection have been addressed: Ruffini et al. [41] considered that the GRB was the trigger of the SN. However, for this scenario to happen it was shown that the companion star had to be in a very fine-tuned phase of its stellar evolution [41]. Ruffini et al. [42] proposed an alternative scenario in a compact binary: the explosion of a Ib/c SN triggering an accretion process onto a NS companion. The NS, reaching the critical mass value, gravitationally collapses leading to the formation of a BH. The formation of the BH consequently leads to the emission of the GRB. Much more about this binary scenario has been discovered since its initial proposal; its theoretical studies and the search for its observational verification have led to the formulation of a much rich phenomenology which will be the main subject of this article.

Therefore, both short and long GRBs appear to be produced by binary systems, well in line with the expectation that most massive stars belong to binary systems (see, e.g., [43,44], and references therein). The increasing amount and quality of the multiwavelength data of GRBs have revealed the richness of the GRB phenomenon which, in a few seconds, spans different regimes from X-ray precursors to the Gamma-rays of the prompt emission, to the optical and X-rays of the early and late afterglow, to the optical emission of the associated SNe and, last but not least, the presence or absence of high-energy GeV emission. This, in addition to the multiyear effort of reaching a comprehensive theoretical interpretation of such regimes, have lead to the conclusion that GRBs separate into subclasses, each with specific energy release, spectra, duration, among other properties and, indeed, all with binary progenitors [45–49].

1.2. GRB Subclasses

Up to 2017 we had introduced seven GRB subclasses summarized in Table 1. In addition, we have recently introduced in [50,51] the possibility of a further GRB subclass produced by WD-WD mergers. We now give a brief description of all the GRB subclasses identified. In [49] we have renominated the GRB subclasses introduced in [45] and in [50,51], and inserted them into two groups: binary-driven hypernovae (BdHNe) and compact-object binary mergers. Below we report both the old and the new names to facilitate the reader when consulting our works prior to [49].

i. **X-ray flashes (XRFs)**. These systems have CO_{core}-NS binary progenitors in which the NS companion does not reach the critical mass for gravitational collapse [52,53]. In the SN explosion, the binary might or might not be disrupted depending on the mass loss and/or the kick imparted [54]. Thus XRFs lead either to two NSs ejected by the disruption, or to binaries composed of a newly-formed $\sim$1.4–1.5 $M_\odot$ NS (hereafter νNS) born at the center of the SN, and a massive NS (MNS) which accreted matter from the SN ejecta. Some observational properties are: Gamma-ray isotropic energy $E_{\rm iso} \lesssim 10^{52}$ erg, rest-frame spectral peak energy $E_{p,i} \lesssim 200$ keV and a local observed rate of $\rho_{\rm XRF} = 100^{+45}_{-34}$ Gpc^{-3} yr^{-1} [45]. We refer the reader to Table 1 and [45,47] for further details on this class. In [49], this class has been divided into BdHN type II, the sources with $10^{50} \lesssim E_{\rm iso} \lesssim 10^{52}$ erg, and BdHN type III, the sources with $10^{48} \lesssim E_{\rm iso} \lesssim 10^{50}$ erg.

ii. **Binary-driven hypernovae (BdHNe)**. Originate in compact CO_{core}-NS binaries where the accretion onto the NS becomes high enough to bring it to the point of gravitational collapse, hence forming a BH. We showed that most of these binaries survive to the SN explosion owing to the short orbital periods ($P \sim 5$ min) for which the mass loss cannot be considered as instantaneous, allowing the binary to keep bound even if more than half of the total binary mass is lost [55]. Therefore, BdHNe produce νNS-BH binaries. Some observational properties are: $E_{\rm iso} \gtrsim 10^{52}$ erg, $E_{p,i} \gtrsim 200$ keV and a local observed rate of $\rho_{\rm BdHN} = 0.77^{+0.09}_{-0.08}$ Gpc^{-3} yr^{-1} [45]. We refer the reader to Table 1 and [45,47] for further details on this class. In [49] this class has been renominated as BdHN type I.

iii. **BH-SN**. These systems originate in CO_{core} (or Helium or Wolf-Rayet star)-BH binaries, hence the hypercritical accretion of the SN explosion of the CO_{core} occurs onto a BH previously formed in the evolution path of the binary. They might be the late evolutionary stages of X-ray binaries such as Cyg X-1 [56,57], or microquasars [58]. Alternatively, they can form following the evolutionary scenario XI in [59]. If the binary survives to the SN explosion BH-SNe produce νNS-BH, or BH-BH binaries when the central remnant of the SN explosion collapses directly to a BH (see, although, [38,39]). Some observational properties are: $E_{\rm iso} \gtrsim 10^{54}$ erg, $E_{p,i} \gtrsim 2$ MeV and an upper limit to their rate is $\rho_{\rm BH-SN} \lesssim \rho_{\rm BdHN} = 0.77^{+0.09}_{-0.08}$ Gpc^{-3} yr^{-1}, namely the estimated observed rate of BdHNe type I which by definition covers systems with the above $E_{\rm iso}$ and $E_{p,i}$ range [45]. We refer the reader to Table 1 and [45,47] for further details on this class. In [49] this class has been renominated as BdHN type IV.

Table 1. Summary of the Gamma-ray bursts (GRB) subclasses. This table is an extended version of the one presented in [49] with the addition of a column showing the local density rate, and it also updates the one in [45,47]. We unify here all the GRB subclasses under two general names, BdHNe and BMs. Two new GRB subclasses are introduced; BdHN Type III and BM Type IV. In addition to the subclass name in "Class" column and "Type" column, as well as the previous names in "Previous Alias" column, we report the number of GRBs with known redshift identified in each subclass updated by the end of 2016 in "number" column (the value in a bracket indicates the lower limit). We recall as well the "in-state" representing the progenitors and the "out-state" representing the outcomes, as well as the the peak energy of the prompt emission, $E_{\rm p,i}$, the isotropic Gamma-ray energy, $E_{\rm iso}$ defined in the 1 keV to 10 MeV energy range, the isotropic emission of ultra-high energy photons, $E_{\rm iso,Gev}$, defined in the 0.1–100 GeV energy range, and the local observed rate $\rho_{\rm GRB}$ [45]. We adopt as definition of kilonova a phenomenon more energetic than a nova (about 1000 times). A kilonova can be an infrared-optical counterpart of a NS-NS merger. In that case the transient is powered by the energy release from the decay of r-process heavy nuclei processed in the merger ejecta [60–63]. FB-KN stands for fallback-powered kilonova [50,51]: a WD-WD merger can emit an infrared-optical transient, peaking at ∼5 day post-merger, with the ejecta powered by accretion of fallback matter onto the newborn WD formed in the merger. The density rate of the GRB subclasses BdHN III (HN) and BM IV (FB-KN) have not yet been estimated.

Class	Type	Previous Alias	Number	*In-State*	*Out-State*	$E_{\rm p,i}$ (MeV)	$E_{\rm iso}$(erg)	$E_{\rm iso,Gev}$ (erg)	$\rho_{\rm GRB}$ (Gpc^{-3} yr^{-1})
Binary-driven hypernova (BdHN)	I	BdHN	329	CO_{core}-NS	νNS-BH	$\sim$0.2–2	$\sim 10^{52}$–10^{54}	$\gtrsim 10^{52}$	$0.77^{+0.09}_{-0.08}$
	II	XRF	(30)	CO_{core}-NS	νNS-NS	$\sim$0.01–0.2	$\sim 10^{50}$–10^{52}	–	100^{+45}_{-34}
	III	HN	(19)	CO_{core}-NS	νNS-NS	$\sim$0.01	$\sim 10^{48}$–10^{50}	–	–
	IV	BH-SN	5	CO_{core}-BH	νNS-BH	$\gtrsim 2$	$>10^{54}$	$\gtrsim 10^{53}$	$\lesssim 0.77^{+0.09}_{-0.08}$
Binary Merger (BM)	I	S-GRF	18	NS-NS	MNS	$\sim$0.2–2	$\sim 10^{49}$–10^{52}	–	$3.6^{+1.4}_{-1.0}$
	II	S-GRB	6	NS-NS	BH	$\sim$2–8	$\sim 10^{52}$–10^{53}	$\gtrsim 10^{52}$	$\left(1.9^{+1.8}_{-1.1}\right) \times 10^{-3}$
	III	GRF	(1)	NS-WD	MNS	$\sim$0.2–2	$\sim 10^{49}$–10^{52}	–	$1.02^{+0.71}_{-0.46}$
	IV	FB-KN	(1)	WD-WD	NS/MWD	<0.2	$<10^{51}$	–	–
	V	U-GRB	(0)	NS-BH	BH	$\gtrsim 2$	$>10^{52}$	–	$\approx 0.77^{+0.09}_{-0.08}$

We proceed with the short bursts which are amply thought to originate from compact-object binary mergers (BMs). First, we discuss the traditionally proposed BMs namely NS-NS and/or NS-BH mergers [6–9,24,64–66]. These BMs can be separated into three subclasses [45,55,67]:

iv. **Short Gamma-ray flashes (S-GRFs)**. They are produced by NS-NS mergers leading to a MNS, namely when the merged core does not reach the critical mass of a NS. Some observational properties are: $E_{\rm iso} \lesssim 10^{52}$ erg, $E_{p,i} \lesssim 2$ MeV and a local observed rate of $\rho_{\rm S-GRF} = 3.6^{+1.4}_{-1.0}$ Gpc^{-3} yr^{-1} [45]. We refer the reader to Table 1 and [45,47] for further details on this class. In [49] this class has been renominated as BM type I.

v. **Authentic short GRBs (S-GRBs)**. They are produced by NS-NS mergers leading to a BH, namely when the merged core reaches the critical mass of a NS, hence it forms a BH as a central remnant [67–69]. Some observational properties are: $E_{\rm iso} \gtrsim 10^{52}$ erg, $E_{p,i} \gtrsim 2$ MeV and a local observed rate of $\rho_{\rm S-GRB} = \left(1.9^{+1.8}_{-1.1}\right) \times 10^{-3}$ Gpc^{-3} yr^{-1} [45]. We refer the reader to Table 1 and [45,47] for further details on this class. In [49] this class has been renominated as BM type II.

vi. **Ultra-short GRBs (U-GRBs)**. This is a theoretical GRB subclass subjected for observational verification. U-GRBs are expected to be produced by νNS-BH mergers whose binary progenitors can be the outcome of BdHNe type I (see II above) or of BdHNe type IV (BH-SN; see III above). The following observational properties are expected: $E_{\rm iso} \gtrsim 10^{52}$ erg, $E_{p,i} \gtrsim 2$ MeV and a local observed rate similar to the one of BdHNe type I since we have shown that most of them are expected to remain bound [55], i.e., $\rho_{\rm U-GRB} \approx \rho_{\rm BdHN} = 0.77^{+0.09}_{-0.08}$ Gpc^{-3} yr^{-1} [45]. We refer the reader to Table 1 and [45,47] for further details on this class. In [49] this class has been renominated as BM type V.

Besides the existence of the above three subclasses of long bursts and three subclasses of short bursts in which the presence of NSs plays a fundamental role, there are two subclasses of bursts in which there is at least a WD component.

vii. **Gamma-ray flashes (GRFs)**. These sources show an extended and softer emission, i.e., they have hybrid properties between long and short bursts and have no associated SNe [70]. It has been proposed that they are produced by NS-WD mergers [45]. These binaries are expected to be very numerous [71] and a variety of evolutionary scenarios for their formation have been proposed [72–75]. GRFs form a MNS and not a BH [45]. Some observational properties are: $10^{51} \lesssim E_{\rm iso} \lesssim 10^{52}$ erg, $0.2 \lesssim E_{p,i} \lesssim 2$ MeV and a local observed rate of $\rho_{\rm GRF} = 1.02^{+0.71}_{-0.46}$ Gpc^{-3} yr^{-1} [45]. It is worth noting that this rate is low with respect to the one expected from the current number of known NS-WD in the Galaxy [71]. From the GRB observations only one NS-WD merger has been identified (GRB 060614 [76]). This implies that most NS-WD mergers are probably under the threshold of current X and Gamma-ray instruments. We refer the reader to Table 1 and [45,47] for further details on this class. In [49] this class has been renominated as BM type III.

viii. **Fallback kilonovae (FB-KNe)**. This is a recently introduced GRB subclass having as progenitors WD-WD mergers [50,51]. The WD-WD mergers of interest are those that do not produce type Ia SNe but that lead to a massive ($M \sim 1\,M_\odot$), fast rotating ($P \sim 1$–10 s), highly-magnetized ($B \sim 10^9$–10^{10} G) WD. Some observational properties are: $E_{\rm iso} \lesssim 10^{51}$ erg, $E_{p,i} \lesssim 2$ MeV and a local observed rate $\rho_{\rm FB-KN} = (3.7$–$6.7) \times 10^5$ Gpc^{-3} yr^{-1} [50,51,77,78]. The coined name FB-KN is due to the fact that they are expected to produce an infrared-optical transient by the cooling of the ejecta expelled in the dynamical phase of the merger and heated up by fallback accretion onto the newly-formed massive WD.

The density rates for all GRB subclasses have been estimated assuming no beaming [45,47,50,51]. The GRB density rates have been analyzed in [45] following the method suggested in [79].

1.3. The Specific Case of BdHNe

We review in this article the specific case of BdHNe type I and II. As we have mentioned, the progenitor system is an exploding CO$_{\rm core}$ as a type Ic SN in presence of a NS companion [45,49]. Figure 1 shows a comprehensive summary of the binary path leading to this variety of compact binaries that are progenitors of the above subclasses of long GRBs and that, at the same time, have an intimate connection with the short GRBs.

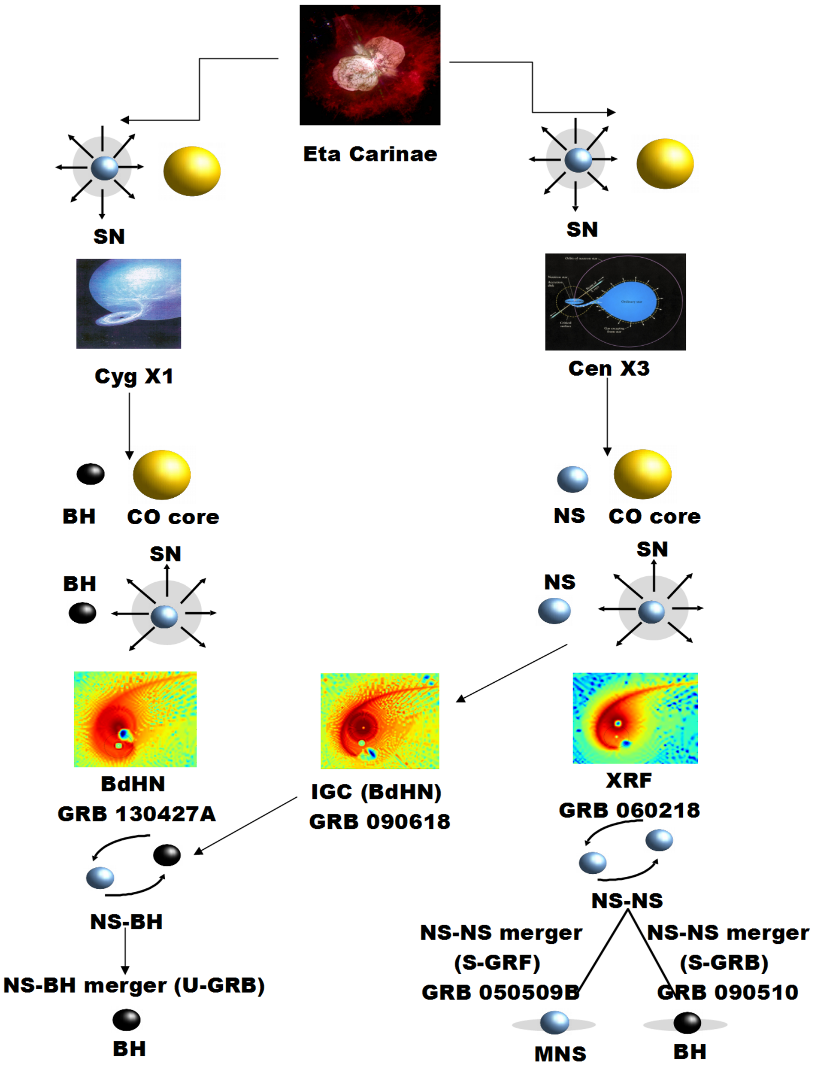

Figure 1. Taken from Figure 1 in [80]. Binary evolutionary paths leading to BdHNe I (previously named BdHNe) and II (previously named XRFs) and whose out-states, in due time, evolve into progenitors of short GRBs. The massive binary has to survive two core-collapse SN events. The first event forms a NS (right-side path) or BH (left-side path). The massive companion continues its evolution until it forms a CO_{core}. This simplified evolution diagram which does not show intermediate stages such as common-envelope phases (see e.g., [53,55], and references therein). At this stage the binary is a CO_{core}-NS (right-side path) or a CO_{core}-BH (left-side path). Then, it occurs the second SN event which forms what we call the νNS at its center. We focus in this article to review the theoretical and observational aspects of interaction of this SN event with the NS companion (BdHNe I and II). We do not treat here the case of a SN exploding in an already formed BH companion (BdHNe IV). At this point the system can form a νNS-BH/NS (BdHN I/II) binary (right-side path), or a νNS-BH (BdHN IV) in the (left-side path). The emission of gravitational waves will make this compact-object binaries to merge, becoming progenitors of short GRBs [55]. We recall to the reader that S-GRBs and S-GRFs stand for, respectively, authentic short GRBs and short Gamma-ray flashes, the two subclasses of short bursts from NS-NS mergers, the former produced when the merger leads to a more massive NS and the latter when a BH is formed [45].

We emphasize on the theoretical framework concerning the CO_{core}-NS binaries which have been extensively studied by our group in a series of publications [52,53,55,81–83]. The CO_{core} explodes as

SN producing an accretion process onto the NS. For sufficiently compact binaries, e.g., orbital periods of the order of few minutes, the accretion is highly super-Eddington (hypercritical) leading to the possibility of the IGC of the NS once it reaches the critical mass, and forms a BH (see Figure 2).

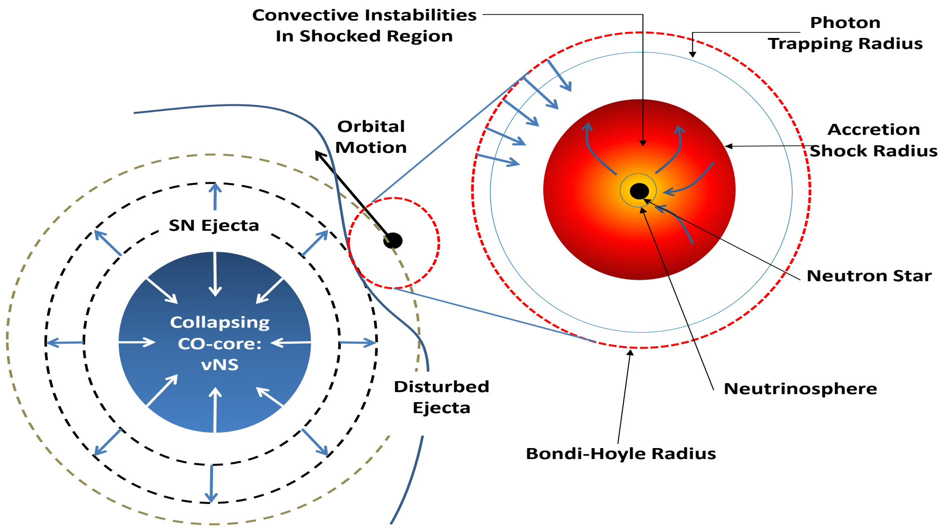

Figure 2. Scheme of the induced gravitational collapse (IGC) scenario (taken from Figure 1 in [83]). The CO_{core} undergoes supernova (SN) explosion, the neutron star (NS) accretes part of the SN ejecta and then reaches the critical mass for gravitational collapse to a black hole (BH), with consequent emission of a GRB. The SN ejecta reach the NS Bondi-Hoyle radius and fall toward the NS surface. The material shocks and decelerates while it piles over the NS surface. At the neutrino emission zone, neutrinos take away most of the gravitational energy gained by the matter infall. The neutrinos are emitted above the NS surface that allow the material to reduce its entropy to be finally incorporated to the NS. For further details and numerical simulations of the above process see [52,53,83].

If the binary is not disrupted by the explosion, BdHNe produces new binaries composed of a new NS (νNS) formed at the center of the SN, and a more massive NS or a BH companion (see Figure 1).

In the case of BH formation, the rotation of the BH together with the presence of the magnetic field inherited from the NS and the surrounding matter conform to what we have called the *inner engine* of the high-energy emission [84–87]. The electromagnetic field of the engine is mathematically described by the Wald solution [88]. The above ingredients induce an electric field around the BH which under the BdHN conditions is initially overcritical, creating electron-positron (e^+e^-) pair plasma which self-accelerates to ultrarelativistic velocities and whose transparency explains to the GRB prompt emission in Gamma-rays. The electric field is also able to accelerate protons which along the rotation axis lead to ultra high-energy cosmic rays (UHECRs) of up to 10^{21} eV. In the other directions the acceleration process lead to proton-synchrotron radiation which explains the GeV emission [84,85]. The interaction/feedback of the GRB into the SN makes it become the hypernova (HN) [89,90] observed in the optical, powered by nickel decay, a few days after the GRB trigger. The SN shock breakout and the hypercritical accretion can be observed as X-ray precursors [52]. The e^+e^- feedback onto the SN ejecta also produces gamma- and X-ray flares observed in the early afterglow [40]. The synchrotron emission by relativistic electrons from the νNS in the expanding magnetized HN ejecta and the νNS pulsar emission explain the early and late X-ray afterglow [91].

The article is organized as follows. In Section 2 we summarized following a chronological order the (1D, 2D and 3D) numerical simulations of BdHNe up to the year 2016, mentioning their salient features. A detailed explanation of the main ingredients of the calculations (equations of motion, accretion modeling, NS evolution equations, critical mass, accretion-zone hydrodynamics, neutrino emission and accretion energy release) can be found in Section 3. The most recent 3D smoothed-particle-hydrodynamics (SPH) numerical simulations of 2018 are presented in Section 4.

Section 5 is devoted to the consequences on these simulations on the analysis and interpretation of the GRB multiwavelength data. In Section 6 we present an analysis of the binary gravitational binding of BdHNe progenitors, so it is shown that most BdHNe type I are expected to be NS-BH binaries. The cosmological evolutionary scenario leading to the formation of BdHN, their occurrence rate and connection with short GRBs is presented in Section 7.

We show in Table 2 a summary of acronyms used in this work.

Table 2. Acronyms used in this work in alphabetical order.

Extended Wording	Acronym
Binary-driven hypernova	BdHN
Black hole	BH
Carbon-oxygen core	$\mathrm{CO_{core}}$
Gamma-ray burst	GRB
Gamma-ray flash	GRF
Induced gravitational collapse	IGC
Massive neutron star	MNS
Neutron star	NS
New neutron star created in the SN explosion	νNS
Short Gamma-ray burst	S-GRB
Short Gamma-ray flash	S-GRF
Supernova	SN
Ultrashort Gamma-ray burst	U-GRB
Ultra high-energy cosmic ray	UHECR
White dwarf	WD
X-ray flash	XRF

2. A Chronological Summary of the IGC Simulations: 2012–2016

2.1. First Analytic Estimates

The IGC scenario was formulated in 2012 [81] presenting a comprehensive astrophysical picture supporting this idea as well as a possible evolutionary scenario leading to the progenitor $\mathrm{CO_{core}}$-NS binaries. It was also there presented an analytic formula for the accretion rate onto the NS companion on the basis of the following simplified assumptions: (1) a uniform density profile of the pre-SN $\mathrm{CO_{core}}$; (2) the ejecta was evolved following an homologous expansion; (3) the mass of the NS (assumed to be initially 1.4 $M_\odot$) and the $\mathrm{CO_{core}}$ (in the range 4–8 $M_\odot$) were assumed nearly constant. So, it was shown that the accretion rate onto the NS is highly super-Eddington, namely it is hypercritical, reaching values of up to 0.1 $M_\odot$ s^{-1} for compact binaries with orbital periods of the order of a few minutes. This estimate implied that the hypercritical accretion could induce the gravitational collapse of the NS which, in a few seconds, would reach the critical mass with consequence formation of a BH. A first test of this IGC first model in real data was soon presented in the case of GRB 090618 [82].

2.2. First Numerical Simulations: 1D Approximation

The first numerical simulations were implemented in 2014 in [83] via a 1D code including (see Figure 3): (1) the modeling of the SN via the 1D core-collapse SN code of Los Alamos [92]; (2) the microphysics experienced by the inflow within the accretion region including the neutrino (ν) emission and hydrodynamics processes such as shock formation; (3) with the above it was followed by the evolution of the material reaching the Bondi-Hoyle capture region and the subsequent in-fall up to the NS surface. Hypercritical accretion rates in the range 10^{-3}–10^{-1} $M_\odot$ s^{-1} were inferred, confirming the first analytic estimates and the IGC of the NS companion for binary component masses similar to the previous ones and for orbital periods of the order of 5 min.

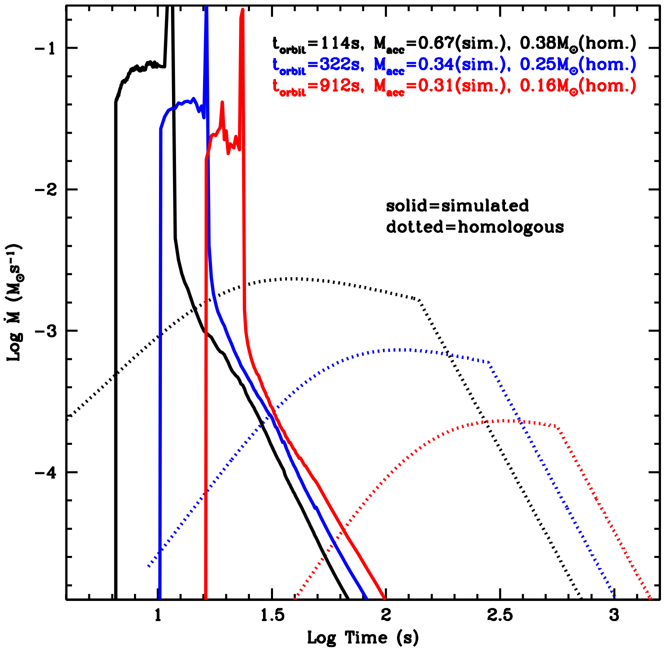

Figure 3. Hypercritical accretion rate onto the NS companion for selected separation distances. The CO_{core} is obtained with a progenitor star of zero-age main-sequence (ZAMS) mass of 20 $M_\odot$, calculated in [83]. The numerical calculation leads to a sharper accretion profile with respect to the one obtained assuming homologous expansion of the SN ejecta. Taken from Figure 3 in [83].

The above simulations were relevant in determining that the fate of the system is mainly determined by the binary period (P); the SN ejecta velocity (v_{ej}) and the NS initial mass. P and v_{ej} enter explicitly in the Bondi-Hoyle accretion rate formula through the capture radius expression, and implicitly via the ejecta density since they influence the decompression state of the SN material at the NS position.

2.3. 2D Simulations including Angular Momentum Transfer

Soon after, in 2015, we implemented in [53] a series of improvements to the above calculations by relaxing some of the aforementioned assumptions (see Figure 4). We adopted for the ejecta a density profile following a power-law with the radial distance and evolved it with an homologous expansion. The angular momentum transport, not included in the previous estimates, was included. With this addition it was possible to estimate the spin-up of the NS companion by the transfer of angular momentum from the in-falling matter which was shown to circularize around the NS before being accreted. General relativistic effects were also introduced, when calculating the evolution of the structure parameters (mass, radius, spin, etc) of the accreting NS, in the NS gravitational binding energy, and in the angular momentum transfer by the circularized particles being accreted from the innermost circular orbit.

One of the most important results of [53] was that, taking into account that the longer the orbital P the lower the accretion rate, it was there computed the maximum orbital period (P_{max}) for which the NS reaches the critical mass for gravitational collapse, so for BH formation. The dependence of P_{max} on the initial mass of the NS was also there explored. The orbital period P_{max} was then presented as the separatrix of two families of long GRBs associated with these binaries: at the time we called them *Family-1*, the systems in which the NS does not reach the critical mass, and *Family-2* the ones in which it reaches the critical mass and forms a BH. It can be seen that the Family-1 and Family-2 long GRBs evolve subsequently into the concepts of *XRFs* and *BdHNe*, respectively.

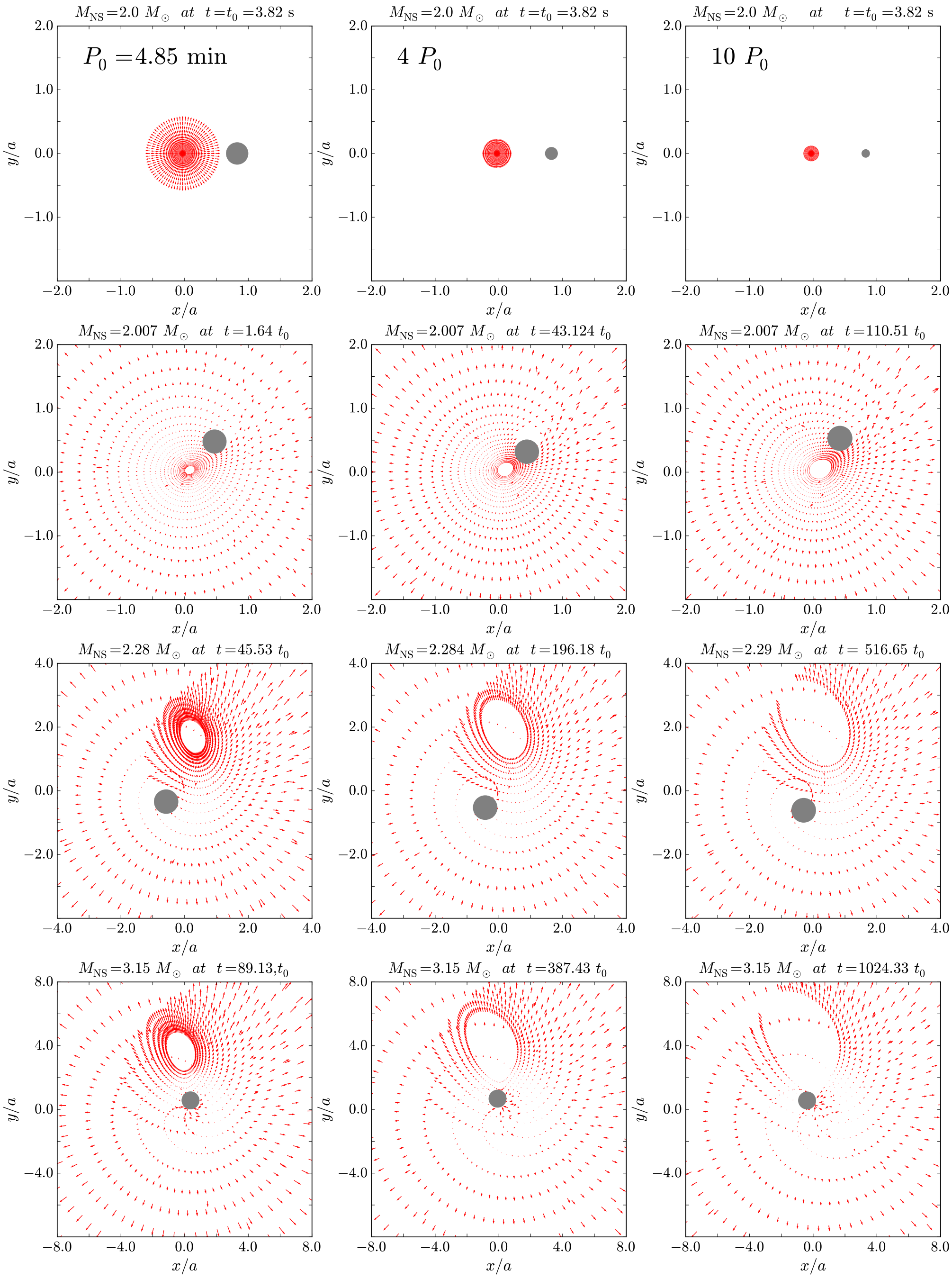

Figure 4. Numerical simulations of the SN ejecta velocity field (red arrows) at selected times of the accretion process onto the NS (taken from Figure 3 in [53]). In these snapshots we have adopted the CO_{core} obtained from a $M_{ZAMS} = 30\,M_\odot$ progenitor; an ejecta outermost layer velocity $v_{0_{star}} = 2 \times 10^9$ cm s^{-1}, an initial NS mass, $M_{NS}(t = t_0) = 2.0\,M_\odot$. The minimum orbital period to have no Roche-lobe overflow is $P_0 = 4.85$ min. In the left, central and right columns of snapshots we show the results for binary periods $P = P_0$, $4P_0$, and $10P_0$, respectively. The Bondi-Hoyle surface, the filled gray circle, increases as the evolution continues mainly due to the increase of the NS mass (the decrease of the lower panels is only apparent due to the enlargement of the x-y scales). The x-y positions refer to the center-of-mass reference frame. The last image in each column corresponds to the instant when the NS reaches the critical mass value. For the initial conditions of these simulations, the NS ends its evolution at the mass-shedding limit with a maximum value of the angular momentum $J = 6.14 \times 10^{49}$ g cm^2 s^{-1} and a corresponding critical mass of $3.15\,M_\odot$.

2.4. First 3D Simulations

A great step toward the most recent simulations was achieved in 2016 in [52] where an SPH-like simulation was implemented in which the SN ejecta was emulated by "point-like" particles. The mass and number of the particles populating each layer were assigned, for self-consistency, according to the power-law density profile. The initial velocity of the particles of each layer was set, in agreement with the chosen power-law density profile, following a radial velocity distribution; i.e., $v \propto r$.

The evolution of the SN particles was followed by Newtonian equations of motion in the gravitational field of the NS companion, also taking into account the orbital motion which was included under the assumption that the NS performs a circular orbit around the $\mathrm{CO_{core}}$ center that acts as the common center-of-mass, namely assuming that the mass of the pre-SN core is much larger than the NS mass.

The accretion rate onto the NS was computed, as in [53], using the Bondi-Hoyle accretion formula and, every particle reaching the Bondi-Hoyle surface, was removed from the system. The maximum orbital period $P_{\rm max}$ in which the NS collapses by accretion could be further explored including the dependence on the mass of the pre-SN $\mathrm{CO_{core}}$, in addition to the dependence on the NS mass.

A detailed study of the hydrodynamics and the neutrino emission in the accretion region on top the NS surface was performed. Concerning the neutrino emission, several ν and antineutrino ($\bar{\nu}$) production processes were considered and showed that electron-positron annihilation ($e^+e^- \to \nu\bar{\nu}$) overcomes by orders of magnitude any other mechanism of neutrino emission in the range of accretion rates 10^{-8}–10^{-2} $M_\odot$ s^{-1}, relevant for XRFs and BdHNe. The neutrino luminosity can reach values of up to 10^{52} erg s^{-1} and the neutrino mean energy of 20 MeV for the above upper value of the accretion rate. For the reader interested in the neutrino emission, we refer to [93] for a detailed analysis of the neutrino production in XRFs and BdHNe including flavor oscillations experienced by the neutrinos before abandoning the system.

Concerning the hydrodynamics, the evolution of the temperature and density of outflows occurring during the accretion process owing to convective instabilities was estimated. It was there shown the interesting result that the temperature of this outflow and its evolution can explain the early (i.e., precursors) X-ray emission that has been observed in some BdHNe and in XRFs, exemplified there analyzing the early X-ray emission observed in GRB 090618, a BdHN I, and in GRB 060218, a BdHN II (an XRF).

A most important result of these simulations was the possibility of having a first glance of the morphology acquired by the SN ejecta: the matter density, initially spherically symmetric, becomes highly asymmetric due to the accretion process and the action of the gravitational field of the NS companion (see Figure 5).

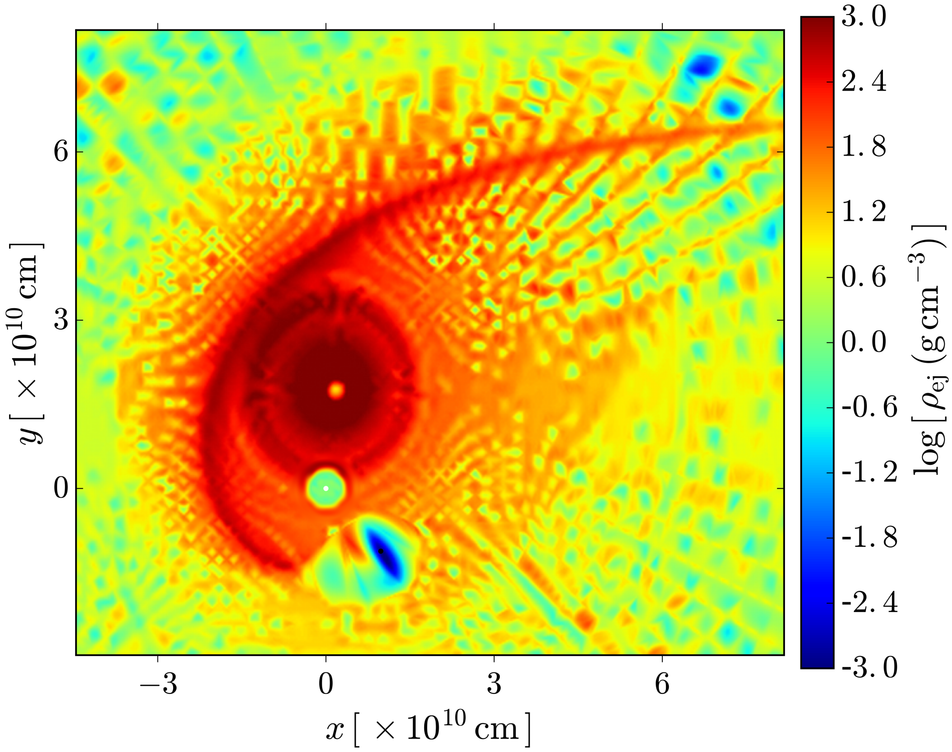

Figure 5. Snapshot of the SN ejecta density in the orbital plane of the CO_{core}-NS binary. Numerical simulation taken from Figure 6 in [52]. The plot corresponds to the instant when the NS reaches the critical mass and forms the BH (black dot), approximately 250 s from the SN explosion. The νNS is represented by the white dot. The binary parameters are: the initial mass of the NS companion is 2.0 $M_\odot$; the CO_{core} leading to an ejecta mass of 7.94 $M_\odot$, and the orbital period is $P \approx 5$ min, namely a binary separation $a \approx 1.5 \times 10^{10}$ cm.

3. The Hypercritical Accretion Process

We now give details of the accretion process within the IGC scenario following [52,53,55,83]. There are two main physical conditions for which hypercritical (i.e., highly super-Eddington) accretion onto the NS occurs in XRFs and BdHNe. The first is that the photons are trapped within the inflowing material and the second is that the shocked atmosphere on top of the NS becomes sufficiently hot ($T \sim 10^{10}$ K) and dense ($\rho \gtrsim 10^6$ g cm^{-3}) to produce a very efficient neutrino-antineutrino ($\nu\bar{\nu}$) cooling emission. In this way the neutrinos become mainly responsible for releasing the energy gained by accretion, allowing hypercritical accretion to continue.

3.1. Accretion Rate and NS Evolution

The first numerical simulations of the IGC were performed in [83], including: (1) realistic SN explosions of the CO_{core}; (2) the hydrodynamics within the accretion region; (3) the simulated evolution of the SN ejecta up to their accretion onto the NS. Becerra et al. [53] then estimated the amount of angular momentum carried by the SN ejecta and how much is transferred to the NS companion by accretion. They showed that the SN ejecta can circularize for a short time and form a disc-like structure surrounding the NS before being accreted. The evolution of the NS central density and rotation angular velocity (the NS is spun up by accretion) was computed from full numerical solutions of the axisymmetric Einstein equations. The unstable limits of the NS are set by the mass-shedding (or Keplerian) limit and the critical point of gravitational collapse given by the secular axisymmetric instability, (see, e.g., [53] for details).

The accretion rate of the SN ejecta onto the NS is given by:

$$\dot{M}_B(t) \;=\; \pi\rho_{\rm ej}R_{\rm cap}^2\sqrt{v_{\rm rel}^2+c_{\rm s,ej}^2}, \qquad R_{\rm cap}(t) \;=\; \frac{2GM_{\rm NS}(t)}{v_{\rm rel}^2+c_{\rm s,ej}^2}, \tag{1}$$

where G is the gravitational constant, $\rho_{\rm ej}$ and $c_{\rm s,ej}$ are the density and sound speed of the ejecta, $R_{\rm cap}$ and $M_{\rm NS}$ are the NS gravitational capture radius (Bondi-Hoyle radius) and gravitational mass, and $v_{\rm rel}$ the ejecta velocity relative to the NS: $\vec{v}_{\rm rel}=\vec{v}_{\rm orb}-\vec{v}_{\rm ej}$; $|\vec{v}_{\rm orb}|=\sqrt{G(M_{\rm core}+M_{\rm NS})/a}$, and $\vec{v}_{\rm ej}$ is the velocity of the supernova ejecta (see Figure 2).

Numerical simulations of the SN explosions suggest the adopted homologous expansion of the SN, i.e., $v_{\rm ej}(r,t)=nr/t$, where r is the position of each layer from the SN center and n is the expansion parameter. The density evolves as

$$\rho_{\rm ej}(r,t)=\rho_{\rm ej}^0(r/R_{\rm star}(t),t_0)\frac{M_{\rm env}(t)}{M_{\rm env}(0)}\left(\frac{R_{\rm star}(0)}{R_{\rm star}(t)}\right)^3, \tag{2}$$

where $M_{\rm env}(t)$ the mass of the CO$_{\rm core}$ envelope, $R_{\rm star}(t)$ is the radius of the outermost layer, and $\rho_{\rm ej}^0$ is the pre-SN CO$_{\rm core}$ density profile; $\rho_{\rm ej}(r,t_0)=\rho_{\rm core}(R_{\rm core}/r)^m$, where $\rho_{\rm core}$, $R_{\rm core}$ and m are the profile parameters obtained from numerical simulations. Typical parameters of the CO$_{\rm core}$ mass are (3.5–9.5) $M_\odot$ corresponding to (15–30) $M_\odot$ zero-age-main-sequence (ZAMS) progenitors (see [53,83] for details). The binary period is limited from below by the request of having no Roche lobe overflow by the CO$_{\rm core}$ before the SN explosion [83]. For instance, for a CO$_{\rm core}$ of 9.5 $M_\odot$ forming a binary system with a 2 $M_\odot$ NS, the minimum orbital period allowed by this condition is $P_{\rm min}\approx 5$ min. For these typical binary and pre-SN parameters, Equation (1) gives accretion rates 10^{-4}–$10^{-2}M_\odot$ s^{-1}.

We adopt an initially non-rotating NS companion so its exterior spacetime at time $t=0$ is described by the Schwarzschild metric. The SN ejecta approach the NS with specific angular momentum, $l_{\rm acc}=\dot{L}_{\rm cap}/\dot{M}_B$, circularizing at a radius $r_{\rm circ}\geq r_{\rm lco}$ if $l_{\rm acc}\geq l_{\rm lso}$ with $r_{\rm lco}$ the radius of the last circular orbit (LCO). For a non-rotating NS $r_{\rm lco}=6GM_{\rm NS}/c^2$ and $l_{\rm lco}=2\sqrt{3}GM_{\rm NS}/c$. For typical parameters, $r_{\rm circ}/r_{\rm lco}\sim 10$–$10^3$.

The accretion onto the NS proceeds from the radius $r_{\rm in}$. The NS mass and angular angular momentum evolve as [53,94]:

$$\dot{M}_{\rm NS}=\left(\frac{\partial M_{\rm NS}}{\partial M_b}\right)_{J_{\rm NS}}\dot{M}_b+\left(\frac{\partial M_{\rm NS}}{\partial J_{\rm NS}}\right)_{M_b}\dot{J}_{\rm NS}, \qquad \dot{J}_{\rm NS}=\xi\, l(r_{\rm in})\dot{M}_{\rm B}, \tag{3}$$

where M_b is the NS baryonic mass, $l(r_{\rm in})$ is the specific angular momentum of the accreted material at $r_{\rm in}$, which corresponds to the angular momentum of the LCO, and $\xi\leq 1$ is a parameter that measures the efficiency of angular momentum transfer. In this picture we have $\dot{M}_b=\dot{M}_B$.

For the integration of Equations (1) and (3) we have to supply the values of the two partial derivatives in Equation (3). They are obtained from the relation of the NS gravitational mass, $M_{\rm NS}$, with M_b and $J_{\rm NS}$, namely from the knowledge of the NS binding energy. For this we use the general relativistic calculations of rotating NSs presented in [95]. They show that, independent on the nuclear EOS, the following analytical formula represents the numerical results with sufficient accuracy (error $<2\%$):

$$\frac{M_b}{M_\odot}=\frac{M_{\rm NS}}{M_\odot}+\frac{13}{200}\left(\frac{M_{\rm NS}}{M_\odot}\right)^2\left(1-\frac{1}{137}j_{\rm NS}^{1.7}\right), \tag{4}$$

where $j_{\rm NS}\equiv cJ_{\rm NS}/(GM_\odot^2)$.

In the accretion process, the NS gains angular momentum and therefore spins up. To evaluate the amount of angular momentum transferred to the NS at any time we include the dependence of the

LCO specific angular momentum as a function of $M_{\rm NS}$ and $J_{\rm NS}$. For corotating orbits, the following relation is valid for the NL3, TM1 and GM1 EOS [53,94]:

$$l_{\rm lco} = \frac{GM_{\rm NS}}{c}\left[2\sqrt{3} - 0.37\left(\frac{j_{\rm NS}}{M_{\rm NS}/M_\odot}\right)^{0.85}\right]. \tag{5}$$

The NS continues the accretion until it reaches an instability limit or up to when all the SN ejecta overcomes the NS Bondi-Hoyle region. We take into account the two main instability limits for rotating NSs: the mass-shedding or Keplerian limit and the secular axisymmetric instability limit. The latter defines critical NS mass. For the aforementioned nuclear EOS, the critical mass can be approximately written as [95]:

$$M_{\rm NS}^{\rm crit} = M_{\rm NS}^{J=0}(1 + kj_{\rm NS}^p), \tag{6}$$

where k and p are EOS-dependent parameters (see Table 3). These formulas fit the numerical results with a maximum error of 0.45%.

Table 3. Critical NS mass in the non-rotating case and constants k and p needed to compute the NS critical mass in the non-rotating case given by Equation (6). The values are for the NL3, GM1 and TM1 EOS.

EOS	$M_{\rm crit}^{J=0}$ $(M_\odot)$	p	k
NL3	2.81	1.68	0.006
GM1	2.39	1.69	0.011
TM1	2.20	1.61	0.017

Additional details and improvements of the hypercritical accretion process leading to XRFs and BdHNe were presented in [52]. Specifically:

1. The density profile included finite size/thickness effects and additional $\rm CO_{core}$ progenitors, leading to different SN ejecta masses being considered.
2. In [53] the maximum orbital period, $P_{\rm max}$, over which the accretion onto NS companion is not sufficient to bring it to the critical mass, was inferred. Thus, binaries with $P > P_{\rm max}$ lead to XRFs while the ones with $P \lesssim P_{\rm max}$ lead to BdHNe. Becerra et al. [52] extended the determination of $P_{\rm max}$ for all the possible initial values of the NS mass. They also examined the outcomes for different values of the angular momentum transfer efficiency parameter.
3. The expected luminosity during the process of hypercritical accretion for a wide range of binary periods covering both XRFs and BdHNe was estimated.
4. It was shown that the presence of the NS companion originates asymmetries in the SN ejecta (see, e.g., Figure 6 in [52]). The signatures of such asymmetries in the X-ray emission was there shown in the specific example of XRF 060218.

3.2. Hydrodynamics in the Accretion Region

The accretion rate onto the NS can be as high as $\sim 10^{-2}$–10^{-1} $M_\odot$ s^{-1}. For such accretion rates:

1. The magnetic pressure is much smaller than the random pressure of the infalling material, therefore the magnetic-field effects on the accretion process are negligible [81,96].
2. The photons are trapped within the infalling matter, hence the Eddington limit does not apply and hypercritical accretion occurs. The trapping radius is defined as [97]: $r_{\rm trapping} = \min\{\dot{M}_B\kappa/(4\pi c), R_{\rm cap}\}$, where κ is the opacity. [83] estimated a Rosseland mean opacity of $\approx 5 \times 10^3$ cm^2 g^{-1} for the $\rm CO_{cores}$. This, together with our typical accretion rates, lead to $\dot{M}_B\kappa/(4\pi c) \sim 10^{13}$–$10^{19}$ cm. This radius is much bigger than the Bondi-Hoyle radius.

3. The above condition, and the temperature-density values reached on top of the NS surface, lead to an efficient neutrino cooling which radiates away the gain of gravitational energy of the infalling material [81,83,96,98,99].

The accretion shock moves outward as the material piles onto the NS. Since the post-shock entropy is inversely proportional to the shock radius position, the NS atmosphere is unstable with respect to Rayleigh-Taylor convection at the beginning of the accretion process. Such instabilities might drive high-velocity outflows from the accreting NS [100,101]. The entropy at the base of the atmosphere is [96]:

$$S_{\rm bubble} \approx 16 \left(\frac{1.4\,M_\odot}{M_{\rm NS}}\right)^{-7/8} \left(\frac{M_\odot\,{\rm s}^{-1}}{\dot{M}_{\rm B}}\right)^{1/4} \left(\frac{10^6\,{\rm cm}}{r}\right)^{3/8} k_B/{\rm nucleon}, \tag{7}$$

where k_B is the Boltzmann constant. The material expands and cools down adiabatically, i.e., T^3/ρ = constant. In the case of a spherically symmetric expansion, $\rho \propto 1/r^3$ and $k_B T_{\rm bubble} = 195\, S_{\rm bubble}^{-1}\,(10^6\,{\rm cm}/r)$ MeV. In the more likely case that the material expand laterally we have [101]: $\rho \propto 1/r^2$, i.e., $T_{\rm bubble} = T_0(S_{\rm bubble})\,(r_0/r)^{2/3}$, where $T_0(S_{\rm bubble})$ is obtained from the above equation at $r = r_0 \approx R_{\rm NS}$. This implies a bolometric blackbody flux at the source from the rising bubbles:

$$F_{\rm bubble} \approx 2\times 10^{40} \left(\frac{M_{\rm NS}}{1.4\,M_\odot}\right)^{-7/2} \left(\frac{\dot{M}_{\rm B}}{M_\odot\,{\rm s}^{-1}}\right) \left(\frac{R_{\rm NS}}{10^6\,{\rm cm}}\right)^{3/2} \left(\frac{r_0}{r}\right)^{8/3} {\rm erg\,s^{-1}cm^{-2}}. \tag{8}$$

The above thermal emission has been shown [83] to be a plausible explanation of the early X-ray (precursor) emission observed in some GRBs. The X-ray precursor observed in GRB 090618 [35,82] is explained adopting an accretion rate of $10^{-2}\,M_\odot$ s^{-1}, the bubble temperature drops from 50 keV to 15 keV while expanding from $r \approx 10^9$ cm to 6×10^9 cm (see Figure 6). More recently, the X-ray precursor has been observed in GRB 180728A and it is well explained by a bubble of ∼7 keV at $\sim 10^{10}$ cm and an accretion rate of $10^{-3}\,M_\odot$ s^{-1} (see [49] for details).

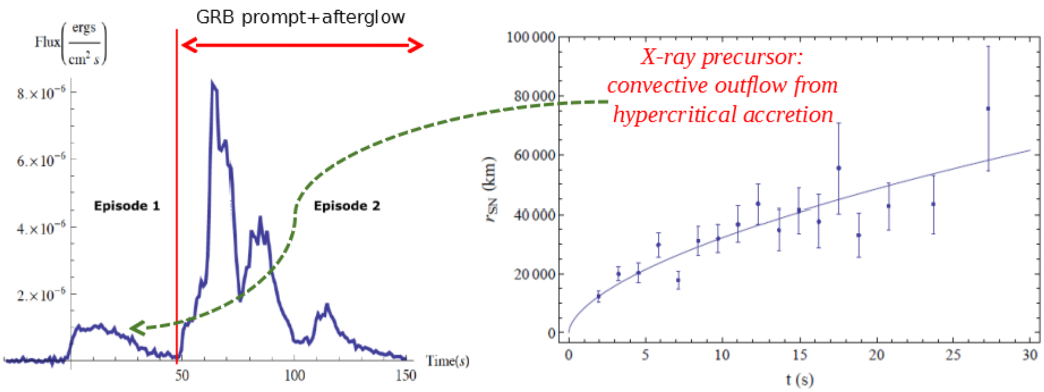

Figure 6. (**a**) Fermi-GBM (NaI 8–440 keV) light-curve of GRB 090618 (adapted from Figure 1 in [35]). (**b**) Expanding radius of the thermal blackbody emission observed in the "Episode 1" of GRB 090618 (adapted from Figure 2 in [35]). The interpretation of such an X-ray precursor as being due to the emission of the convective bubbles during the process of hypercritical accretion onto the NS was proposed for the first time in [83].

3.3. Neutrino Emission and Effective Accretion Rate

For the accretion rate conditions characteristic of our models at peak $\sim 10^{-4}$–$10^{-2}\,M_\odot$ s^{-1}, pair annihilation dominates the neutrino emission and electron neutrinos remove the bulk of the energy [52]. The e^+e^- pairs producing the neutrinos are thermalized at the matter temperature. This temperature is approximately given by:

$$T_{\rm acc} \approx \left(\frac{3P_{\rm shock}}{4\sigma/c}\right)^{1/4} = \left(\frac{7}{8}\frac{\dot{M}_{\rm acc}v_{\rm acc}c}{4\pi R_{\rm NS}^2\sigma}\right)^{1/4}, \tag{9}$$

where $P_{\rm shock}$ is the pressure of the shock developed on the accretion zone above the NS surface, $\dot{M}_{\rm acc}$ is the accretion rate, $v_{\rm acc}$ is the velocity of the infalling material, σ is the Stefan-Boltzmann constant and c the speed of light. It can be checked that, for the accretion rates of interest, the system develops temperatures and densities $T \gtrsim 10^{10}$ K and $\rho \gtrsim 10^6$ g cm^{-3}; respectively (see Figure 7).

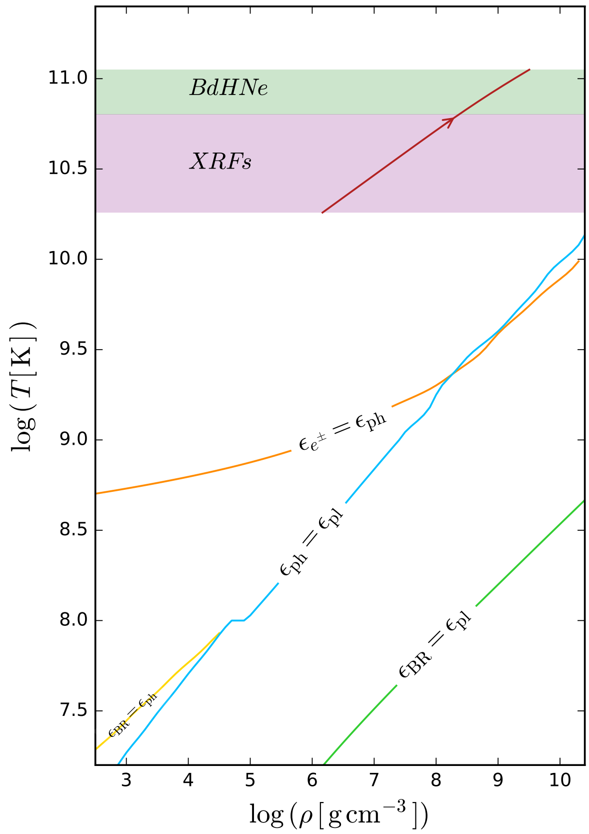

Figure 7. Temperature-density reached by the accreting atmosphere (taken from Figure 16 in [52]). The contours indicate where the emissivity of the different neutrinos processes becomes quantitatively equal to each other. We considered the following processes: pair annihilation ($\epsilon_{e^\pm}$), photo-neutrino emission (ϵ_γ), plasmon decay ($\epsilon_{\rm pl}$) and Bremsstralung emission ($\epsilon_{\rm BR}$). The solid red curve spans $T - rho$ values corresponding to accretion rates from 10^{-8} to 10^{-1} $M_\odot$ s^{-1} from the lower to the upper end. For any accretion rate of interest, the electron-positron pair annihilation dominates the neutrino emission.

Under these conditions of density and temperature the neutrino emissivity of the e^+e^- annihilation process can be estimated by the simple formula [102]:

$$\epsilon_{e^-e^+} \approx 8.69 \times 10^{30} \left(\frac{k_B T}{1\,{\rm MeV}}\right)^9 \;{\rm MeV\,cm^{-3}\,s^{-1}}, \tag{10}$$

where k_B is the Boltzmann constant.

The accretion zone is characterized by a temperature gradient with a typical scale height $\Delta r_{\rm ER} = T/\nabla T \approx 0.7\, R_{\rm NS}$. Owing to the aforementioned strong dependence of the neutrino emission on temperature, most of the neutrinos are emitted from a spherical shell around the NS of thickness

$$\Delta r_\nu = \frac{\epsilon_{e^-e^+}}{\nabla \epsilon_{e^-e^+}} = \frac{\Delta r_{\rm ER}}{9} \approx 0.08 R_{\rm NS}. \tag{11}$$

Equations (9) and (10) imply the neutrino emissivity satisfies $\epsilon_{e^-e^+} \propto \dot{M}_{\rm acc}^{9/4}$ as we had anticipated. These conditions lead to the neutrinos to be efficient in balancing the gravitational potential energy gain, allowing the hypercritical accretion rates. The effective accretion onto the NS can be estimated as:

$$\dot{M}_{\rm eff} \approx \Delta M_\nu \frac{L_\nu}{E_g}, \tag{12}$$

where ΔM_ν, L_ν are, respectively, the mass and neutrino luminosity in the emission region, and $E_g = (1/2)GM_{\rm NS}\Delta M_\nu/(R_\nu + \Delta r_\nu)$ is half the gravitational potential energy gained by the material falling from infinity to the $R_{\rm NS} + \Delta r_\nu$. The neutrino luminosity is

$$L_\nu \approx 4\pi R_{\rm NS}^2 \Delta r_\nu \epsilon_{e^-e^+}, \tag{13}$$

with $\epsilon_{e^-e^+}$ being the neutrino emissivity in Equation (10). For $M_{\rm NS} = 2\, M_\odot$ and temperatures 1–10 MeV, the Equations (12) and (13) result $\dot{M}_{\rm eff} \approx 10^{-10}$–$10^{-1}\, M_\odot\, {\rm s}^{-1}$ and $L_\nu \approx 10^{48}$–10^{57} MeV s^{-1}.

Therefore, the neutrino emission can reach luminosities of up to 10^{57} MeV s^{-1}, mean neutrino energies 20–30 MeV, and neutrino densities 10^{31} cm^{-3}. Along their path from the vicinity of the NS surface outward, such neutrinos experience flavor transformations dictated by the neutrino to electron density ratio. We have determined in [93] the neutrino and electron on the accretion zone and use them to compute the neutrino flavor evolution. For normal and inverted neutrino-mass hierarchies and within the two-flavor formalism ($\nu_e\nu_x$), we estimated the final electronic and non-electronic neutrino content after two oscillation processes: (1) neutrino collective effects due to neutrino self-interactions where the neutrino density dominates and, (2) the Mikheyev-Smirnov-Wolfenstein (MSW) effect, where the electron density dominates. We find that the final neutrino content is composed by $\sim$55% ($\sim$62%) of electronic neutrinos, i.e., $\nu_e + \bar{\nu}_e$, for the normal (inverted) neutrino-mass hierarchy (see Figure 8). This is a first step toward the characterization of a novel source of astrophysical MeV-neutrinos in addition to core-collapse SNe. We refer the reader to [93] for additional details of the flavor-oscillations as well as the final neutrino spectra after such a process.

3.4. Accretion Luminosity

The energy release in a time-interval dt, when an amount of mass dM_b with angular momentum $l\dot{M}_b$ is accreted, is [52]:

$$L_{\rm acc} = (\dot{M}_b - \dot{M}_{\rm NS})c^2 = \dot{M}_b c^2 \left[1 - \left(\frac{\partial M_{\rm NS}}{\partial J_{\rm NS}}\right)_{M_b} l - \left(\frac{\partial M_{\rm NS}}{\partial M_b}\right)_{J_{\rm NS}}\right]. \tag{14}$$

This is the amount of gravitational energy gained by the matter by infalling to the NS surface that is not spent in NS gravitational binding energy. The total energy release in the time interval from t to $t + dt$,

$$\Delta E_{\rm acc} \equiv \int L_{\rm acc} dt, \tag{15}$$

is given by the NS binding energy difference between its initial and final state. The typical luminosity is $L_{\rm acc} \approx \Delta E_{\rm acc}/\Delta t_{\rm acc}$, where $\Delta t_{\rm acc}$ is the duration of the accretion process.

The value of $\Delta t_{\rm acc}$ is approximately given by the flow time of the slowest layers of the SN ejecta to the NS companion position. If we denote the velocity of these layers by $v_{\rm inner}$, we have $\Delta t_{\rm acc} \sim a/v_{\rm inner}$, where a is the binary separation. For $a \sim 10^{11}$ cm and $v_{\rm inner} \sim 10^8$ cm s^{-1}, $\Delta t_{\rm acc} \sim 10^3$ s. For shorter separations, e.g., $a \sim 10^{10}$ cm ($P \sim 5$ min), $\Delta t_{\rm acc} \sim 10^2$ s. For a binary with $P = 5$ min, the NS accretes $\approx 1\ M_\odot$ in $\Delta t_{\rm acc} \approx 100$ s. From Equation (4) one obtains that the binding energy difference of a 2 $M_\odot$ and a 3 $M_\odot$ NS, is $\Delta E_{\rm acc} \approx 13/200(3^2 - 2^2)\ M_\odot c^2 \approx 0.32\ M_\odot c^2$. This leads to $L_{\rm acc} \approx 3 \times 10^{-3}\ M_\odot c^2 \approx 0.1\ \dot{M}_b c^2$. The accretion power can be as high as $L_{\rm acc} \sim 0.1 \dot{M}_b c^2 \sim 10^{47}$–$10^{51}$ erg s^{-1} for accretion rates in the range $\dot{M}_b \sim 10^{-6}$–$10^{-2}\ M_\odot$ s^{-1}.

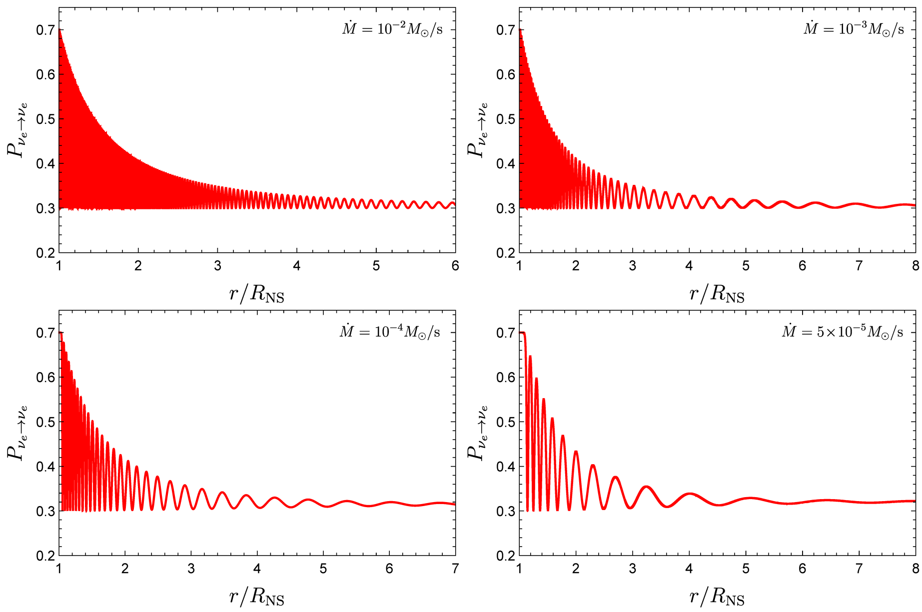

Figure 8. Neutrino flavor evolution in the case of the neutrino-mass inverted hierarchy (taken from Figure 4 in [93]). The electron-neutrino survival probability is shown as a function of the radial distance from the NS surface. The curves for the electron antineutrino overlap the ones for electron-neutrinos.

4. New 3D SPH Simulations

We have recently presented in [90] new, 3D hydrodynamic simulations of the IGC scenario by adapting the SPH code developed at Los Alamos, *SNSPH* [103], which has been tested and applied in a variety of astrophysical situations [104–107].

The time $t = 0$ of the simulation is set as the time at which the SN shock breaks out the CO$_{\rm core}$ external radius. We calculate the accretion rate both onto the NS companion and onto the νNS (via fallback), and calculate the evolution of other binary parameters such as the orbital separation, eccentricity, etc. Figure 9 shows an example of simulation for a binary system composed of a CO$_{\rm core}$ of mass $\approx 6.85\ M_\odot$, the end stage of a ZAMS progenitor star of $M_{\rm zams} = 25\ M_\odot$, and a 2 $M_\odot$ NS companion. The initial orbital period is ≈ 5 min.

The accretion rate onto both stars was estimated from the flux of SPH particles falling, per unit time, into the Bondi-Hoyle accretion region of the NS (see Figure 10). It is confirmed that the accretion onto the NS companion occurs from a disk-like structure formed by the particles that circularize before being accreted; see vortexes in the upper panel of Figure 9 and the disk structure is clearly seen in the lower panel.

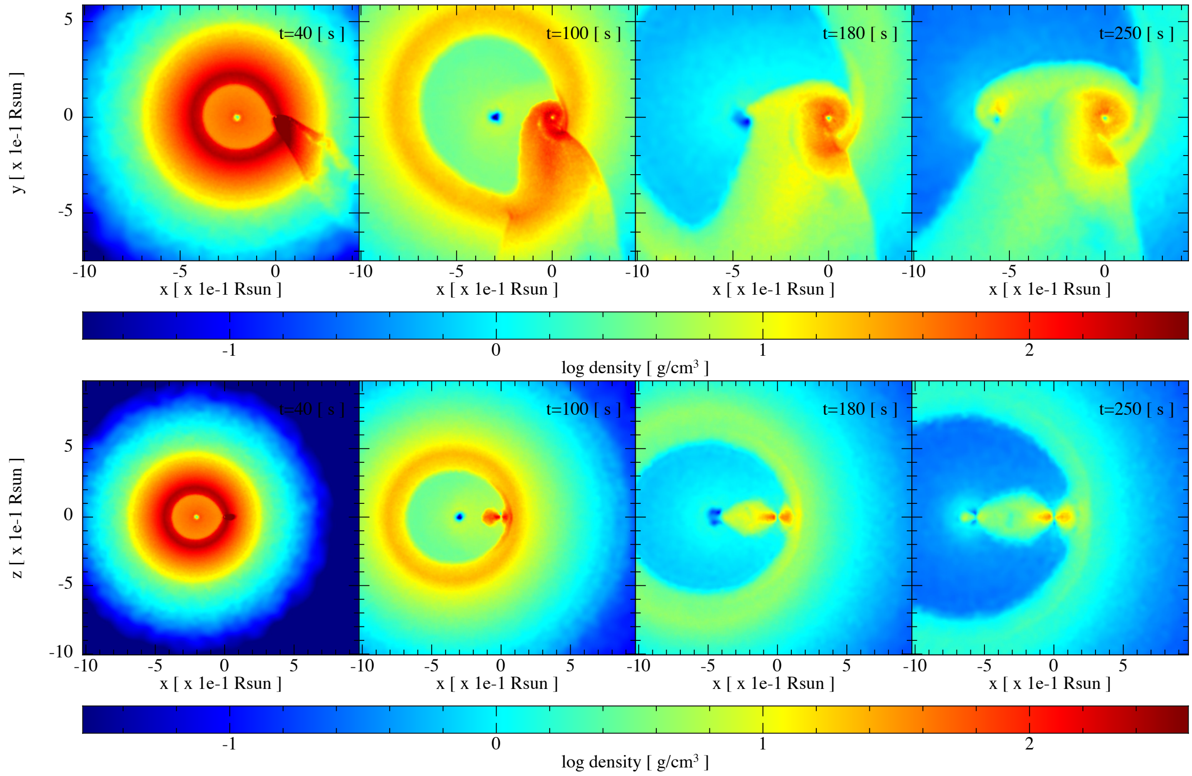

Figure 9. Snapshots of the 3D SPH simulations of the IGC scenario (taken from Figure 2 in [90]). The initial binary system is formed by a CO_{core} of mass $\approx 6.85\ M_{\odot}$, from a ZAMS progenitor star of 25 $M_{\odot}$, and a 2 $M_{\odot}$ NS with an initial orbital period of approximately 5 min. The upper panel shows the mass density on the equatorial (orbital) plane, at different times of the simulation. The time $t = 0$ is set in our simulations at the moment of the SN shock breakout. The lower panel shows the plane orthogonal to the orbital one. The reference system has been rotated and translated for the x-axis to be along the line joining the νNS and the NS centers, and its origin is at the NS position.

Several binary parameters were explored thanks to the new code. We performed simulations changing the CO_{core} mass, the NS companion mass, the orbital period, the SN explosion energy (so the SN kinetic energy or velocity). We also explored intrinsically asymmetric SN explosion. We checked if the νNS and/or the NS companion reach the mass-shedding (Keplerian) limit or the secular axisymmetric instability, i.e., the critical mass. The NS can also become just a more massive, fast rotating, stable NS when the accretion is moderate. All this was done for various NS nuclear equations of state (NL3, TM1 and GM1).

We followed the orbital evolution up to the instant when most of the ejecta has abandoned the system to determine if the system remains bound or becomes unbound by the explosion. We thus assessed the CO_{core}-NS parameters leading to the formation of νNS-NS (from XRFs) or νNS-BH (from BdHNe) binaries. The first proof that BdHNe remain bound leading to νNS-BH binaries was presented in [55] (see next section).

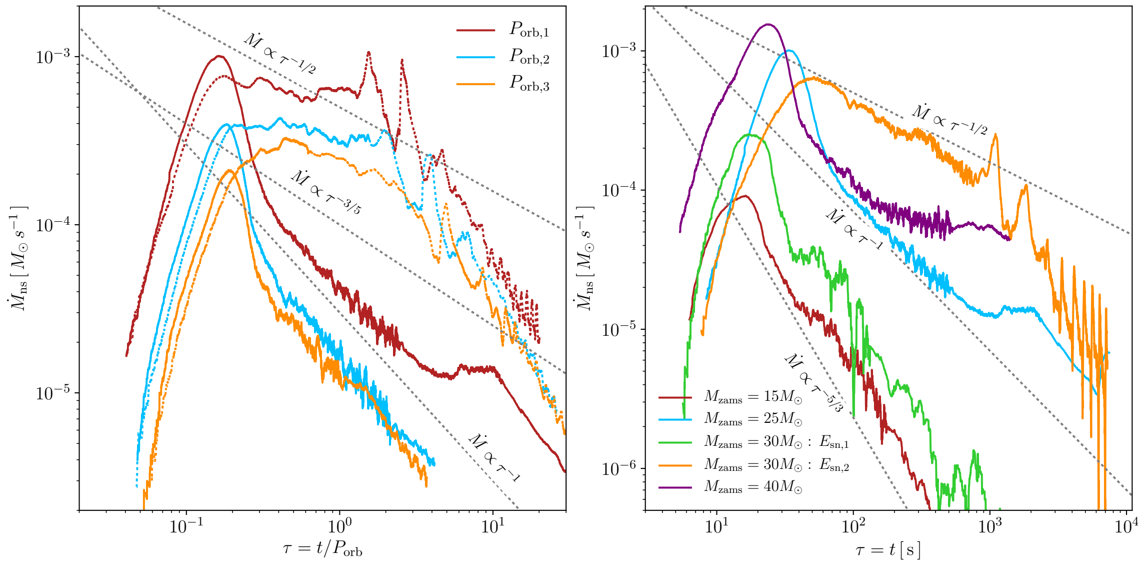

Figure 10. (**a**) Mass-accretion rate onto the NS companion in the IGC scenario (taken from Figure 9 in [90]). Different colors correspond to different initial orbital periods: $P_{\rm orb,1} = 4.8$ min (red line), $P_{\rm orb,1} = 8.1$ min (blue line), $P_{\rm orb,1} = 11.8$ min (orange line). The other parameters that characterize the initial binary system are the same as in Figure 9. The solid lines correspond to a SN energy of 1.57×10^{51} erg, while the dotted ones correspond to a lower SN energy of 6.5×10^{50} erg. It can be seen that the mass-accretion rate scales with the binary orbital period. (**b**) Mass-accretion rate on the NS companion for all the $\rm CO_{core}$ progenitors (see Table 1 and Figure 13 in [90]). The NS companion has an initial mass of $2\,M_\odot$ and the orbital period is close to the minimum period that the system can have in order that there is no Roche-lobe overflow before the collapse of the $\rm CO_{core}$: 6.5 min, 4.8 min, 6.0 min and 4.4 min for the $M_{\rm zams} = 15 M_\odot$, $25 M_\odot$, $30 M_\odot$ and $40 M_\odot$ progenitors, respectively.

5. Consequences on GRB Data Analysis and Interpretation

In a few seconds a BdHN shows different physical processes that lead to a specific sequence of observables at different times and at different wavelengths. Starting with the at-times-observed X-ray precursors, to the Gamma-ray prompt emission, to the GeV emission, to the early and late X-ray afterglow in which, respectively, are observed flares and a distinct power-law luminosity.

5.1. X-ray Precursor

X-ray precursors can comprise the presence of both the SN shock breakout as well as the hypercritical accretion onto the NS companion until it reaches the critical mass. These processes have been identified in [49,52,82,83].

The conversion of the SN shockwave kinetic energy (see [108] for details on the SN physics) into electromagnetic energy imply that about 10^{50} erg can be emitted.

Once it reached the NS companion, the ejecta induced a hypercritical accretion onto the NS at a rate $\sim 10^{-3} M_\odot\ \rm s^{-1}$ for an assumed orbital separation of few 10^{10} cm. As we have recalled (see Figure 6 in Section 3), the accretion process triggers the expansion of thermal convective bubbles on top of the NS owing to the Rayleigh-Taylor instability [49,52,82,83].

It is of special interest to refer the reader to the results presented in [49] on GRB 180728A, a BdHN II. It has been identified in the precursor of this GRB, for the first time, the presence of both the emergence of the SN shockwave as well as the hypercritical accretion process. From this the binary parameters have been extracted and further confirmed by the analysis of the prompt and the afterglow emission.

5.2. GRB Prompt Emission

A BdHN I leaves as a remnant a νNS-BH binary surrounded by the asymmetric SN ejecta (see Figure 5 and [52,90]). The asymmetric ejecta includes a "cavity" of $\sim 10^{11}$ cm of very low-density matter around the newborn BH. The hydrodynamics inside such a low-density cavity have been recently studied by numerical simulations in [87].

The asymmetric character acquired by the SN ejecta implies that the e^+e- plasma, expanding from the BH site in all directions with equal initial conditions, experiences a different dynamics along different directions. The reason for this is that the e^+e- plasma engulfs different amounts of baryonic mass (see Figure 11). This leads to observable signatures as a function of the viewing angle.

The newborn Kerr BH, surrounded by ejecta and immersed in a test magnetic field (likely the one left by the magnetized, collapsed NS), represents what we have called the *inner engine* of the high-energy emission [84–87]. The rotating BH, of mass M and angular momentum J, in the presence of the magnetic field B_0, induces an electromagnetic field described by the Wald solution [88].

The induced electric field at the BH horizon $r_+ = M(1+\sqrt{1-\alpha^2})$ is [84,85]

$$E_{r_+} \approx \frac{1}{2}\alpha B_0 = 6.5 \times 10^{15} \cdot \alpha \left(\frac{B_0}{B_c}\right) \frac{\mathrm{V}}{\mathrm{cm}}, \tag{16}$$

where $\alpha = J/M^2$ is the dimensionless angular momentum of the BH and $B_c = m_e^2 c^3/(e\hbar) \approx 4.4 \times 10^{13}$ G. This field acquires values over the critical one, $E_c = m_e^2 c^3/(e\hbar)$ if the following conditions are verified:

$$\alpha(B_0/B_c) \geq 2, \qquad B_0/B_c \geq 2, \tag{17}$$

where the second condition comes from the constraint that a rotating BH must satisfy: $\alpha \leq 1$. The above huge value of the electric field (16) guarantees the production of the e^+e^- pair plasma around the newborn BH via the quantum electrodynamics (QED) process of vacuum polarization [109].

In the direction pointing from the CO_{core} to the accreting NS outwards and lying on the orbital plane, the aforementioned cavity represents a region of low baryonic contamination [86,87]. The e^+e- plasma can then self-accelerate to Lorentz factors $\Gamma \sim 10^2$–10^3 reaching transparency and impacting on the CBM filaments as described in [37,110,111]. At transparency, MeV-photons are emitted which are observed in the ultrarelativistic prompt emission. This picture has been successfully applied and verified on plenty of GRBs, e.g., GRBs 050904, 080319B, 090227, 090618 and 101023 [35,69,112,113].

5.3. Early X-ray Afterglow: Flares

It was recently addressed in [40] the role of X-ray flares as a powerful tool to differentiate the BdHN model from the "collapsar-fireball" model [114].

First, it is known that the GRB prompt emission shows Gamma-ray spikes occurring at 10^{15}–10^{17} cm from the source and have Lorentz factor $\Gamma \sim 10^2$–10^3.

Second, the thermal emission observed in the X-ray flares of the early (rest-frame time $t \sim 10^2$ s) afterglow of BdHNe, implies occurrence radii $\sim 10^{12}$ cm expanding at mildly-relativistic velocity, e.g., $\Gamma \lesssim 4$ [40] (see below). The latter observational fact evidences that the X-ray afterglow is powered by a mildly-relativistic emitter. These model-independent observations contrast with the assumption of an ultrarelativistic expansion starting from the GRB prompt emission and extending to the afterglow. Such a "traditional" approach to GRBs has been adopted in a vast number of articles over decades as it is summarized in review articles (see, e.g., [20–25].

In the other directions, the GRB e^+e- plasma impacts the SN ejecta at approximately 10^{10} cm, evolves carrying a large amount of baryons reaching transparency at radii 10^{12} cm with a mildly $\Gamma \lesssim 4$. The theoretical description and the consequent numerical simulation have been addressed in [40].

Such a mildly-relativistic photospheric emission is experimentally demonstrated by the thermal radiation observed in the early X-ray afterglow and in the X-ray flares [115,116]. For instance, in the early hundreds of seconds, GRB 090618 is found to have a velocity of $\beta \sim 0.8$ [117,118], GRB 081008 has a velocity $\beta \sim 0.9$ [40], and GRB 130427A has a velocity of $\beta \sim 0.9$ as well [91,119,120]. We emphasize that the mildly-relativistic photo-sphere velocity is derived from the data in a model-independent way, summarising from [40]:

$$\frac{\beta^5}{4[\ln(1+\beta) - (1-\beta)\beta]^2}\left(\frac{1+\beta}{1-\beta}\right)^{1/2} = \frac{D_L(z)}{1+z}\frac{1}{t_2 - t_1}\left(\sqrt{\frac{F_{\rm bb,obs}(t_2)}{\sigma T^4_{\rm obs}(t_2)}} - \sqrt{\frac{F_{\rm bb,obs}(t_1)}{\sigma T^4_{\rm obs}(t_1)}}\right), \quad (18)$$

The left-hand side is a function of velocity β, the right-hand side is only from observables, $D_L(z)$ is the luminosity distance and z the cosmological redshift. From the observed thermal flux $F_{\rm bb,obs}$ and temperature $T_{\rm obs}$ in two times t_1 and t_2, the velocity β is obtained. This model-independent equation has been derived in a fully relativistic way so it remains valid in the Newtonian non-relativistic regime.

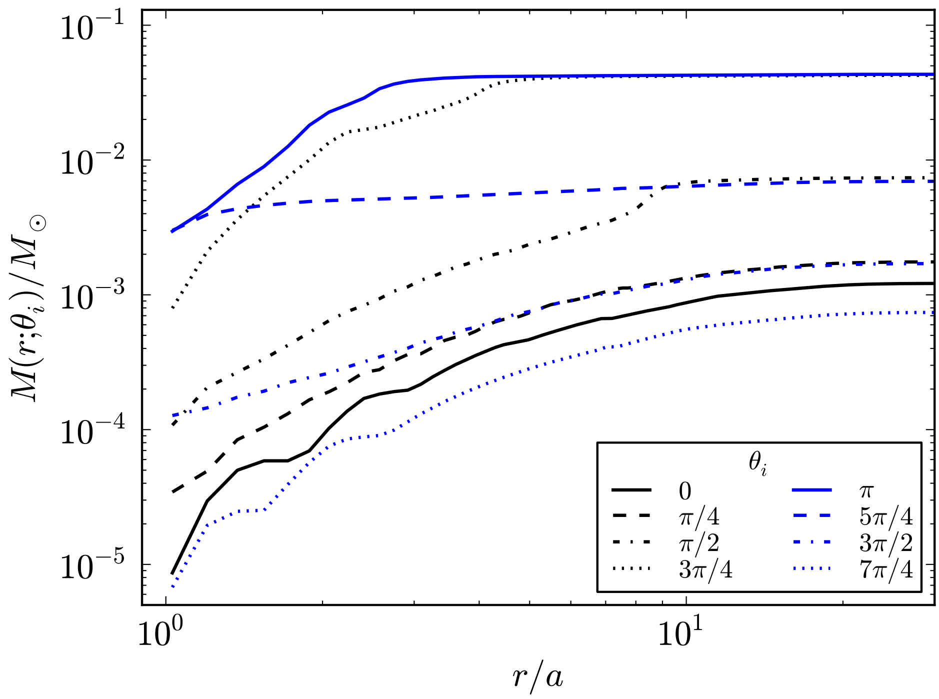

Figure 11. Cumulative radial mass profiles of the SN ejecta enclosed within a cone of 5° of semi-aperture angle with vertex at the BH position (taken from Figure 35 in [40]). These profiles have been extracted from the simulations at the time of BH formation. The binary parameters are: the initial mass of the NS companion is 2.0 $M_\odot$; the $\mathrm{CO_{core}}$ leading to an ejecta mass of 7.94 $M_\odot$, and the orbital period is $P \approx 5$ min, namely a binary separation $a \approx 1.5 \times 10^{10}$ cm.

An additional, and very important prediction of this scenario, is that the injection of energy and momentum from the GRB plasma into the ejecta transforms the SN into an HN (see [89] for the specific case of GRB 151027A).

5.4. Late X-ray Afterglow

We have shown in Ruffini *et al.* [91] that the synchrotron emission by relativistic electrons from the νNS, injected into the expanding magnetized HN ejecta, together with the νNS pulsar emission that extracts its rotational energy, power the X-ray afterglow. This includes the early part and the late power-law behavior. An exceptional by-product of this analysis is that it gives a glimpse on the νNS magnetic field strength and structure (dipole+quadrupole).

Based on the above model [91], GRB 130427A (a BdHN I) and GRB 180728A (a BdHN II) have been analyzed in [49]. The explanation of the afterglow data of GRB 130427A led to an initial 1 ms rotation period for the νNS. For GRB 180728A, a slower spin of 2.5 ms was there obtained. A simple analysis showed how this result is in agreement with the BdHN I and II nature of these GRBs. First, we recall that compact binary systems have likely synchronized components with the orbital period. Second, we can infer the orbital period from the analysis of the X-ray precursor and the prompt emission (see [49] for the procedure). Then, we can infer the CO_{core} rotation period too. Finally, assuming angular momentum conservation in the core-collapse SN process, we can estimate the rotation period of the νNS formed at the SN center. This method led to a binary separation remarkably in agreement with the one inferred from the precursor and the prompt emission, demonstrating the self-consistency of this scenario [49].

5.5. High-Energy GeV Emission

We turn back again to the already introduced *inner engine*. The joint action of rotation and magnetic field induces an electric potential [84,85]

$$\Delta\phi = -\int_{\infty}^{r_+} E dr = E_{r_+} r_+ = 9.7 \times 10^{20} \cdot \alpha \left(\frac{B_0}{B_c}\right)\left(\frac{M}{M_\odot}\right)(1+\sqrt{1-\alpha^2}) \quad \frac{\mathrm{V}}{e}, \tag{19}$$

capable to accelerate protons to ultrarelativistic velocities and energies up to $\epsilon_p = e\Delta\phi \approx 10^{21}$ eV.

Along the rotation axis, there are no radiation losses and so the *inner engine* leads to UHECRs. In the off-polar directions, the protons radiate synchrotron photons, e.g., at GeV and TeV energies.

In [84] it has been estimated that the available electrostatic energy to accelerate protons is

$$\mathcal{E} = \frac{1}{2} E_{r_+}^2 r_+^3 \approx 7.5 \times 10^{41} \cdot \alpha^2 \left(\frac{B_0}{B_c}\right)^2 \left(\frac{M}{M_\odot}\right)^3 (1+\sqrt{1-\alpha^2})^3 \quad \mathrm{erg}, \tag{20}$$

so the number of protons that the *inner engine* can accelerate is

$$N_p = \frac{\mathcal{E}}{\epsilon_p} \approx 4.8 \times 10^{32} \alpha \left(\frac{B_0}{B_c}\right)\left(\frac{M}{M_\odot}\right)^2 (1+\sqrt{1-\alpha^2})^2. \tag{21}$$

The timescale of the first elementary process is dictated by the acceleration time, i.e.,:

$$\Delta t_{\mathrm{el}} = \frac{\Delta\phi}{E_{r_+} c} = \frac{r_+}{c} \approx 4.9 \times 10^{-6} \left(\frac{M}{M_\odot}\right)(1+\sqrt{1-\alpha^2}) \quad \mathrm{s}. \tag{22}$$

so the emission power of the *inner engine* is approximately:

$$\frac{d\mathcal{E}}{dt} \approx \frac{\mathcal{E}}{\Delta t_{\mathrm{el}}} = 1.5 \times 10^{47} \cdot \alpha^2 \left(\frac{B_0}{B_c}\right)^2 \left(\frac{M}{M_\odot}\right)^2 (1+\sqrt{1-\alpha^2})^2 \quad \mathrm{erg} \cdot \mathrm{s}^{-1}. \tag{23}$$

The timescale of the subsequent processes depends crucially on the time required to rebuild the electric field. It has been shown that this condition implies an essential role of the density profile of the ionic matter surrounding the BH and its evolution with time [85,86].

For a BH mass of the order of the NS critical mass, say $M \sim 3\, M_\odot$, a BH spin parameter $\alpha \sim 0.3$, and a strength of the magnetic field $B_0 \sim 10^{14}$ G, the above numbers are in agreement with the observed GeV emission data. See, for instance, in [85] and [86], respectively, the details of the analysis of GRB 130427A and GRB 190114C. We refer to [84,85] for details on the synchrotron emission of the accelerated protons in the above magnetic field.

5.6. Additional Considerations

The strong dependence of $P_{\max}$ on the initial mass of the NS companion opens the interesting possibility of producing XRFs and BdHNe from binaries with similar short (e.g., $P \sim$ few minutes) orbital periods and CO_{core} properties: while a system with a massive (e.g., $\gtrsim 2\ M_\odot$) NS companion would lead to a BdHN, a system with a lighter (e.g., $\lesssim 1.4\ M_\odot$) NS companion would lead to an XRF. This predicts systems with a similar initial SN, leading to a similar νNS, but with different GRB prompt and afterglow emission. Given that the GRB energetics are different, the final SN kinetic energy should also be different being that it is larger for the BdHNe. This has been clearly shown by specific examples in [49].

There are also additional novel features unveiled by the new 3D SPH simulations which can be observable in GRB light-curves and spectra, e.g.,:

(1) the hypercritical accretion occurs not only on the NS companion but also on the νNS and with a comparable rate.
(2) This implies that BdHNe might be also be able to form, in special cases, BH-BH binaries. Since the system remains bound the binary will quickly merge by emitting gravitational waves. Clearly, no electromagnetic emission is expected from these mergers. However, the typically large cosmological distances of BdHNe would make it extremely difficult to detect their gravitational waves e.g., by LIGO/Virgo.
(3) Relatively weak SN explosions produce a long-lived hypercritical accretion process leading and enhance, at late times, the accretion onto the νNS. The revival of the accretion process at late times is a unique feature of our binary and does not occur for single SNe, namely in the absence of the NS companion. This feature increases the probability of detection of weak SNe by X-ray detectors via the accretion phase in an XRF/BdHN.
(4) For asymmetric SN explosions the accretion rate shows a quasi-periodic behavior that might be detected by X-rays instruments, possibly allowing a test of the binary nature and the identification of the orbital period of the progenitor.

6. Post-Explosion Orbits and Formation of NS-BH Binaries

The SN explosion leaves as a central remnant a νNS and the induced gravitational collapse of the NS companion leads to BH formation. Therefore, BdHNe potentially leads to νNS-BH binaries, providing the binary keeps bound. This question was analyzed via numerical simulations in [55].

Typical binaries become unbound during an SN explosion because of mass loss and the momentum imparted (kick) to the νNS by the explosion. A classical astrophysical result shows that, assuming the explosion as instantaneous (sudden mass loss approximation), disruption occurs if half of the binary mass is lost. For this reason the fraction of massive binaries that can produce double compact-object binaries is usually found to be very low (e.g., $\sim$0.001–1%) [54,59,121].

Assuming instantaneous mass loss, the post-explosion semi-major axis is [122]:

$$\frac{a}{a_0} = \frac{M_0 - \Delta M}{M_0 - 2a_0 \Delta M/r}, \tag{24}$$

where a_0 and a are the initial and final semi-major axes respectively, M_0 is the (initial) binary mass, ΔM is the change of mass (in this case the amount of mass loss), and r is the orbital separation before the explosion. For circular orbits, the system is unbound if it loses half of its mass. For the very tight BdHNe, however, additional effects have to be taken into account to determine the fate of the binary.

The shock front in an SN moves at roughly 10^4 km s^{-1}, but the denser, lower-velocity ejecta, can move at velocities as low as 10^2–10^3 km s^{-1} [83]. This implies that the SN ejecta overcomes an NS companion in a time 10–1000 s. For wide binaries this time is a small fraction of the orbital period and the "instantaneous" mass-loss assumption is perfectly valid. BdHNe have instead orbital periods as short as 100–1000 s, hence the instantaneous mass-loss approximation breaks down.

We recall the specific examples studied in [55]: close binaries in an initial circular orbit of radius 7×10^9 cm, CO_{core} radii of (1–4) $\times 10^9$ cm with a 2.0 $M_\odot$ NS companion. The CO_{core} leaves a central 1.5 $M_\odot$ NS, ejecting the rest of the core. The NS leads to a BH with a mass equal to the NS critical mass. For these parameters it was there obtained that even if 70% of the mass is lost the binary remains bound, providing the explosion time is of the order of the orbital period ($P = 180$ s) with semi-major axes of less than 10^{11} cm (see Figure 12).

The tight νNS-BH binaries produced by BdHNe will, in due time, merge owing to the emission of gravitational waves. For the above typical parameters the merger time is of the order of 10^4 year, or even less (see Figure 12). We expect little baryonic contamination around such merger site since this region has been cleaned-up by the BdHN. These conditions lead to a new family of sources which we have called ultrashort GRBs, U-GRBs.

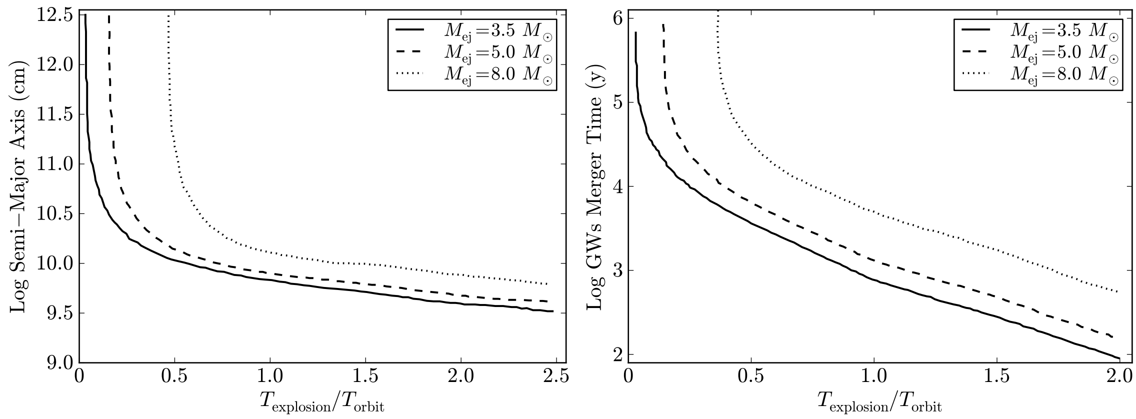

Figure 12. (**a**) Semi-major axis versus explosion time for three different mass ejecta scenarios: 3.5 $M_\odot$ (solid), 5.0 $M_\odot$ (dotted), 8.0 $M_\odot$ (dashed), including mass accretion and momentum effects (taken from Figure 2 in [55]). Including these effects, all systems with explosion times above 0.7 times the orbital time are bound and the final separations are on par with the initial separations. (**b**) Merger time due to gravitational wave emission as a function of explosion time for the same three binaries of the left panel (taken from Figure 3 in [55]). Note that systems with explosion times 0.1–0.6 $T_{\rm orbit}$ have merger times less than roughly 10^4 y. For most of our systems, the explosion time is above this limit and we expect most of these systems to merge quickly.

7. BdHN Formation, Occurrence Rate and Connection with Short GRBs

7.1. An Evolutionary Scenario

The X-ray binary and SN communities have introduced a new evolutionary scenario for the formation of compact-object binaries (NS-NS or NS-BH). After the collapse of the primary star forming a NS, the binary undergoes mass-transfer episodes finally leading to the ejection of both the hydrogen and helium shells of the secondary star. These processes lead naturally to a binary composed of a $\rm CO_{core}$ and an NS companion (see Figure 1). In the X-ray binary and SN communities these systems are called "ultra-stripped" binaries [123]. These systems are expected to comprise 0.1–1% of the total SNe [124].

The existence of ultra-stripped binaries supports our scenario from the stellar evolution side. In the above studies most of the binaries have orbital periods in the range 3×10^3–3×10^5 s which are longer with respect to the short periods expected in the BdHN scenario. Clearly, XRF and BdHN progenitors should be only a small subset that result from the binaries with initial orbital separation and component masses leading to $\rm CO_{core}$-NS binaries with short orbital periods, e.g., 100–1000 s for the occurrence of BdHNe. This requires fine-tuning both of the $\rm CO_{core}$ mass and the binary orbit. From an astrophysical point of view the IGC scenario is characterized by the BH formation induced by the hypercritical accretion onto the NS companion and the associated GRB emission. Indeed, GRBs are a rare phenomenon and the number of systems approaching the conditions for their occurrence must be low (see [55] for details).

7.2. Occurrence Rate

If we assume that XRFs and BdHNe can be final stages of ultra-stripped binaries, then the percentage of the ultra-stripped population leading to these long GRBs must be very small. The observed occurrence rate of XRFs and BdHNe has been estimated to be $\sim$100 Gpc^{-3} yr^{-1} and $\sim$1 Gpc^{-3} yr^{-1}, respectively [45], namely the 0.5% and 0.005% of the Ibc SNe rate, 2×10^4 Gpc^{-3} yr^{-1} [125]. It has been estimated that (0.1–1%) of the SN Ibc could originate from ultra-stripped binaries [124], which would lead to an approximate density rate of (20–200) Gpc^{-3} yr^{-1}. This would imply that a small fraction ($\lesssim$5%) of the ultra-stripped population would be needed to explain the BdHNe while, roughly speaking, almost the whole population would be needed to explain the XRFs (see Table 1). These numbers, while waiting for a confirmation by further population synthesis analyses, would suggest that most SNe originated from ultra-stripped binaries should be accompanied by an XRF. It is interesting that the above estimates are consistent with traditional estimates that only $\sim$0.001–1% of massive binaries lead to double compact-object binaries [54,59,121].

7.3. Connection with Short GRBs

It is then clear that XRFs and BdHNe lead to νNS-NS and νNS-BH binaries. In due time, the emission of gravitational waves shrink their orbit leading to mergers potentially detectable as short GRBs. This implies a connection between the rate of long and short GRBs. It is clear from the derived rates (see Table 1 and [45,47]) that the short GRB population is dominated by the low-luminosity class of short Gamma-ray flashes (S-GRFs), double NS mergers that do not lead to BH formation. It can be seen that it is sufficient $\lesssim$4% of XRFs to explain the S-GRFs population, which would be consistent with the fact that many XRF progenitor binaries will get disrupted by the SN explosion. Therefore, by now, the observed rates of the GRB subclasses are consistent with the interesting possibility of a connection between the progenitors of the long and the ones of the short GRBs.

8. Conclusions

It is by now clear that short and long Gamma-ray bursts subclassify into eight different families and have as progenitors binary systems of a variety of flavors (see Table 1). We have focused in this work on the specific class of BdHNe of two types: type I and type II BdHNe, what in our old classification [45] we called BdHNe and XRFs, respectively.

We have devoted this article mostly to the theoretical aspects of the *induced gravitational collapse scenario* and its evolution into BdHN as a complete model of long GRBs. We have also discussed, although briefly, the observable features of the model and how they compare with the observational data, providing to the reader the appropriate references for deepening this important aspect.

BdHNe I and II have as a common progenitor a CO$_{\rm core}$-NS binary. The CO$_{\rm core}$ explodes as type Ic SN, forming at its center a new NS, which we denote νNS, and produces onto the NS companion a hypercritical accretion process accompanied by an intense neutrino emission. The intensity of the accretion process and the neutrino emission depends mainly on the binary period, being more intense for tighter binaries. The NS companion in such an accretion process can reach or not the critical mass for gravitational collapse, i.e., to form a BH. The former binaries leading to a BH by accretion are the BdHNe I, while the ones in which the NS companion becomes just a more massive NS, are the BdHNe II (the old XRFs) (see Table 1).

We have reviewed the results of the numerical simulations performed of the above physical process starting from the 1D ones all the way to the latest 3D SPH ones. The simulation of this binary process has opened our eyes to a new reality: long GRBS are much richer and more complex systems than every one of us thought before, with the 3D morphology of the SN ejecta, that becomes asymmetric by the accretion process, playing a fundamental role in the GRB analysis.

We have recalled the relevance of each of the following processes in a BdHN:

(1) the SN explosion;

(2) the hypercritical accretion onto the NS companion;
(3) the NS collapse with consequent BH formation;
(4) the initiation of the *inner engine*;
(5) the e^+e^- plasma production;
(6) the e^+e^- plasma feedback onto the SN which converts the SN into a HN;
(7) the formation of the cavity around the newborn BH;
(8) the transparency of the e^+e^- plasma along different directions;
(9) the HN emission powered by the νNS;
(10) the action of the *inner engine* in accelerating protons leading to UHECRs and to the high-energy emission.

The aforementioned involved physical processes in a BdHN have specific signatures observable (and indeed observed) in the long GRB multiwavelength lightcurves and spectra. We have recalled for each process its energetics, spectrum, and associated Lorentz factor: from the mildly-relativistic X-ray precursor, to the ultrarelativistic prompt Gamma-ray emission, to the mildly-relativistic X-ray flares of the early afterglow, to the mildly-relativistic late afterglow and to the high-energy GeV emission.

All of the above is clearly in contrast with a simple GRB model attempting to explain the entire GRB process with the kinetic energy of an ultrarelativistic jet extending through all of the above GRB phases, as in the traditional collapsar-fireball model.

If the binaries keep bound during the explosion, BdHNe I lead to νNS-BH binaries and BdHNe II lead to νNS-NS binaries. In due time, via gravitational wave emission, such binaries merge producing short GRBs. This unveiled clear interconnection between long and short GRBs and their occurrence rates needs to be accounted for in the cosmological evolution of binaries within population synthesis models for the formation of compact-object binaries.

We have taken the opportunity to include a brief summary of very recent developments published during the peer-review process of this article. These results cover the explanation of the observed GeV emission in BdHNe [84–87]. One of the most relevant aspects of this topic is that it requests the solution of one of the fundamental problems in relativistic astrophysics: how to extract the rotational energy from a BH. This implies the role of a magnetic field around the newborn BH and the presence of surrounding matter as predicted in a BdHN. We have called this part of the system the *inner engine* of the high-energy emission. The BH rotation and surrounding magnetic field, for appropriate values induces an electric field via the Wald's mechanism [88]. Such an electric field is of paramount importance in accelerating surrounding protons to ultrarelativistic velocities leading to the high-energy emission via proton-synchrotron radiation. The details of this exciting new topic are beyond the scope of the present article but we encourage the reader to go through the above references for complementary details.

Funding: This research received no external funding.

Conflicts of Interest: The authors declare no conflict of interest.

References

1. Mazets, E.P.; Golenetskii, S.V.; Ilinskii, V.N.; Panov, V.N.; Aptekar, R.L.; Gurian, I.A.; Proskura, M.P.; Sokolov, I.A.; Sokolova, Z.I.; Kharitonova, T.V. Catalog of cosmic Gamma-ray bursts from the KONUS experiment data. I. *Astrophys. Space Sci.* **1981**, *80*, 3–83. [CrossRef]
2. Klebesadel, R.W. The durations of Gamma-ray bursts. In *Gamma-ray Bursts—Observations, Analyses and Theories*; Ho, C., Epstein, R.I., Fenimore, E.E., Eds.; Cambridge University Press: Cambridge, UK, 1992; pp. 161–168.
3. Dezalay, J.P.; Barat, C.; Talon, R.; Syunyaev, R.; Terekhov, O.; Kuznetsov, A. Short cosmic events—A subset of classical GRBs? In *American Institute of Physics Conference Series*; Paciesas, W.S., Fishman, G.J., Eds.; American Institute of Physics: College Park, MD, USA, 1992; Volume 265, pp. 304–309.

4. Kouveliotou, C.; Meegan, C.A.; Fishman, G.J.; Bhat, N.P.; Briggs, M.S.; Koshut, T.M.; Paciesas, W.S.; Pendleton, G.N. Identification of two classes of Gamma-ray bursts. *Astrophys. J. Lett.* **1993**, *413*, L101–L104. [CrossRef]
5. Tavani, M. Euclidean versus Non-Euclidean Gamma-ray Bursts. *Astrophys. J. Lett.* **1998**, *497*, L21–L24. [CrossRef]
6. Goodman, J. Are Gamma-ray bursts optically thick? *Astrophys. J. Lett.* **1986**, *308*, L47. [CrossRef]
7. Paczynski, B. Gamma-ray bursters at cosmological distances. *Astrophys. J. Lett.* **1986**, *308*, L43. [CrossRef]
8. Eichler, D.; Livio, M.; Piran, T.; Schramm, D.N. Nucleosynthesis, neutrino bursts and Gamma-rays from coalescing neutron stars. *Nature* **1989**, *340*, 126–128. [CrossRef]
9. Narayan, R.; Piran, T.; Shemi, A. Neutron star and black hole binaries in the Galaxy. *Astrophys. J. Lett.* **1991**, *379*, L17–L20. [CrossRef]
10. Pian, E.; Amati, L.; Antonelli, L.A.; Butler, R.C.; Costa, E.; Cusumano, G.; Danziger, J.; Feroci, M.; Fiore, F.; Frontera, F.; et al. BEPPOSAX Observations of GRB 980425: Detection of the Prompt Event and Monitoring of the Error Box. *Astrophys. J. Lett.* **2000**, *536*, 778–787. [CrossRef]
11. Galama, T.J.; Vreeswijk, P.M.; van Paradijs, J.; Kouveliotou, C.; Augusteijn, T.; Böhnhardt, H.; Brewer, J.P.; Doublier, V.; Gonzalez, J.F.; Leibundgut, B.; et al. An unusual supernova in the error box of the γ-ray burst of 25 April 1998. *Nature* **1998**, *395*, 670–672. [CrossRef]
12. Della Valle, M. Supernovae and Gamma-ray Bursts: A Decade of Observations. *Int. J. Mod. Phys. D* **2011**, *20*, 1745–1754. [CrossRef]
13. Cano, Z.; Wang, S.Q.; Dai, Z.G.; Wu, X.F. The Observer's Guide to the Gamma-ray Burst Supernova Connection. *Adv. Astron.* **2017**, *2017*, 8929054. [CrossRef]
14. Woosley, S.E.; Bloom, J.S. The Supernova Gamma-ray Burst Connection. *Annu. Rev. Astron. Astrophys.* **2006**, *44*, 507–556. [CrossRef]
15. Blandford, R.D.; McKee, C.F. Fluid dynamics of relativistic blast waves. *Phys. Fluids* **1976**, *19*, 1130–1138. [CrossRef]
16. Shemi, A.; Piran, T. The appearance of cosmic fireballs. *Astrophys. J. Lett.* **1990**, *365*, L55–L58. [CrossRef]
17. Meszaros, P.; Laguna, P.; Rees, M.J. Gasdynamics of relativistically expanding Gamma-ray burst sources—Kinematics, energetics, magnetic fields, and efficiency. *Astrophys. J. Lett.* **1993**, *415*, 181–190. [CrossRef]
18. Piran, T.; Shemi, A.; Narayan, R. Hydrodynamics of Relativistic Fireballs. *MNRAS* **1993**, *263*, 861. [CrossRef]
19. Mao, S.; Yi, I. Relativistic beaming and Gamma-ray bursts. *Astrophys. J. Lett.* **1994**, *424*, L131–L134. [CrossRef]
20. Piran, T. Gamma-ray bursts and the fireball model. *Phys. Rep.* **1999**, *314*, 575–667. [CrossRef]
21. Piran, T. The physics of Gamma-ray bursts. *Rev. Mod. Phys.* **2004**, *76*, 1143–1210. [CrossRef]
22. Mészáros, P. Theories of Gamma-ray Bursts. *Annu. Rev. Astron. Astrophys.* **2002**, *40*, 137. [CrossRef]
23. Mészáros, P. Gamma-ray bursts. *Rep. Prog. Phys.* **2006**, *69*, 2259–2321. [CrossRef]
24. Berger, E. Short-Duration Gamma-ray Bursts. *Annu. Rev. Astron. Astrophys.* **2014**, *52*, 43–105. [CrossRef]
25. Kumar, P.; Zhang, B. The physics of Gamma-ray bursts and relativistic jets. *Phys. Rep.* **2015**, *561*, 1–109. [CrossRef]
26. Smith, N.; Li, W.; Silverman, J.M.; Ganeshalingam, M.; Filippenko, A.V. Luminous blue variable eruptions and related transients: Diversity of progenitors and outburst properties. *MNRAS* **2011**, *415*, 773–810. [CrossRef]
27. Nomoto, K.; Hashimoto, M. Presupernova evolution of massive stars. *Phys. Rep.* **1988**, *163*, 13–36. [CrossRef]
28. Iwamoto, K.; Nomoto, K.; Höflich, P.; Yamaoka, H.; Kumagai, S.; Shigeyama, T. Theoretical light curves for the type IC supernova SN 1994I. *Astrophys. J. Lett.* **1994**, *437*, L115–L118. [CrossRef]
29. Fryer, C.L.; Mazzali, P.A.; Prochaska, J.; Cappellaro, E.; Panaitescu, A.; Berger, E.; van Putten, M.; van den Heuvel, E.P.J.; Young, P.; Hungerford, A.; et al. Constraints on Type Ib/c Supernovae and Gamma-ray Burst Progenitors. *Publ. Astron. Soc. Pac.* **2007**, *119*, 1211–1232. [CrossRef]
30. Yoon, S.C.; Woosley, S.E.; Langer, N. Type Ib/c Supernovae in Binary Systems. I. Evolution and Properties of the Progenitor Stars. *Astrophys. J. Lett.* **2010**, *725*, 940–954. [CrossRef]
31. Frail, D.A.; Kulkarni, S.R.; Sari, R.; Djorgovski, S.G.; Bloom, J.S.; Galama, T.J.; Reichart, D.E.; Berger, E.; Harrison, F.A.; Price, P.A.; et al. Beaming in Gamma-ray Bursts: Evidence for a Standard Energy Reservoir. *Astrophys. J. Lett.* **2001**, *562*, L55–L58. [CrossRef]

32. Covino, S.; Malesani, D.; Tagliaferri, G.; Vergani, S.D.; Chincarini, G.; Kann, D.A.; Moretti, A.; Stella, L.; Mistici Collaboration. Achromatic breaks for Swift GRBs: Any evidence? *Nuovo C. Ser.* **2006**, *121*, 1171–1176.
33. Sato, G.; Yamazaki, R.; Ioka, K.; Sakamoto, T.; Takahashi, T.; Nakazawa, K.; Nakamura, T.; Toma, K.; Hullinger, D.; Tashiro, M.; et al. Swift Discovery of Gamma-ray Bursts without a Jet Break Feature in Their X-ray Afterglows. *Astrophys. J. Lett.* **2007**, *657*, 359–366. [CrossRef]
34. Burrows, D.; Garmire, G.; Ricker, G.; Bautz, M.; Nousek, J.; Grupe, D.; Racusin, J. Chandra Searches for Late-Time Jet Breaks in GRB X-ray Afterglows. In *Chandra's First Decade of Discovery*; Wolk, S., Fruscione, A., Swartz, D., Eds.; Chandra X-ray Center: Cambridge, MA, USA, 2009.
35. Izzo, L.; Ruffini, R.; Penacchioni, A.V.; Bianco, C.L.; Caito, L.; Chakrabarti, S.K.; Rueda, J.A.; Nandi, A.; Patricelli, B. A double component in GRB 090618: A proto-black hole and a genuinely long Gamma-ray burst. *A&A* **2012**, *543*, A10.
36. Ruffini, R. Fundamental Physics from Black Holes, Neutron Stars and Gamma-ray Bursts. *Int. J. Mod. Phys. D* **2011**, *20*, 1797–1872. [CrossRef]
37. Ruffini, R.; Salmonson, J.D.; Wilson, J.R.; Xue, S.S. On the pair-electromagnetic pulse from an electromagnetic black hole surrounded by a baryonic remnant. *A&A* **2000**, *359*, 855–864.
38. Smartt, S.J. Observational Constraints on the Progenitors of Core-Collapse Supernovae: The Case for Missing High-Mass Stars. *PASA* **2015**, *32*, e016. [CrossRef]
39. Smartt, S.J. Progenitors of Core-Collapse Supernovae. *Annu. Rev. Astron. Astrophys.* **2009**, *47*, 63–106. [CrossRef]
40. Ruffini, R.; Wang, Y.; Aimuratov, Y.; Barres de Almeida, U.; Becerra, L.; Bianco, C.L.; Chen, Y.C.; Karlica, M.; Kovacevic, M.; Li, L.; et al. Early X-ray Flares in GRBs. *Astrophys. J. Lett.* **2018**, *852*, 53. [CrossRef]
41. Ruffini, R.; Bianco, C.L.; Fraschetti, F.; Xue, S.S.; Chardonnet, P. On a Possible Gamma-ray Burst-Supernova Time Sequence. *Astrophys. J. Lett.* **2001**, *555*, L117–L120. [CrossRef]
42. Ruffini, R.; Bernardini, M.G.; Bianco, C.L.; Caito, L.; Chardonnet, P.; Cherubini, C.; Dainotti, M.G.; Fraschetti, F.; Geralico, A.; Guida, R.; et al. On Gamma-ray Bursts. In *The Eleventh Marcel Grossmann Meeting On Recent Developments in Theoretical and Experimental General Relativity, Gravitation and Relativistic Field Theories*; Kleinert, H., Jantzen, R.T., Ruffini, R., Eds.; World Scientific Publishing Co. Pte Ltd.: Hackensack, NJ, USA, 2008; pp. 368–505.
43. Sana, H.; de Mink, S.E.; de Koter, A.; Langer, N.; Evans, C.J.; Gieles, M.; Gosset, E.; Izzard, R.G.; Le Bouquin, J.B.; Schneider, F.R.N. Binary Interaction Dominates the Evolution of Massive Stars. *Science* **2012**, *337*, 444. [CrossRef]
44. Smith, N. Mass Loss: Its Effect on the Evolution and Fate of High-Mass Stars. *Annu. Rev. Astron. Astrophys.* **2014**, *52*, 487–528. [CrossRef]
45. Ruffini, R.; Rueda, J.A.; Muccino, M.; Aimuratov, Y.; Becerra, L.M.; Bianco, C.L.; Kovacevic, M.; Moradi, R.; Oliveira, F.G.; Pisani, G.B.; et al. On the Classification of GRBs and Their Occurrence Rates. *Astrophys. J. Lett.* **2016**, *832*, 136. [CrossRef]
46. Rueda, J.A.; Aimuratov, Y.; de Almeida, U.B.; Becerra, L.; Bianco, C.L.; Cherubini, C.; Filippi, S.; Karlica, M.; Kovacevic, M.; Fuksman, J.D.M.; et al. The binary systems associated with short and long Gamma-ray bursts and their detectability. *Int. J. Mod. Phys. D* **2017**, *26*, 1730016. [CrossRef]
47. Ruffini, R.; Rodriguez, J.; Muccino, M.; Rueda, J.A.; Aimuratov, Y.; Barres de Almeida, U.; Becerra, L.; Bianco, C.L.; Cherubini, C.; Filippi, S.; et al. On the Rate and on the Gravitational Wave Emission of Short and Long GRBs. *Astrophys. J. Lett.* **2018**, *859*, 30. [CrossRef]
48. Ruffini, R.; Moradi, R.; Wang, Y.; Aimuratov, Y.; Amiri, M.; Becerra, L.; Bianco, C.L.; Chen, Y.C.; Eslam Panah, B.; Mathews, G.J.; et al. On the universal GeV emission in binary-driven hypernovae and their inferred morphological structure. *arXiv* **2018**, arXiv:1803.05476.
49. Wang, Y.; Rueda, J.A.; Ruffini, R.; Becerra, L.; Bianco, C.; Becerra, L.; Li, L.; Karlica, M. Two Predictions of Supernova: GRB 130427A/SN 2013cq and GRB 180728A/SN 2018fip. *Astrophys. J. Lett.* **2019**, *874*, 39. [CrossRef]
50. Rueda, J.A.; Ruffini, R.; Wang, Y.; Aimuratov, Y.; Barres de Almeida, U.; Bianco, C.L.; Chen, Y.C.; Lobato, R.V.; Maia, C.; Primorac, D.; et al. GRB 170817A-GW170817-AT 2017gfo and the observations of NS-NS, NS-WD and WD-WD mergers. *J. Cosmol. Astropart. Phys.* **2018**, *2018*, 006. [CrossRef]

51. Rueda, J.A.; Ruffini, R.; Wang, Y.; Bianco, C.L.; Blanco-Iglesias, J.M.; Karlica, M.; Lorén-Aguilar, P.; Moradi, R.; Sahakyan, N. Electromagnetic emission of white dwarf binary mergers. *J. Cosmol. Astropart. Phys.* **2019**, *2019*, 044. [CrossRef]
52. Becerra, L.; Bianco, C.L.; Fryer, C.L.; Rueda, J.A.; Ruffini, R. On the Induced Gravitational Collapse Scenario of Gamma-ray Bursts Associated with Supernovae. *Astrophys. J. Lett.* **2016**, *833*, 107. [CrossRef]
53. Becerra, L.; Cipolletta, F.; Fryer, C.L.; Rueda, J.A.; Ruffini, R. Angular Momentum Role in the Hypercritical Accretion of Binary-driven Hypernovae. *Astrophys. J. Lett.* **2015**, *812*, 100. [CrossRef]
54. Postnov, K.A.; Yungelson, L.R. The Evolution of Compact Binary Star Systems. *Living Rev. Relativ.* **2014**, *17*, 3. [CrossRef]
55. Fryer, C.L.; Oliveira, F.G.; Rueda, J.A.; Ruffini, R. Neutron-Star-Black-Hole Binaries Produced by Binary-Driven Hypernovae. *Phys. Rev. Lett.* **2015**, *115*, 231102. [CrossRef]
56. Giacconi, R.; Ruffini, R. (Eds.) *Physics and Astrophysics of Neutron Stars and Black Holes*; North Holland Publishing Co.: Amsterdam, The Netherlands, 1978.
57. Belczynski, K.; Bulik, T.; Bailyn, C. The Fate of Cyg X-1: An Empirical Lower Limit on Black-hole-Neutron-star Merger Rate. *Astrophys. J. Lett.* **2011**, *742*, L2. [CrossRef]
58. Mirabel, I.F.; Rodríguez, L.F. Microquasars in our Galaxy. *Nature* **1998**, *392*, 673–676. [CrossRef]
59. Fryer, C.L.; Woosley, S.E.; Hartmann, D.H. Formation Rates of Black Hole Accretion Disk Gamma-ray Bursts. *Astrophys. J. Lett.* **1999**, *526*, 152–177. [CrossRef]
60. Li, L.X.; Paczyński, B. Transient Events from Neutron Star Mergers. *Astrophys. J. Lett.* **1998**, *507*, L59–L62. [CrossRef]
61. Metzger, B.D.; Martínez-Pinedo, G.; Darbha, S.; Quataert, E.; Arcones, A.; Kasen, D.; Thomas, R.; Nugent, P.; Panov, I.V.; Zinner, N.T. Electromagnetic counterparts of compact object mergers powered by the radioactive decay of r-process nuclei. *MNRAS* **2010**, *406*, 2650–2662. [CrossRef]
62. Tanvir, N.R.; Levan, A.J.; Fruchter, A.S.; Hjorth, J.; Hounsell, R.A.; Wiersema, K.; Tunnicliffe, R.L. A 'kilonova' associated with the short-duration γ-ray burst GRB 130603B. *Nature* **2013**, *500*, 547–549. [CrossRef]
63. Berger, E.; Fong, W.; Chornock, R. An r-process Kilonova Associated with the Short-hard GRB 130603B. *Astrophys. J. Lett.* **2013**, *774*, L23. [CrossRef]
64. Meszaros, P.; Rees, M.J. Poynting Jets from Black Holes and Cosmological Gamma-ray Bursts. *Astrophys. J. Lett.* **1997**, *482*, L29. [CrossRef]
65. Rosswog, S.; Ramirez-Ruiz, E.; Davies, M.B. High-resolution calculations of merging neutron stars—III. Gamma-ray bursts. *MNRAS* **2003**, *345*, 1077–1090. [CrossRef]
66. Lee, W.H.; Ramirez-Ruiz, E.; Page, D. Opaque or Transparent? A Link between Neutrino Optical Depths and the Characteristic Duration of Short Gamma-ray Bursts. *Astrophys. J. Lett.* **2004**, *608*, L5–L8. [CrossRef]
67. Ruffini, R.; Muccino, M.; Kovacevic, M.; Oliveira, F.G.; Rueda, J.A.; Bianco, C.L.; Enderli, M.; Penacchioni, A.V.; Pisani, G.B.; Wang, Y.; et al. GRB 140619B: A short GRB from a binary neutron star merger leading to black hole formation. *Astrophys. J. Lett.* **2015**, *808*, 190. [CrossRef]
68. Ruffini, R.; Muccino, M.; Aimuratov, Y.; Bianco, C.L.; Cherubini, C.; Enderli, M.; Kovacevic, M.; Moradi, R.; Penacchioni, A.V.; Pisani, G.B.; et al. GRB 090510: A Genuine Short GRB from a Binary Neutron Star Coalescing into a Kerr-Newman Black Hole. *Astrophys. J. Lett.* **2016**, *831*, 178. [CrossRef]
69. Muccino, M.; Ruffini, R.; Bianco, C.L.; Izzo, L.; Penacchioni, A.V. GRB 090227B: The Missing Link between the Genuine Short and Long Gamma-ray Bursts. *Astrophys. J. Lett.* **2013**, *763*, 125. [CrossRef]
70. Della Valle, M.; Chincarini, G.; Panagia, N.; Tagliaferri, G.; Malesani, D.; Testa, V.; Fugazza, D.; Campana, S.; Covino, S.; Mangano, V.; et al. An enigmatic long-lasting γ-ray burst not accompanied by a bright supernova. *Nature* **2006**, *444*, 1050. [CrossRef]
71. Cadelano, M.; Pallanca, C.; Ferraro, F.R.; Salaris, M.; Dalessandro, E.; Lanzoni, B.; Freire, P.C.C. Optical Identification of He White Dwarfs Orbiting Four Millisecond Pulsars in the Globular Cluster 47 Tucanae. *Astrophys. J. Lett.* **2015**, *812*, 63. [CrossRef]
72. Bildsten, L.; Cutler, C. Tidal interactions of inspiraling compact binaries. *Astrophys. J. Lett.* **1992**, *400*, 175–180. [CrossRef]
73. Fryer, C.L.; Woosley, S.E.; Herant, M.; Davies, M.B. Merging White Dwarf/Black Hole Binaries and Gamma-ray Bursts. *Astrophys. J. Lett.* **1999**, *520*, 650–660. [CrossRef]

74. Tauris, T.M.; van den Heuvel, E.P.J.; Savonije, G.J. Formation of Millisecond Pulsars with Heavy White Dwarf Companions:Extreme Mass Transfer on Subthermal Timescales. *Astrophys. J. Lett.* **2000**, *530*, L93–L96. [CrossRef]
75. Lazarus, P.; Tauris, T.M.; Knispel, B.; Freire, P.C.C.; Deneva, J.S.; Kaspi, V.M.; Allen, B.; Bogdanov, S.; Chatterjee, S.; Stairs, I.H.; et al. Timing of a young mildly recycled pulsar with a massive white dwarf companion. *MNRAS* **2014**, *437*, 1485–1494. [CrossRef]
76. Caito, L.; Bernardini, M.G.; Bianco, C.L.; Dainotti, M.G.; Guida, R.; Ruffini, R. GRB060614: A "fake" short GRB from a merging binary system. *A&A* **2009**, *498*, 501–507.
77. Maoz, D.; Hallakoun, N. The binary fraction, separation distribution, and merger rate of white dwarfs from SPY. *MNRAS* **2017**, *467*, 1414–1425. [CrossRef]
78. Maoz, D.; Hallakoun, N.; Badenes, C. The separation distribution and merger rate of double white dwarfs: Improved constraints. *MNRAS* **2018**, *476*, 2584–2590. [CrossRef]
79. Sun, H.; Zhang, B.; Li, Z. Extragalactic High-energy Transients: Event Rate Densities and Luminosity Functions. *Astrophys. J. Lett.* **2015**, *812*, 33. [CrossRef]
80. Rueda, J.A.; Ruffini, R.; Becerra, L.M.; Fryer, C.L. Simulating the induced gravitational collapse scenario of long Gamma-ray bursts. *Int. J. Mod. Phys. A* **2018**, *33*, 1844031. [CrossRef]
81. Rueda, J.A.; Ruffini, R. On the Induced Gravitational Collapse of a Neutron Star to a Black Hole by a Type Ib/c Supernova. *Astrophys. J. Lett.* **2012**, *758*, L7. [CrossRef]
82. Izzo, L.; Rueda, J.A.; Ruffini, R. GRB 090618: A candidate for a neutron star gravitational collapse onto a black hole induced by a type Ib/c supernova. *A&A* **2012**, *548*, L5.
83. Fryer, C.L.; Rueda, J.A.; Ruffini, R. Hypercritical Accretion, Induced Gravitational Collapse, and Binary-Driven Hypernovae. *Astrophys. J. Lett.* **2014**, *793*, L36. [CrossRef]
84. Ruffini, R.; Rueda, J.A.; Becerra, L.; Bianco, C.L.; Chen, Y.C.; Cherubini, C.; Filippi, S.; Karlica, M.; Melon Fuksman, J.D.; Moradi, R.; et al. The inner engine of GeV-radiation-emitting Gamma-ray bursts. *arXiv* **2018**, arXiv:1811.01839.
85. Ruffini, R.; Moradi, R.; Rueda, J.A.; Becerra, L.; Bianco, C.L.; Cherubini, C.; Filippi, S.; Chen, Y.C.; Karlica, M.; Sahakyan, N.; et al. On the GeV emission of the type I BdHN GRB 130427A. *arXiv* **2018**, arXiv:1812.00354.
86. Ruffini, R.; Li, L.; Moradi, R.; Rueda, J.A.; Wang, Y.; Xue, S.S.; Bianco, C.L.; Campion, S.; Melon Fuksman, J.D.; Cherubini, C.; et al. Self-similarity and power-laws in GRB 190114C. *arXiv* **2019**, arXiv:1904.04162.
87. Ruffini, R.; Melon Fuksman, J.D.; Vereshchagin, G.V. On the role of a cavity in the hypernova ejecta of GRB190114C. *arXiv* **2019**, arXiv:1904.03163.
88. Wald, R.M. Black hole in a uniform magnetic field. *Phys. Rev. D* **1974**, *10*, 1680–1685. [CrossRef]
89. Ruffini, R.; Becerra, L.; Bianco, C.L.; Chen, Y.C.; Karlica, M.; Kovačević, M.; Melon Fuksman, J.D.; Moradi, R.; Muccino, M.; Pisani, G.B.; et al. On the Ultra-relativistic Prompt Emission, the Hard and Soft X-Ray Flares, and the Extended Thermal Emission in GRB 151027A. *Astrophys. J. Lett.* **2018**, *869*, 151. [CrossRef]
90. Becerra, L.; Ellinger, C.L.; Fryer, C.L.; Rueda, J.A.; Ruffini, R. SPH Simulations of the Induced Gravitational Collapse Scenario of Long Gamma-ray Bursts Associated with Supernovae. *Astrophys. J. Lett.* **2019**, *871*, 14. [CrossRef]
91. Ruffini, R.; Karlica, M.; Sahakyan, N.; Rueda, J.A.; Wang, Y.; Mathews, G.J.; Bianco, C.L.; Muccino, M. A GRB Afterglow Model Consistent with Hypernova Observations. *Astrophys. J. Lett.* **2018**, *869*, 101. [CrossRef]
92. Fryer, C.; Benz, W.; Herant, M.; Colgate, S.A. What Can the Accretion-induced Collapse of White Dwarfs Really Explain? *Astrophys. J. Lett.* **1999**, *516*, 892–899. [CrossRef]
93. Becerra, L.; Guzzo, M.M.; Rossi-Torres, F.; Rueda, J.A.; Ruffini, R.; Uribe, J.D. Neutrino Oscillations within the Induced Gravitational Collapse Paradigm of Long Gamma-ray Bursts. *Astrophys. J. Lett.* **2018**, *852*, 120. [CrossRef]
94. Cipolletta, F.; Cherubini, C.; Filippi, S.; Rueda, J.A.; Ruffini, R. Last stable orbit around rapidly rotating neutron stars. *PRD* **2017**, *96*, 024046. [CrossRef]
95. Cipolletta, F.; Cherubini, C.; Filippi, S.; Rueda, J.A.; Ruffini, R. Fast rotating neutron stars with realistic nuclear matter equation of state. *Phys. Rev. D* **2015**, *92*, 023007. [CrossRef]
96. Fryer, C.L.; Benz, W.; Herant, M. The Dynamics and Outcomes of Rapid Infall onto Neutron Stars. *Astrophys. J. Lett.* **1996**, *460*, 801. [CrossRef]
97. Chevalier, R.A. Neutron star accretion in a supernova. *Astrophys. J. Lett.* **1989**, *346*, 847–859. [CrossRef]

98. Zel'dovich, Y.B.; Ivanova, L.N.; Nadezhin, D.K. Nonstationary Hydrodynamical Accretion onto a Neutron Star. *Sov. Astron.* **1972**, *16*, 209.
99. Ruffini, R.; Wilson, J. Possibility of Neutrino Emission from Matter Accreting into a Neutron Star. *Phys. Rev. Lett.* **1973**, *31*, 1362–1364. [CrossRef]
100. Fryer, C.L.; Herwig, F.; Hungerford, A.; Timmes, F.X. Supernova Fallback: A Possible Site for the r-Process. *Astrophys. J. Lett.* **2006**, *646*, L131–L134. [CrossRef]
101. Fryer, C.L. Neutrinos from Fallback onto Newly Formed Neutron Stars. *Astrophys. J. Lett.* **2009**, *699*, 409–420. [CrossRef]
102. Yakovlev, D.G.; Kaminker, A.D.; Gnedin, O.Y.; Haensel, P. Neutrino emission from neutron stars. *Phys. Rep.* **2001**, *354*, 1–155. [CrossRef]
103. Fryer, C.L.; Rockefeller, G.; Warren, M.S. SNSPH: A Parallel Three-dimensional Smoothed Particle Radiation Hydrodynamics Code. *Astrophys. J. Lett.* **2006**, *643*, 292–305. [CrossRef]
104. Fryer, C.L.; Warren, M.S. Modeling Core-Collapse Supernovae in Three Dimensions. *Astrophys. J. Lett.* **2002**, *574*, L65–L68. [CrossRef]
105. Young, P.A.; Fryer, C.L.; Hungerford, A.; Arnett, D.; Rockefeller, G.; Timmes, F.X.; Voit, B.; Meakin, C.; Eriksen, K.A. Constraints on the Progenitor of Cassiopeia A. *Astrophys. J. Lett.* **2006**, *640*, 891–900. [CrossRef]
106. Diehl, S.; Fryer, C.; Herwig, F. The Formation of Hydrogen Deficient Stars through Common Envelope Evolution. Hydrogen-Deficient Stars. In *Astronomical Society of the Pacific Conference Series*; Werner, A., Rauch, T., Eds.; Astronomical Society of the Pacific: San Francisco, CA, USA, 2008; Volume 391, p. 221.
107. Batta, A.; Ramirez-Ruiz, E.; Fryer, C. The Formation of Rapidly Rotating Black Holes in High-mass X-ray Binaries. *Astrophys. J. Lett.* **2017**, *846*, L15. [CrossRef]
108. Arnett, D. *Supernovae and Nucleosynthesis: An Investigation of the History of Matter from the Big Bang to the Present*; Princeton University Press: Princeton, NJ, USA, 1996.
109. Ruffini, R.; Vereshchagin, G.; Xue, S. Electron-positron pairs in physics and astrophysics: From heavy nuclei to black holes. *Phys. Rep.* **2010**, *487*, 1–140. [CrossRef]
110. Preparata, G.; Ruffini, R.; Xue, S.S. The dyadosphere of black holes and Gamma-ray bursts. *A&A* **1998**, *338*, L87–L90.
111. Ruffini, R.; Salmonson, J.D.; Wilson, J.R.; Xue, S.S. On evolution of the pair-electromagnetic pulse of a charged black hole. *Astron. Astrophys. Suppl.* **1999**, *138*, 511–512. [CrossRef]
112. Penacchioni, A.V.; Ruffini, R.; Izzo, L.; Muccino, M.; Bianco, C.L.; Caito, L.; Patricelli, B.; Amati, L. Evidence for a proto-black hole and a double astrophysical component in GRB 101023. *A&A* **2012**, *538*, A58.
113. Patricelli, B.; Bernardini, M.G.; Bianco, C.L.; Caito, L.; de Barros, G.; Izzo, L.; Ruffini, R.; Vereshchagin, G.V. Analysis of GRB 080319B and GRB 050904 within the Fireshell Model: Evidence for a Broader Spectral Energy Distribution. *Astrophys. J. Lett.* **2012**, *756*, 16. [CrossRef]
114. Woosley, S.E. Gamma-ray bursts from stellar mass accretion disks around black holes. *Astrophys. J. Lett.* **1993**, *405*, 273–277. [CrossRef]
115. Starling, R.L.C.; Page, K.L.; Pe'Er, A.; Beardmore, A.P.; Osborne, J.P. A search for thermal X-ray signatures in Gamma-ray bursts - I. Swift bursts with optical supernovae. *MNRAS* **2012**, *427*, 2950–2964. [CrossRef]
116. Wang, Y.; Aimuratov, Y.; Moradi, R.; Peresano, M.; Ruffini, R.; Shakeri, S. Revisiting the statistics of X-ray flares in Gamma-ray bursts. *Mem. Soc. Astron. Ital.* **2018**, *89*, 293.
117. Ruffini, R.; Muccino, M.; Bianco, C.L.; Enderli, M.; Izzo, L.; Kovacevic, M.; Penacchioni, A.V.; Pisani, G.B.; Rueda, J.A.; Wang, Y. On binary-driven hypernovae and their nested late X-ray emission. *A&A* **2014**, *565*, L10.
118. Page, K.L.; Starling, R.L.C.; Fitzpatrick, G.; Pandey, S.B.; Osborne, J.P.; Schady, P.; McBreen, S.; Campana, S.; Ukwatta, T.N.; Pagani, C.; et al. GRB 090618: Detection of thermal X-ray emission from a bright Gamma-ray burst. *MNRAS* **2011**, *416*, 2078–2089. [CrossRef]
119. Ruffini, R.; Wang, Y.; Enderli, M.; Muccino, M.; Kovacevic, M.; Bianco, C.L.; Penacchioni, A.V.; Pisani, G.B.; Rueda, J.A. GRB 130427A and SN 2013cq: A Multi-wavelength Analysis of An Induced Gravitational Collapse Event. *Astrophys. J. Lett.* **2015**, *798*, 10. [CrossRef]
120. Wang, Y.; Ruffini, R.; Kovacevic, M.; Bianco, C.L.; Enderli, M.; Muccino, M.; Penacchioni, A.V.; Pisani, G.B.; Rueda, J.A. Predicting supernova associated to Gamma-ray burst 130427a. *Astron. Rep.* **2015**, *59*, 667–671. [CrossRef]

121. Dominik, M.; Belczynski, K.; Fryer, C.; Holz, D.E.; Berti, E.; Bulik, T.; Mandel, I.; O'Shaughnessy, R. Double Compact Objects. I. The Significance of the Common Envelope on Merger Rates. *Astrophys. J. Lett.* **2012**, *759*, 52. [CrossRef]
122. Hills, J.G. The effects of sudden mass loss and a random kick velocity produced in a supernova explosion on the dynamics of a binary star of arbitrary orbital eccentricity—Applications to X-ray binaries and to the binary pulsars. *Astrophys. J. Lett.* **1983**, *267*, 322–333. [CrossRef]
123. Tauris, T.M.; Langer, N.; Podsiadlowski, P. Ultra-stripped supernovae: Progenitors and fate. *MNRAS* **2015**, *451*, 2123–2144. [CrossRef]
124. Tauris, T.M.; Langer, N.; Moriya, T.J.; Podsiadlowski, P.; Yoon, S.C.; Blinnikov, S.I. Ultra-stripped Type Ic Supernovae from Close Binary Evolution. *Astrophys. J. Lett.* **2013**, *778*, L23. [CrossRef]
125. Guetta, D.; Della Valle, M. On the Rates of Gamma-ray Bursts and Type Ib/c Supernovae. *Astrophys. J. Lett.* **2007**, *657*, L73–L76. [CrossRef]

Time evolution of rotating and magnetized white dwarf stars

L. Becerra,[1,2]⋆ K. Boshkayev,[3,4]† J. A. Rueda[1,2,5]‡ R. Ruffini[1,2,5]§
[1] *ICRANet, Piazza della Repubblica 10, I–65122 Pescara, Italy*
[2] *Dipartimento di Fisica and ICRA, Sapienza Università di Roma, P.le Aldo Moro 5, I–00185 Rome, Italy*
[3] *NNLOT, al-Farabi Kazakh National University, Al-Farabi av. 71, 050040 Almaty, Kazakhstan*
[4] *Department of Physics, Nazarbayev University, Kabanbay Batyr 53, 010000 Astana, Kazakhstan*
[5] *ICRANet-Rio, CBPF, Rua Dr. Xavier Sigaud 150, Rio de Janeiro, RJ, 22290–180, Brazil*

18 May 2019

ABSTRACT

We investigate the evolution of isolated, zero and finite temperature, massive, uniformly rotating and highly magnetized white dwarf stars under angular momentum loss driven by magnetic dipole braking. We consider the structure and thermal evolution of the white dwarf isothermal core taking also into account the nuclear burning and neutrino emission processes. We estimate the white dwarf lifetime before it reaches the condition either for a type Ia supernova explosion or for the gravitational collapse to a neutron star. We study white dwarfs with surface magnetic fields from 10^6 to 10^9 G and masses from 1.39 to 1.46 $M_\odot$ and analyze the behavior of the WD parameters such as moment of inertia, angular momentum, central temperature and magnetic field intensity as a function of lifetime. The magnetic field is involved only to slow down white dwarfs, without affecting their equation of state and structure. In addition, we compute the characteristic time of nuclear reactions and dynamical time scale. The astrophysical consequences of the results are discussed.

1 INTRODUCTION

In this work we investigate the time evolution of massive, uniformly rotating, highly magnetized white dwarfs (WDs) when they lose angular momentum owing to magnetic dipole braking. We have different important reasons to perform such an investigation: 1) there is incontestable observational data on the existence of massive ($M \sim 1\ M_\odot$) WDs with magnetic fields all the way to 10^9 G (see (Kepler et al. 2015), and references therein); 2) WDs can rotate with periods as short as $P \approx 0.5$ s (Boshkayev et al. 2013b); 3) they can be formed in double WD mergers (García-Berro et al. 2012; Rueda et al. 2013; Kilic et al. 2018); 4) they have been invoked to explain type Ia supernovae within the *double degenerate scenario* (Webbink 1984; Iben & Tutukov 1984); 5) they constitute a viable model to explain soft gamma-repeaters and anomalous X-ray pulsars (Malheiro et al. 2012; Boshkayev et al. 2013a; Rueda et al. 2013; Boshkayev et al. 2015a; Belyaev et al. 2015).

Thus, it is of astrophysical importance to determine qualitatively and quantitatively the evolution of micro and macro physical properties such as density, pressure, temperature, mass, radius, moment of inertia, and angular velocity/rotation period of massive, uniformly rotating, highly magnetized WDs. We constrain ourselves in this work to study the specific case when the WD is isolated and it is losing angular momentum via magnetic dipole braking. In addition, we explore WDs with surface magnetic fields from 10^6 to 10^9 G and masses from 1.39 to 1.46 $M_\odot$.

Depending on their mass, WDs can exhibit different timing properties by losing angular momentum: uniformly and differentially rotating super-Chandrasekhar WDs (hereafter SCWDs) spin-up, whereas sub-Chandrasekhar WDs spin-down. The possibility that a rotating star spin-up by angular momentum loss was first revealed by Shapiro et al. (1990), and later by Geroyannis & Papasotiriou (2000). In both articles the WDs were studied within the Newtonian framework, though the effects of general relativity are crucial to determine the stability of massive, fast rotating WDs (see, e.g., (Shapiro & Teukolsky 1983; Rotondo et al. 2011b; Boshkayev et al. 2013b, 2015b; Carvalho et al. 2016, 2018b,a)). Besides the above timing features, we shall quantify the compression that the WD suffers while evolving via angular momentum loss which is relevant for some models of type Ia supernovae.

Specifically, we focus on the compression of isolated zero-temperature super-Chandrasekhar WDs and their isothermal cores by angular momentum loss based on our previous results (Boshkayev et al. 2013b, 2014a,b, 2017). We shall estimate the lifetime (τ) of zero temperature WDs via magnetic dipole braking taking into due account the effect of the time evolution of all relevant parameters of the WDs. In addition, for hot isothermal WD cores we compute the times of the nuclear burning and neutrino emission phenomena. For both cold and hot WDs, we consider two magnetic field evolution: (1) a constant magnetic field during the entire evolution and, (2) a varying magnetic field according to magnetic flux conservation (Boshkayev et al. 2014a,b, 2017).

The influence of the extreme magnetic field on the structure of a white dwarf has been studied by Das & Mukhopadhyay (2013, 2014). They showed that the inclusion of an interior huge magnetic field (of up to $\sim 10^{18}$ G), for the case of static white dwarfs, would increase the Chandrasekhar mass limit up to $\approx 2.58M_\odot$. However, the detailed analyses performed by Coelho et al. (2014); Malheiro et al. (2018) on the microscopic and macroscopic stability of such objects demonstrated that those masses are not attainable. Manreza Paret et al. (2015); Alvear Terrero et al. (2015) also calculated the effect of the magnetic field in white dwarfs. They showed that it was not possible to obtain stable magnetized white dwarfs with super-Chandrasekhar masses because the values of the surface magnetic field needed for them were higher than 10^{13} G. Thus Manreza Paret et al. (2015); Alvear Terrero et al. (2015) concluded that highly magnetized super-Chandrasekhar white dwarfs should not exist. Similar stability analyses were carried out by Chatterjee et al. (2017). They concluded that strongly magnetized super-Chandrasekhar white dwarfs could not be totally excluded from current theoretical considerations, though there are not any observational evidences.

The study of the structure of white dwarfs in the presence of spatially varying internal magnetic field that yields surface magnetic field $\sim 10^{13}$ G need further investigations (Chamel et al. 2013). This is, however, out of the scope of the current work. We constrain ourselves here to a surface dipole magnetic field up to the maximum observed values $\sim 10^9$ G (Kepler et al. 2015). This field is involved only as the mechanism to slow down uniformly rotating white dwarfs. Therefore, we do not consider the influence of the magnetic field to the structure of white dwarfs.

Our paper is organized as follows: in section 2, we discuss about WD equation of state, stability conditions and spin-up and spin-down effects; in section 3 we estimate the lifetime of SCWDs at zero temperature; in section 4 we show the compression of the WD during its evolution; and in section 5 we consider the central temperature evolution for isothermal WD cores. Finally, we summarize our results in section 6, discuss their significance, and draw our conclusions.

2 WD EQUATION OF STATE AND STABILITY

In this work, we will consider WDs surface magnetic field from 10^6 to 10^9 G, that are the highest magnetic field strengths observationally inferred with polarimetry and Zeeman spectroscopy from WDs data (see e.g. Wickramasinghe & Ferrario 2000). If one assumes that the magnetic field inside the star is uniform for a WD with $M_{\rm wd} = 1.44 M_\odot$ and $R_{\rm wd} = 3000$ km (Boshkayev et al. 2013b), its magnetic energy is about $E_m \approx (4\pi R_{\rm wd}^3/3)(B^2/8\pi) \sim 10^{39} - 10^{45}$ erg, much smaller than its gravitational energy $E_g \approx G M_{\rm wd}^2/R_{\rm wd} \sim 10^{50}$ erg. Thus, for the magnetic field strengths we are considering, the contribution of the magnetic energy to the structure equations of the star can be neglected.

It also is well known that a strong magnetic field will modify the equation of state of the matter due to the Landau quantization. However, even for magnetic field closed to the critical magnetic, field, which it is defined by $B_c = m_e^2 c^3/\hbar e \approx 4.41 \times 10^{13}$ G, the Landau quantization of the electron gas has an negligible effect on the global properties of WDs as on its mass-radius relation (Bera & Bhattacharya 2014; Chamel & Fantina 2015; Bera & Bhattacharya 2016; Chatterjee et al. 2017).

Although we model magnetized WDs, the unmagnetized description of the WD EoS and the WD structure will be a correct approximation, for the purposes of this article. Then, we follow in this work the treatment of Boshkayev et al. (2013b). It is worth mentioning that for high magnetic fields a self-consistent study must be conducted, taking into account the effects of the magnetic field in the WD equation of state and structure equations (see e.g. Chatterjee et al. 2017). For example, the spherical symmetry of the star will be broken and the stability of a star will be limited by microphysical processes affected also by the magnetic field Coelho et al. (2014). However, this treatment is out of the scope of this work.

In this work we compute general relativistic configurations of uniformly rotating WDs within Hartle's formalism (Hartle 1967; Boshkayev et al. 2011; Alvear Terrero et al. 2017; Terrero et al. 2017, 2018) and use the relativistic Feynman-Metropolis-Teller equation of state (Rotondo et al. 2011b,a) for WD matter. This equation of state generalizes the traditionally-used ones by Chandrasekhar (1931) and Salpeter (1961). A detailed description of this equation of state and the differences with respect to other approaches are given by Rotondo et al. (2011b).

The stability of uniformly rotating WDs has been analyzed taking into account the Keplerian sequence (mass-shedding limit), inverse β-decay instability, and secular axisymmetric instability by Boshkayev et al. (2013b). The mass-central density diagram of rotating WDs composed of pure ^{12}C for various angular momentum J=constant and angular velocity Ω=constant sequences has been illustrated in Fig 6 (Left panel) by (Boshkayev et al. 2013b). In addition, there we have included the critical density for pycnonuclear instability (in this case C+C reaction at zero temperature) with reaction time scales 10^5 and 10^{10} years. For ^{12}C WD, the maximun mass of the static configurations is $M_{\rm max}^{J=0} = 1.386\ M_\odot$ while for the uniformly rotating stars is $M_{\rm max}^{J\neq 0} = 1.474\ M_\odot$.

3 SUPER-CHANDRASEKHAR WD LIFETIME

We are interested in estimating the evolution of magnetized WDs when they are losing angular momentum via the magnetic dipole braking. It is well known that this braking mechanism needs, for a rotating magnetic dipole in vacuum, that the magnetic field is misaligned with the rotation axis. It has been shown that such WDs with misaligned fields could be formed in the merger of double degenerate binaries, and the degree of misalignment depends on the difference between the masses of the WD components of the binary (García-Berro et al. 2012).

Particularly interesting are the SCWDs which are stable by virtue of their angular momentum. Thus, by loosing angular momentum, they will evolve toward one of the aforementioned instability borders. This is the reason why, for example, magnetic braking of SCWDs has been invoked as a possible mechanism to explain the delayed time distribution of type Ia supernovae (Ilkov & Soker 2012): a type Ia supernova can be delayed for a time typical of the spin-down time scale τ due to magnetic braking, providing the result of the merging process of a WD binary system is a magnetic SCWD rather than a sub-Chandrasekhar one. It is important to recall that in such a model it is implicitly assumed that the fate of the WD is a supernova explosion instead of gravitational collapse. The competition between these two possibilities is an important issue which deserves to be further analyzed but it is out of the scope of this work.

Since SCWDs spin-up by angular momentum loss the reference to a “spin-down” time scale for them can be misleading. Thus, we prefer hereafter to refer the time the WD spend in reaching an instability border (either mass-shedding, secular or inverse β instability, see (Boshkayev et al. 2013b)).

As we have shown, the evolution track followed by a SCWD depends strongly on the initial conditions of mass and angular momentum, as well as on the nuclear (chemical) composition and the evolution of the moment of inertia. Clearly, the assumption of fixed moment of inertia leads to a lifetime scale that depends only on the magnetic field's strength. A detailed computation will lead to a strong dependence on the mass of the SCWD, resulting in a two-parameter family of lifetime $\tau = \tau(M, B) = t$. Indeed, we see from Fig. 1 that the moment of inertia even for a static case is not

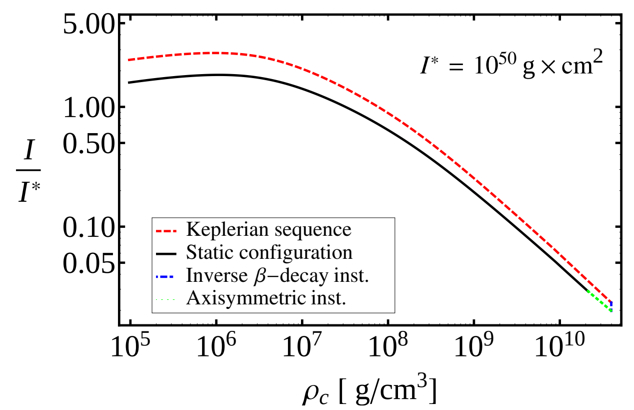

Figure 1. (Color online) Moment of inertia versus central density.

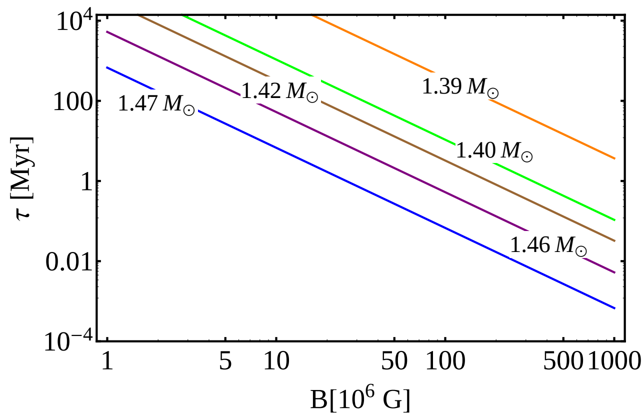

Figure 2. (Color online) Characteristic life time τ in Myr versus WD surface magnetic field B in Gauss for rotating ^{12}C WDs.

constant since it is a function of the central density. In the rotating case it is a function of both central density and angular velocity.

Thus, we have estimated the characteristic lifetime relaxing the constancy of the moment of inertia, radius and other parameters of rotating WDs. In fact we show here that all WD parameters are functions of the central density and the angular velocity. We used the original form of the lifetime formula

$$dt = -\frac{3}{2}\frac{c^3}{B^2}\frac{1}{R^6\Omega^3}dJ, \quad (1)$$

where c is the speed of light, B is the magnetic field intensity in Gauss, J is the angular momentum, Ω is the angular velocity and R is the mean radius calculated along the specific constant-rest-mass sequences.

Hence, we performed more refined analyses with respect to Ilkov & Soker (2012) by taking into consideration all the stability criteria, with the only exception of the instabilities related to nuclear reactions (either pynonuclear or enhanced by finite temperature effects) which we will consider in Sec. 5.

The characteristic lifetime τ as a function of the surface magnetic field for given sets of constant mass sequences is demonstrated in Fig. 2. Here each straight line corresponds to a certain fixed constant mass sequence. By choosing one value or the whole range of the magnetic field intensity one can estimate the lifespan of a SCWD for a given mass. One can see that the higher the magnetic field, the shorter the lifetime of the rotating SCWD. Correspondingly, a more massive WD will have a shorter lifespan and vice versa.

Another interesting representation of the characteristic lifetime τ as a function of WD mass in units of $M_{max}^{J=0}$ for zero temperature uniformly rotating ^{12}C WDs has been considered in Fig. 3 by Boshkayev et al. (2014b). There, one can see how for a fixed magnetic field value, the lifetime has a wide range of values as a function of the mass, being inversely proportional to the latter. The time scales of Ilkov & Soker (2012); Külebi et al. (2013) appear to be consistent with the one in Fig. 2 only for the maximum mass value $M/M_{max}^{J=0} \approx 1.06$.

4 INDUCED COMPRESSION

To investigate the evolution of isolated white dwarfs with time we made use of Eq. (1) and modified it depending on what parameter we are interested in (see (Boshkayev et al. 2014a, 2017) for details). Consequently, we adopt two cases: 1) when the magnetic field is constant and 2) when magnetic flux is conserved

$$B = B_0, \quad (2)$$

$$B = B_0\frac{R_0^2}{R^2}, \quad (3)$$

where B_0 is the surface dipole magnetic field corresponding to the initial value of B at $t = 0$, R_0 is the mean radius corresponding to the initial values of R at $t = 0$. Plugging B in Eq. (1) we obtain two separate equations that describe the evolution of a considered parameter with time taking into account two cases when magnetic field is constant and when magnetic flux is conserved. The behavior of the central density, mean radius and the magnetic field intensity as a function of the characteristic lifetime for both cases have been investigated by Boshkayev et al. (2014a). Similar analyses have been performed for the angular velocity as a function of the characteristic lifetime by Boshkayev et al. (2017).

For isolated rotating white dwarfs the rest mass remains unchanged in their entire evolution time and hence the moment of inertia of WDs in Fig. 3 has a direct correlation with the mean radius (see Boshkayev et al. (2017)). Since the angular momentum is lost by magnetic dipole braking in Fig. 4 we see for larger masses it decreases even faster than for smaller masses.

Overall, as one can see from the plots above the isolated WDs regardless of their masses due to magnetic dipole braking will always lose angular momentum (see e.g. Fig. 4). Therefore WDs will tend to reach a more stable configuration by increasing their central density and by decreasing their mean radius (see e.g. Boshkayev et al. (2017)). Ultimately, super-Chandrasekhar WDs will spin-up and sub-Chandrasekhar WDs spin-down. As for the WDs having masses near the Chandrasekhar mass limit, they will experience both spin up and spin down epochs at certain time of their evolution (Boshkayev et al. 2013b).

5 CENTRAL TEMPERATURE EVOLUTION

In this section, we model a SCWD as an isothermal core and follow its thermal evolution by solving the equation of energy conservation:

$$\frac{dL}{dm} = \epsilon_{\rm nuc} - \epsilon_\nu + T\dot{s} \quad (4)$$

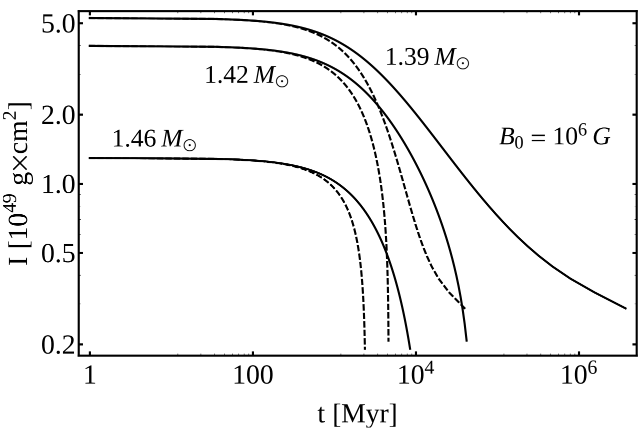

Figure 3. Moment of inertia versus time. Solid curves indicate the evolution path when the magnetic field is constant and dashed curves indicate the evolution path when the magnetic flux is conserved with $B_0 = 10^6$ G for selected constant mass sequences.

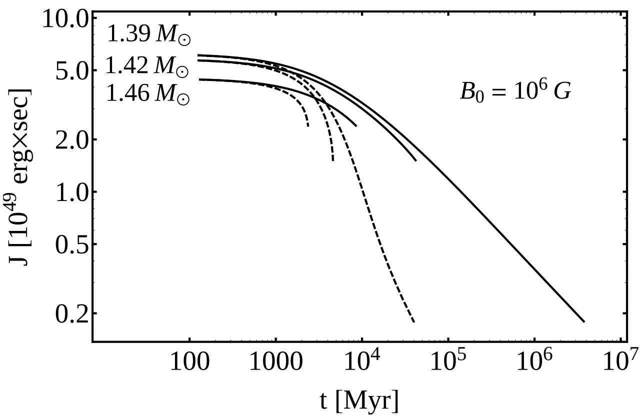

Figure 4. Angular momentum versus time. Solid curves indicate the evolution path when the magnetic field is constant and dashed curves indicate the evolution path when the magnetic flux is conserved with $B_0 = 10^6$ G for selected constant mass sequences.

where L is the luminosity, $\epsilon_{\rm nuc}$ is the nuclear reactions energy release per unit mass, ϵ_ν is the energy loss per unit mass by the emission of neutrinos, T is the temperature and s is the specific entropy. The last term of Eq. (4) can be written as:

$$T\dot{s} = c_{\rm v}\dot{T} - \left[\frac{P}{\rho^2} - \left(\frac{\partial u}{\partial \rho}\right)_T\right]\dot{\rho} \tag{5}$$

where u is the internal energy and $c_{\rm v}$ is the heat capacity at constant volume. For the latter, we used the analytic fits of Chabrier & Potekhin (1998); Potekhin & Chabrier (2000). The heat capacity is calculated from the Helmholtz free energy assuming a fully ionized plasma consisting of point-like ions immersed in an electron background. The plasma is characterized by the Coulomb coupling parameter, defined as the ratio between the potential energy and the thermal energy: $\Gamma = (Ze)^2/(\kappa_B T a)$, where $a = (4\pi/3\,n_i)^{-1/3}$ is the mean inter-ion distance and n_i is the ion number density. At $\Gamma \lesssim 1$ the ions behave as a gas, at $\Gamma > 1$ as a strongly coupled Coulomb liquid, while crystallization occurs at $\Gamma = \Gamma_m \approx 175$. The quantum effects are taken into account when $T_p \ll \hbar\omega_p/\kappa_B$, where $\omega_p = (4\pi Z^2 e^2 n_i/m_i)^{1/2}$ is the ion plasma frequency.

First, we integrate Eq. (4) with Eq. (5) neglecting the nuclear burning and neutrino emission processes. Fig. 5 shows the evolution of the WD central temperature for constant mass sequences ($M_{\rm WD} = 1.39, 1.42$ and $1.46\,M_\odot$) with two different initial temperature: $T(0) = 10^7$ K and $T(0) = 10^8$ K, respectively. They were obtained by solving simultaneously Eq. (1) and:

$$dT = \frac{P}{c_{\rm v}(\rho, T)\rho}\frac{\partial \log\rho}{\partial J}\,dJ\,. \tag{6}$$

For the magnetic field evolution, we have adopted the two cases of the previous section: constant surface magnetic field (see Eq. (2)) and constant magnetic flux (see Eq. (3)) with $B_0 = 10^6$ G. It is obvious that regardless of the initial temperature, the WD configuration heats up while it is compressing, as it is seen in Fig. 5.

In particular case, when $T(0) = 10^7$ K (left panel of Fig. 5), there is a phase transition from solid to liquid state while the system is heating. This could change the thermal evolution due to the latent heat and will depend on the abundance of chemical species (see e.g. (Isern et al. 1997; Chabrier 1997)). However, when $T(0) = 10^8$ K (right panel of Fig. 5), the configuration of the WD has a Coulomb parameter $\Gamma < 175$, i.e. the matter is in liquid state along its entire evolution.

In order to introduce the nuclear burning and the neutrinos emission process we have considered that for the rotating ^{12}C WDs the thermonuclear energy is essentially released by two nuclear reactions:

$$^{12}{\rm C} + {}^{12}{\rm C} \;\rightarrow\; {}^{20}{\rm Ne} + \alpha + 4.62\,{\rm MeV}, \tag{7}$$

$$^{12}{\rm C} + {}^{12}{\rm C} \;\rightarrow\; {}^{23}{\rm Na} + {\rm p} + 2.24\,{\rm MeV}, \tag{8}$$

with nearly the same probability. For the carbon fusion reaction rate, we used the fits obtained by Gasques et al. (2005) and for the neutrino energy losses we used the analytical fits calculated by Itoh et al. (1996), which account for the electron-positron pair annihilation ($e^-e^+ \to \nu\bar{\nu}$), photo-neutrino emission ($e + \gamma \to e\nu\bar{\nu}$), plasmon decay ($\gamma \to \nu\bar{\nu}$), and electron-nucleus bremsstrahlung [$e(Z,A) \to e(Z,A)\nu\bar{\nu}$].

The central temperature evolution is shown in Fig. 6 when the carbon fusion energy release and the neutrinos energy loses are taken into account. This was done by solving:

$$dT = \frac{P}{c_{\rm v}(\rho, T)\rho}\frac{\partial \log\rho}{\partial J}\,dJ + \frac{\epsilon_{\rm nuc} - \epsilon_\nu}{c_{\rm v}(\rho, T)}\,dt \tag{9}$$

At the beginning, when $T(0) = 10^7$ K (left panel of Fig. 6), the configuration heats via the energy release from the carbon fusion and the compression of the configuration. However, when $T(0) = 10^8$ K (right panel of Fig. 6), the energy losses from the neutrino emission process is the dominant process and it cools the configurations.

Fig. 7 shows the evolutionary path of some constant mass sequences in the central temperature and central density plane. It also exhibits the lines where the neutrino emissivity equals the nuclear energy release (i.e. carbon-ignition line: $\epsilon_{\rm nuc} = \epsilon_\nu$) and the lines along which the characteristic time of nuclear reactions, $\tau_{\rm nuc}$, equals one second (1 s) and equals the dynamical timescale, $\tau_{\rm dyn}$. The dynamical timescale $\tau_{\rm dyn}$ is defined as:

$$\tau_{\rm dyn} = \frac{1}{\sqrt{24\pi G\rho}}\,, \tag{10}$$

and the characteristic time of nuclear reactions is:

$$\tau_{\rm nuc} = \frac{\epsilon_{\rm nuc}}{\dot{\epsilon}_{\rm nuc}} = c_p\left(\frac{\partial \epsilon_{\rm nuc}}{\partial T}\right)^{-1} \tag{11}$$

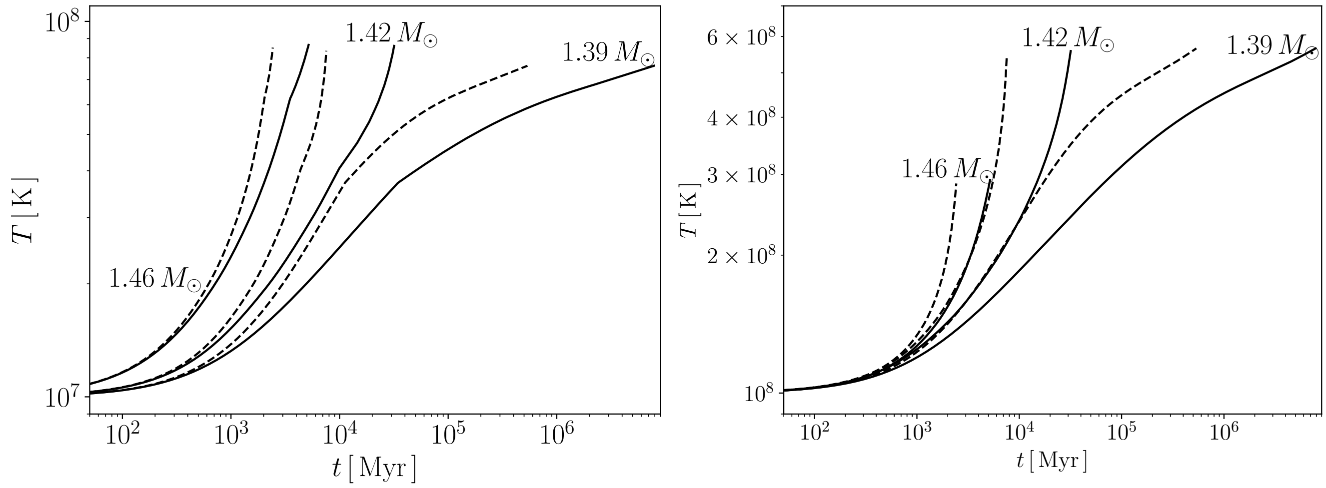

Figure 5. Central temperature versus time for constant mass sequences. Solid curves indicate the evolution path when the magnetic field is constant and dashed curves indicate the evolution path when the magnetic flux is conserved with $B_0 = 10^6$ G. Left panel: $T(0) = 10^7$ K. Right panel: $T(0) = 10^8$ K.

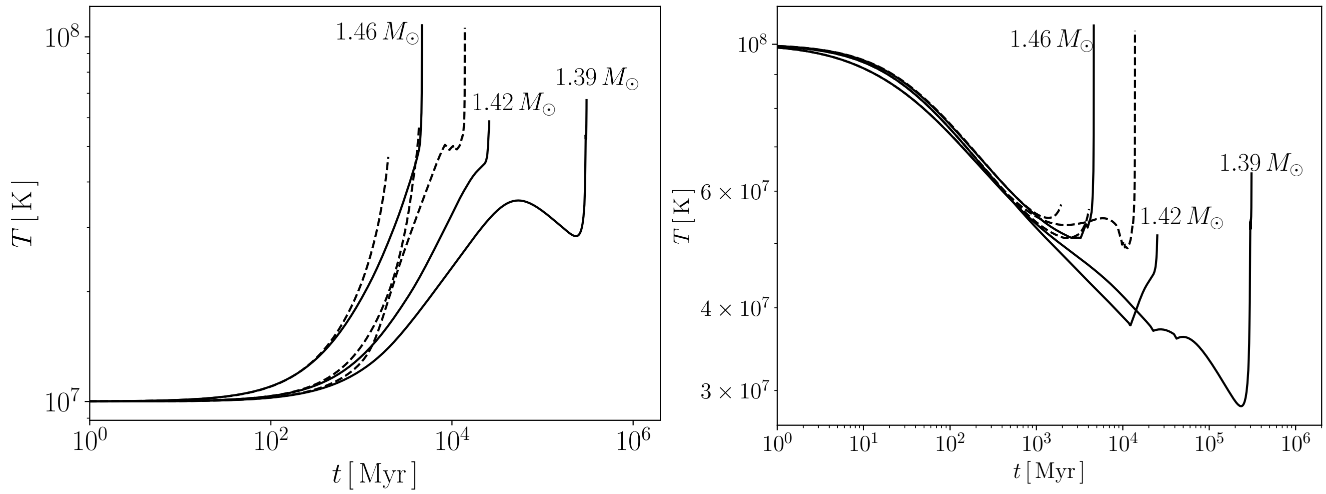

Figure 6. Central temperature versus time introducing carbon fusion energy release and neutrino energy losses. Solid curves indicate the evolution path when the magnetic field is constant and dashed curves indicate the evolution path when the magnetic flux is conserved with $B_0 = 10^6$ G for fixed constant mass sequences. Left panel: $T(0) = 10^7$ K. Right panel: $T(0) = 10^8$ K.

As seen in Fig. 7, all the configurations cross the carbon-ignition line. When this happens, the star will be heated evolving to a state at which the fusion reactions becomes instantaneous ($\tau_{\rm nuc} < \tau_{\rm dyn}$), possibly leading to a supernova. For some constant mass sequence, the configuration crosses the crystallization line, labelled as $\Gamma = 175$ in Fig. 7. When $T(0) = 10^8$ K, it happens just for $M = 1.39\,M_\odot$, while for lower initial temperature it happens for all the constant mass sequence considered here.

In Tab. 1, we compare the time needed by the configuration to reach an instability limit (mass-shedding, secular axisymmetric instability and/or inverse β decay instability), τ (see Eq. (1)), with the one needed to reach the carbon-ignition line when one just considers the compression of the star, $\Delta\tau_\rho$ (solving Eq. (6)), and when energy released from the carbon fusion and neutrino emission are introduced, $\Delta\tau_{\rm CC}$ (solving Eq. (9)), for the both magnetic field evolution: constant magnetic field and constant magnetic flux with $B_0 = 10^6$ G.

We have also specified the mass of the configuration, M, the initial angular velocity, Ω_0, the magnitude of the initial dynamical timescale, $\tau_{\rm dyn,0}$ as well as the initial central temperature, $T(0)$. In all cases the star arrives first to the ignition line then to the instability limit. This time difference is greater for less massive WDs than for more massive ones.

Finally, in Fig. 8, we show the τ, $\Delta\tau_\rho$ and $\Delta\tau_{\rm CC}$ as a function of the surface magnetic field strength when the field intensity is assumed to be constant along all the evolution, for different constant mass sequences and different initial temperature. The stronger surface magnetic field the shorter the WD lifetime.

6 CONCLUDING REMARKS

We have investigated in this work the evolution of the WD structure while it loses angular momentum via magnetic dipole braking. We obtained the following conclusions:

(i) We have computed the lifetime of SCWDs as the total time it

Table 1. Total WD Time Evolution ($B_0 = 10^6$ G): the first four columns correspond to the WD total mass, M, WD initial angular velocity, Ω_0, initial dynamical timescale, $\tau_{\rm dyn,0}$ and initial central temperature, $T(0)$, respectively. The following three columns correspond to the time needed by the WD to reach an instability boundary, τ, and to reach the carbon-ignition line when only the compression of the star is considered, $\Delta\tau_\rho$, and when the energy release from the carbon fusion and neutrino emission is introduced, $\Delta\tau_{\rm CC}$. First when the surface magnetic field is constant and then when the magnetic flux is conserved.

WD Parameters				Constant Magnetic Field			Constant Magnetic Flux		
M $M_\odot$	Ω_0 s^{-1}	$\tau_{\rm dyn,0}$ 10^{-4} s	$T(0)$ K	τ Myr	$\Delta\tau_\rho$ Myr	$\Delta\tau_{\rm CC}$ Myr	τ Myr	$\Delta\tau_\rho$ Myr	$\Delta\tau_{\rm CC}$ Myr
1.39	1.59	7.07	10^8	3.76×10^6	3.68×10^4	2.64×10^5	3.99×10^4	6.54×10^3	1.31×10^4
			10^7		3.09×10^5	2.64×10^5		1.35×10^4	1.31×10^4
			10^6		3.13×10^5	2.64×10^5		3.54×10^4	1.31×10^4
1.42	1.94	42.4	10^8	4.28×10^4	1.12×10^4	2.53×10^4	4.59×10^3	3.46×10^3	4.28×10^3
			10^7		2.54×10^4	2.53×10^4		4.31×10^3	4.28×10^3
			10^6		2.57×10^4	2.53×10^4		3.99×10^3	4.28×10^3
1.46	3.06	13.5	10^8	8.51×10^3	2.83×10^3	4.39×10^3	2.37×10^3	1.91×10^3	2.03×10^3
			10^7		2.34×10^3	4.45×10^3		2.24×10^3	2.03×10^3
			10^6		4.53×10^3	4.45×10^3		2.03×10^3	2.03×10^3

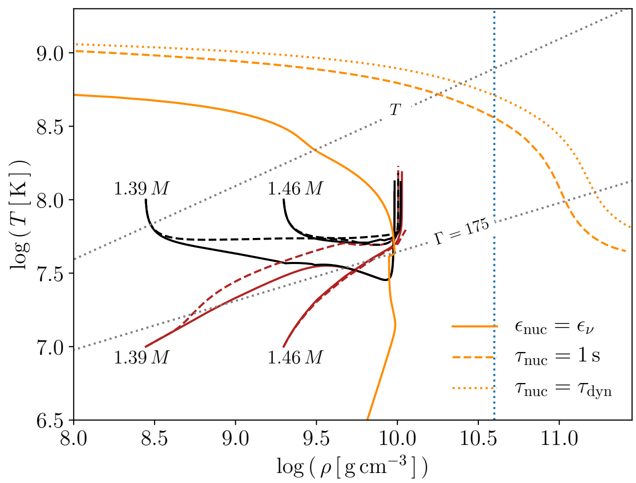

Figure 7. (Color online) The evolution track in the central density and central temperature plane with carbon fusion energy release and neutrino energy losses. We also show the carbon-ignition line (solid orange line), the line along which $\tau_{\rm nuc} = 1$ s and $\tau_{\rm nuc} = \tau_{\rm dyn}$. the crystallization line labeled as $\Gamma = 175$, and the plasma temperature line defined as $\kappa_B T_p = \hbar\omega_p$.

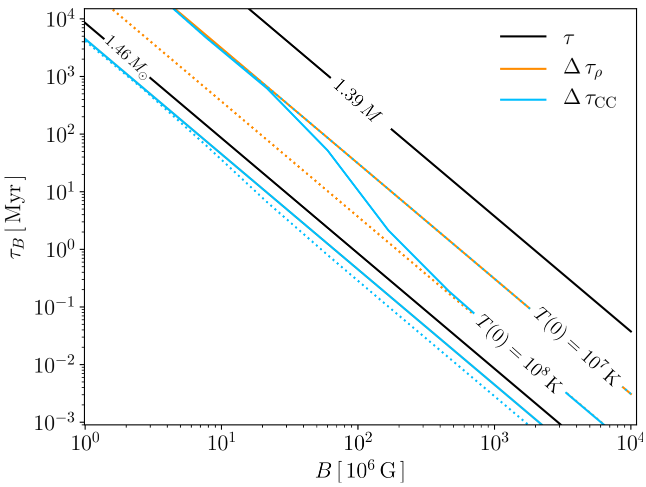

Figure 8. (Color online) Characteristic times of the WD evolution as a function of the surface magnetic field. Here, it is compared with the total time needed by the WD configuration to reach an instability limit, τ (solid black lines), the one needed to reach the carbon-ignition line when the compression of the star is considered, only, $\Delta\tau_\rho$ (orange lines), and when the energy release from the carbon fusion and neutrino emission is introduced, $\Delta\tau_{\rm CC}$ (blue lines).

spends in reaching one of the following possible instabilities: mass-shedding, secular axisymmetric instability and inverse β decay instability. The lifetime is inversely proportional both to the magnetic field and to the mass of the WD (see Fig. 2).

(ii) We showed how the parameters of rotating WDs evolve with time. For the sake the of comparison we considered two cases: a constant magnetic field and a varying magnetic field conserving magnetic flux. We showed that the WD is compressed with time. It turns out that, in the case of magnetic flux conservation, the evolution times are shorter than for the constant magnetic field, hence the WD lifetime.

(iii) The time scales of Ilkov & Soker (2012); Külebi et al. (2013) are consistent with the ones in Fig. 2 only for the maximum mass value $M/M^{J=0}_{max} \approx 1.06$.

(iv) Whether or not the SCWD can end its evolution as a type Ia supernova as assumed e.g. by Ilkov & Soker (2012) is a question that deserves to be further explored. Here, we have computed the evolution of the WD central temperature while it losses angular momentum along constant mass sequence. In general, the WD will increase its temperature while it is compressed. When carbon fusion reaction and neutrino emission cooling are considered, the evolution depends on the initial temperature. However, in all the cases studied, the configurations reach the carbon-ignition line. In this point the speed of the carbon fusion reactions increases until reaching conditions for a thermonuclear explosion.

(v) We have also computed the time that the SCWDs need in reaching the carbon-ignition line (central temperature and density conditions at which the energy release from the carbon fusion reactions equals the neutrino emissivity). This time is shorter than the timescale needed by the WD to reach mass-shedding, secular axisymmetric instability and/or inverse β decay instability.

(vi) If a magnetized sub-Chandrasekhar WD has a mass which is not very close to the non-rotating Chandrasekhar mass, then it evolves slowing down and on a much longer time scales with respect to SCWDs. It gives us the possibility to observe them during their life as active pulsars. Soft gamma-repeaters and anomalous X-ray pulsars appear to be an exciting possibility to confirm such a hypothesis (Malheiro et al. 2012; Boshkayev et al. 2013a; Rueda et al. 2013; Coelho & Malheiro 2014; Lobato et al. 2016). The massive, highly magnetized WDs produced by WD binary mergers, recently introduced as a new class of low-luminosity gamma-ray bursts (Rueda et al. 2018, 2019) would be another interesting case.

(vii) A magnetized WD produced in a WD binary merger will be surrounded by a Keplerian disk (García-Berro et al. 2012). Thus, to compute its evolution we have to consider the star-disk coupling and the angular momentum transfer from the disk to the WD (Rueda et al. 2013). These new ingredients would appear to invalidate our assumption of an isolated WD and the general picture drawn in this work. However, as shown by Rueda et al. (2013), accretion from the disk occurs in very short time scales and the WD lives most of its evolution in the dipole magnetic braking phase. Thus, we expect the WD lifetime computed in this work to be a good estimate also for those systems. In that case it is important to estimate the lifetime for the final WD mass after the accretion process since, as we have shown in Fig. 2, even a small increase in mass shortens drastically the lifetime.

ACKNOWLEDGEMENT

The work was supported by the Ministry of Education and Science of the Republic of Kazakhstan, Programs IRN: BR05236494.

REFERENCES

Alvear Terrero D., Castillo García M., Manreza Paret D., Horvath J. E., Pérez Martínez A., 2015, Astronomische Nachrichten, 336, 851
Alvear Terrero D., Manreza Paret D., Pérez Martínez A., 2017, Astronomische Nachrichten, 338, 1056
Belyaev V. B., Ricci P., Šimkovic F., Adam J., Tater M., Truhlík E., 2015, Nuclear Physics A, 937, 17
Bera P., Bhattacharya D., 2014, MNRAS, 445, 3951
Bera P., Bhattacharya D., 2016, MNRAS, 456, 3375
Boshkayev K., Rueda J., Ruffini R., 2011, International Journal of Modern Physics E, 20, 136
Boshkayev K., Izzo L., Rueda Hernandez J. A., Ruffini R., 2013a, A&A, 555, A151
Boshkayev K., Rueda J. A., Ruffini R., Siutsou I., 2013b, ApJ, 762, 117
Boshkayev K., Rueda J., Muccino M., 2014a, International Journal of Mathematics and Physics, 5, 33
Boshkayev K., Rueda J. A., Ruffini R., Siutsou I., 2014b, Journal of Korean Physical Society, 65, 855
Boshkayev K., Rueda J. A., Ruffini R., 2015a, in Rosquist K., ed., Thirteenth Marcel Grossmann Meeting On General Relativity. pp 2295–2300 (arXiv:1503.04176), doi:10.1142/9789814623995˙0424
Boshkayev K., Rueda J. A., Ruffini R., Siutsou I., 2015b, in Rosquist K., ed., Thirteenth Marcel Grossmann Meeting On General Relativity. pp 2468–2474 (arXiv:1503.04171), doi:10.1142/9789814623995˙0472
Boshkayev K., Rueda J. A., Ruffini R., Zhami B., 2017, in Jantzen R., ed., Forteenth Marcel Grossmann Meeting On General Relativity. pp 4379–4384 (arXiv:1604.02393)
Carvalho A., MarinhoJr R. M., Malheiro M., 2016, in Journal of Physics Conference Series. p. 052016, doi:10.1088/1742-6596/706/5/052016
Carvalho G. A., Marinho R. M., Malheiro M., 2018a, in Bianchi M., Jansen R. T., Ruffini R., eds, Fourteenth Marcel Grossmann Meeting - MG14. pp 4319–4324, doi:10.1142/9789813226609˙0579
Carvalho G. A., Marinho R. M., Malheiro M., 2018b, General Relativity and Gravitation, 50, 38
Chabrier G., 1997, in Bedding T. R., Booth A. J., Davis J., eds, IAU Symposium Vol. 189, IAU Symposium. pp 381–388 (arXiv:astro-ph/9705062)
Chabrier G., Potekhin A. Y., 1998, Phys. Rev. E, 58, 4941
Chamel N., Fantina A. F., 2015, Phys. Rev. D, 92, 023008
Chamel N., Fantina A. F., Davis P. J., 2013, Phys. Rev. D, 88, 081301
Chandrasekhar S., 1931, ApJ, 74, 81
Chatterjee D., Fantina A. F., Chamel N., Novak J., Oertel M., 2017, MNRAS, 469, 95
Coelho J. G., Malheiro M., 2014, PASJ, 66, 14
Coelho J. G., Marinho R. M., Malheiro M., Negreiros R., Cáceres D. L., Rueda J. A., Ruffini R., 2014, ApJ, 794, 86
Das U., Mukhopadhyay B., 2013, Physical Review Letters, 110, 071102
Das U., Mukhopadhyay B., 2014, J. Cosmology Astropart. Phys., 6, 050
García-Berro E., et al., 2012, ApJ, 749, 25
Gasques L. R., Afanasjev A. V., Aguilera E. F., Beard M., Chamon L. C., Ring P., Wiescher M., Yakovlev D. G., 2005, Phys. Rev. C, 72, 025806
Geroyannis V. S., Papasotiriou P. J., 2000, ApJ, 534, 359
Hartle J. B., 1967, ApJ, 150, 1005
Iben Jr. I., Tutukov A. V., 1984, ApJS, 54, 335
Ilkov M., Soker N., 2012, MNRAS, 419, 1695
Isern J., Mochkovitch R., García-Berro E., Hernanz M., 1997, ApJ, 485, 308
Itoh N., Hayashi H., Nishikawa A., Kohyama Y., 1996, ApJS, 102, 411
Kepler S. O., et al., 2015, MNRAS, 446, 4078
Kilic M., Hambly N. C., Bergeron P., Genest-Beaulieu C., Rowell N., 2018, MNRAS, 479, L113
Külebi B., Ekşi K. Y., Lorén-Aguilar P., Isern J., García-Berro E., 2013, MNRAS, 431, 2778
Lobato R. V., Malheiro M., Coelho J. G., 2016, International Journal of Modern Physics D, 25, 1641025
Malheiro M., Rueda J. A., Ruffini R., 2012, PASJ, 64, 56
Malheiro M., Marinho R. M., Lobato R. V., Coelho J. G., 2018, in Bianchi M., Jansen R. T., Ruffini R., eds, Fourteenth Marcel Grossmann Meeting - MG14. pp 4363–4371, doi:10.1142/9789813226609˙0586
Manreza Paret D., Horvath J. E., Perez Martínez A., 2015, Research in Astronomy and Astrophysics, 15, 1735
Potekhin A. Y., Chabrier G., 2000, Phys. Rev. E, 62, 8554
Rotondo M., Rueda J. A., Ruffini R., Xue S.-S., 2011a, Phys. Rev. C, 83, 045805
Rotondo M., Rueda J. A., Ruffini R., Xue S.-S., 2011b, Phys. Rev. D, 84, 084007
Rueda J. A., Boshkayev K., Izzo L., Ruffini R., Lorén-Aguilar P., Külebi B., Aznar-Siguán G., García-Berro E., 2013, ApJ, 772, L24
Rueda J. A., et al., 2018, J. Cosmology Astropart. Phys., 10, 006
Rueda J. A., et al., 2019, J. Cosmology Astropart. Phys., 3, 044
Salpeter E. E., 1961, ApJ, 134, 669
Shapiro S. L., Teukolsky S. A., 1983, Black holes, white dwarfs, and neutron stars: The physics of compact objects. New York, Wiley-Interscience
Shapiro S. L., Teukolsky S. A., Nakamura T., 1990, ApJ, 357, L17
Terrero D. A., Paret D. M., Martínez A. P., 2017, in International Journal of Modern Physics Conference Series. p. 1760025 (arXiv:1701.08792), doi:10.1142/S2010194517600254
Terrero D. A., Paret D. M., Martínez A. P., 2018, International Journal of Modern Physics D, 27, 1850016
Webbink R. F., 1984, ApJ, 277, 355
Wickramasinghe D. T., Ferrario L., 2000, PASP, 112, 873
d

THE ASTROPHYSICAL JOURNAL, 886:82 (13pp), 2019 December 1 https://doi.org/10.3847/1538-4357/ab4ce6

On the GeV Emission of the Type I BdHN GRB 130427A

R. Ruffini[1,2,3,4,5], R. Moradi[1,2], J. A. Rueda[1,2,4,6], L. Becerra[7], C. L. Bianco[1,2,6], C. Cherubini[2,8], S. Filippi[2,8], Y. C. Chen[1,2], M. Karlica[1,2,3], N. Sahakyan[2,9], Y. Wang[1,2], and S. S. Xue[1,2]

[1] ICRA, Dipartimento di Fisica, Sapienza Università di Roma, P.le Aldo Moro 5, I-00185 Rome, Italy; rahim.moradi@icranet.org, jorge.rueda@icra.it
[2] ICRA Net, P.zza della Repubblica 10, I-65122 Pescara, Italy
[3] Université de Nice Sophia Antipolis, CEDEX 2, Grand Château Parc Valrose, Nice, France
[4] ICRA Net-Rio, Centro Brasileiro de Pesquisas Físicas, Rua Dr. Xavier Sigaud 150, 22290–180 Rio de Janeiro, Brazil
[5] INAF, Viale del Parco Mellini 84, I-00136 Rome, Italy
[6] INAF, Istituto di Astrofisica e Planetologia Spaziali, Via Fosso del Cavaliere 100, I-00133 Rome, Italy
[7] Escuela de Física, Universidad Industrial de Santander, A.A.678, Bucaramanga, 680002, Colombia
[8] ICRA and Department of Engineering, University Campus Bio-Medico of Rome, Via Alvaro del Portillo 21, I-00128 Rome, Italy
[9] ICRA Net-Armenia, Marshall Baghramian Avenue 24a, Yerevan 0019, Armenia

Received 2018 December 6; revised 2019 August 23; accepted 2019 October 9; published 2019 November 22

Abstract

We propose that the inner engine of a type I binary-driven hypernova (BdHN) is composed of Kerr black hole (BH) in a non-stationary state, embedded in a uniform magnetic field B_0 aligned with the BH rotation axis and surrounded by an ionized plasma of extremely low density of 10^{-14} g cm^{-3}. Using GRB 130427A as a prototype, we show that this inner engine acts in a sequence of elementary impulses. Electrons accelerate to ultrarelativistic energy near the BH horizon, propagating along the polar axis, $\theta = 0$, where they can reach energies of $\sim 10^{18}$ eV, partially contributing to ultrahigh-energy cosmic rays. When propagating with $\theta \neq 0$ through the magnetic field B_0, they produce GeV and TeV radiation through synchroton emission. The mass of BH, $M = 2.31 M_{\odot}$, its spin, $\alpha = 0.47$, and the value of magnetic field $B_0 = 3.48 \times 10^{10}$ G, are determined self consistently to fulfill the energetic and the transparency requirement. The repetition time of each elementary impulse of energy $\mathcal{E} \sim 10^{37}$ erg is $\sim 10^{-14}$ s at the beginning of the process, then slowly increases with time evolution. In principle, this "inner engine" can operate in a gamma-ray burst (GRB) for thousands of years. By scaling the BH mass and the magnetic field, the same inner engine can describe active galactic nuclei.

Key words: black hole physics – binaries: general – gamma-ray burst: general – stars: neutron – supernovae: general

1. Introduction

Nine subclasses of gamma-ray bursts (GRBs) with binary progenitors have been recently introduced in Ruffini et al. (2016a, 2018c), Rueda et al. (2018), and Wang et al. (2019). One of the best prototypes of the long GRBs emitting 0.1–100 GeV radiation is GRB 130427A (Ruffini et al. 2015). GRB 130427A belongs to a special subclass of GRBs originating from a tight binary system with an orbital period of $\sim$5 minutes, and is composed of a carbon–oxygen core (CO_{core}) undergoing a supernova (SN) event in presence of a neutron star (NS) companion. The SN, as usual, gives rise to a new NS (νNS). For binary periods $\lesssim$5 minutes, the hypercritical accretion of the SN ejecta onto the companion NS leads it to exceed the critical mass for gravitational collapse and form a Kerr black hole (BH). We call these systems binary-driven hypernovae of type I (BdHNe I) with $E_{iso} > 10^{52}$ erg, as opposed to BdHNe II with binary periods $\gtrsim$5 minutes and $E_{iso} < 10^{52}$ erg when the NS critical mass is not exceeded (Wang et al. 2019). Figure 1 shows the ejecta density distribution of a BdHN I on the binary equatorial plane (left panel) and in a plane orthogonal to it (right panel) at the moment of gravitational collapse of the NS companion, namely at the moment of BH formation. These plots are the result of three-dimensional, numerical smoothed-particle-hydrodynamic (SPH) simulations of BdHNe recently described in Becerra et al. (2019).

In the specific case of GRB 130427A, this BdHN I is seen from "the top," with the viewing angle in a plane orthogonal to the plane of the orbit of the binary progenitor. This allows us to follow all the details of the high-energy activities around the BH. These include (a) the first appearance of the supernova (the *SN-rise*); (b) the observation of the ultrarelativistic prompt emission (UPE) following the BH formation (Ruffini et al. 2019a); (c) the feedback of the SN ejecta accreting onto the νNS leading to the X-ray afterglow (Ruffini et al. 2018b); and (d) the ultrahigh-energy process extracting the rotational energy of the BH, reducing its mass and spin, and generating the GeV and TeV radiation are presented in this article.

Soon after the BH formation, approximately 10^{57} baryons, which include the ones composing the NS companion, are enclosed in the BH horizon beyond any possible measurable effect apart from the total mass and spin of the BH.

A cavity of approximately 10^{11} cm is formed around the BH with a finite density of 10^{-6} g cm^{-3}; see Becerra et al. (2018, 2019). The evolution of such a cavity following the GRB explosion and its overtones inside the cavity has been addressed in Ruffini et al. (2019b), finally reaching a density of 10^{-13} g cm^{-3} inside the cavity.

The Kerr BH formation occurs in such a cavity in presence of an external uniform magnetic field aligned with the BH rotation axis, which we estimate to be $B_0 \sim 10^{10}$ G. For quantitative estimates, we consider it as mathematically described by a non-stationary Papapetrou solution (Wald 1974; Rueda et al. 2019).

As we will quantify later in this article, a sufficient amount of low-density ionized matter will be needed in the cavity to feed this inner engine.

In this article, we assume that the magnetic field and the BH spin are parallel. In that case, the induced electric field given by

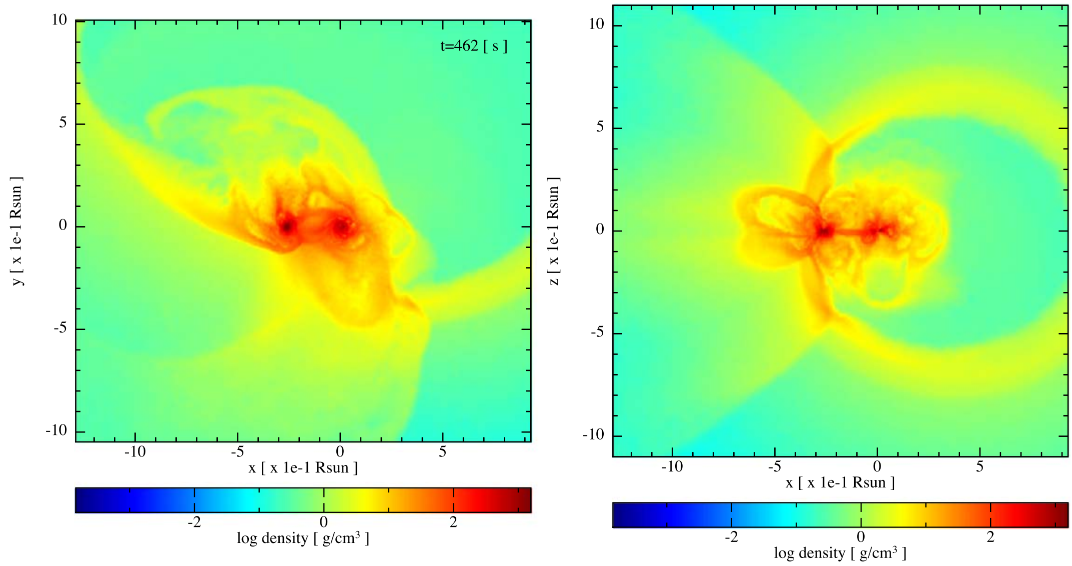

Figure 1. Selected SPH simulation from Becerra et al. (2019) of the exploding CO_{core} as SN in the presence of a companion NS: Model "25m1p07e" with $P_{orb} \approx 5$ minutes. The CO_{core} is taken from the 25 $M_{\odot}$ zero-age main-sequence (ZAMS) progenitor, so it has a mass $M_{CO} = 6.85\ M_{\odot}$. The mass of the NS companion is $M_{NS} = 2\ M_{\odot}$. The plots show the surface density on the equatorial binary plane (left panel) and on a plane orthogonal to it (right panel) at the time in which the NS companion reaches the critical mass and collapses to a BH, $t = 462$ s from the SN shock breakout ($t = 0$ of our simulation). The coordinate system has been rotated and translated in such a way that the NS companion is at the origin and the νNS is along the $-x$ axis.

the Wald solution is such that electrons (protons) along and near the rotation axis in the surrounding ionized circumburst medium are repelled (attracted) by the BH. The behavior is vice versa in the antiparallel case. As pointed out by Gibbons et al. (2013), the stability of Wald-like solutions is guaranteed only if the uniform field is confined to a radius smaller than the Melvin radius,

$$R_M \sim 2/B_0, \tag{1}$$

which imposes an upper limit for this geometry of about 10^{15} cm in our present case.[10] In this article, we show that the particle acceleration occurs near the BH horizon within distance of approximately 10^5 cm, much smaller than R_M.

We recall the definition of the critical electric and magnetic fields, E_c and B_c, i.e.,

$$E_c = \frac{m_e^2 c^3}{e\hbar}, \quad B_c = \frac{m_e^2 c^2}{e\hbar} = 4.4 \times 10^{13}\ \mathrm{G} \tag{2}$$

where m_e and e are the electron mass and charge, respectively.

Particular attention is devoted to identify the regimes in which the electric and magnetic fields are undercritcal or overcritical and, correspondingly, study the pair creation process and the associated absorption or transparency conditions for the GeV emission. In this article we focus on the undercritical regime in GRB 130427A.

Our main goal is to develop an "inner engine" model consistent with the transparency condition of the GeV and high-energy emissions from GRB 130427A. The model makes use of

(1) the rotational energy of the BH as its energy source;
(2) the acceleration and radiation processes of ultrarelativistic electrons near the horizon of the BH and in presence of the uniform magnetic field B_0, determined by using the electrodynamical properties of the Wald solution; and
(3) the determination of the highly anisotropic GeV, TeV, and UHECR emission by the synchrotron radiation, as a function of the injection angle of the ultrarelativistic electrons in the Wald solution.

As a byproduct, we show that

(1) the high-energy emission of GRB 130427A, far from being emitted continuously, actually occurs in a repetitive sequence of discrete, quantized, elementary impulsive events (or "quanta" for short);
(2) each quantum carries an energy of the order of 10^{37} erg; and
(3) each quantum is repetitively emitted with a repetition time $\sim 10^{-14}$ s.

The three fundamental parameters of the model, i.e., the Kerr BH mass, M, spin parameter, $\alpha = cJ/(GM^2)$, where J is the BH angular momentum, and the magnetic field B_0, are determined as follows:

(1) The magnetic field B_0 is obtained by imposing the transparency condition of the GeV luminosity, as well as the coincidence between the theoretical predicted repetition time of the "quanta" and the timescale of first impulsive event.
(2) The BH mass M and spin parameter α, as well as their their temporal evolution, are determined by obtaining the GeV luminosity via the extractable energy of the BH.
(3) In each one of these elementary impulsive events, we can estimate the depletion of the rotational energy of the Kerr BH; consequently, we can estimate that the high-energy emission process can indeed last for thousands of years.

The article is organized as follows. In Section 2 we recall the count rate and light curves of Fermi-GBM and *Fermi*-LAT for GRB 130427A. In Section 3 the basic equations for determining

[10] The conversion factor from CGS to geometric units for the magnetic field is $\sqrt{G}/c^2 \approx 2.86 \times 10^{-25}$, where G and c are the gravitational constant and speed of light in CGS units, respectively. Therefore, a magnetic field on the order of 10^{10} G in geometric units is $\approx 2 \times 10^{-25} \times 10^{10} \approx 2 \times 10^{-15}$ cm^{-1}, which leads to the Melvin radius of $R = 2/B_0 \approx 10^{15}$ cm.

the extraction of rotational energy from a Kerr BH to explain the GeV energetic are expressed in terms of the BH mass and spin. In Section 4 the electrodynamics of the "inner engine" is presented. In Section 5 the basic equations governing the synchrotron radiation in the magnetic field B_0, the first elementary event and the limit on the magnetic field to ground the transparency of the GeV radiation, are established. In Section 6 we determine the mass and spin of the BH to fulfill the GeV energy, and we address the decrease of the mass and spin of the BH as a function of the extracted rotational energy. In Section 7 the synchrotron radiation power and the need of a low-density ionized plasma in order to explain the number of needed electrons to feed the system is presented. In Section 8 the sequence of quanta and their repetition times are indicated. We also outline the mounting evidence that this system, developed here for the Wald solution applied for GRB 130427A, may well be extended to the much more massive BHs of $10^9 M_\odot$ in AGN such as M87.

2. Count Rate and Light Curves of Fermi-GBM and *Fermi*-LAT

As detailed in Levan et al. (2013), von Kienlin (2013), Xu et al. (2013), Flores et al. (2013), and Ruffini et al. (2015), GRB 130427A records a well-observed fluence in the optical, X-ray, gamma-ray, and GeV bands; see Figure 2.

The Fermi-GBM count rate of GRB 130427A with isotropic energy $E_{\rm iso} = (9.2 \pm 1.3) \times 10^{53}$ erg and $z = 0.34$ is shown in Figure 2(a). Clearly dentified are (a) the supernova raise (SN-rais; Liang et al. 2019) (b) the UPE phase following the BH formation (c) the emission of the cavity mentioned in the introduction, details in Liang et al. (2019). During the UPE phase, the event count rate of n9 and n10 of Fermi-GBM surpasses $\sim 8 \times 10^4$ counts per second in the prompt radiation between rest-frame times $T_0 + 3.4$ s and $T_0 + 8.6$ s. The GRB is affected by pile-up, which significantly deforms the spectrum; for details, see Ackermann et al. (2014) and Ruffini et al. (2015).

We therefore impose as the starting point of our analysis, the value $t_{\rm rf} = 16$ s, with $t_{\rm rf}$ being the rest-frame time, and cover all of the successive Fermi-GBM and *Fermi*-LAT data; see Figure 7(a).

In Figure 2(b) we give the luminosity of *Fermi*-LAT (red) and Fermi-GBM (blue); for details, see Ruffini et al. (2015) and Ajello et al. (2019). From the observations in Figure 2(b), at the onset of the GeV emission, the magnetic field B_0 and the corresponding electric field are largely overcritical, $E > E_c$ (Ruffini et al. 2019a). In these conditions, a plasma consisting of a vast number of e^+e^- pairs is produced by the vacuum polarization process. Such a plasma self-accelerates and emits at transparency region the MeV radiation; see, e.g., the vast literature quoted in Ruffini et al. (1999, 2000, 2007, 2010).

The vacuum polarization process creates the optically thick condition by which the GeV radiation is drastically reduced until the end of the UPE phase is reached (Ruffini et al. 2019a).

It was already shown in Damour & Ruffini (1975) that the feedback of such a vacuum polarization process can reduce the original overcritical magnetic field down to $\sim 10^{11}$ G.

One of the new issues raised by the data in Figure 2(b) (shown in more detail in Figure 2(c)), is precisely the conversion of the GeV photons into the MeV photons for $t_{\rm rf} < 16$ s. The conversion mechanism likely involves the Breit–Wheeler (Breit & Wheeler 1934) photon–photon pair creation $\gamma + \gamma \to e^+ + e^-$ (for details, see Ruffini et al. 2010, 2016b), because for GeV photons, their energy is larger than the threshold energy for pair production. Such a process is indeed responsible for absorption of GeV emission in some GRBs (see, e.g., Ackermann et al. 2011). This process leads to significant production of optically thick e^+e^- plasma and thermalization of high-energy photons at MeV energy. As the luminosity of photons in the MeV energy range decreases approaching $t_{\rm rf} = 16$ s, its number density decreases and consequently the opacity decreases as well. This implies less absorption of GeV photons: indeed, the flux of GeV photons increases.

Based on our recent work about the hard and soft X-ray flares (Ruffini et al. 2018a), the flare in the MeV band around $t_{\rm rf} = 100$ s observed in Figure 2(b) clearly occurs in the accreting hypernova ejecta that is well outside the conical GeV emission region. This feature is therefore not associated with the GeV emission mechanism treated in this article, and as it occurs outside the cone of the GeV emission, these GeV and MeV radiations are not interacting.

In view of the pile-up effect of GBM data indicated in Figure 2(a) and the absence of accurate data at $t_{\rm rf} < 16$ s, we will not approach the study of the overcritical field in GRB 130427A in this article.

We address instead the observation after $t_{\rm rf} = 16$ s, see Figure 2, where the condition of transparency of the GeV radiation is reached. We determine the self-consistent set of parameters that allow the transparency condition to be implemented and the mass and the spin of the BH will be in this context uniquely determined (see Section 5).

3. Determination of the Mass and Spin of the BH

In this section we identify the rotational energy of a Kerr BH as the energy source powering the GeV emission at $t > t_{\rm rf} = 16$ s; consequently, the mass and spin of the BH have to be determined.

The luminosity of *Fermi*-LAT (0.1–100 GeV), together with a power law best fit to the GeV luminosity of this GRB after $t > t_{\rm rf} = 16$ s are shown in Figure 3.

After $t > t_{\rm rf} = 16$ s, $E_{\rm GeV} = (1.2 \pm 0.01) \times 10^{53}$ erg, and the GeV luminosity is best fitted by

$$L = A \left(\frac{t}{1\,\rm s}\right)^{-\eta} \text{erg s}^{-1}, \tag{3}$$

with a slope of $\eta = 1.2 \pm 0.04$ and an amplitude of $A = (5.125 \pm 0.2) \times 10^{52}$; data and energy are retrieved from the second *Fermi*-LAT catalog (Ajello et al. 2019).

We now verify that the energetics of the GeV radiation can be explained by the extractable rotational energy of the Kerr BH, i.e.,

$$E_{\rm GeV} = E_{\rm extr} = (1.2 \pm 0.01) \times 10^{53}\,\text{erg}. \tag{4}$$

From the mass–energy formula of the Kerr BH (Christodoulou 1970; Christodoulou & Ruffini 1971; Hawking 1971; see also Misner et al. 1973), we have

$$M^2 = \frac{c^2 J^2}{4G^2 M_{\rm irr}^2} + M_{\rm irr}^2, \tag{5a}$$

$$S = 16\,\pi\, G^2\, M_{\rm irr}^2/c^4, \tag{5b}$$

where J, M, $M_{\rm irr}$, and S are the angular momentum, mass, irreducible mass, and horizon surface area of the Kerr BH, from

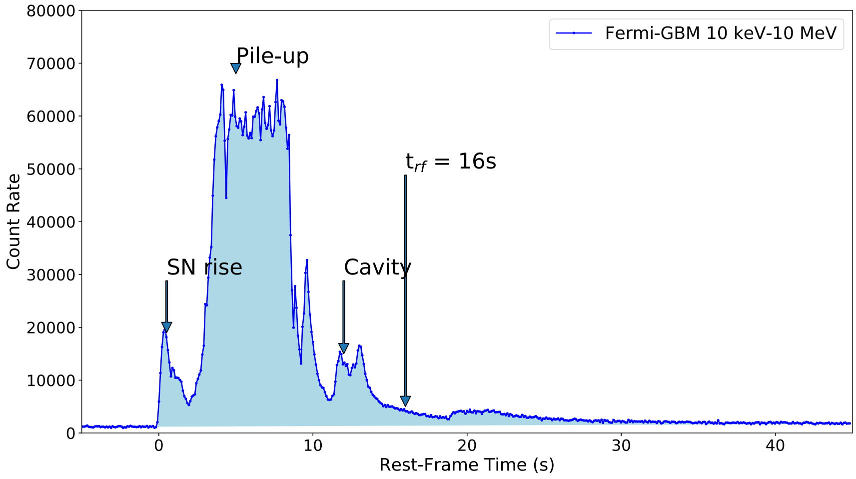

[a]

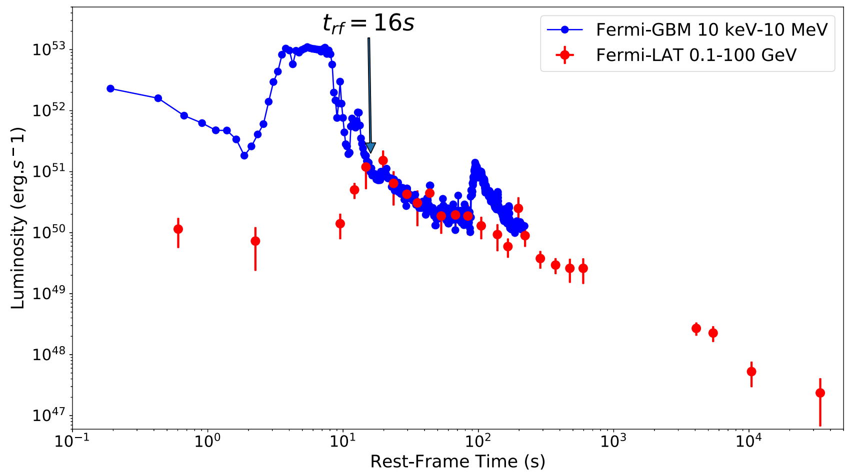

[b]

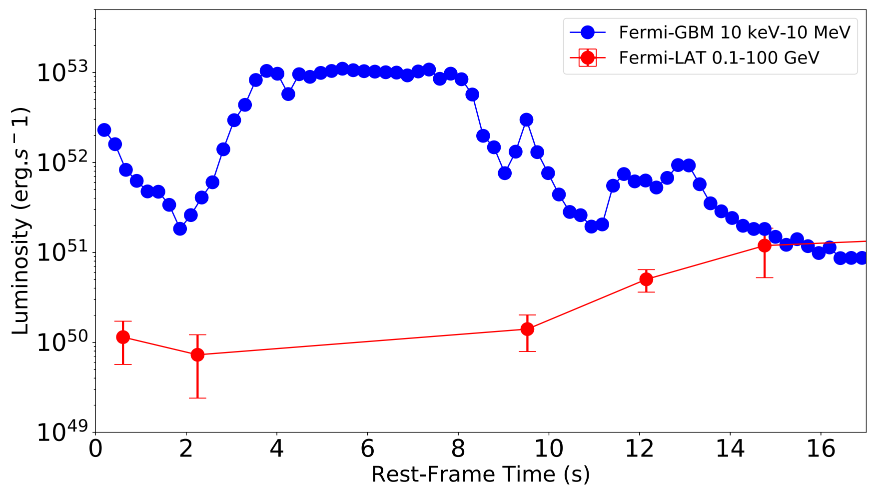

[c]

Figure 2. (a) The Fermi-GBM count rate of GRB 130427A. In the rest-frame time interval [T_0 + 3.4 s,T_0 + 8.6 s], the GRB is affected by pile-up. (b) The luminosity of GRB 130427A in the Fermi energy range. (c) The anticorrelation between the flux (luminosity) received by Fermi-GBM and *Fermi*-LAT in the time interval [1 s, 16 s], indicates that the primary photons in the GeV energy range are converted to the MeV photons due to the high opacity; for details, see Ruffini et al. (2015).

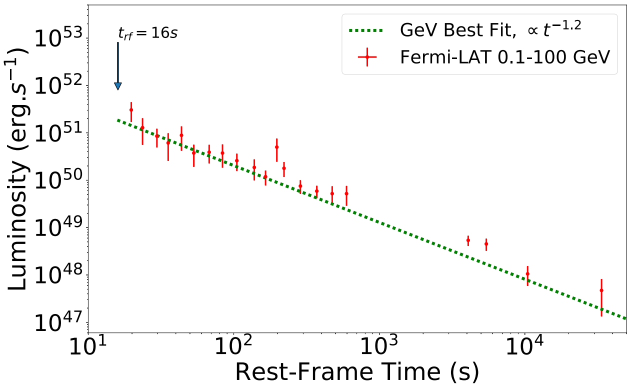

Figure 3. Rest-frame 0.1–100 GeV luminosity light curve of GRB 130427A obtained from *Fermi*-LAT, respectively. The green line shows the best fit for power-law behavior of the luminosity with slope of 1.2 ± 0.04 and amplitude of 5.125×10^{52} erg s^{-1}.

which we obtain consequently the extractable energy:

$$E_{\rm extr} = Mc^2 - M_{\rm irr}c^2 = \left(1 - \sqrt{\frac{1 + \sqrt{1 - \alpha^2}}{2}}\right)Mc^2, \quad (6)$$

where $\alpha = c\,a/(GM) = cJ/(GM^2)$ is the dimensionless angular momentum parameter, being $a = J/M$ the angular momentum per unit mass.

As we have two unknowns, M and α, and only one equation for one observable (Equation (4)), we need to provide a closure equation to the system to determining the two BH parameters.

In Section 5 we show how the transparency condition and the demand of the synchrotron radiation timescale to be equal to the timescale of the first impulsive event, inferred from the theory of "inner engine," gives the additional constraint to determine the mass and spin of the Kerr BH in this GRB.

4. On the Electrodynamics of the "Inner Engine"

We turn now to the electrodynamical mechanism which extracts the rotational energy in the inner engine.

We focus on a Wald solution within a cone of opening angle $\pi/3$ about the magnetic field direction; see Figure 4. In Figure 4 we consider the case of magnetic field "parallel," Figure 4(a) (antiparallel, Figure 4(b)) to the Kerr BH rotation axis, in which the electrons (protons) are accelerated away in the polar direction.

In this article we shall address the case of magnetic field parallel to the Kerr BH rotation axis, in which the electrons are accelerated away in the polar direction; see Figure 4(a).

We address only the leading in the angular and radial dependence of the field in the equation of motion. The electromagnetic field of the inner engine, in the first-order, slow rotation approximation and at second-order, small angle approximation, reads

$$E_{\hat{r}} \approx \frac{aB_0}{r}\left[\left(1 + \frac{GM}{c^2 r}\right)\theta^2 - \frac{2GM}{c^2 r}\right], \quad (7)$$

$$E_{\hat{\theta}} \approx \frac{aB_0}{r}\left(1 - \frac{2GM}{c^2 r}\right)^{1/2}\theta, \quad (8)$$

$$B_{\hat{r}} \approx B_0\left(1 - \frac{\theta^2}{2}\right), \quad (9)$$

$$B_{\hat{\theta}} \approx -B_0\left(1 - \frac{2GM}{c^2 r}\right)^{1/2}\theta. \quad (10)$$

Up to linear order in θ, the radial component of the electric field can be approximated by the expression

$$E_r \approx -\frac{1}{2}\alpha B_0\, c\frac{r_+^2}{r^2}. \quad (11)$$

At the BH horizon, $r_+ = (1 + \sqrt{1 - \alpha^2})GM/c^2$, the above electromagnetic field becomes

$$E_{\hat{r}} \approx -\frac{1}{2}\alpha B_0\, c\left(1 - \frac{3}{2}\theta^2\right), \quad (12)$$

$$E_{\hat{\theta}} \approx 0, \quad (13)$$

$$B_{\hat{r}} \approx B_0\left(1 - \frac{\theta^2}{2}\right), \quad (14)$$

$$B_{\hat{\theta}} \approx 0. \quad (15)$$

It can be seen from the full numerical solution, keeping all orders in the angular momentum (shown in Figure 4), that this approximation is valid up to $\theta_\pm = \pi/3$ and for the arbitrary value of α and within such limits our small angle approximation gives accurate qualitative and quantitative results.

We show how in the presence of a fully ionized low-density plasma, the GRB inner engine accelerates electrons up to ultrarelativistic energies in the abovementioned cavity. We assume that the emission process occurs near the BH and within magnetic field lines constant in time and uniform in space. The equations of motion for the electrons injected for selected angles θ are given below and specific examples in the Section 5.

When emitted in the polar direction $\theta = 0$, the inner engine can give rise to UHECRs. For $\theta \neq 0$, we integrate the equations of motion and evaluate the synchrotron emission keeping the leading terms.

5. Synchrotron Emission from the Wald Solution and the First Elementary Impulsive Event

The relativistic expression for the Lorentz force is

$$\frac{dp^\mu}{d\tau} = \frac{e}{c}F^{\mu\nu}u_\nu, \qquad p^\mu = mu^\mu, \qquad u^\mu = \frac{dx^\mu}{d\tau}, \quad (16)$$

where τ is the proper time, p^μ is the four-momentum, u^μ is the four-velocity, x^μ are the coordinates, $F^{\mu\nu}$ is the electromagnetic field tensor, m is the particle mass, e is the elementary charge, and c is the speed of light. This expression can be rewritten in the laboratory frame using vector notation as

$$mc\frac{d(\gamma\boldsymbol{v})}{dt} = e(\boldsymbol{E} + \boldsymbol{v} \times \boldsymbol{B}). \quad (17)$$

Assuming the one-dimensional motion along the radial directions, the dynamics of the electrons in the electromagnetic field (12)–(15), for $\gamma \gg 1$, is determined by the equation (see, e.g., de Jager et al. 1996)

$$m_e c^2\frac{d\gamma}{dt} = e\frac{1}{2}\alpha B_0\, c^2 - \frac{2}{3}e^4\frac{B_0^2\sin^2\langle\theta\rangle}{m_e^2 c^3}\gamma^2 c^2, \quad (18)$$

where γ is the electron Lorentz factor, $\langle\theta\rangle$ is the injection angle between the direction of motion and the magnetic field, and m_e is the electron mass. This equation is here

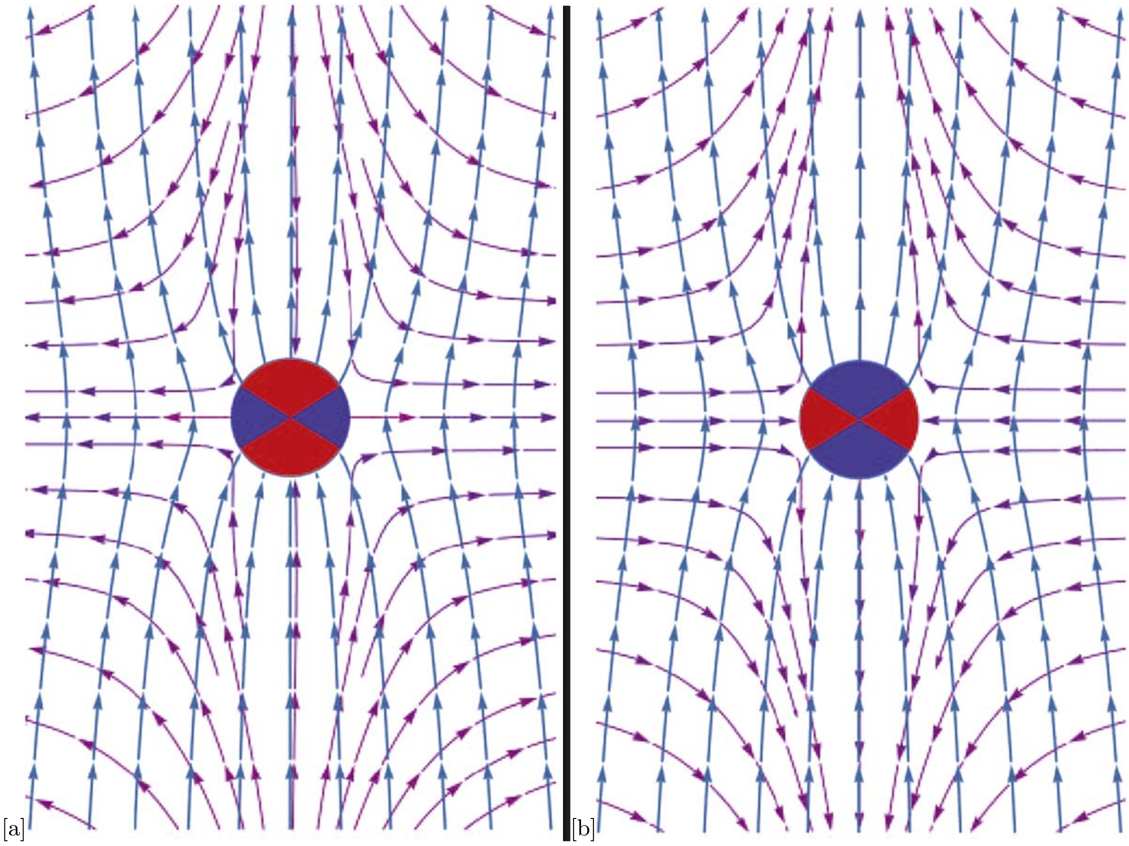

Figure 4. Electromagnetic field lines of the Wald solution. The blue lines show the magnetic field lines, and the violet show the electric field lines. (a) Magnetic field is "parallel" to the spin of the Kerr BH, so therefore parallel to the rotation axis. On the polar axis up to $\theta \sim \pi/3$, electric field lines are inwardly directed; therefore, electrons are accelerated away from the BH. For $\theta >$ pi/3, electric field lines are outwardly directed, and consequently protons are accelerated away from the BH. (b) Magnetic field is antiparallel to the Kerr BH rotation axis. On the polar axis up to $\theta \sim \pi/3$, electric field lines are outwardly directed; therefore, protons will be accelerated away from the BH. For $\theta > \pi/3$, electric field lines are inwardly directed, and consequently electrons will be accelerated away from the BH.

integrated for electrons assumed to be injected near the horizon, for the selected value of the injection angle $\langle\theta\rangle$, with an initial Lorentz factor of $\gamma = 1$ at $t = 0$.

Equation (18) is valid for every injection angle θ. The angle dependence in the electric field in Equation (18) is neglected, because the second term of the right-hand side of Equation (18), namely the synchrotron radiation term, is largely dominant for the parameters of interest in this work.

Assuming all parameters are constant, the approximate solution in the limit $\gamma \gg 1$ is

$$\gamma = \gamma_{\max} \tanh\left[\frac{2}{3}\frac{e^2}{\hbar c}\left(\frac{B_0 \sin\langle\theta\rangle}{B_c}\right)^2 \gamma_{\max}\frac{t}{\hbar/m_e c^2}\right], \tag{19}$$

which has the following asymptotic value:

$$\gamma = \begin{cases} \frac{1}{2}\frac{B_0}{B_c}\alpha\frac{t}{\hbar/m_e c^2}, & t \ll t_c, \\ \gamma_{\max}, & t \gg t_c, \end{cases} \tag{20}$$

where

$$\gamma_{\max} = \frac{1}{2}\left(\frac{3}{\frac{e^2}{\hbar c}}\alpha\frac{B_c}{B_0 \sin^2\langle\theta\rangle}\right)^{1/2} \tag{21}$$

and the critical time is

$$t_c = \frac{\hbar}{m_e c^2}\frac{3}{\sin\langle\theta\rangle}\left[\frac{e^2}{\hbar c}\left(\frac{B_0}{B_c}\right)^3\alpha\right]^{-1/2}. \tag{22}$$

The maximum peak photon energy of the synchrotron spectrum is obtained by using the maximum Lorentz factor of the radiating electrons, which is given by the equilibrium between energy gain and energy loss in Equation (18). Consequently, the following maximum energy of the electron-synchrotron photons is found:

$$\begin{aligned} \epsilon_{\max,\gamma} &= \frac{3e\hbar}{2m_e c}B_0 \sin\langle\theta\rangle\gamma_{\max}^2 = \frac{9}{8}\frac{m_e c^2}{e^2/\hbar c}\frac{\alpha}{\sin\langle\theta\rangle} \\ &\approx \frac{80}{\sin\langle\theta\rangle}\alpha \text{ MeV}. \end{aligned} \tag{23}$$

The maximum energy is independent of the magnetic field strength, which for different angles leads to different energy bands for the photons; see Figure 8. From this upper limit, some inferences on the TeV emission are in preparation, awaiting the publication of the TeV data. Here, we return to the GeV emission and to its energy originating from the BH rotational energy.

A vast amount of literature exists on the propagation of ultrahigh-energy protons/electrons in a magnetic field with $\theta = \pi/2$ (see e.g., Erber 1966 and references therein). Very little has been published for computations for small injection angles, $\theta \approx 0$ (an important exception being Harding 1991), which we also address here.

The maximum electric potential difference associated with the electric field is obtained by bringing an electron from the BH horizon to infinity along the symmetry/rotation ($\theta = 0$) axis:

$$\Delta\phi = \frac{\epsilon_e}{e} = \int_{r_+}^{\infty} E dr = E_{r_+} r_+ = 9.7 \times 10^{20} \cdot \xi\beta\mu(1 + \sqrt{1 - \xi^2}) \ \frac{\text{eV}}{e}, \tag{24}$$

where we have introduced $\beta \equiv B_0/B_c$ and $\mu \equiv M/M_\odot$, and E_{r_+} is the electric field evaluated at the horizon (see Equation (12)),

$$E_{r_+} = \frac{1}{2}\alpha B_0 c. \tag{25}$$

This potential can accelerate electrons along the symmetry axis up to a maximum Lorentz factor and energy given by

$$\epsilon_{e,\max} = e\Delta\phi = \gamma m_e c^2. \tag{26}$$

For $\theta = 0$, there is no energy loss due to synchrotron radiation, hence the total electrostatic energy goes into electron acceleration. The time of acceleration for $\theta = 0$ can be obtained from Equation (18) when the synchrotron loss term in the right-hand side is zero, i.e.,

$$m_e c^2 \frac{d\gamma}{dt} = e\frac{1}{2}\alpha B_0\, c^2 = eE_{r_+} c, \tag{27}$$

therefore,

$$t(\theta = 0) = \frac{m_e c^2 \gamma}{eE_{r_+} c} = \frac{E_{r_+} r_+}{E_{r_+} c} = \frac{r_+}{c}, \tag{28}$$

where we have used Equations (24) and (26).

5.1. Timescale of the First Impulsive Event

The electrostatic energy available is

$$\mathcal{E} = \frac{1}{2} E_{r_+}^2 r_+^3 = 7.5 \times 10^{41} \cdot \alpha^2\beta^2\mu^3(1 + \sqrt{1 - \alpha^2})^3 \ \text{erg}, \tag{29}$$

where we have used Equation (25).

Therefore, the timescale of the first impulsive event obtained from the GeV luminosity at $t_{\rm rf} = 16$ s, denoted as $\mathcal{E}_1 \equiv \mathcal{E}_{t_{\rm rf}=16\,\rm s}$, is

$$\tau_1 = \frac{\mathcal{E}_{t_{\rm rf}=16\,\rm s}}{L_{\rm GeV}(t_{\rm rf} = 16\ \rm s)}, \tag{30}$$

which reads

$$\tau_1 = 4.08 \times 10^{-10} \alpha^2\beta^2\mu^3(1 + \sqrt{1 - \alpha^2})^3 \ \text{s}, \tag{31}$$

where we have used Equation (3) we turn now to a crucial relation between α and β.

5.2. Transparency of GeV Photons

The hypercritical accretion onto the NS and its subsequent collapse forming the BH, depletes the BdHN by $\approx 10^{57}$ baryons, creating a cavity of $\approx 10^{11}$ cm of radius in the hypernova ejecta around the BH site (see Becerra et al. 2016, 2019). The density inside the cavity at BH formation is about 10^{-6} g cm^{-3} (Becerra et al. 2016, 2019), and is further decreased to about 10^{-13} g cm^{-3} by the GRB explosion (Ruffini et al. 2019b). The low density of this cavity guarantees a condition of low baryon density necessary for the transparency and therefore for the observation of the MeV emission in the UPE, as well as the higher-energy band emission discussed in the present work (see Ruffini et al. 2019a, 2019b for details). However, this condition for transparency, while necessary, is not sufficient.

There is a most stringent condition imposed by the interaction of the synchrotron photons with the field B_0.

Synchrotron photons of energy ϵ_γ may produce e^+e^- pairs in external magnetic field. The inverse of the attenuation coefficient (Daugherty & Harding 1983),

$$\bar{R} \sim 0.23 \frac{e^2}{\hbar c}\left(\frac{\hbar}{m_e c^2}\right)^{-1} \beta \sin\langle\theta\rangle \exp\left(-\frac{4/3}{\frac{\epsilon_\gamma}{2m_e c^2}\beta\sin\langle\theta\rangle}\right). \tag{32}$$

Imposing the following transparency condition for 0.1 GeV photons, $\bar{R}^{-1} \geqslant 10^{16}$ cm, we obtain

$$\beta \leqslant 3.67 \times 10^{-4}\alpha^{-1}, \tag{33}$$

where we have replaced Equation (23) with (32) to express the dependence of $\bar{R}$ on the pitch angle in terms of the peak photon energy and the spin parameter (see Figure 6).

We shall use this equation in next section to obtain mass and spin of BH in GRB 130427A.

6. Mass and Spin of BH

As there are three unknown parameters, namely M, α, and β, and only two equations, namely Equation (4) via (6), and Equation (33), an additional equation is needed to determine the three parameters of the inner engine.

For this purpose, we request the additional constraint that the timescale of the synchrotron radiation, obtained from Equation (22), be equal to the radiation timescale obtained from Equation (30), at the time $t_{\rm rf} = 16$ s, i.e., the following three equations must be solved simultaneously:

$$E_{\rm GeV} = E_{\rm extr}(\mu, \alpha), \tag{34}$$

$$\beta = 3.67 \times 10^{-4}\alpha^{-1}, \tag{35}$$

$$t_c(\langle\theta\rangle, \alpha, \beta) = \tau_{\rm ob,1}(\mu, \alpha, \beta, L_{\rm GeV}). \tag{36}$$

We can solve this system of equations as follows. First, from Equation (34), we can isolate μ as a function of $E_{\rm GeV}$ and α:

$$\mu = \left(1 - \sqrt{\frac{1 + \sqrt{1 - \alpha^2}}{2}}\right)^{-1} \frac{E_{\rm GeV}}{M_\odot c^2}. \tag{37}$$

Then, by replacing Equation (37) with (36), we obtain an expression for β as a function of the observables $E_{\rm GeV}$ and $L_{\rm GeV}$, and α:

$$\beta = \beta(\epsilon_\gamma, E_{\rm GeV}, L_{\rm GeV}, \alpha) = \frac{1}{\alpha}\left(\frac{64}{9}\sqrt{3\frac{e^2}{\hbar c}}\frac{\epsilon_\gamma}{B_c^2\, r_+(\mu, \alpha)^3}\frac{L_{\rm GeV}}{e\, B_c\, c^2}\right)^{2/7}, \tag{38}$$

where we have replaced Equation (23) into (22) to express t_c as a function of the peak photon energy ϵ_γ instead of the pitch

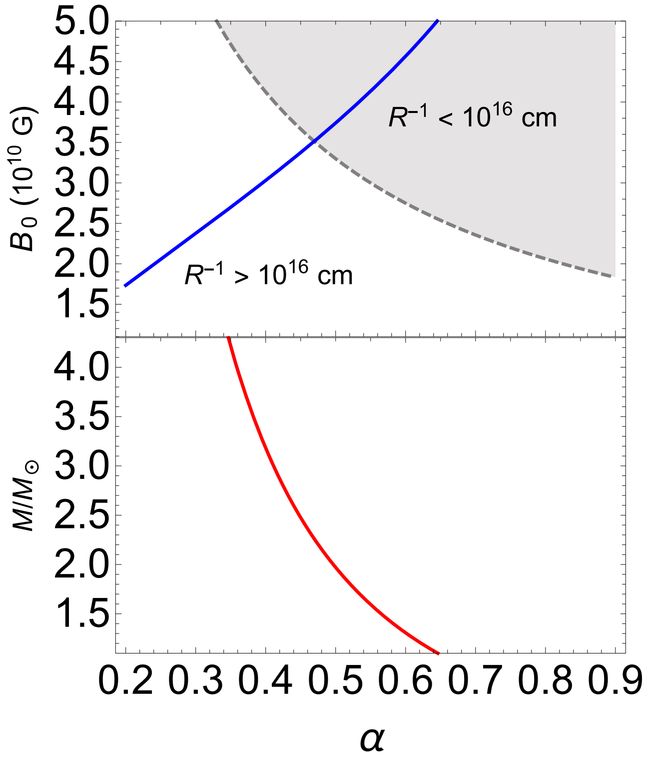

Figure 5. Upper panel: self-consistent family of solutions of the magnetic field B_0 as a function of the BH spin parameter α (blue curve), Equation (38), for given values of $E_{\rm GeV} = 1.2 \times 10^{53}$ erg, $L_{\rm GeV} = 1.84 \times 10^{51}$ erg s^{-1}, and $\epsilon_\gamma = 0.1$ GeV. Inside the gray shaded region 0.1 GeV photons have $\bar{R}^{-1} < 10^{16}$ cm, while in the white one they fulfill the condition of transparency $\bar{R}^{-1} \geqslant 10^{16}$ cm, namely Equation (33). The crossing between the blue curve and the border of the gray region gives us the upper limit of the magnetic field $B_0 \approx 3.5 \times 10^{10}$ G and the spin parameter $\alpha = 0.47$, to have transparency of the GeV photons. Lower panel: self-consistent solution of the BH mass as a function of the BH spin parameter α (red curve). To the maximum spin parameter for transparency, it corresponds a lower limit to the BH mass, $M = 2.31 M_\odot$.

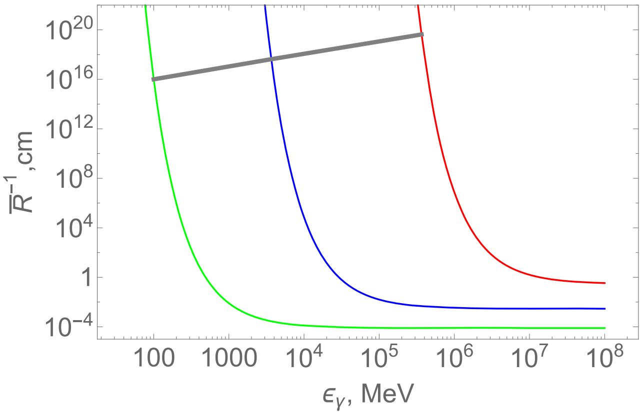

Figure 6. Inverse of the attenuation coefficient for pair production in magnetic field (Equation (32)) computed for $\beta = B_0/B_c = 7.84 \times 10^{-4}$, and selected $\langle\theta\rangle$ of $\pi/8$ (green), 10^{-2} (blue) and 10^{-4} (red). The peak of the synchrotron spectrum, given by Equation (23) and shown by the gray line, is in the transparent region.

angle, and r_+ is the BH horizon, which is a function of μ and α, but via Equation (37), becomes a function of $E_{\rm GeV}$ and α.

Therefore, given the energy $E_{\rm GeV}$ (integrated for times $t_{\rm rf} \geqslant 16$ s) and luminosity $L_{\rm GeV}$ (at $t_{\rm rf} = 16$ s), Equation (38) gives the self-consistent family of solutions of the magnetic field β as a function of the BH spin parameter α. In Figure 5 (blue curve in the upper panel) we show such a family of self-consistent solutions in the case of $E_{\rm GeV} = 1.2 \times 10^{53}$ erg (see Equation (4)), $L_{\rm GeV} = 1.84 \times 10^{51}$ erg s^{-1} given by Equation (3), and photon energy $\epsilon_\gamma = 0.1$ GeV.

From Equation (33), we know β as a function of α, for which the condition of transparency is satisfied. Therefore, by equating Equations (38) and (33), we obtain, as can be seen from Figure 5, a maximum spin parameter, α, to fulfill the transparency condition for 0.1 GeV photons. Correspondingly, there is the maximum magnetic field value that can be obtained by substituting the upper value of α either into Equation (38) or (33). Then, the maximum α is used in Equation (37) to obtain the corresponding lower limit for the BH mass. For the above numbers, the upper magnetic field value to have transparency is $\beta = 7.8 \times 10^{-4}$, i.e., $B_0 \approx 3.5 \times 10^{10}$ G. The maximum spin and a minimum BH mass are, respectively, $\alpha \approx 0.47$ and $M = 2.31\, M_\odot$. For the above spin value, we obtain from Equation (23) the pitch angle to emit 0.1 GeV photons, $\theta \approx \pi/8$. The corresponding BH irreducible mass is $M_{\rm irr} = 2.24\, M_\odot$, which is close to critical mass of the NS for some specific nuclear equation of state, in particular to the TM1 one (see Cipolletta et al. 2017). These parameters will be used in next subsection as the initial values of mass and spin parameters to find the spin-down of the BH.

The inverse of the attenuation coefficient from Equation (32) computed for $\beta = 7.84 \times 10^{-4}$ and different $\langle\theta\rangle$ is presented in Figure 6. The peak of the synchrotron spectrum (Equation (23)) shown by the gray line in Figure 6 is located in the transparent region. We can see from the figure that synchrotron photons, when produced in the 0.1 GeV to 1 TeV energy band, do not produce pairs if magnetic field is below $B_0 < 3.5 \times 10^{10}$ G. Therefore, this region is transparent for such photons.

6.1. The Decrease of the Mass and Spin of the BH as a Function of the Extracted Rotational Energy

From the luminosity expressed in the rest-frame of the sources, and from the initial values of the spin and of the mass of the BH, we can now derive the slowing down of the BH due to the energy loss in the GeV emission. The time derivative of Equation (6) gives the luminosity

$$L = -\frac{dE_{\rm extr}}{dt} = -\frac{dM}{dt}. \tag{39}$$

Because $M_{\rm irr}$ is constant for each BH during the energy-emission process, and using our relation for luminosity from Equation (3), we obtain the relation of the loss of mass–energy of the BH by integrating Equation (39):

$$M = M_0 + 5At^{-0.2} - 5At_0^{-0.2}, \tag{40}$$

where M_0 is the initial BH mass at, $t_0 = 16$ s, and $A = (5.125 \pm 0.2) \times 10^{52}$. From the mass–energy formula of the BH we have

$$J = 2M_{\rm irr}\sqrt{M^2 - M_{\rm irr}^2}, \tag{41}$$

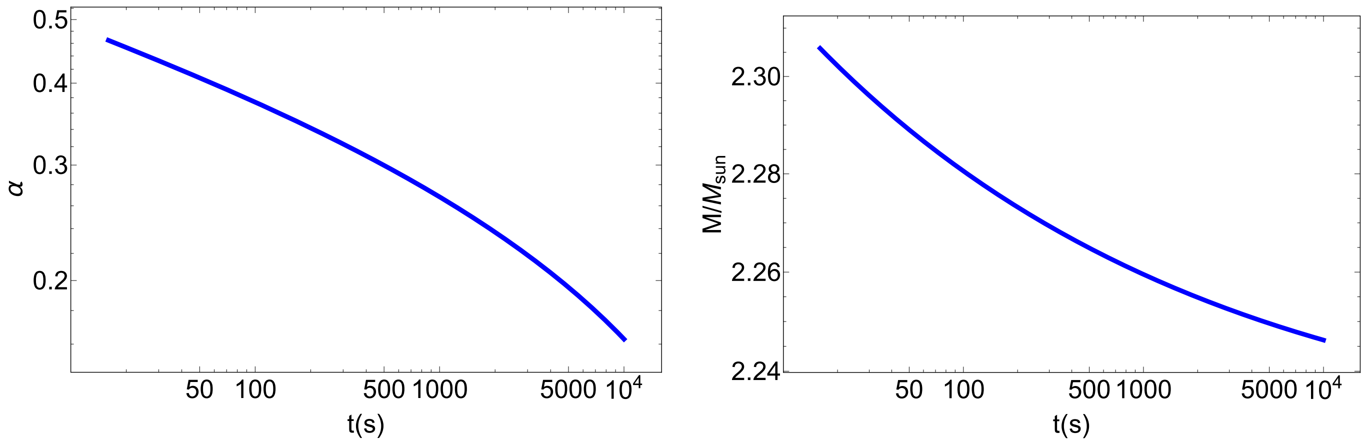

(a) (b)

Figure 7. (a) and (b) The decrease of the BH spin and Mass, as a function of rest-frame time for GRB 130427A. The values of spin and mass at the moment which prompt is finished, which has been assumed to occur at the rest-frame time of $t_{\rm rf} = 16$ s, are: $\alpha = 0.47$ and $M(\alpha) = 2.31 M_{\odot}$.

therefore,

$$a = \frac{J}{M} = 2M_{\rm irr}\sqrt{1 - \frac{M_{\rm irr}^2}{(M_0 + 5At^{-0.2} - 5At_0^{-0.2})^2}}. \tag{42}$$

The values of mass and spin parameters at $t_0 = t_{\rm rf} = 16$ s; see Figure 3 are $M_0 = 2.31 M_{\odot}$ and $\alpha = 0.47$, and the irreducible mass is $M_{\rm irr} = 2.24\, M_{\odot}$. The behavior of $\alpha = J/M^2$ and M with time are shown in Figure 7. Both α and M decrease with time, which shows the decrease of rotational energy of the BH due to the energy loss in GeV radiation; see Figure 7. It is important to recall that, since we are here inferring the BH energy budget using only the GeV emission data after the UPE phase, the above BH mass and spin have to be considered as lower limits.

7. Synchrotron Radiation Power and the Need of a Low Density Ionizes Plasma

Having obtained the values of spin, $\alpha = 0.47$, mass $M = 2.31 M_{\odot}$, and magnetic field, $B_0/B_c = 7.8 \times 10^{-4}$, we integrate the equation of motion given by Equation (18) to obtain the radiation in the GeV and TeV bands corresponding to selected values of θ.

As an example, we show the results for the electron propagation and radiation for selected angles, i.e., $\theta = \pi/8$, $\theta = 1 \times 10^{-2}$, $\theta = 1 \times 10^{-4}$ with respect to the direction of the magnetic field. According to Equation (23), these angles are related to $\sim$0.1 GeV, $\sim$4 GeV and $\sim$0.4 TeV energy of photons, respectively, which covers the lower limit of *Fermi*-LAT instrument until the lower limit of MAGIC telescope; see Figure 8(a). The numerical solution of Equation (18), along with analytic solutions, are represented in Figure 8(a). The electron-synchrotron luminosity from the right-hand side of Equation (18) is

$$\dot{E}_{\rm sync} = \frac{2}{3} e^4 \frac{B_0^2 \sin^2\langle\theta\rangle}{m_e^2 c^3}\gamma^2. \tag{43}$$

In Figure 8(c), we present the total power of the synchrotron emission by a single electron as a function of time for selected injected angles θ. The power increases with time, and then at $t > t_c$ approaches a constant value, which does not depend on the angle

$$\dot{E}_{{\rm sync},\gamma_{\rm max}} = \frac{1}{2}\frac{(m_e c^2)^2}{\hbar}\frac{B_0}{B_c}\alpha = 1.16 \times 10^{11}\ {\rm erg\ s^{-1}}. \tag{44}$$

In Figure 8(d) we show the peak energy of the synchrotron photons given by Equation (23) as a function of the electron injection angle and the magnetic field.

The total energy emitted by an electron in synchrotron radiation, computed by integrating the synchrotron power with time, gives

$$E_{\rm sync} = \begin{cases} \dfrac{1}{18}\dfrac{e^2}{\hbar c}\left(\dfrac{B_0}{B_c}\right)^4 \alpha^2 \left(\dfrac{t}{\hbar/m_e c^2}\right)^3 \sin^2\langle\theta\rangle m_e c^2, & t < t_c,\\[2ex] \dfrac{1}{2}\alpha\dfrac{B_0}{B_c}\dfrac{t}{\hbar/m_e c^2} m_e c^2, & t > t_c, \end{cases} \tag{45}$$

where, from Equation (22), the critical time for $\alpha = 0.47$, $B_0/B_c = 7.8 \times 10^{-4}$ is

$$t_c \simeq \frac{5.9 \times 10^{-15}}{\sin\langle\theta\rangle}\ {\rm s}. \tag{46}$$

The synchrotron timescale, obtained from Equation (46), has values between 1.6×10^{-14} s and 2×10^{-5} s; see Figure 8(a). According to Equation (45), the total energy available for the synchrotron radiation of one electron is a function of synchrotron timescale; see Figure 8(b). Each timescale corresponds to the time which takes for one electron to radiate by synchrotron mechanism its acceleration energy $\epsilon_e = \gamma_{\rm max} m_e c^2$, where $\gamma_{\rm max}$ is given by Equation (21). For $\theta = \pi/8$, which is related to the lower limit of *Fermi*-LAT energy bandwidth, namely 0.1 GeV, $t_c = 1.6 \times 10^{-14}$ s, corresponds to $\epsilon_e = 1.02 \times 10^9$ eV. Therefore,

$$t_{\rm c,GeV} = 1.6 \times 10^{-14}\ {\rm s}. \tag{47}$$

For the available electromagnetic energy budget, the system can accelerate a total number of electrons with the above energy:

$$N_e = \mathcal{E}_1/\epsilon_e \approx 6.6 \times 10^{39}, \tag{48}$$

where $\mathcal{E}_1 \approx 10^{37}$ erg is electrostatic energy available, the blackholic quantum (Rueda & Ruffini 2019), for the first impulsive event obtained from Equation (29).

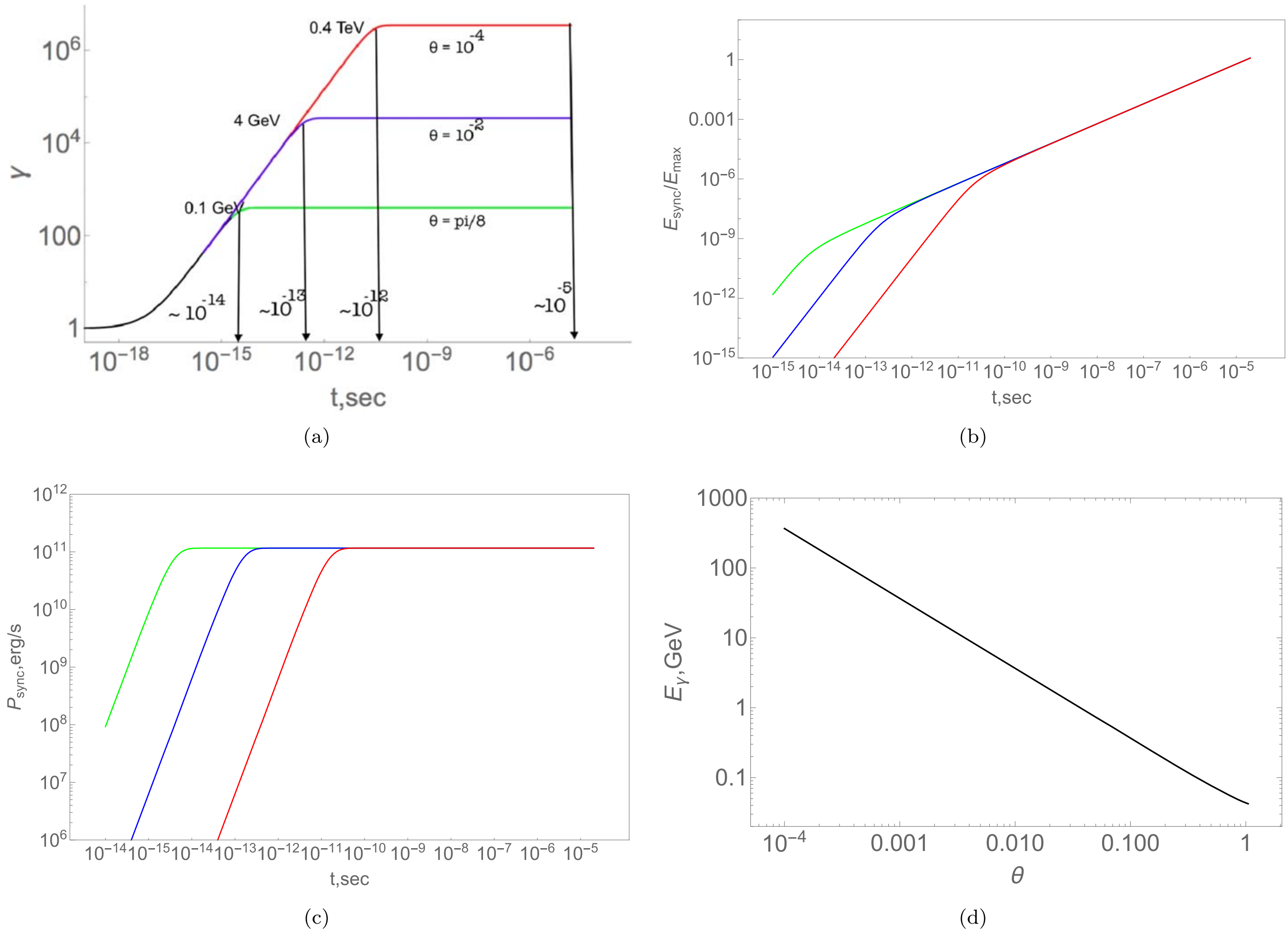

Figure 8. (a) The electron Lorentz gamma factor obtained from solutions of Equation (18) as functions of time: numerical (black), and analytic for selected angles: $\theta = \pi/8$ (green), $\theta = 1 \times 10^{-2}$ (blue), $\theta = 1 \times 10^{-4}$ (red) which according to Equation (23), they are related to $\sim$0.1 GeV, $\sim$4 GeV and $\sim$0.4 TeV energy of synchrotron photons, respectively. Parameters assumed: $a/M = 0.47$, $B_0/B_c = 7.8 \times 10^{-4}$. The arrow indicates the time when the energy emitted in synchrotron radiation equals $\epsilon_{\max,\gamma} = 10^{18}$ eV, which is $t = r_+/c \sim 2 \times 10^{-5}$ s. (b) Total energy emitted in synchrotron radiation from Equation (45) as a function of time for selected angles given in Figure 8(a). (c) Power of synchrotron emission by a single electron as a function of time for selected angles given in Figure 8(a). (d) Peak energy of synchrotron photons as a function of the angle between the electron velocity and the magnetic field.

In principle, as the timescale increases, the total available electron will decrease; we will return to this subject in Section 8, when we study the evolution of the time of sequence of elementary impulses.

Using Equation (23), the maximum energy $\epsilon_e \sim 1.6 \times 10^{18}$ eV is reached at the critical angle $\langle\theta\rangle \approx 2.2 \times 10^{-11}$. This gives an absolute lower limit on the $\langle\theta\rangle$ value for emitting synchrotron radiation. For $\langle\theta\rangle$ smaller than this critical angle, only UHECRs are emitted. See Figures 8(a) and 9.

The timescale of the process is in general set by the density of particles around the BH, which is provided by the structure of the cavity and SN ejecta; see Section 5.

We have already shown that during each such elementary process the BH experiences a very small fractional change of angular momentum:

$$|\Delta J|/J \approx (|\dot{J}|/J)\tau_{\rm ob} \approx 10^{-16},$$
$$|\Delta M|/M \approx (|\dot{M}|/M)\tau_{\rm ob} \approx 10^{-16}. \quad (49)$$

The electromagnetic energy of the first impulsive event given above is a small fraction of total extractable rotational energy of the Kerr BH; see Equation (4):

$$\frac{\mathcal{E}_1}{E_{\rm ext}} \approx 10^{-16}. \quad (50)$$

This clearly indicates that the rotational energy extraction from Kerr BH

(1) occurs in "discrete quantized steps";
(2) is temporally separated by 10^{-14}–10^{-10} s; and
(3) that the luminosity of the GeV emission in GRB 130427A is not describable by a continuous function as traditionally assumed: it occurs in a "discrete sequence of elementary quantized events" (Rueda & Ruffini 2019).

There are two main conclusions which can be inferred from the theory of synchrotron radiation implemented in this section.

1. Synchrotron radiation is not emitted isotropically and is angle dependent: the smaller the angle, the higher the synchrotron photon energy (see Equation (23) and Figure 9).

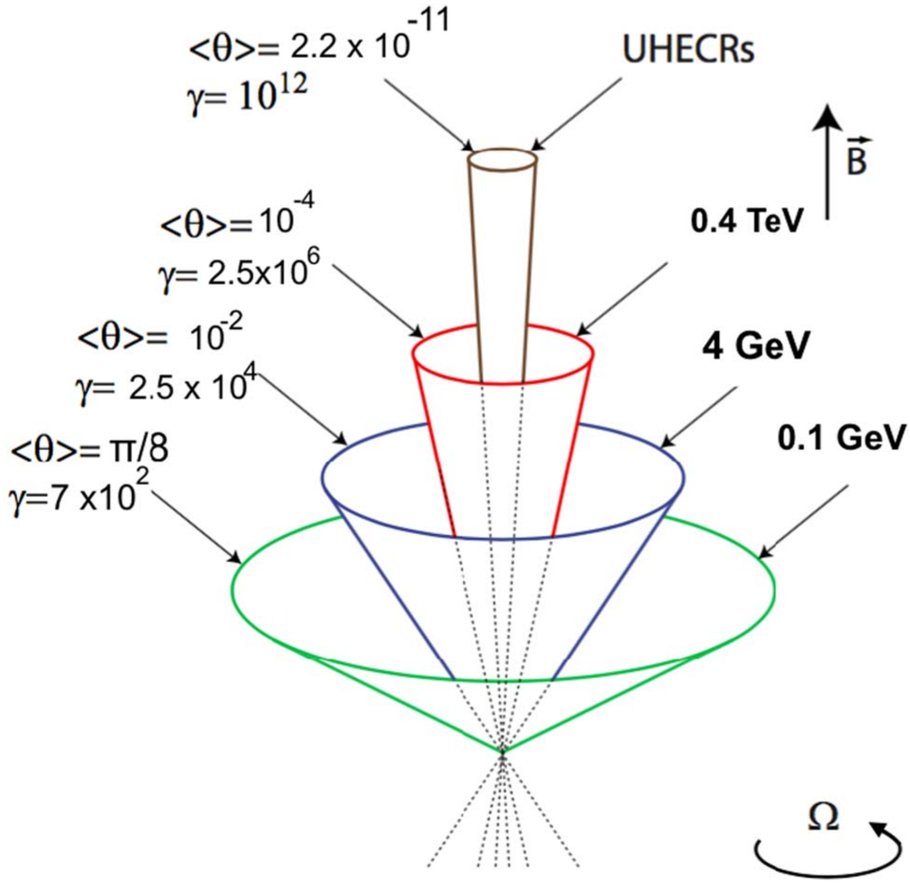

(a)

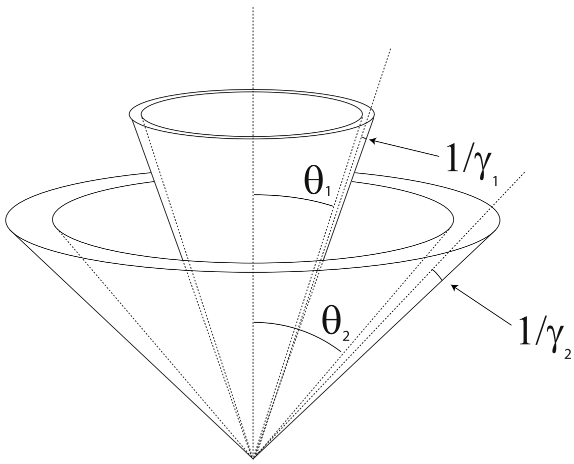

(b)

Figure 9. (Not to scale) (a) Having the values of spin and magnetic field, $a/M = 0.47$, $B_0/B_c = 7.8 \times 10^{-4}$, from Equation (23) for selected injection angles, we obtain the radiation in the different bands, 0.1 GeV to 0.4 TeV. Using Equation (23), the maximum energy $\epsilon_e \sim 1.6 \times 10^{18}$ eV is reached at the critical angle $\langle\theta\rangle = 2.2 \times 10^{-11}$. This angle is an absolute lower limit for emitting synchrotron radiation, therefore for $\langle\theta\rangle < 2.9 \times 10^{-11}$, electrons are accelerated to give rise to UHECRs. In this figure, the magnetic field is "parallel" to the Kerr BH rotation axis and electrons are accelerated outward and electrons captured by the horizon. (b) Synchrotron emission from electrons with pitch angle, θ. Radiation is concentrated in a cone of angle of $1/\gamma$.

2. The energy emitted in synchrotron radiation before reaching its asymptotic value is a function of injection angle θ; see the first line of Equation (45) and Figure 8(b).

To compare and contrast the results based on this essential theoretical treatment with observation, we need to determine (1) the number of electrons for each selected injection angle θ

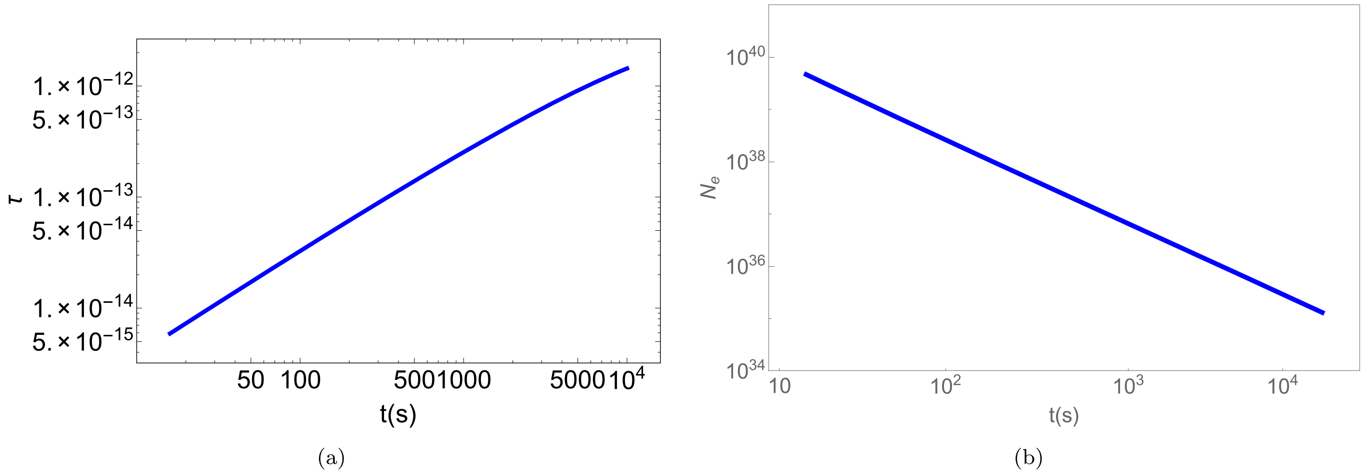

Figure 10. (a) The value of $\tau_{ob}(t) = E^2_{r_+} r^3_+ / (2L_{GeV})$ calculated from the GeV luminosity data obtained from *Fermi*-LAT together with the values of E_{r_+} and r_+ obtained in each impulsive event. This timescale increases linearly with the time t (in s) as $\tau_{ob} \approx 3 \times 10^{-16}\, t^1$. (b) The number of electrons available in each impulse to fulfill the observed properties of the inner engine of GRB 130427A.

and (2) to verify that the radiated synchrotron energy is compatible with the electrostatic energy for each electron. (3) Taking into due account the role of the beaming angle which we have here derived; see Figure 9 and extending the number of parameters by allowing the anisotropic distribution of electrons.

8. The Repetition Time of Sequence of the Discrete Elementary Impulsive Events

Finally, we study the sequence of iterative impulsive events in which the system starts over with a new value of the electric field set by the new values of the BH angular momentum and mass, $J = J_0 - \Delta J$ and $M = M_0 - \Delta M$, keeping the magnetic field value constant B_0.

We infer from the luminosity the evolution of the timescale $\tau(t)$ of the repetition time of the impulsive events by requiring it to explain the GeV emission, i.e.,

$$L_{GeV} = \frac{\mathcal{E}}{\tau(t)}, \tag{51}$$

where $\mathcal{E}$ is electrostatic energy available for each impulsive event. Therefore, we obtain for the timescale

$$\tau(t) = \frac{1}{2}\frac{E^2_{r_+} r^3_+}{L_{GeV}}, \tag{52}$$

where E_{r_+} is the electric field evaluated at the horizon determined from the new values of J and M for each elementary impulsive event consisted with Equation (49). Figure 10(a) shows that τ_{ob} is a increasing power-law function of time, i.e.,

$$\tau_{ob} \propto \frac{\alpha^2}{L_{GeV}} \propto t. \tag{53}$$

We identify the timescale τ_{ob} with the repetition time of each impulsive event. The efficiency of the system diminishes with time, as shown by the increasing value of τ_{ob} (see Figure 10(a)). This can be understood by the evolution of the density of particles near the BH decreasing in time owing to the expansion of the SN remnant, making the iterative process become less efficient. As we have mentioned, in the immediate vicinity of the BH a cavity is created of approximate radius 10^{11} cm and with very low density on the order of 10^{-13} g cm^{-3} (Ruffini et al. 2019b). This implies an approximate number of $\sim 10^{47}$ electrons inside the cavity. Then, the electrons of the cavity can power the iterative process only for a short time of 1–100 s. We notice that at the beginning of the gamma-ray emission, the required number of electrons per unit time for the explanation of the prompt and the GeV emission can be as large as 10^{46}–10^{54} s^{-1}. This confirms that this iterative process has to be sustained by the electrons of the remnant, at $r \gtrsim 10^{11}$ cm, which are brought from there into the region of low density and then into the BH. The synchrotron timescale, obtained from Equation (46), has values between 1.6×10^{-14} s and 2×10^{-5} s; see Figure 8(a). According to Equation (45) and Figure 8(b), the total energy available for the synchrotron radiation of one electron is a function of synchrotron timescale.

Therefore, when $t_c = 1.6 \times 10^{-14}$ s the total energy available for each electron is $\epsilon_e = 1.02 \times 10^9$ eV, which leads to the total number of electrons from Equation (48), $N_e = \mathcal{E}_1/\epsilon_e \approx 6.6 \times 10^{39}$ and when $t_c = 2 \times 10^{-5}$ s, the total energy available for each electron is $\epsilon_{e,\max} = 1.65 \times 10^{18}$ eV and the total number of electrons is $N_e = \mathcal{E}/\epsilon_{e,f} \approx 4 \times 10^{30}$, which can be seen in Figure 10(b).

It is worth mentioning that since the TeV synchrotron photons, in this picture, will start to be produced at $t_c \sim 10^{-11}$ s; see Figure 8(a). Therefore, according to Equation (53), the onset of TeV photons for GRB 130427A should be around 10^5 s (see Figure 10). This is clearly a zero-order approximation since, considering the effect of angle-dependent distribution of electrons, this time could be shorter (J. A. Rueda 2019, in preparation). In any case, the feedback from the observations is needed in order to improve the model.

9. Conclusions

In this paper, we confirm that the high-energy GeV radiation observed by *Fermi*-LAT originate from the rotational energy of a Kerr BH of mass $M = 2.31 M_\odot$ and a spin parameter of $\alpha = 0.47$ immersed in an homogeneous magnetic field of $B_0 \sim 3.48 \times 10^{10}$ G and an ionized plasma of a very low density, 10^{-14} g cm^{-3} (Ruffini et al. 2019b). The radiation occurs following the formation of the BH, via synchrotron radiation emitted by ultrarelativistic electrons accelerating and radiating in the framework of the Wald solution in the sequence of elementary impulses.

In the traditional approach, see e.g., Zhang (2018), there is a blast wave originating in the prompt radiation phase and propagating in a ultrarelativistic jet into the ISM medium emitting synchrotron radiation following the approach of Sari et al. (1999). There, the kinetic energy of the blast wave is used as the energy source. This process of emission occurs at large distances typically of 10^{15}–10^{16} cm and is traditionally used to explain the GeV emission observed by *Fermi*-LAT, as well as the X-ray afterglow emission observed by *SWIFT* and the radio emission observed by radio interferometers like the Westerbork Synthesis Radio Telescope (WSRT).

In our approach, the model is only a function of three parameters: the mass, M, and spin, α, of the Kerr BH, and the background magnetic test field, which have been self-consistently derived in this article. They fulfill all the energetic and transparency requirements. The acceleration and synchroton radiation process occurs within 10^5 cm from the horizon. The photon energy emitted by the syncrhoton radiation process is a very strong function of the injection angle of the ultrarelativistic electrons with respect to the polar axis. The outcome is an emission over a large angle, up to $\theta = \pi/3$: GeV at angle $\theta = \pi/8$ and TeV at $\theta = 10^{-4}$ all the way up to UHECR at angle $\theta < 10^{-11}$. The particles accelerated by the electromagnetic field of the Wald solution gyrate into the magnetic field, B_0. The highly anisotropic distribution in the energy and in the spectra is a specific consequence of the current model.

A byproduct of our model has been to evidence for the first time that the high-energy emission of GRB 130427A is not emitted continuously, but in a repetitive sequence of discrete and quantized "elementary impulsive events," each of energy 10^{37} erg and with a repetition time of $\sim 10^{-14}$ s and slowly increasing with time. This implies a very long time of extraction of the BH rotational energy via this electromagnetic process each utilizing a fraction of $\sim 10^{-16}$ of the mass-rotational energy of the BH. This result was truly unexpected, and it appears to be a general property both of GRBs and of much more massive Kerr BHs in active galactic nuclei. The results obtained in this paper lead to the concept of a "Blackholic Quantum" affecting our fundamental knowledge of physics and astrophysics (Rueda & Ruffini 2019).

It is appropriate here to recall that within BdHN model the GeV and TeV emission observed by *Fermi*-LAT and MAGIC detectors, originating from the Kerr BH, have a separate origin from the X-ray and radio observation of the afterglow. As recently demonstrated in five BdHN, GRB 130427A, GRB 160509A, GRB 160625B, GRB 180728A, and GRB 190114C (Rueda et al. 2019), the afterglow emission occurs due to the accretion process of the hypernova ejecta on the νNS spinning with a few millisecond period and the associated syncroton emission.

We thank the referee for the detailed reports and precise questions, which motivated a more precise formulation of our paper. We are grateful to Prof. G. V. Vereshchagin and to S. Campion for discussions in formulating the synchrotron radiation considerations and the related figures in the revised version. M.K. is supported by the Erasmus Mundus Joint Doctorate Program grant No. 2014–0707 from EACEA of the European Commission. N.S. acknowledges the support of the RA MES State Committee of Science, in the framework of the research project No. 18T-1C335.

ORCID iDs

J. A. Rueda https://orcid.org/0000-0002-3455-3063
N. Sahakyan https://orcid.org/0000-0003-2011-2731

References

Ackermann, M., Ajello, M., Asano, K., et al. 2011, ApJ, 729, 114
Ackermann, M., Ajello, M., Asano, K., et al. 2014, Sci, 343, 42
Ajello, M., Arimoto, M., Axelsson, M., et al. 2019, ApJ, 878, 52
Becerra, L., Bianco, C. L., Fryer, C. L., Rueda, J. A., & Ruffini, R. 2016, ApJ, 833, 107
Becerra, L., Ellinger, C. L., Fryer, C. L., Rueda, J. A., & Ruffini, R. 2019, ApJ, 871, 14
Becerra, L., Guzzo, M. M., Rossi-Torres, F., et al. 2018, ApJ, 852, 120
Breit, G., & Wheeler, J. A. 1934, PhRv, 46, 1087
Christodoulou, D. 1970, PhRvL, 25, 1596
Christodoulou, D., & Ruffini, R. 1971, PhRvD, 4, 3552
Cipolletta, F., Cherubini, C., Filippi, S., Rueda, J. A., & Ruffini, R. 2017, PhRvD, 96, 024046
Damour, T., & Ruffini, R. 1975, PhRvL, 35, 463
Daugherty, J. K., & Harding, A. K. 1983, ApJ, 273, 761
de Jager, O. C., Harding, A. K., Michelson, P. F., et al. 1996, ApJ, 457, 253
Erber, T. 1966, RvMP, 38, 626
Flores, H., Covino, S., Xu, D., et al. 2013, GCN, 14491
Gibbons, G. W., Mujtaba, A. H., & Pope, C. N. 2013, CQGra, 30, 125008
Harding, A. K. 1991, Sci, 251, 1033
Hawking, S. W. 1971, PhRvL, 26, 1344
Levan, A. J., Cenko, S. B., Perley, D. A., & Tanvir, N. R. 2013, GCN, 14455
Liang, L., Ruffini, R., Rueda, J. A., et al. 2019, arXiv:1910.12615
Misner, C. W., Thorne, K. S., & Wheeler, J. A. 1973, Gravitation (San Francisco, CA: Freeman)
Rueda, J. A., & Ruffini, R. 2019, arXiv:1907.08066
Rueda, J. A., Ruffini, R., Karlica, M., Moradi, R., & Wang, Y. 2019, ApJ, submitted (arXiv:1905.11339)
Rueda, J. A., Ruffini, R., Wang, Y., et al. 2018, JCAP, 10, 006
Ruffini, R., Becerra, L., Bianco, C. L., et al. 2018a, ApJ, 869, 151
Ruffini, R., Bernardini, M. G., Bianco, C. L., et al 2007, in AIP Conf. Proc. 910, XIIth Brazilian School of Cosmololy and Gravitation, ed. M. Novello & S. E. Perez Bergliaffa (Cambridge: Cambridge Univ. Press), 55
Ruffini, R., Karlica, M., Sahakyan, N., et al. 2018b, ApJ, 869, 101
Ruffini, R., Li, L., Moradi, R., et al. 2019a, arXiv:1904.04162
Ruffini, R., Melon Fuksman, J. D., & Vereshchagin, G. V. 2019b, ApJ, 883, 191
Ruffini, R., Rodriguez, J., Muccino, M., et al. 2018c, ApJ, 859, 30
Ruffini, R., Rueda, J. A., Muccino, M., et al. 2016a, ApJ, 832, 136
Ruffini, R., Salmonson, J. D., Wilson, J. R., & Xue, S.-S. 1999, A&A, 350, 334
Ruffini, R., Salmonson, J. D., Wilson, J. R., & Xue, S.-S. 2000, A&A, 359, 855
Ruffini, R., Vereshchagin, G., & Xue, S.-S. 2010, PhR, 487, 1
Ruffini, R., Vereshchagin, G. V., & Xue, S. S. 2016b, Ap&SS, 361, 82
Ruffini, R., Wang, Y., Enderli, M., et al. 2015, ApJ, 798, 10
Sari, R., Piran, T., & Halpern, J. P. 1999, ApJL, 519, L17
von Kienlin, A. 2013, GCN, 14473
Wald, R. M. 1974, PhRvD, 10, 1680
Wang, Y., Rueda, J. A., Ruffini, R., et al. 2019, ApJ, 874, 39
Xu, D., de Ugarte Postigo, A., Schulze, S., et al. 2013, GCN, 14478
Zhang, B. 2018, The Physics of Gamma-Ray Bursts (Cambridge: Cambridge Univ. Press)